DYNAMIC PROPERTIES OF PHASE CHANGE IN $Ge_2Sb_2Te_5$ (GST) BASED NANO MEMORY CELLS & MAGNETIC BUBBLES IN THIN FILM PERPENDICULAR ANISOTROPY NANOMAGNETS

by

İbrahim Çinar

B.S., Physics Education, Marmara University, 2005

Submitted to the Institute for Graduate Studies in
Science and Engineering in partial fulfillment of
the requirements for the degree of
Doctor of Philosophy

Graduate Program in Physics

Boğaziçi University

2017

DYNAMIC PROPERTIES OF PHASE CHANGE IN $Ge_2Sb_2Te_5$ (GST) BASED NANO MEMORY CELLS &
MAGNETIC BUBBLES IN THIN FILM PERPENDICULAR ANISOTROPY NANOMAGNETS

APPROVED BY:

Assoc. Prof. Özhan Özatay (Thesis Supervisor)	.....
Prof. Gülen Aktaş	.....
Assoc. Prof. Leyla Çolakerol Arslan	.....
Assoc. Prof. Başak Kayıtmazer	.....
Prof. V. Erkcan Özcan	.....

DATE OF APPROVAL: 23.08.2017

ACKNOWLEDGEMENTS

Firstly, I would like to express my sincere gratitude to my advisor Assoc. Prof. Özhan Özatay for the continuous support of my Ph.D study and related research, for his patience, motivation, and immense knowledge. His guidance helped me in all the time of research and writing of this thesis. I could not have imagined having a better advisor and mentor for my Ph.D study.

My sincere thanks also goes to Assoc. Prof. Thomas Hauet in Jean Lamour Institude in Nancy, France and Dr. Nicolas Reyren in Thales in Paris, France who provided me an opportunity to join their team as as a researcher, and who gave access to the laboratory and research facilities for the last year of my PhD. Without their precious support it would not be possible to conduct magnetic bubble research.

I would like to express my sincere gratitude to Dr. Ayşe Özbay for her valuable guidance for the experiment step of the PCM study and the beginning of the bubble study. I gratefully acknowledge her for helpful discussions and for her efforts in constructing the setup and taking data in the PCM study. I also thank Dr. Vito Puliafito and Assoc. Prof. Giovanni Finocchio for simulation of the bubble study.

I thank my fellow lab-friends Özgür Burak Aslan, Onur Dinçer, Vedat Karakaş and Egecan Çoğulu for the PCM study, Aytaç Paçal, Taha Dikici, Sevdenur Arpacı, Ali Taha Habiboğlu and Kaan Özbozduman and for bubble study for the stimulating discussions, helping me allocate resources, run experiments and collect results, for the sleepless nights we were working together before deadlines, and for all the fun we have had in the last seven years. Their friendship and assistance, which meant a lot to me and my research, would not have been possible without their help. I also thank especially Mehmet Yumak for his friendship and assistance which meant a lot to me.

A very special gratitude goes out to TUBITAK (Grant No: 113F385), Bogazici University Research Fund (Grant no :12B03M1) and European Union FP7 Marie Curie

International Re-integration Grant (Grant No: PCM-256281) for funding of the PCM work and TUBITAK (Grant No: 114F318) and TUBITAK 2214/A BIDEP Grant for funding of the Bubble work.

Last but not least, I am deeply appreciative of the support given to me by my parents, Kadir Çinar and Emine Güler Çinar, my elder sister Zeliha Oğuz, my older brother Yusuf Alper Çinar and my elder sister Zübeyde Akbal and especially my twin Mustafa Çinar and my sisters' husbands Fahrettin Oğuz and Esat Akbal. Their love provided my inspiration and was my driving force.

ABSTRACT

DYNAMIC PROPERTIES OF PHASE CHANGE IN $Ge_2Sb_2Te_5$ (GST) BASED NANO MEMORY CELLS & MAGNETIC BUBBLES IN THIN FILM PERPENDICULAR ANISOTROPY NANOMAGNETS

In this thesis, two different technologies with memory applications were studied. The first one, Phase Change Memory (PCM), is considered a potentially revelation technology for future ultra-high density data storage applications. To visualize the complex nature of the switching dynamics, 3D finite element modeling was carried out in PCM cell based on single layer $Ge_2Sb_2Te_5$ (GST) alloy, incorporating temperature and phase dependent thermal and electrical conductivities as well as Seeback coefficient to account for the thermoelectric effect. The experimentally determined resistance maps, those that are indicative of the crystallinity, show good agreement with the simulated phase change behavior confirming the existence of stable intermediate states. The potential stabilization of resistance levels in between the 0 and 1 states enables storage of several data in a single device cell. Current findings give way to a more stable ultrahigh-density PCM device. The second one is magnetic bubble. The nucleation of stable magnetic bubble in Co/Ni multilayer circular dots and nano-microwires with perpendicular magnetic anisotropy (PMA) and, patterned Spin-Valve are essential for fabrication of new devices for future technologies such as rf oscillator, detector or sensor. The parameters affecting the formation of bubbles such as the AC in-plane field demagnetization process, the diameter of dot and the width of wire were investigated. Beside bubble formation in dots, bubble behavior under in-plane magnetic field, motion induced by current pulses and bubble nucleation in spin-valves were studied.

ÖZET

$Ge_2Sb_2Te_5$ (GST) TABANLI NANO HAFIZA HÜCRELERİNDEKİ FAZ GEÇİŞİNİN VE İNCE FİLM DİKEY ANİSOTROPİLİ NANO MIKNATISLARDAKİ MANYETİK BALONCUKLARIN DİNAMİK ÖZELLİKLERİ

Bu tezde bellek uygulaması olan iki farklı teknoloji üzerinde çalışmalar yapılmıştır. İlki, Faz Değişim Belleği (PCM), gelecekte ultra yüksek yoğunluklu veri depolama uygulamaları için devrim açma potansiyeli olan teknoloji olarak düşünülmektedir. Anahtarlanma dinamiklerinin karmaşık yapısını görselleştirmek için, 3D sonlu elemanlar modellemesi, sıcaklık ve faz bağımlılığını içeren termal ve elektriksel iletkenlikleri ile birlikte termoelektrik etkiyi hesaba katmak için Seeback katsayısı eklenerek tek katmanlı $Ge_2Sb_2Te_5$ (GST) alaşım tabanlı PCM hücresinde uygulandı. Deneysel olarak elde edilen kristaliniteyi veren direnç haritaları kararlı ara geçiş durumlarının varlığını gösteren simüle edilmiş faz değişim davranışı ile iyi bir uyum göstermektedir. 0 ve 1 arasındaki direnç seviyelerinin kararlı olma potansiyeli dengelenmesi, tek bir cihaz hücresinde birkaç veri depolamanın mümkün olmasını sağlar. Mevcut bulgular, daha kararlı bir ultra-yüksek yoğunluklu PCM cihazına götürmektedir. İkinci, manyetik baloncuk, Co/Ni çok katmanlı dikey manyetik anizotropi (PMA) dairesel disklerde, nano-mikro tellerde ve desenlenmiş spin-valflerinde kararlı manyetik baloncuk oluşumu, RF osilatör, dedektör veya sensör gibi gelecek teknolojiler için yeni cihazların üretilmesi açısından önemlidir. AC düzlem içi demanyetizasyon işlemi, disk çapı ve tel genişliği gibi baloncuk oluşumunu etkileyen parametreler araştırılmıştır. Baloncuk oluşumunun yanı sıra, düzlem içi manyetik alan altında baloncuk hareketleri, akım darbelerinden kaynaklanan baloncuk hareketleri ve spin-vanasında baloncuk oluşumu çalışıldı.

TABLE OF CONTENTS

ACKNOWLEDGEMENTS . . . iii
ABSTRACT . . . v
ÖZET . . . vi
LIST OF FIGURES . . . ix
LIST OF TABLES . . . xxvii
LIST OF SYMBOLS . . . xxviii
LIST OF ACRONYMS/ABBREVIATIONS . . . xxix
1. INTRODUCTION . . . 1
1.1. Phase Change Memory (PCM) Study . . . 1
1.1.1. Phase Change Memory (PCM) . . . 5
1.1.2. Structural Properties of the Phase Change Materials . . . 9
1.1.2.1. Structural Properties of the Crystalline State . . . 9
1.1.2.2. Structural Properties of the Amorphous and Liquid States 12
1.1.3. Electrical Properties of The Phase Change Materials . . . 15
1.1.3.1. The Band Diagram for Chalcogenide Semiconductors . 15
1.1.3.2. Electrical Conduction in the Crystalline Phase . . . 17
1.1.3.3. Electrical Conduction in the Amorphous Phase . . . 20
1.2. Magnetic Bubble Study . . . 24
2. THREE DIMENSIONAL FINITE ELEMENT MODELING OF PCM . . . 42
2.1. Description of the Three-Dimensional Finite Element Modeling . . . 42
2.1.1. Electrical Model . . . 43
2.1.2. Thermal Model . . . 46
2.1.3. Phase Change and Percolation Model . . . 47
2.2. Simulation Results . . . 50
2.2.1. Electrical Conductivity and Resistivity Results . . . 61
2.2.2. Thermal Conductivity Results . . . 64
2.2.3. Phase Change Dynamics and Percolation Results . . . 67
2.2.4. Nucleation and Growth Rate Results . . . 73
2.2.5. Intermediate Resistance State Results . . . 79

3. DRIFT OF RESISTANCE IN TIME 83
3.1. Experimental Results 85
4. MAGNETIC BUBBLE STABILIZATION AND DYNAMICS 109
4.1. Deposition of Perpendicular Magnetic Anisotropy (PMA) Thin Film . . 109
4.1.1. Magnetic and Surface Characterization of the Thin Films . . . 112
4.1.2. Fabrication of Nano-Micro Dot Arrays and Wires 119
4.1.3. Stabilization of Bubbles in Dot Arrays and Wires 124
4.1.4. Spin-Valve Thin Film Deposition and VSM Measurements . . . 129
4.2. Single Bubble Formation Conditions in Spin-Valve Device 136
4.3. Fabrication of Nano-Micro Contacted Wires 143
4.4. Bubble Motion Induced By a Current Pulse Experiment Results 146
4.4.1. First Experiment Results 149
4.4.2. Second Experiment Results 152
4.5. Bubble Motion Under In-plane External Magnetic Field in a Dot . . . 156
4.5.1. First Experiment results 156
4.5.2. Second experiment results 161
5. CONCLUSION 172
5.1. Phase Change Memory Study Conclusions 172
5.2. Magnetic Bubble Study Conclusions 175
REFERENCES 179
APPENDIX A: MODELING OF PCM IN COMSOL MULTIPHYSICS 195
A.1. Model Navigator 195
A.1.1. Geometry Modeling 195
A.1.2. Global Definitions 197
A.1.2.1. Parameters 197
A.1.3. Model 1 200
A.1.3.1. Variables 200
A.1.3.2. Pairs 200
A.1.4. Joule Heating (jh) 203
A.1.5. Mesh 1 207
A.1.6. Study 1 208

LIST OF FIGURES

Figure 1.1. Electrical switching of phase change materials for non-volatile electronic storage. 3

Figure 1.2. Schematic of a PCM cell. 6

Figure 1.3. Programming scheme of PCM. 8

Figure 1.4. I-V characteristics of phase change material [2]. 9

Figure 1.5. Many alloys which are utilized as phase change materials lie on the GeTe - Sb_2Te_3 pseudobinary line [2]. 10

Figure 1.6. Rock-salt structure of GeTe. In ternary phase change materials, one sublattice is statistically occupied by germanium, antimony, and vacancy sites. 11

Figure 1.7. Rock-salt structure (a) and trigonal structure (b) of GeTe in the primitive unit cell. 12

Figure 1.8. Distribution of the local order parameter q for Ge with different coordination numbers N_c [40]. 14

Figure 1.9. Schematic drawing of the band diagrams for a chalcogenide semiconductor in either the crystalline (a) or the amorphous (b) phase. Ref 31. 16

Figure 1.10. Measured I-V curves for a PCM cell in the set (open symbols) or reset (filled symbols) states. The latter displays the threshold switching effect at about V_T, 1.2 V. From [52]. 17

Figure 1.11. Arrhenius plots of the resistance for a fully reset state, a fully set state, and two incomplete set states, A and B, obtained by the application of a voltage pulse to a phase change memory cell in the initial reset state. 18

Figure 1.12. Schematic drawings of two different mixed-phase configurations, characterized by an incomplete (A) or complete (B) percolation path through low-resistivity crystalline grains. In state A, the electrical current is limited by a small amorphous "barrier" whereas no amorphous barrier exists for state B. Yellow, crystalline; blue, amorphous. 19

Figure 1.13. Measured I-V characteristics in the subthreshold regime for amorphous $Ge_2Sb_2Te_5$ with increasing temperature. From [49]. 20

Figure 1.14. Arrhenius plot of the measured current for increasing voltage V ; 0.4, 0.7, and 1 V (right). From [56]. 21

Figure 1.15. Schematic for the analytical model for subthreshold transport. The potential barrier is equal to $\Delta\varphi(0)$ when no voltage is applied (a), and it drops to $\Delta\varphi(V)$ as a voltage V is applied, resulting in an exponential enhancement of the forward current in(b). The reverse contribution to the current I is exponentially lowered by the increase of the potential barrier $\Delta\varphi(-V)$ (c). From [56]. 22

Figure 1.16. Activation energy E_A, as a function of voltage, obtained from experimental I-V curves at variable temperature, and simulation results from the full analytical expression for E_A. From [56]. 23

Figure 1.17. a)Vortex and b) Antivortex magnetic configurations [65] 25

Figure 1.18. Vortex and Antivortex magnetic configurations properties, p (polarity) , n (chirality) and q (winding number or skyrmion number) [65] 26

Figure 1.19. Vortex center motion under external magnetic field [65]. 27

Figure 1.20. Vortex center motion under external magnetic field [67]. 27

Figure 1.21. Gyrotropic vortex motion in Co squares of different dimensions. (a) TR-PEEM images of domains in Co squares of patterns I($1\times1\mu m^2$), II ($1.5 \times 1\mu m^2$) and III ($2 \times 1\mu m^2$), taken at the specified delay times after the field pulse. (b) Trajectories of the vortex core [67, 70]. 28

Figure 1.22. Magneto-resistive cell and magneto-resistance. a) Schematic diagram of a magneto-resistive cell consisting of a perpendicular b) Schematic diagram of the IP and OP precession trajectories polarizer 29

Figure 1.23. a) Spin-Valve structure b)Part of the cross-sectional view of a nanowire sketched in panel and c) Nanowire is electrodeposited in a pore of a polycarbonate ion-track etched membrane [78] . . . 30

Figure 1.24. Magnetic bubble observation [79]. Magnetic domain images (a) as grown sample and (b) after applying a nearly in-plane magnetic field pulse. (c) Zoom-in image of the bubble domains in the SRT region. (d) Domain width as a function of the Fe film thickness, . 31

Figure 1.25. Magnetic bubble images for D0 0.5 μm and 50 nm thickness FePt disk. a)AFM and b)MFM image [84] 32

Figure 1.26. Illustration of MFM Measurement 33

Figure 1.27. Illustration of magnetic configuration in a magnetic bubble [84, 85]. 33

Figure 1.28. Magnetic texture of magnetic bubble [85]. 34

Figure 1.29. Skyrmion number and magnetic bubbles. a) skyrmion, N_{sk}=-1, b)antiskyrmion, N_{sk}=+1, c)and d) magnetic bubbles, N_{sk}=0. . . 34

Figure 1.30. Lorentz TEM observations [87] 35

Figure 1.31. Evolution of magnetic domain patterns with perpendicular magnetic anisotropy [88]. 36

Figure 1.32. Skyrmions for future storage devices [90]. 36

Figure 1.33. Schematics of magnetic skyrmion formation in constricted wires [91]. 37

Figure 1.34. MOKE microscopy images of pulse current-driven skyrmion motion [96]. 38

Figure 1.35. MFM images for 1.25 μm dot array and simulation results for thickness and H_{max} vs dot diameter [97]. 38

Figure 1.36. Snapshots from the simulation for a bubble with N=1 under external field gradient [99]. 39

Figure 1.37. Snapshots from the simulation for a bubble with N=0 under external field gradient [99]. 39

Figure 1.38. XMCD-PEEM image of the skyrmion during the application of an external magnetic field perpendicular to the film plane [103]. . . . 40

Figure 1.39. Schematic of the spin-valve point-contact geometry [105]. 41

Figure 2.1. Three-dimensional structure of PCM in the simulation is drawn in the figure a and figure b shows the material types in the PCM device used in the simulation. 44

Figure 2.2. Applied Potential in the simulation for 1 V with 100 ns pulse width and 42 ns trailing edge. 50

Figure 2.3. Potential Distribution in device during reset process at t = 100 ns for 1 V applied potential with 100 ns pulse width and 42 ns trailing edge. 51

Figure 2.4. Current versus time graph at z = 75 nm for 1 V applied potential with 100 ns pulse width and 42 ns trailing edge. 51

Figure 2.5. Current distribution through the PCM device at t =100 ns for 1 V applied potential with 100 ns pulse width and 42 ns trailing edge. 52

Figure 2.6. Current – time graph [108] 53

Figure 2.7. Current Density in the PCM cell for 1 V applied potential with 100 ns pulse width and 42 ns trailing edge. 53

Figure 2.8. Current Density in the PCM cell [108]. 54

Figure 2.9. Temperature versus time of two different points in GST bulk for 1 V applied potential with 100 ns pulse width and 42 ns trailing edge. 55

Figure 2.10. The temperature distribution in PCM device for 1 V applied potential with 100 ns pulse width and 42 ns trailing edge. 56

Figure 2.11. Temperature distribution inside the circular top contact PCM cell for 1 V applied potential with 100 ns pulse width and 42 ns trailing edge. 57

Figure 2.12. Temperature distribution inside the square top contact PCM cell for 1 V applied potential with 100 ns pulse width and 42 ns trailing edge. 58

Figure 2.13. Temperature distribution in z-direction for 1 V applied potential with 100 ns pulse width and 42 ns trailing edge. 58

Figure 2.14. Temperature distribution in z-direction [109]. 59

Figure 2.15. A three dimensional illustration of temperature distribution is plotted for different vertical and horizontal slices for a-c: 75 nm circular top contact PCM device and d-f: 90 nm square top contact device. During a programming voltage pulse of 1V, with 100 ns width and 42 ns trailing edge. Figures a and d specifically show the horizontal slice 5 nm below the interface between the top contact and the GST layer. 60

Figure 2.16. Electrical Conductivity versus temperature for Crystalline Phase 0.85 V applied potential with 100 ns pulse width and 42 ns trailing edge. 61

Figure 2.17. Electrical Conductivity versus temperature for Crystalline Phase 1 V applied potential with 100 ns pulse width and 42 ns trailing edge. 62

Figure 2.18. Resistivity versus temperature for Crystalline Phase 1 V applied potential with 100 ns pulse width and 42 ns trailing edge. 63

Figure 2.19. Resistivity versus temperature for Amorphous and Crystalline Phase REF 52. 64

Figure 2.20. Thermal Conductivity versus temperature for Crystalline Phase for 1 V applied potential with 100 ns pulse width and 42 ns trailing edge [108]. 65

Figure 2.21. Thermal Conductivity versus temperature for Amorphous and Crystalline Phases [56]. 66

Figure 2.22. Results of Electrical Conductivity, Thermal Conductivity and Heat Capacity of the phase change material obtained from the simulation [115]. 66

Figure 2.23. Crystallization fraction versus time for the GST material. 68

Figure 2.24. Percolation for blocked and open situation. 69

Figure 2.25. Normalized conductivity versus Crystallization fraction for 1 V applied potential with 100 ns pulse width and 42 ns trailing edge. . . 70

Figure 2.26. Crystallization fraction inside the circular top contact PCM cell after Reset operation for 1 V applied potential with 100 ns pulse width and 42 ns trailing edge. 70

Figure 2.27. Crystallization fraction inside the square top contact PCM cell after Reset operation for 1 V applied potential with 100 ns pulse width and 42 ns trailing edge. 71

Figure 2.28. Crystallization fraction, f, inside the phase change layer is shown for circular (a-c) and square (d-f) top contact PCM cells after the application of a 100 ns reset pulse with a 42 ns trailing edge. The color scale corresponds to f = 1, red, for crystalline and f = 0, blue, for amorphous phases. The colors between the two represent regions with a mixture of crystalline and amorphous phases. A vertical cross-section of the device taken through the center is given for different pulse amplitudes resulting in different device resistances: a) 0.9 V, 1.7 kΩ; b) 1V, 167 kΩ; d) 1.3 V, 194 kΩ; e) 1 V, 15 kΩ (The figures represent a 150 nm width device and a set of dashed lines indicating the contact region are provided as guide to the eye). The three dimensional figures c and f correspond to the same pulse amplitudes as figures b and e, respectively. 72

Figure 2.29. Nucleation rate versus temperature for the GST material for 1 V applied potential with 100 ns pulse width and 42 ns trailing edge. 74

Figure 2.30. Nucleation rate versus time for the GST material for 1 V applied potential with 100 ns pulse width and 42 ns trailing edge. 74

Figure 2.31. Growth rate versus time for the GST material for 1 V applied potential with 100 ns pulse width and 42 ns trailing edge. 75

Figure 2.32. Growth rate versus temperature for the GST material for 1 V applied potential with 100 ns pulse width and 42 ns trailing edge. 75

Figure 2.33. Pulse width and pulse amplitude corresponding to normalized resistance for 90 nm square top contact with 2 ns and 42 ns trailing edge. 76

Figure 2.34. Pulse width and pulse amplitude corresponding to normalized resistance for 90 nm square top contact with 1, 5, 10 x NR and GR Values. 77

Figure 2.35. Pulse width and pulse amplitude corresponding to normalized resistance for 75 nm circular contact square top contact with 1, 2, 3 x NR and GR Values. 77

Figure 2.36. Pulse width and pulse amplitude corresponding to normalized resistance for 90 nm square top contact 42 ns trailing edge for two different NR and GR values. 78

Figure 2.37. Pulse width and pulse amplitude corresponding to normalized resistance for 75 nm circular top contact with 42 ns trailing edge. 79

Figure 2.38. Normalized resistance vs pulse width & amplitude for 75 nm circular top contact with 42 ns trailing edge (simulation result). 80

Figure 2.39. Normalized resistance vs pulse width & amplitude for 75 nm circular top contact with 42 ns trailing edge (experimental result). 80

Figure 2.40. Normalized resistance vs pulse width & amplitude for 90 nm square top contact with 42 ns trailing edge (experimental result). 81

Figure 2.41. Normalized resistance vs pulse width & amplitude for 90 nm square top contact with 42 ns trailing edge (simulation result). 82

Figure 3.1. Phase change memory device measurement circuit diagram. . . . 83

Figure 3.2. Experimental setup for measuring the switching characteristics of phase change memory devices. 85

Figure 3.3. For a selected 130 nm square contact PCM device, I-V and R-V graphs after reading. 86

Figure 3.4. For a selected 500 nm square contact PCM device, I-V and R-V graphs after reading. 87

Figure 3.5. Set Operation for a selected 130 nm square contact PCM device. . 87

Figure 3.6. Reset Operation for a selected 75 nm circular contact PCM device. 88

Figure 3.7. Reset Operation for a selected 130 nm square contact PCM device. 89

Figure 3.8. Set Operation for a selected 130 nm square contact PCM device. . 90

Figure 3.9. The voltage pulse applied to obtain intermediate resistance for a 500 nm contact PCM device and Resistance values. 91

Figure 3.10. Reset Operations for a selected 75 nm circular and a 90 nm square contact PCM device. Experimental and Simulation results are given for comparison. a and c are the experimental results and b and d are the simulation results [115]. 92

Figure 3.11. Resistance change of the crystalline phase (SET state) in time for a selected 130 nm square contact PCM device. 93

Figure 3.12. For a selected 130 nm square contact PCM device R/R_0–t/t_0. ν parameter is 0.0009. 94

Figure 3.13. Resistance change of the amorphous phase (Reset state) in time for a selected 500 nm square contact PCM device. 95

Figure 3.14. For a selected 500 nm square contact PCM device R/R_0–t/t_0. ν parameter is 0.107 and initial resistance value is 0.9 $M\Omega$ 96

Figure 3.15. The resistance change of PCM device and the ν parameter is less than 0.01 for LRS and about 0.1 for HRS [59]. 96

Figure 3.16. Resistance change for a selected 130 nm square contact PCM device and initial resistance value is 116 $k\Omega$ 97

Figure 3.17. For a selected 130 nm square contact PCM device R/R_0–t/t_0. ν parameter is 0.0102. 98

Figure 3.18. Resistance changes of LRS, HRS and IRS for a selected 130 nm square contact PCM device. 98

Figure 3.19. Temperature dependence of the initial resistance levels of HRS (squares), IRS (circles) and LRS (stars). 99

Figure 3.20. Variation of the drift coefficient with temperature for reset, (a), and intermediate, (b), states. Drift coefficients are extracted at each temperature from the resistance drift after programming. . . 101

Figure 3.21. Schematic representation of the hopping conduction mechanism through traps in a PCM device. 101

Figure 3.22. I-V characteristics in the subthreshold regime for reset (squares) and intermediate (circles) states of a 90 nm square contact PCM cell . The linear fits to lnI(V), indicated by dashed lines, reveal the STS. The inset shows the full switching dynamic, I on the left scale with a dotted line and R on the right scale with a solid line, starting from a HRS to an IRS then to LRS with a limit current of 1 mA. 104

Figure 3.23. Effective number of defects is calculated for various wait times after programming in IRS and HRS. 106

Figure 3.24. A simulation of the vertical cross-section of a 130 nm square top contact device taken through the center right after a programming pulse of 100 ns width and 42 ns trailing edge. Crystallization fraction, f, inside the phase change layer is shown in color code which corresponds to f = 1, red, for crystalline and f = 0, blue, for amorphous phases. The colors between the two represent regions with a mixture of crystalline and amorphous phases. 107

Figure 4.1. a) AJA magnetron sputtering system b) PPMS Vibrating Sample Magnetometer (VSM). 110

Figure 4.2. Magnetic thin film with perpendicular magnetic anisotropy (PMA) and the thickness of the layers and repeat numbers. 110

Figure 4.3. X-ray diffraction (XRD) measurements for grown C0 (a) and Pt (b) to obtain deposition rate. 113

Figure 4.4. VSM results of the thin film with perpendicular magnetic anisotropy (PMA)under out of plane external magnetic field. 114

Figure 4.5. (Ta(5)/Pt(10)/[Co(0,2)/Ni(0,6)]$_N$/Pt(5nm)) PMA thin films out of plane VSM results at room temperature. 115

Figure 4.6. (Ta(5)/Pt(10)/[Co(0,2)/Ni(0,6)]$_N$/Pt(5nm)) PMA thin films in-plane VSM results at room temperature. 116

Figure 4.7. Line fit to find H_k value for (Ta(5)/Pt(10)/[Co(0,2)/Ni(0,6)]$_8$/Pt(5)) PMA thin film B2 from the in-plane VSM result at room temperature. 116

Figure 4.8. AFM surface topography and MFM image of the thin film. . . . 118

Figure 4.9. AC demagnetization field with 4-minute period and 120 minutes from max 650 mT (6500 Oe) to 0 fields. 119

Figure 4.10. a) Nano-micro dot arrays pattern b) applied dose values. 120

Figure 4.11. Optic microscope image of dot arrays after patterning process. . . 120

Figure 4.12. Nano-micro wires pattern and applied dose values. 121

Figure 4.13. Optic microscope image of wires after patterning process. 122

Figure 4.14. Optic microscope image of dot arrays and wires after patterning process. 122

Figure 4.15. Ion milling process steps for patterning of nano-micro disk arrays and wires. 123

Figure 4.16. $3\mu m$ dot arrays AFM surface topography a) 2 D b) 3 D images. . 123

Figure 4.17. After 6500 Oe in-plane AC demagnetization $1.25\mu m$ dot arrays AFM and MFM images. a) 2D AFM b) 3 D AFM images c) MFM images. 124

Figure 4.18. After 5000 Oe in-plane AC demagnetization, MFM images for different diameter dot arrays (yellow circles single domain structures, red ones bubbles and blue ones multi-domains, as examples of the magnetic structures). 125

Figure 4.19. MFM images for $1.5\mu m$ dot arrays with different AC demagnetization treatments. 126

Figure 4.20. After 6500 Oe in-plane AC demagnetization, MFM images for different diameter dot arrays $1.0\mu m$, $1.25\mu m$ and $1.5\mu m$. 127

Figure 4.21. After 6250 Oe in-plane AC demagnetization, MFM image for $1.5\mu m$ dot array. 128

Figure 4.22. After 6500 Oe in-plane AC demagnetization, MFM images for different wire thicknesses $0.8\mu m$, $1.0\mu m$ and $1.2\mu m$. 128

Figure 4.23. After 6250 Oe in-plane AC demagnetization, MFM images for different wire thicknesses $0.8\mu m$, $1.0\mu m$ and $1.2\mu m$. 129

Figure 4.24. Schematic drawing of a Spin-valve structure. 129

Figure 4.25. VSM data for as grown Co/Pt with PMA. 131

Figure 4.26. VSM measurements for out of plane and in plane of Hard (or Fixed) layer. 131

Figure 4.27. VSM measurement data analysis to find Hk for Hard (or Fixed) layer. 132

Figure 4.28. Spin-valve structures with layers and thicknesses. 133

Figure 4.29. Spin-valve structure VSM results. 133

Figure 4.30. Spin-valve structures with layers and thicknesses. 134

Figure 4.31. Spin-valve structure VSM results. 134

Figure 4.32. Spin-valve structure VSM results. 135

Figure 4.33. VSM results for different type of wafers. 136

Figure 4.34. Spin-valve structures with layers and thicknesses. 137

Figure 4.35. Spin-valve structure VSM results. 137

Figure 4.36. MFM images for 1.5μm dot size after 6450 Oe Hmax AC in-plane external magnetic field demagnetization. 138

Figure 4.37. MFM images for 1.25μm dot size after 6450 Oe Hmax AC in-plane external magnetic field demagnetization. 139

Figure 4.38. MFM images for 1.0μm dot size after 6450 Oe Hmax AC in-plane external magnetic field demagnetization. 140

Figure 4.39. MFM images for 1.0μm dot size after 6950 Oe Hmax AC in-plane external magnetic field demagnetization. 141

Figure 4.40. MFM images for different width wires after 6450 Oe Hmax AC in-plane external magnetic field demagnetization. 142

Figure 4.41. The contacted wires Layout editor design. 143

Figure 4.42. Optical microscope image of wire and markers after patterning process and dimension of wire. 145

Figure 4.43. Optical microscope images of wires, contacts and markers after patterning process. 146

Figure 4.44. Image of wires, contacts and markers in the E-beam Lithography system. 147

Figure 4.45. MFM Image of 0.8 μm wire. Bubbles are clear on the wire. . . . 147

Figure 4.46. MFM Images of 0.8 μm wire. Bubbles are vanishing due to tip moment. 148

Figure 4.47. MFM Images of 0.8 μm wire. Bubbles are vanishing due to tip moment. 149

Figure 4.48. MFM Image of 0.8 μm wire after applying 1000 pulse 3 V 1 μs pulse width, current I = 11.1 mA and current density J = 5.3 10^{11} A/m^2. 149

Figure 4.49. MFM Images of 0.8 μm wire after applying three different pulses and annihilation of bubble. 150

Figure 4.50. MFM Images of 0.8 μm wire after applying three different pulses, changing in the size of the middle bubble and later domains. . . . 151

Figure 4.51. MFM Images of 0.8 μm wire after applying different pulses. Nucleation and annihilation of bubbles with current pulses are observed. 151

Figure 4.52. MFM Images of 0.8 μm wire after applying different pulses. Nucleation and annihilation of bubbles with current pulse are observed.152

Figure 4.53. MFM Images of 0.8 μm wire after applying current pulse and annihilation of bubbles. 153

Figure 4.54. MFM Images of 0.8 μm wire to check tip, annihilation of bubble are observed in reservoir. 153

Figure 4.55. MFM Images of 1.0 μm wire to check tip. 154

Figure 4.56. MFM Images of 1.0 μm wire after different current pulses. 155

Figure 4.57. MFM Images of 1.0 μm wire to nucleate bubble with current pulse. 156

Figure 4.58. MFM Images of 1.0 μm wire after different pulses, and enlargement of bubbles. 157

Figure 4.59. MFM Images of 1.0 μm wire after applying different pulses and, enlargement and destruction of bubbles. 158

Figure 4.60. MFM image of 1.5 μm bubble in dot for initial case. 158

Figure 4.61. MFM images of 1.5 μm dot at zero fields. 159

Figure 4.62. MFM images of 1.5 μm dot at different external magnetic field values. 160

Figure 4.63. MFM images of 1.5 μm dot at different external magnetic field values. 161

Figure 4.64. MFM images of 1.5 μm dot at different external magnetic field values. 162

Figure 4.65. MFM images of 1.5 μm dot at different external magnetic field values in second experiment. 163

Figure 4.66. Simulation results of z component of magnetization for different in-plane external magnetic fields. 166

Figure 4.67. Simulation results of second derivative of y component of magnetization for different in-plane external magnetic fields. 169

Figure 4.68. Comparisons of simulation and experimental results. 170

LIST OF TABLES

Table 1.1. Comparison of Flash Memory and PCM (OUM) 2

Table 1.2. Crucial Properties of Phase-Change Materials 4

Table 2.1. The resistivity and temperature coefficient values used in the simulation 45

Table 2.2. The thermal conductivity, density and heat capacity values used in the simulation 47

Table 3.1. Parameters Extracted From I-V Curves 105

Table 4.1. Growth conditions and deposition rates of the materials in the PMA thin films 111

Table 4.2. Ms, Hc, Hk ve K values of the thin films 117

Table A.1. Parameters 1 198

Table A.2. Parameters 2 199

Table A.3. Variables 1 201

Table A.4. Variables 2 202

LIST OF SYMBOLS

H_c	Coercive Field
H_k	Anisotropic (Magnetic) Field
K	Anisotropy Coefficient
M_s	Saturation Magnetization
N_{sk}	Skyrmion Number
ν	Drift Coefficient

LIST OF ACRONYMS/ABBREVIATIONS

2D	Two Dimensional
3D	Three Dimensional
AC	Alternating Current
AFM	Atomic Force Microscopy
BE	Bottom Electrode
CD	Compact Disc
DC	Direct Current
DVD	Digital Versatile Disc
EMA	Effective medium approximation
EXAFS	Extended X-ray Absorption Fine Structure
FCC	Face Center Cubic
FMR	Ferromagnetic resonance
GHz	Giga Hertz
GPIB	General Purpose Interface Bus
GR	Growth Rate
GST	$Ge_2Sb_2Te_5$
HRS	High Resistance State - Reset (or Amorphous) State
IRS	Intermediate Resistance State - Intermediate State
LM	Low Moment
LRS	Low Resistance State - Set (or Crystalline) State
MFM	Magnetic Force Microscopy
MIBK	Methyl Isobutyl Ketone
MRAM	Magnetoresistive Random-Access Memory
NMP	N-Methyl-2-Pyrrolidone
NR	Nucleation Rate
NVM	Non-Volatile Memory
OUM	Ovonyx United Memory
PCM	Phase Change Memory

PDE	Partial Differential Equation
PEEM	Photoemission Electron Microscopy
PF	Poole–Frenkel
PMA	Perpendicular Magnetic Anisotropy
PMMA	Poly methyl methacrylate
PPMS	Physical Properties Measurement System
RF	Radio Frequency
SMA	Sub Miniature version A
TE	Top Electrode
TEM	Transmission Electron Microscopy
TMAH	Tetramethylammonium Hydroxide
VSM	Vibrating Sample Magnetometer
XMCD	X-ray Magnetic Circular Dichroism
XRD	X-Ray Powder Diffraction

1. INTRODUCTION

1.1. Phase Change Memory (PCM) Study

People always need to store information to transfer to future generations. For example, pictures in caves, parchments in ancient Egypt, books in the Middle Ages are well-known means of transfer data. Nowadays, the requirement to store more data in a limited area has been increasing day by day and it is the fundamental issue for the new age that we live in. Up to now, many available different types of data storage technologies have met this demand. In the last decade, the digital media industry has achieved great improvements to replace traditional data storage devices like Compact-Disc players and film cameras with digital ones like iPods and digital cameras. However, the amount of information that we have to store is increasing day by day. This requirement is an important driving factor to produce or design better and better and, faster and faster non-volatile memory (NVM), which can be used in these digital devices to store huge amount of information in a limited area. Thanks to many different types of non-volatile memory technologies, there are many available mass-production data storage devices in the market such as hard disks and magnetic tapes and so on. New types of NVMs are still under development.

Since the last decade, Flash random access memories have been of widespread use as non-volatile solid-phase memories. However, flash memory has some inherent physical limitations like charge leakage due to lack of scalability and block erasure because of the programming problem. Therefore, there is an intense research effort to come up with new non-volatile solid-phase memories as contenders to replace flash random access memory. One of these contenders is the phase change random access memory (PCRAM or PCM) utilizing phase change materials. PCM is also called as OUM (Ovonyx United Memory). PCM has a lot of advantages over flash memory such as GHz scale write and read rates, low power consumption, low cost, scalability, long term reliability and so on [1–8].

Table 1.1. Comparison of Flash Memory and PCM (OUM) [9].

	FLASH	**OUM**
Cell size F^2	7 – 11	5 - 8
Volume @.18μm (F^3)	1	0.028
Endurance write / read	1×10^6 / ∞	$> 1 \times 10^{12}$ / ∞
Direct over-write	No	Yes
Bit / Byte Write / Erase	Block	Yes
Read dynamic current range	Delta Current	$10\times$ - $100 \times R$
Programming energy	High	Low
Write / Erase / Read time	1μs / 1 – 100ms (block) / 60ns	10ns / 50ns / 20ns
3D potential	No	Yes
Relative cost per bit	Medium	Low

For PCM technologies, the write time for different phases is about 50 ns and 150 ns [10], while Flash memory needs about 1ms to 100ms to erase data and a few μs for write. Because of the high write speed, researchers have considered using PCM as Random Access Memory in computers. Excellent endurance and data retention ability are also important properties for the non-volatile memory. The application possibility to increase the data storage density of a PCM device is also an important advantage, having the capability to produce multi-bit-per cell device by obtaining stable states between the amorphous and crystalline phases.

The basic principle of the PCM concept is displayed in Figure 1.1 which shows how information is stored in phase change materials depending on the properties of applied electrical or laser pulse [11].

In a PCM device, information is stored in the form of the electrical resistance or optical reflectance of phase change material. When applying an electrical pulse or laser pulse to the device, the pulse width and its magnitude are very important to achieve phase transition between the amorphous and crystalline phase. For a phase change

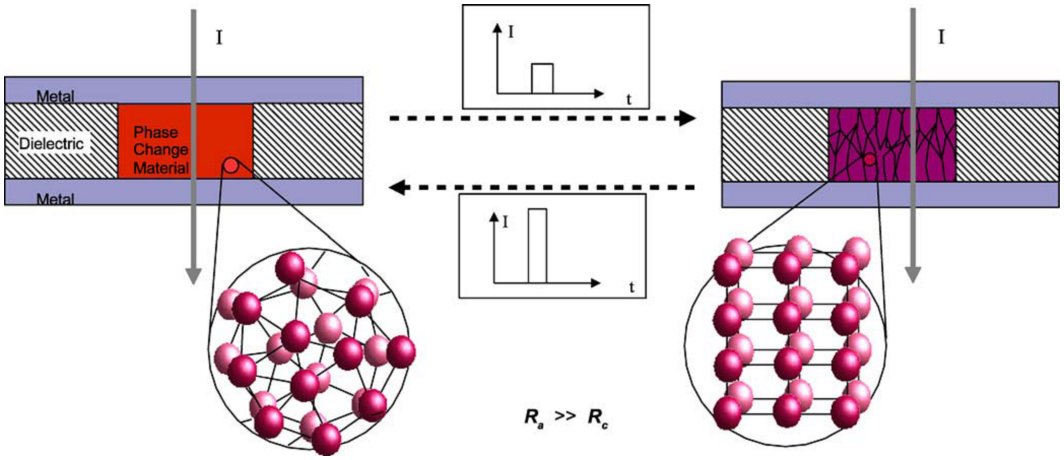


Figure 1.1. Electrical switching of phase change materials for non-volatile electronic storage.

material in amorphous phase (disordered phase), like Figure 1.1, the amorphous phase has a high resistance and low reflectance. Applying a long electrical or laser pulse (several hundred ns, the pulse should increase the temperature of the material above the crystallization or glass transition temperature) locally heats the amorphous region, and phase change material rearranges into the crystalline phase (ordered phase), if there is enough time for the rearrangement of phase change material atoms. During cooling to switch back to the amorphous phase, applying a larger electrical pulse or laser pulse to the crystalline phase leads to local melting and forms an amorphous region on rapid quenching (several ns). The stored information can be easily read-out by applying an electrical pulse or laser pulse with low enough amplitudes as not to disturb the phase via heating since there is a huge difference in the resistance and reflectance in the amorphous and crystalline phases.

Even though there are many alloys, which can be used as phase change materials due to forming amorphous and crystalline phase through switching process, there are only a few of them which show a distinct contrast in electrical and optical properties between the amorphous and crystalline phases. Therefore, only few of them can be used to construct PCM data storage device. The physical explanation behind the contrast in electrical and optical properties comes from particularly having different

atomic arrangements between the amorphous and crystalline phase. However, for the re-crystallization during switching process, the atomic rearrangement takes place in a very short time scale (several ten to one hundred nanoseconds) [3, 12]. The required properties of the phase change materials are summarized in Table 1.2.

Table 1.2. Crucial Properties of Phase-Change Materials

Required property of PC material	**Specification**
High-speed phase transition	Induced by nanosecond laser or voltage pulse
Long term thermal stability of amorphous state	At least several decades at room temperature
Large optical change between the two states (for rewriteable optical storage)	Considerable difference in refractive index or absorption coefficient
Large resistance change between the states (for non-volatile electronic storage)	Natural consequence of the transformation from amorphous to crystalline state
Large cycle number of reversible transitions	More than 100,000 cycles with stable composition
High chemical stability	High water-resistivity

PCM based on $Ge_2Sb_2Te_5$ (GST) has been the most widely used and studied because of this material's outstanding thermal and electrical properties [13–17]. The correlation between the crystallinity of the phase change material and its optical properties is well described [9, 18] and has been utilized successfully in optical recording systems for more than two decades. Even though there are many rewritable optical storage media like CD and DVD, many candidates for non-volatile memory may be much more because of having large contrast between phases and easy switching from one phase to another phase with electrical pulses. In this study, for non-volatile memory media, I focus on the high signal to noise ratio between amorphous and crystalline phase of the phase change material to investigate the possibility of having multi-bit-per cell operation by obtaining a stable intermediate resistance level [5, 11, 13–15, 17]. The

accompanying large contrast in the resistance states will allow multiple-bit-per-cell operation provided that stable intermediate resistance levels corresponding to multilevel phase transition between the high resistance (amorphous (or Reset) state) (HRS) and low resistance (crystalline (or Set) state) (LRS) can be obtained.

In literature, there have been new strategies introduced to construct a multiple-bit-per-cell nonvolatile phase change memory device. These strategies can be separated into two groups, which are to modify the phase change properties by doping such as N implanted GST, Se doped GeSb, $Ga_2Te_2Sb_5$, and to use multilayer stacks of phase change alloys with different phase transition properties such as $Sb_2Te_3/Ge_2Sb_2Te_5$, $GeTe/Ge_2Sb_2Te_5$ and $InSe/\ Ge_2Sb_2Te_5$. Although, using these strategies, intermediate resistance states can be obtained, they suffer from lack of long term stability due to bulk defects in doped thin films and interfacial defects in multilayer stacks. To resolve this issue I introduce a different way to construct a multiple-bit-per-cell PCM device via changing the top contact geometry of the device [16, 19–26].

In my study, both experimentally and by finite element modeling, I show that a single active layer GST based PCM device can display multiple resistance levels between HRS and LRS. My model suggests that such multi-level switching behavior can be explained as being due to inhomogeneous current distribution and locally modified phase change kinetics (crystalline nucleation and growth rates) and is observed in devices with non-circular contact electrodes. Before giving further details about this study, I will introduce PCM device concept.

1.1.1. Phase Change Memory (PCM)

Due to extraordinary properties of phase change materials like having two phases with unique phase change characteristics upon heat treatments depending on the applied electrical or laser pulse, there is growing interest from not only researchers in academic institutions but also from many commercial companies, like IBM, Intel, Samsung and so on, searching new data storage media. PCM architecture has two fundamental parts: the active region for information storage and contacts to electrically access the

device. Data storage part consists of some special chemical compounds called as phase change materials. These compounds are glasses containing one or more chalcogenide elements as a substantial constituent. (Chalcogenide elements are in the Group 6 in the periodic table e.g. Sulfur, selenium or tellurium). The chalcogenide glasses are strong glass formers. In 1968, Ovshinsky from Stanford University first discovered characteristics of phase change materials [27]. Figure 1.2 illustrates a typical PCM cell.

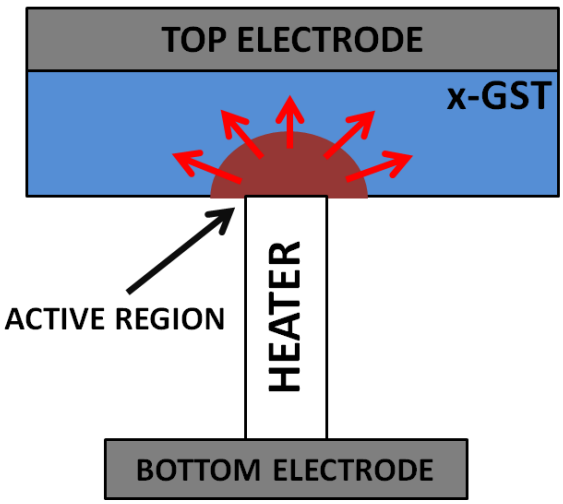


Figure 1.2. Schematic of a PCM cell.

The PCM device is made-up of a metallic pillar in contact with the GST layer. For switching between the phases of a phase change material, the applied electrical or laser pulse's width and its magnitude is very important to heat the phase change material above its crystallization (glass transition) temperature or melting temperature. When a large amount of heat is applied to the material in a short time (Reset pulse duration, for example 20 ns) to drive the heated region in the phase change material above the melting temperature and subsequently cooled within a very short time (several ns), phase change occurs and the melted region is driven into amorphous phase. This process is called as Reset operation. When relatively moderate amounts of heat is applied to the material in a much longer time to increase the temperature of the region between the melting point and the glass transition point and then kept at this elevated temperature for longer time (Set pulse duration, for example 100 ns), the

re-crystallization of the amorphous material is triggered and the amorphous regions crystallize. This process is called the Set operation.

In my study, instead of using laser beams to heat the phase change material, I focus on electrical pulses. When I use a large amplitude driving current to heat the phase change material to different temperature values (glass or crystallization temperature and melting temperature) I can achieve switching between phases (depending on the switching process from amorphous to crystalline or from crystalline to amorphous phase). The phases of the phase change material are identified by measuring the resistivity of the material. The phase with higher resistivity is called amorphous phase (off or "0" phase) and the one with low resistivity is called crystalline phase (on or "1" phase). The difference in resistivity between these two phases can be 4 to 6 orders of magnitude. The role of the access device is to supply sufficient driving current to heat the phase change material and force it to switch between different phases. Programming PCM to different phase needs different types of driving current. If PCM is in the crystalline phase, to switch it to amorphous phase, a short and large voltage pulse followed by a quick quench is needed. If it is in the amorphous phase, a long and small voltage is needed to switch it back to the crystalline phase. To identify which phase the PCM is in, a very small non-destructive DC current will be applied to the structure and the phase will be determined by a measurement of the output current. Figure 1.3 shows the programming schemes of PCM.

Figure 1.3 shows the required Set and Reset pulses for switching between the amorphous and crystalline phases of the phase change material. The red pulse is the Reset Pulse (amorphising the phase change material) and this process is known as Reset operation. The blue one is the Set pulse (crystalizing the phase change material) and this process is known as Set operation. The duration of the Set and Reset pulse and the temperatures that the Set and Reset pulses can heat the phase change material to can be seen in the Figure 1.3.

Figure 1.4 shows the typical I-V characteristics of the phase change material [28]. There are three important regions in the I-V curve. The first one is the Read region in

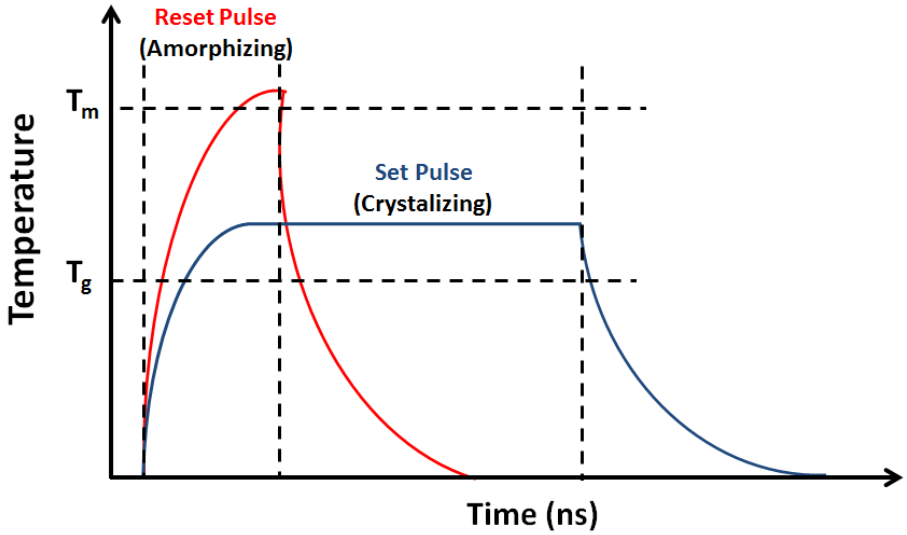


Figure 1.3. Programming scheme of PCM.

which the applied voltage is small and PCM works like a resistance no matter whether the initial phase is crystalline or amorphous. The output current is quite different because of the difference in the resistances of the crystalline and amorphous phase for same applied voltage. The second important region is the Write region which is also separated into two parts. While in the Write region 1, the I-V curves for the crystalline and amorphous phases overlap at very high voltage.

For phase change material, there is an important parameter known as electrical field for switching. Critical electrical field ϵ_m is a constant value for a specific phase change material, which is the critical electrical field value for phase change from one phase to another. Under high voltage when the electrical field in the material increases to ϵ_m, an electrical path will be formed in the phase change material layer. Depending on the thickness of the phase change material, the required voltage to reach write region increases. Phase change material in the electrical path for write region has very small resistivity and needs less voltage to generate the required driving current. This will reduce the power consumption during programming. If the initial phase of PCM is amorphous, before entering the write region, it has a snap-back phenomenon, when voltage increases to V_{th} (threshold voltage). V_{th} is normally about 1.2 V-1.4 V for

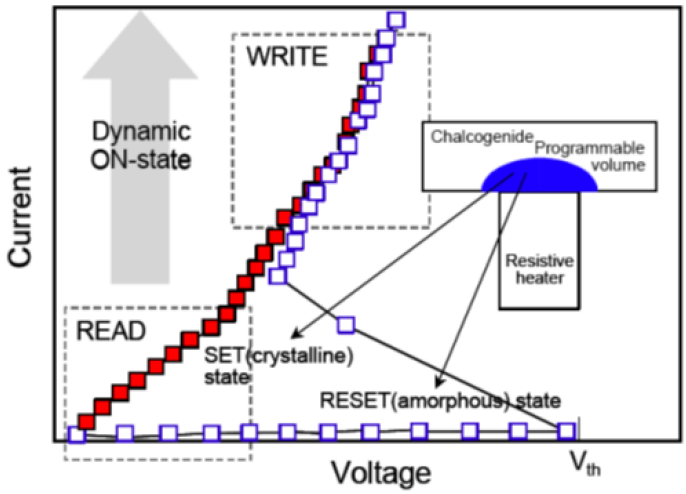


Figure 1.4. I-V characteristics of phase change material [2].

phase change material.

1.1.2. Structural Properties of the Phase Change Materials

1.1.2.1. Structural Properties of the Crystalline State. Phase change materials show prominently different physical properties depending on the phase of the material. While the amorphous phase has high electrical resistivity and low optical reflectivity, for the crystalline phase, it has low resistivity and high reflectivity properties. The reason behind the change in physical properties has to do with the presence or lack of an ordered atomic arrangement. However, especially for the amorphous phase, a study of the structural properties is very difficult because this phase does not only lack long-range order and periodicity, but also presents difficulties in measuring physical quantities.

Because of the possibility of having a phase transition in phase change materials, there have been many studies about these materials for several decades. In Figure 1.5, typical phase change materials are shown in a chart. Here, I focus on compositions that lie on the pseudobinary line GeTe - Sb_2Te_3 because these materials are used to enable phase change in optical storage technology.

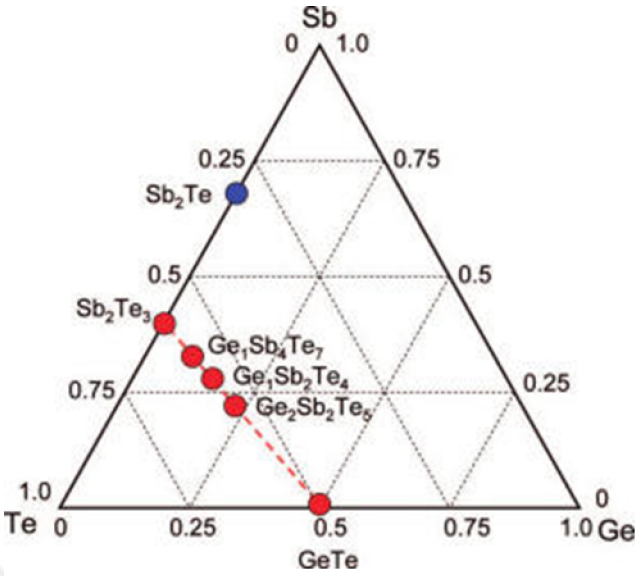


Figure 1.5. Many alloys which are utilized as phase change materials lie on the GeTe - Sb_2Te_3 pseudobinary line [2].

On the pseudobinary line GeTe - Sb_2Te_3, depending on the percentage of Ge, Sb and Te atoms, there are many unique alloys which show different physical properties. For example at high temperatures above 400 °C [29],GeTe exhibits a rock-salt structure, as shown in Figure 1.6, which consists of two FCC sublattices shifted by half the lattice parameter in each direction (0.5 0.5 0.5) with respect to each other.

In GeTe, while one sublattice is occupied by tellurium atoms, the other one is occupied by germanium atoms. At a lower temperature, a rock-salt phase is also found as a metastable phase after annealing amorphous GeTe thin films at $\sim$ 180 °C.

In fact, in the crucial phase transition employed in phase-change data storage, the material switches between the amorphous and the metastable rock-salt structure. However, in the ground phase at lower temperatures, GeTe adopts a trigonal phase, which can be described as a rock-salt structure, slightly distorted by freezing in a TO-phonon along the [111]- direction (see e.g. [29]). Figure 1.7 shows a comparison of the rock-salt and the trigonal phases in the primitive cell. Upon the phase transition to the trigonal structure, the unit cell is stretched along the $<111>$-direction. Additionally,

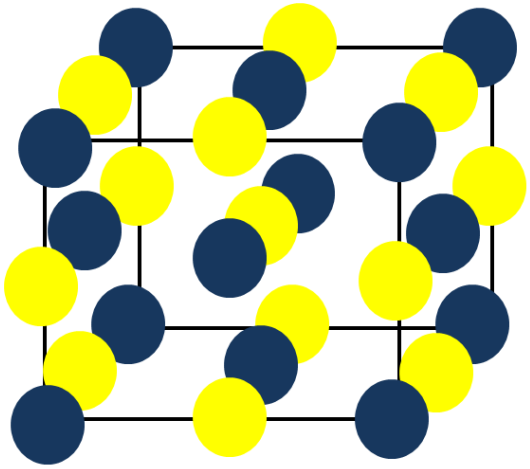


Figure 1.6. Rock-salt structure of GeTe. In ternary phase change materials, one sublattice is statistically occupied by germanium, antimony, and vacancy sites.

the central atom is displaced also along the $< 111 >$-direction from the center of the rhombohedron, which results in a geometry with alternating short and long bonds. Furthermore, it has been found that GeTe exhibits a large concentration of point defects. Ge-vacancies are known to be the dominant point defects (see e.g. [30, 31]).

For the ternary alloys such as $Ge_2Sb_2Te_5$ and $Ge_1Sb_2Te_4$, the rock-salt structure has not been observed as a high temperature phase in bulk samples, as it was found in GeTe, but only as a metastable phase in thin films [32]. Here it is widely accepted that one sublattice is occupied by tellurium atoms, the other one by a random distribution of germanium atoms, antimony atoms, and vacancy sites. However, recent results from ab initio calculations indicate that the occupation on the Ge/Sb-sublattice in ternary Ge-Sb-Te alloys might be ordered [33]. The most remarkable feature of this phase is the surprisingly high vacancy concentration of 25% on the Ge/Sb sublattice. This has been observed also for other alloys along the GeTe-Sb_2Te_3 pseudobinary line.

The role of these vacancies for the stability of the structure and the electronic properties of the compound is still not fully understood. However, an important step in understanding the presence of the vacancies has been achieved recently. By employing ab initio calculations for fictitious systems along the stoichiometric line $Ge_1Sb_2Te_4$-

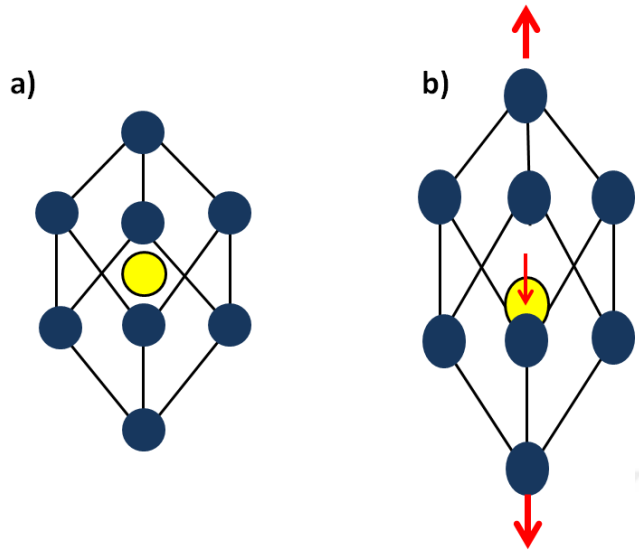


Figure 1.7. Rock-salt structure (a) and trigonal structure (b) of GeTe in the primitive unit cell.

$Ge_2Sb_2Te_4$ in the rock-salt phase, the influence of differences in the vacancy concentration on the electronic properties were studied numerically [34]. $Ge_1Sb_2Te_4$ contains 25% of vacancies on the Ge/Sb sublattice while in $Ge_2Sb_2Te_4$ all vacant lattice sites have been filled with Ge atoms. It is commonly believed that the existence of vacancies in the structure has an important role in the switching process between the amorphous and crystalline phases.

1.1.2.2. Structural Properties of the Amorphous and Liquid States. For the amorphous and liquid structure, it is particularly difficult to define a general characteristic property of these two phases due to the lack of long-range order and periodicity. Therefore, a unit cell for the amorphous and liquid structure phase cannot be well-defined as given in the crystalline. For this reason, this lack of long-range order significantly complicates a clear identification of the structural properties of these two phases. Nevertheless, statistical properties such as the structure factor or correlation functions are successfully employed to determine and classify the structure of amorphous solids and liquids by analyzing their short and medium range structural order.

Besides experimental methods such as neutron diffraction or EXAFS (extended X-ray absorption fine structure) spectroscopy, molecular dynamics and, recently, ab initio molecular dynamics have been employed in order to study the amorphous and liquid phases of a wide range of elements and alloys. In particular, these methods allow a detailed analysis of the local structural properties and the relationship between structural and electronic properties. For example, Kresse and Haffner investigated the liquid-amorphous transition in Ge and the defect properties of the amorphous phase of germanium [35]. Structural properties of glassy binary IV-VI alloys have also been studied [36, 37].

Moreover, thanks to massively improved computer performance, molecular dynamics simulations of amorphous GeTe or ternary Ge-Sb-Te-alloys have become feasible [38, 39]. The analysis of these calculations results in a very detailed model of the local structure of amorphous $Ge_2Sb_2Te_5$ [40]. It is found that Ge and Sb atoms have four nearest neighbors while Te exhibits three nearest neighbors. The bond angles have maxima mainly at 90 and 180 deg, recalling the distorted rock-salt environment found in the metastable crystalline phase. However, 38% of the Ge atoms are tetrahedrally coordinated, in particular if homo-polar bonds are present. This can be analyzed using a local order parameter q [41] where the sum of q runs over the couples of atoms bonded to a central atom j. For more details, see Figure 1.8.

Further information is obtained from an analysis of the ring structures in amorphous GeTe and $Ge_2Sb_2Te_5$ [39]. 4-fold rings are found to be the dominant ring structure in $Ge_2Sb_2Te_5$. In this configuration, A and B generally correspond to Ge and /or Sb and Te in the ABAB ring, respectively. This is also true for GeTe; however, there is no clear evidence to determine for any n-fold ring configuration. Furthermore, the molecular dynamics calculations reveal the vacancy structure in the amorphous alloys. It is found that a total volume of 11.8% in $Ge_2Sb_2Te_5$ and 6.4% in GeTe consists of cavities or voids respectively. The vacancies, which tend to be surrounded by Te atoms, repel each other. Hence, only a few di- or multi vacancies are identified. These findings allow for an interpretation of the phase transition process.

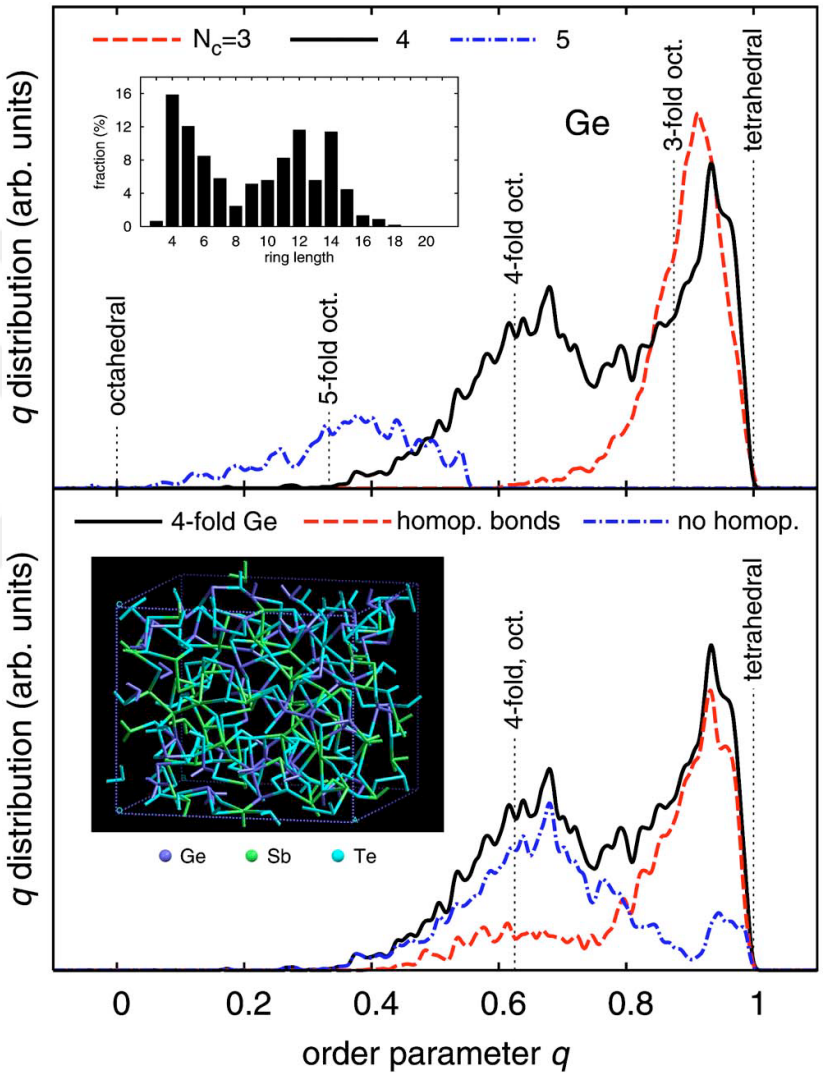


Figure 1.8. Distribution of the local order parameter q for Ge with different coordination numbers N_c [40].

Experimentally it has been particularly burdensome to determine the amorphous structure. When the materials recrystallize easily, a sufficiently large amount of amorphous material is needed for experimental techniques such as neutron diffraction. However, it is very difficult due to the lack of long-range order and periodicity. EXAFS has been identified as a promising technique to solve this problem. Recent publications of EXAFS data [42, 43] revealing the local order of amorphous GeTe and $Ge_2Sb_2Te_5$ have led to a remarkable paradigm shift for phase change alloys. These studies clearly showed that the local order in the crystalline and amorphous phases is very different. While in the crystalline phase, the germanium atoms occupy octahedral positions, they switch to a tetrahedral coordination in the amorphous phase.

1.1.3. Electrical Properties of The Phase Change Materials

A clear understanding of the electrical properties of phase change materials is essential for this study. This section is divided into three subsections as Band Diagram for Chalcogenide Semiconductors, Electrical Conduction in the Crystalline Phase and in the Amorphous Phase.

1.1.3.1. The Band Diagram for Chalcogenide Semiconductors. In this part, first I discuss the semiconductor band diagrams for chalcogenide semiconductors in the crystalline and amorphous phases. After briefly describing the electrical properties of the crystalline phase, I focus on electrical phenomena in the amorphous phase, including transport, threshold switching, and transient delay effects.

Figure 1.9 schematically shows band diagrams for a chalcogenide semiconductor in either the crystalline (a) or the amorphous phase (b) [44, 45]. There are three important differences between the two diagrams. First, most generally the energy gap for the amorphous phase is wider compared to the crystalline phase. For instance, optical absorption and photoconductivity data indicate that the gap of amorphous $Ge_2Sb_2Te_5$ is about 0.7 eV, however, the crystalline phase has an energy gap of about 0.5 eV [46, 47]. Second, while the forbidden gap and conduction / valence bands are

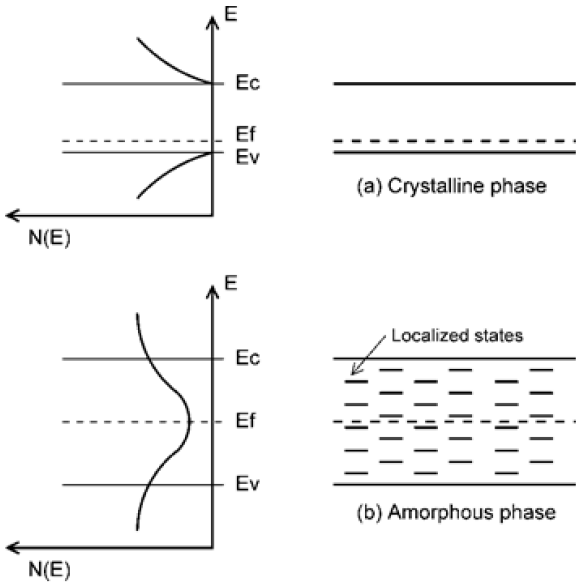


Figure 1.9. Schematic drawing of the band diagrams for a chalcogenide semiconductor in either the crystalline (a) or the amorphous (b) phase. Ref 31.

clearly distinct in the crystalline phase, the amorphous phase is characterized by a large concentration of localized states in the gap [48]. These localized states significantly contribute to the density of states. Therefore, the band diagrams differ according to that whether or not localized states are present or absent in the gap. They have an important role for the conductivity of the phase change material depending on mobility of carriers occupying such states. Deep states tend to be highly localized, while mobility increases for energies approaching the conduction or valence bands. For this reason, the energy gap in an amorphous semiconductor is generally referred to as a mobility gap, namely an energy range with insufficient mobility of phases, rather than a forbidden range with no states, as in standard crystalline semiconductors.

The third difference is regarding the position of the Fermi level: due to the large concentration of localized states. The Fermi level is pinned at about mid-gap in the amorphous chalcogenide [44]. For this reason, the electrical resistivity and the respective activation energy E_A are relatively large. For instance, activation energies around 0.25-0.35 eV have been observed in amorphous $Ge_2Sb_2Te_5$ [49]. On the other hand; the crystalline chalcogenides generally display small activation energy for conduction,

which is compatible with a self-doping behavior, probably due to point defects (e.g., vacancies) in some Te compounds [30].

1.1.3.2. Electrical Conduction in the Crystalline Phase. At least for a classical phase-change material such as $Ge_2Sb_2Te_5$, the crystalline phase appears as a relatively low band gap, doped semiconductor, for which the standard semiconductor theory can be straightforwardly applied. The typical approach to describe electrical conduction in the crystalline phase is the drift-diffusion equation [50, 51]. This results in a typically ohmic behavior for relatively low applied voltage, as shown by the measured I-V curve in Figure 1.10 [52].

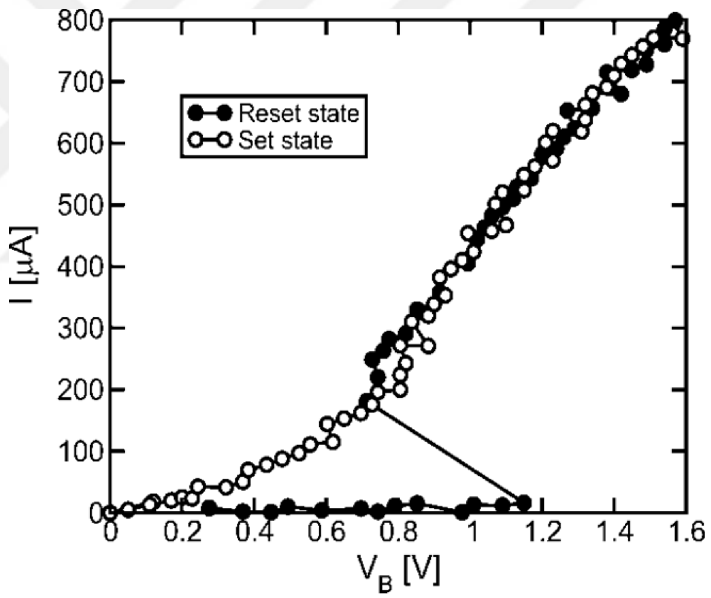


Figure 1.10. Measured I-V curves for a PCM cell in the set (open symbols) or reset (filled symbols) states. The latter displays the threshold switching effect at about V_T, 1.2 V. From [52].

Also, the measured E_A is relatively low, as shown by the Arrhenius plot of resistance for the set phase (corresponding to the crystalline phase) in Figure 1.11, giving a value of about 20 meV for E_A. On the contrary, the reset phase (corresponding to the amorphous phase) displays large resistance and activation energy , consistent with the band diagram in Figure 1.9.

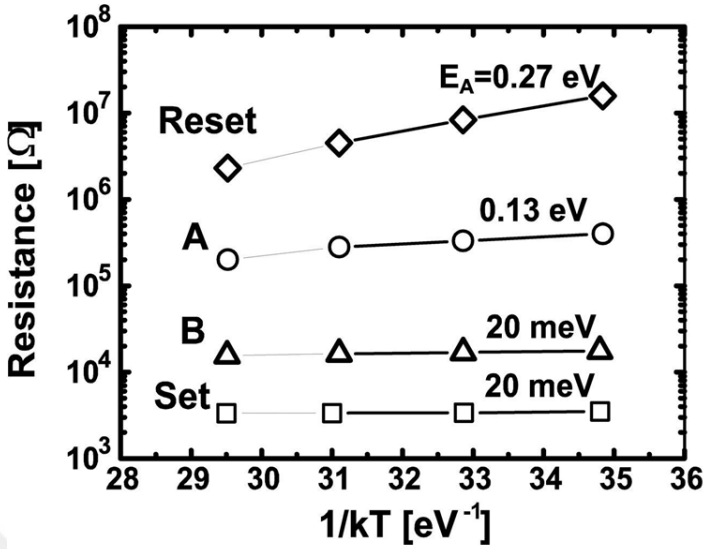


Figure 1.11. Arrhenius plots of the resistance for a fully reset state, a fully set state, and two incomplete set states, A and B, obtained by the application of a voltage pulse to a phase change memory cell in the initial reset state.

The I-V curve for the crystalline phase displays a nonlinear behavior for relatively large voltage in Figure 1.10. To explain this feature, we may recall that measurements in the figure were obtained for μTrench phase change memory cells, where electrical conduction and heating were strongly confined for the purpose of low-current phase change in the memory cell [53].

As a result, a current of a few 100 μA may result in significant heating, thus causing significant thermal carrier generation in the low band gap semiconductor. The increase of the carrier density results in a conductivity increase within voltage, responsible for the nonlinear I-V curve in Figure 1.10.

An important aspect from the perspective of a phase change memory operation is electrical conduction in intermediate phases, which display resistance values between the set (crystalline) and reset (amorphous) values and consist of a mixed amorphous-crystalline phase.

To study the electrical properties of intermediate phases, Figure 1.11 shows the Arrhenius plot for two incomplete set phases, obtained by the application of a voltage pulse to a phase change memory cell in the initial reset states. The current during the applied pulse results in a significant Joule heating and a consequent crystallization of the amorphous phase. Crystallization can be described by nucleation and growth effects, resulting in a fine mixture of crystalline grains embedded in the amorphous network. Electrical conduction in this mixed-phase volume can be explained by percolation of the carriers through dispersed low-resistivity crystalline grains [54, 55]. This is schematically shown in Figure 1.12 for two different mixed-phase phases, characterized by an incomplete (A) or complete (B) percolation path through low-resistivity crystalline grains.

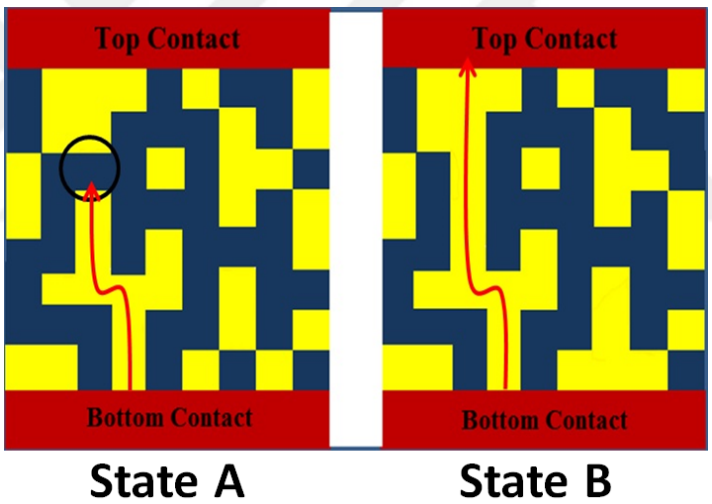


Figure 1.12. Schematic drawings of two different mixed-phase configurations, characterized by an incomplete (A) or complete (B) percolation path through low-resistivity crystalline grains. In state A, the electrical current is limited by a small amorphous "barrier" whereas no amorphous barrier exists for state B. Yellow, crystalline; blue, amorphous.

In Figure 1.12, yellow and blue correspond to crystalline and amorphous, respectively. In phase A, the electrical current is limited by a small amorphous "barrier", accounting for the relatively large values of resistance and activation energy (0.13 eV) in Figure 1.11. No amorphous barrier exists for phase B; thus, the activation energy is

the same as that of the bulk crystalline phase (full set state). However, the resistance still remains higher than the set state due to geometrical effects, namely a small cross section and a relatively large percolation length through the mixed phase.

1.1.3.3. Electrical Conduction in the Amorphous Phase. Figure 1.13 shows the measured I-V curves for a phase change memory cell in the reset phase at different temperatures [56]. The common interpretation is that the fundamental contribution for the conduction comes from Poole-Frenkel (PF) conduction; namely, electrons at localized states. These electrons are thermally emitted into free states in the conduction band, in which they can freely move [51]. Recently, it has been found that the significant contributions to conduction comes from not only pure thermal emission above the conduction band edge, but also thermally activated tunneling below the conduction band [44]. Figure 1.13 also shows that thermally activated PF and tunneling mechanisms lead to a strong temperature dependence of the current. From the measured current in an Arrhenius plot for variable voltage, the activation energy for conductivity can be extracted easily.

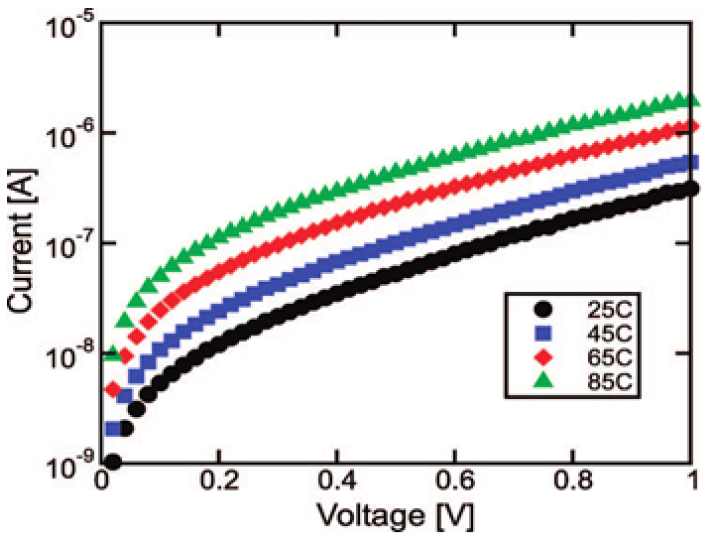


Figure 1.13. Measured I-V characteristics in the subthreshold regime for amorphous $Ge_2Sb_2Te_5$ with increasing temperature. From [49].

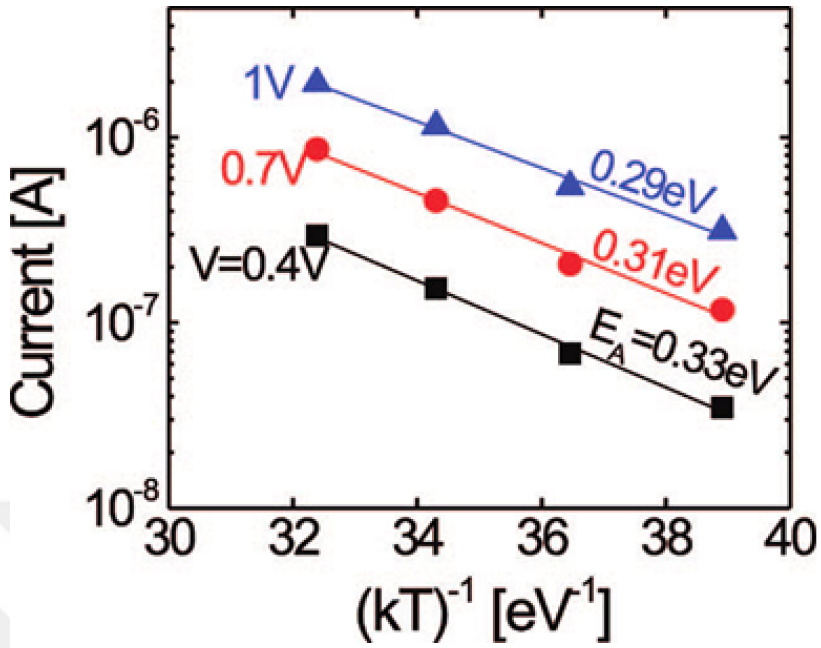


Figure 1.14. Arrhenius plot of the measured current for increasing voltage V ; 0.4, 0.7, and 1 V (right). From [56].

The extracted activation energies, which can be obtained from the slope of data in the Arrhenius plot, for the applied voltage V = 0.4, 0.7, and 1 V are given in Figure 1.14 [49]. The activation energy decreases with increase in the applied voltage, which is consistent with the PF model. In fact, as described in Figure 1.15, the energy barrier between two localized states changes depending on the applied voltage. The energy barrier $\Delta\varphi(0)$ is for zero applied voltage (a) and, the energy barrier is lowered to a value $\Delta\varphi(V)$ by the application of a voltage (b). Thus, the activation energy for the conduction process, which is equal to the potential barrier $\Delta\varphi(V)$, decreases with V as shown in Figure 1.14.

In particular, the sinh-like voltage dependence accounts for the ohmic behavior of the current at very low voltages (approximately below 0.2 V) and for the exponential increase of the current for relatively high voltages. An expression for the activation energy can be defined as the logarithm of the current versus 1/kT.

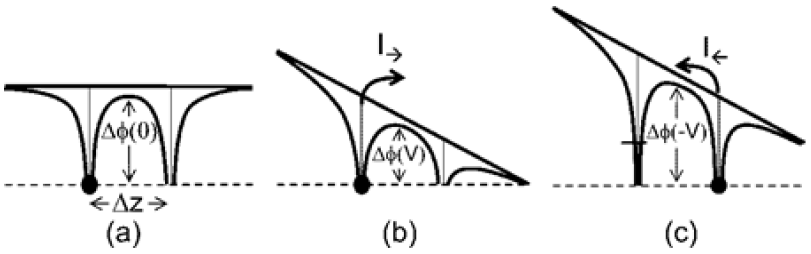


Figure 1.15. Schematic for the analytical model for subthreshold transport. The potential barrier is equal to $\Delta\varphi(0)$ when no voltage is applied (a), and it drops to $\Delta\varphi$(V) as a voltage V is applied, resulting in an exponential enhancement of the forward current in(b). The reverse contribution to the current I is exponentially lowered by the increase of the potential barrier $\Delta\varphi$(-V) (c). From [56].

$$E_A = -\frac{d\,logI}{d\,(1/kT)}.E\prime_C - E_{F_0} - qV\frac{\Delta z}{2u_a}.coth\Big(\frac{qV}{kT}\frac{\Delta z}{2u_a}\Big) \tag{1.1}$$

Where $E\prime_C$ is the conduction-band mobility edge, E_{F_0} is the equilibrium Fermi level, the average distance Δz between traps, and u_a is the total thickness of the amorphous chalcogenide layer where the voltage V is applied ([56]). The mobility edge $E\prime_C$ is used instead of the proper conduction band edge to take into account the tunneling contribution ([44, 57]). This formula, for sufficiently large voltage, can be linearly approximated as $E\prime_C - E_{F_0} - qV\frac{\Delta z}{2u_a}$.

The measured and calculated activation energies, as a function of voltage, are given in Figure 1.16. The calculated activation energy is obtained from the I-V characteristics at variable temperature in Figure 1.13. From Figure 1.16, it is clear that at low voltage activation energy goes to saturation, however, at high voltage, it decreases linearly with increase in the applied voltage due to the lowering of the potential barrier between two trapped phases for increasing voltage. In the ohmic regime, the activation energy saturates to $E\prime_C - E_{F_0} - kT$. This originates from the competition between forward and reverse conduction [56].

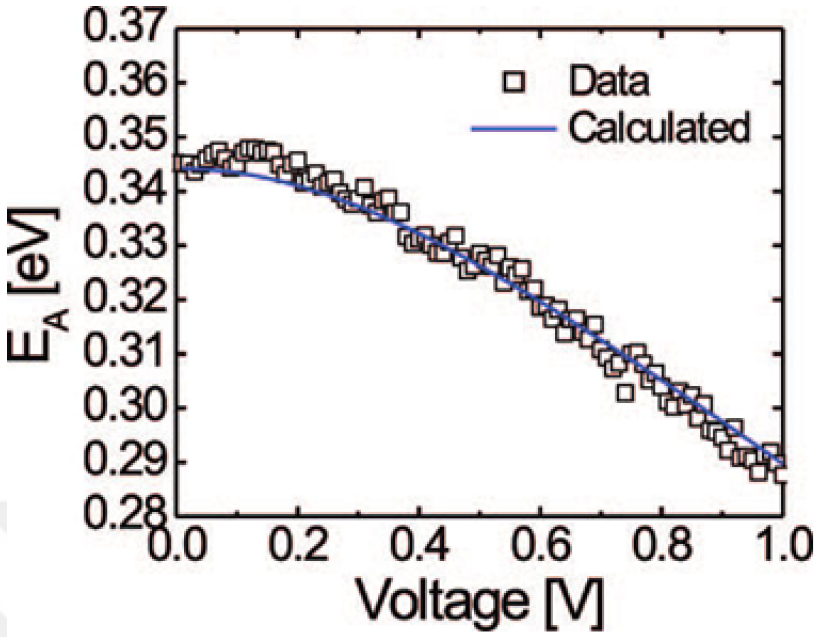


Figure 1.16. Activation energy E_A, as a function of voltage, obtained from experimental I-V curves at variable temperature, and simulation results from the full analytical expression for E_A. From [56].

The voltage-dependent E_A for transport is a strong evidence for the PF transport model in Figure 1.15. Some localized states, originating from the positively charged defects acting as trapping centers, correspond to already present ionized donor states, which become neutral at the capture of one electron [58]. From the subthreshold slope (Figure 1.14) or the voltage-dependence of E_A (Figure 1.16), the obtained ratio $\Delta z/2u_a$ is used to estimate the concentration of donor states. The donor-trap concentration is found to be in the range of a few $10^{18} cm^{-3}$ for E_A estimated thickness of the amorphous layer u_a of about 30 nm from TEM observations. When the defect-annihilation dynamics accompanying the structural relaxation (SR) of the amorphous chalcogenide are compared, this kind of donor states is low and causes the steady increase of resistivity [44, 59]

The increase of reset-states resistance during SR may indicate a concentration of localized states larger than a few $10^{19} cm^{-3}$. This discrepancy may be explained by assuming that the donor states are only a minority of the localized states [60]. Electrons

traveling by PF transport through the neutral sites are still affected by the potential landscape due to donor phases. Alternatively, the local positive charge accounting for the trapping potential may result from the self-trapping, or polaron, effect [44, 61, 62]. Trapping of an electron may induce a local polarization, resulting in the buildup of a local positive charge. According to this explanation, the measured activation energy for electron transport includes the energy required for the local structural rearrangement to accommodate the electron and the potential barrier between the trapped level around E_{F0} and the conduction band edge $E\prime_C$ [57].

1.2. Magnetic Bubble Study

The growing demand for improvements in applications , such as data storage, sensors, detectors or oscillators acts as a driving force for researchers to develop new technologies. In order to address these requirements, apart from semiconductors, technologies based on magnetic materials are also quite promising. New results from such studies are getting published every day in many high impact journals.

In the last several decades, studies on magnetic materials, especially magnetic properties in nanomagnets (nanoscale or micro scale), led to the discovery of exotic spin-ordered systems. Vortex, which have a specific rotation around the center point, and vortex-like structures have been observed in many physical systems and are quite common in nature. Figure 1.17 shows vortex and antivortex magnetic configuration in in-plane magnetization magnetic material. In circular dots made of magnetic materials with poor in-plane magnetocrystalline anisotropy, magnetic vortices are widely observed and they originate from the delicate interaction between long-term dipole interactions with localized energy terms bounded by circular symmetric endpoints [63]. The spin structure of vortex and vortex-like structures and their behavior under magnetic field have been the subject of many experimental and theoretical studies [64].

Following the identification of magnetic configurations such as Vortex and vortex-like structures, studies on the formation conditions of these structures and the factors affecting these magnetic configurations have became more frequent [65]. The main fac-

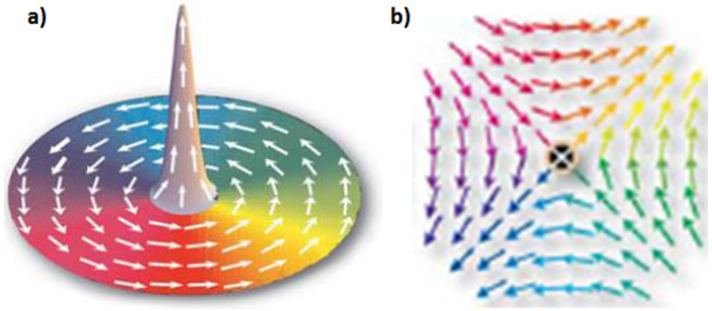


Figure 1.17. a)Vortex and b) Antivortex magnetic configurations [65]

tors determining the magnetic moment distribution in magnetic materials are the relation between energy terms. These energy terms are the magnetostatic energy describing the interaction with the external magnetic field, the magnetocrystalline anisotropy energy defining the easy orientation axes of the magnetization and the exchange energy defining the harmony between atomic moments based on shape, size, and material properties.

In addition to these energy terms, the Zeeman energy term that emerges in the presence of an external magnetic field is another important term that determines magnetic configuration in nano or microwave magnetic materials. When the magnetic materials are reduced to nanoscale, the interactions between these energies are of great importance and different micromagnetic arrangements such as Vortex and vortex-like structures can become stable [65, 66]. Moreover, these structures can be used in magnetic recording readers, magneto-resistance random access memories (MRAM). Current-dependent dynamic behaviors also have applications in many spintronic devices such as microwave oscillators, rf detectors and modulators.

The smallest changes in the geometry of nano-sized devices made from magnetic materials lead to very different magnetic configurations. For example, magnetic thin films with low magnetocrystalline anisotropy energy tend to be in a magnetic vortex arrangement when they are above the critical size for the formation of a single domain. This is a consequence of the dominance of the magnetostatic energy over other energies.

Magnetic vortices are generally classified by a topological parameter called skyrmion number, which depends on the polarity of the singular points in its center, the winding number of the magnetic moments around the center, and the winding direction (chirality, as clockwise or counterclockwise). In Figure 1.18, vortex and antivortex properties are given. While the polarity of the vortex center can be observed by the magnetic force microscopy (MFM) imaging technique, the photoemission electron microscope (PEEM) can determine the chirality [65].

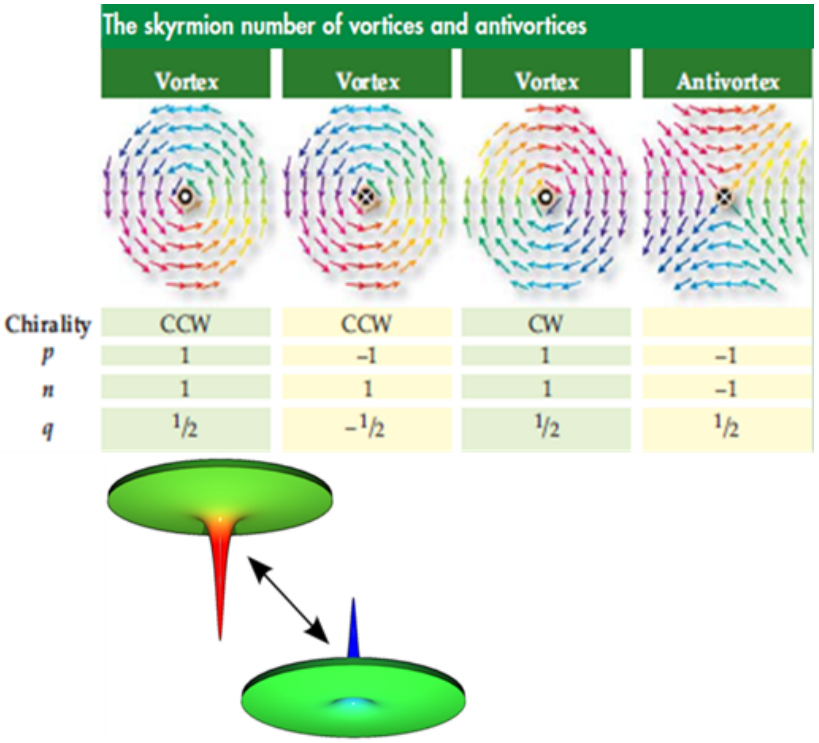


Figure 1.18. Vortex and Antivortex magnetic configurations properties, p (polarity) , n (chirality) and q (winding number or skyrmion number) [65]

The vortex tends to be influenced by the magnetic properties of the external magnetic field. The behavior of vortex structures under DC and AC external magnetic fields varies. Depending on the direction of the applied field and the direction of winding of the vortex, the vortex slides back towards the center of the vortex within a DC magnetic field applied parallel to the plane of the vortex. At zero magnetic field vortex center will return to the center. In Figure 1.19, this motion is shown. This is only when the external field is less than vortex-single dominant transition threshold.

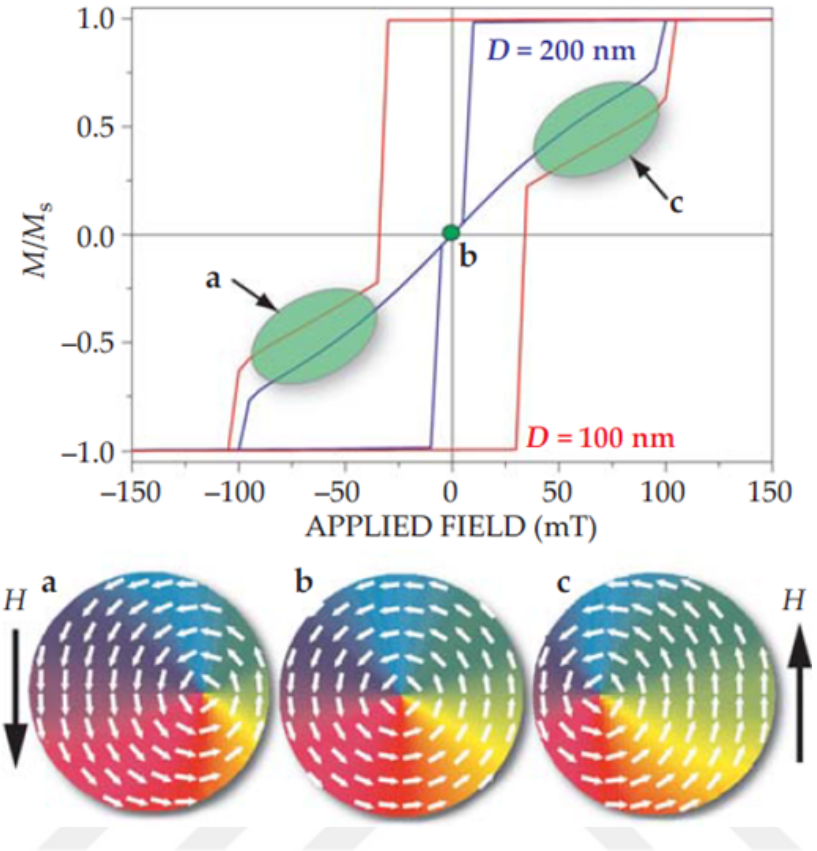


Figure 1.19. Vortex center motion under external magnetic field [65].

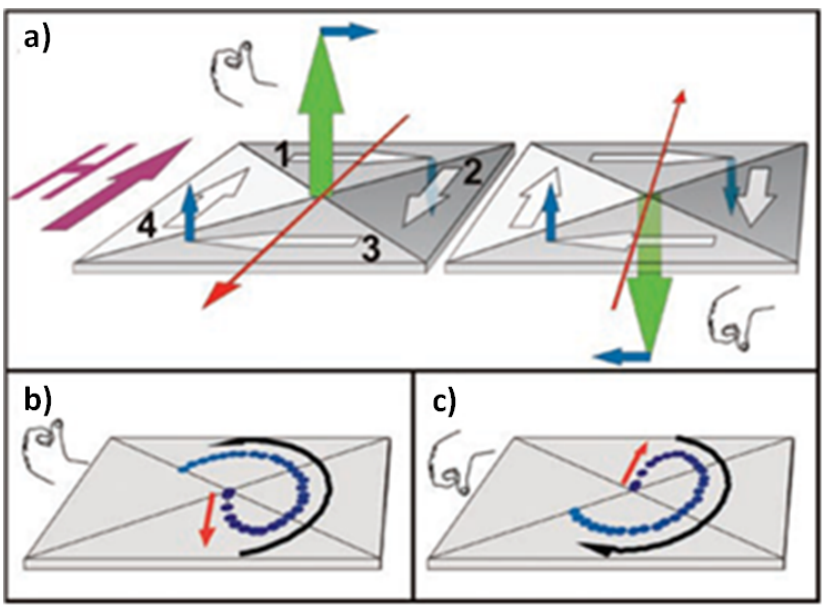


Figure 1.20. Vortex center motion under external magnetic field [67].

In Figure 1.20 a, the field direction is in plane and we can see precession motion of center from the blue arrows. However, depending on the magnetization direction of the center, up or down, the precession motion is opposite to each other. We can see this in Figure 1.20 b and c. Here, hands show the center of the magnetization direction.

At the same time, in the low amplitude AC magnetic field, the vortex center performs a gyration with a natural frequency of oscillation in GHz range. This circular motion can be directly observed with high resolution X-ray magnetic circular dichroism (XMCD) technique. A schematic representation of this circular motion for a square magnetic thin film is given in Figure 1.21 [67–69].

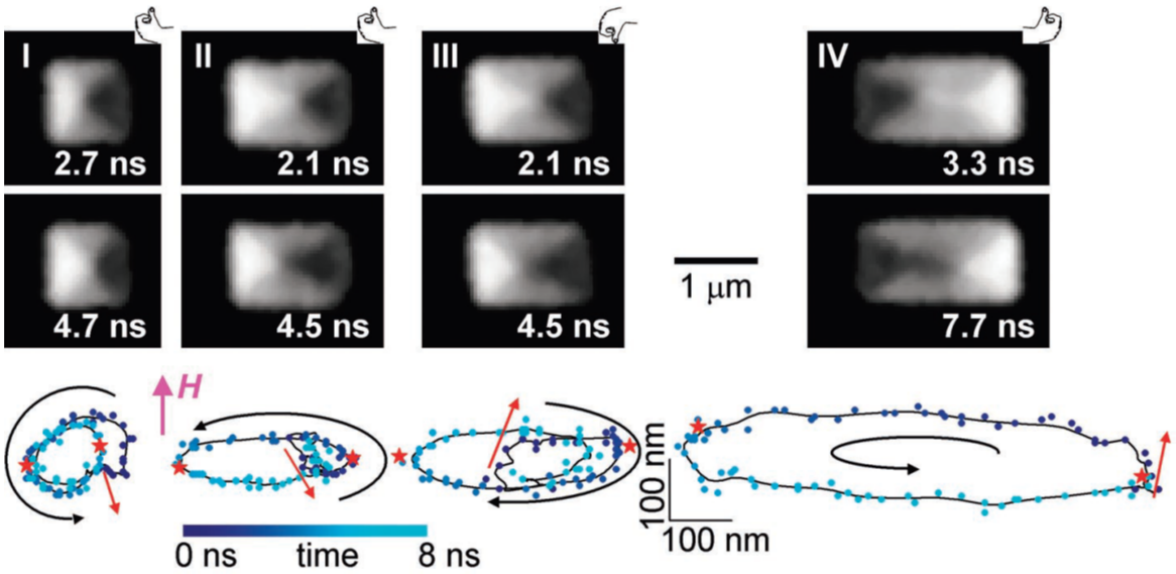


Figure 1.21. Gyrotropic vortex motion in Co squares of different dimensions. (a) TR-PEEM images of domains in Co squares of patterns I($1 \times 1\mu m^2$), II ($1.5 \times 1\mu m^2$) and III ($2 \times 1\mu m^2$), taken at the specified delay times after the field pulse. (b) Trajectories of the vortex core [67, 70].

In addition to these areas of application, there is also a potential for very high-impact biological applications such as targeted cancer-destroying cells [71]. In addition, recent work has shown that magnetic vortices have the potential to create many applications such as nano-scale memories, oscillators, radio frequency modulators, and detectors with controlled spin transfer (spin transfer) [72, 73]. Spin transfer mechanism

involves the vortex stimulation by spin-polarized electric current rather than magnetic field.

Vortices, thanks to their static properties, can be used in magnetic recording heads and magnetoresistive random access memories (MRAM) and due to their dynamic behavior under magnetic field they promote the design of spintronic devices like microwave oscillators, rf detectors and modulators [69, 70, 74, 75].

Magnetic vortices can also be achieved by transferring spin angular momentum to local moments in the thin film from a spin polarized electric current through the sample outside the motion through the applied external DC or AC magnetic fields [76]. Such behavior of vortex structure has many application areas in technological sense, such as RF oscillators, data storage systems, or microwave generators [77].

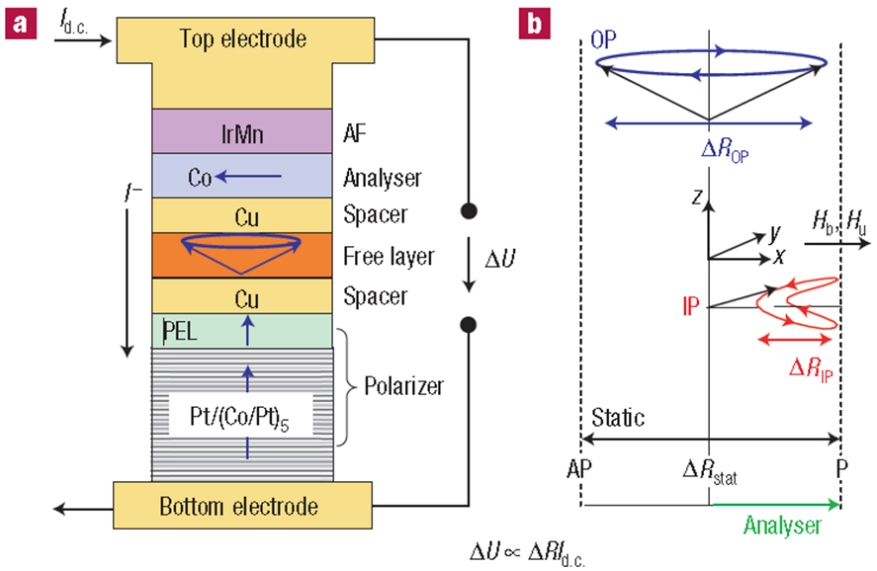


Figure 1.22. Magneto-resistive cell and magneto-resistance. a) Schematic diagram of a magneto-resistive cell consisting of a perpendicular b) Schematic diagram of the IP and OP precession trajectories polarizer

A microwave resonator was fabricated by combining three nanomagnets and this cell works in zero external magnetic field. We can see the device in Figure 1.22. By applying a microwave signal to the cell, the magnetization of the middle nanomagnet

performs the ferromagnetic resonance (FMR). The cell outputs a measurable direct current which is spin-torque diode effect. Alternatively, the nanodevice can be used as a microwave oscillator functioning in zero field [75]. In another study, a spin-valve structure was constructed [78]. In Figure 1.23 the spin-valve structure and measurement setup can be seen clearly.

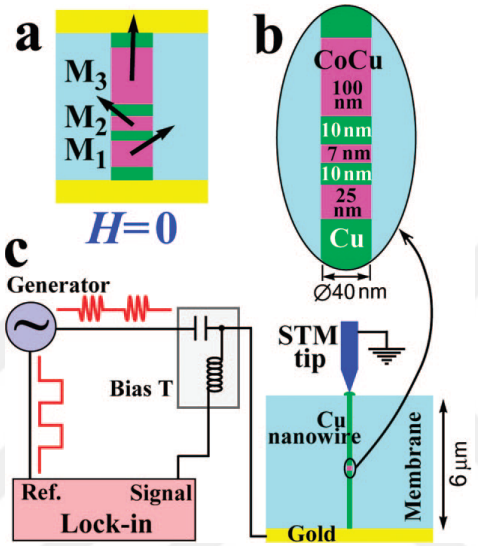


Figure 1.23. a) Spin-Valve structure b)Part of the cross-sectional view of a nanowire sketched in panel and c) Nanowire is electrodeposited in a pore of a polycarbonate ion-track etched membrane [78]

A study in 2007 showed that depending on the thickness of the magnetic layer to have perpendicular magnetization, a new phase of bubble domains was observed. In this study, they investigated temperature dependence of skyrmions [79]. In Figure 1.24 by changing the thickness of the Fe layer, magnetic bubbles were appearing for specific thickness. The reason behind the formation of vortex like configurations is to minimize the magnetostatic energy of the material. Also, vortex like configurations are energetically favorable. Magnetic bubble is the equivalent of vortex micromagnetic structure in materials with perpendicular magnetic anisotropy (PMA).

Magnetic bubbles are a special type of magnetic vortex configuration. The structures in which magnetic bubbles are formed have been known since the 1970s in thin films with high perpendicular magnetic anisotropy (PMA) in the presence of external

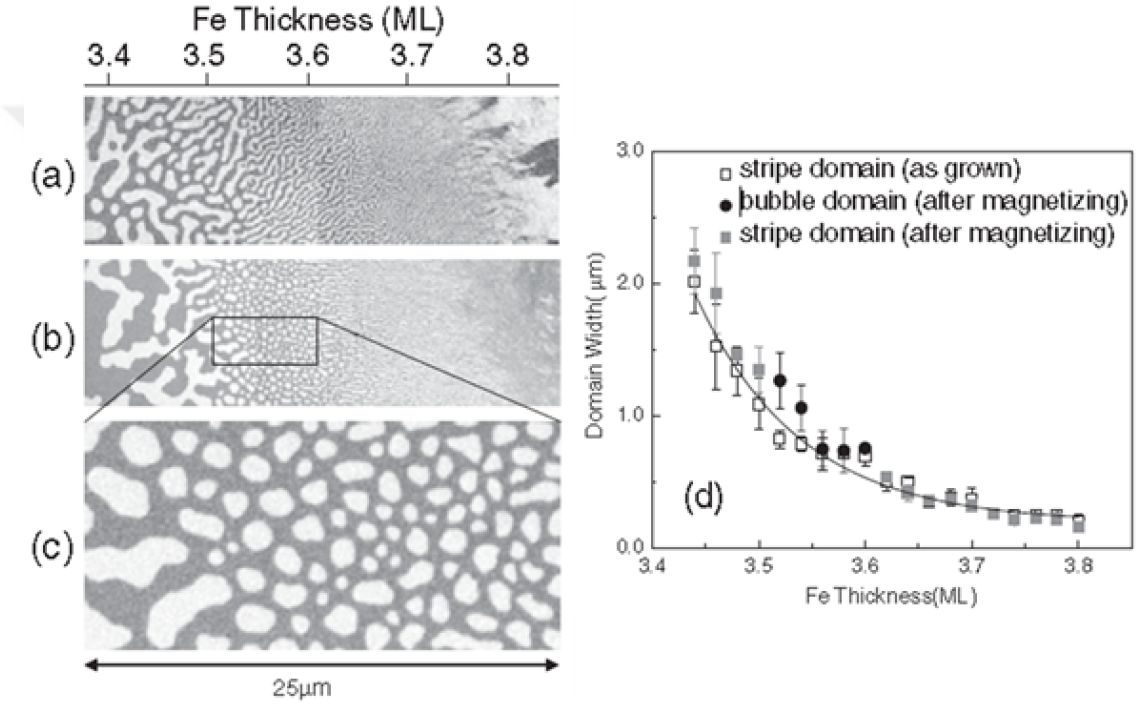


Figure 1.24. Magnetic bubble observation [79]. Magnetic domain images (a) as grown sample and (b) after applying a nearly in-plane magnetic field pulse. (c) Zoom-in image of the bubble domains in the SRT region. (d) Domain width as a function of the Fe film thickness,

magnetic field, and in the zero magnetic field at low temperatures in some exotic ferromagnets [80–82]. The formation of magnetic bubbles were predicted in Komineas et al [83]. In materials with high PMA in their magnetic simulations. After this study, with magnetic force microscopy (MFM), stable magnetic bubbles without external magnetic field was observed in FePt magnetic nano disks with high PMA materials [84]. A magnetic bubble can be seen in Figure 1.25.

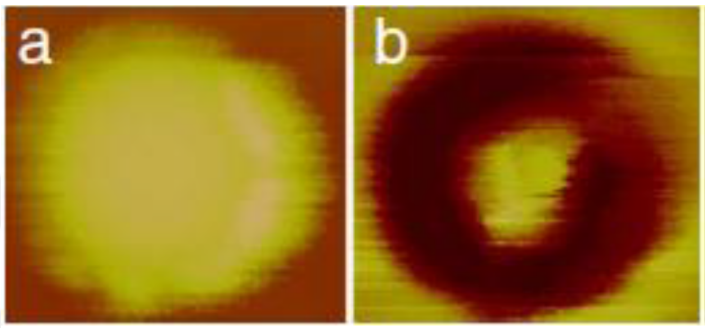


Figure 1.25. Magnetic bubble images for D0 0.5 μm and 50 nm thickness FePt disk. a)AFM and b)MFM image [84]

To observe the magnetic configuration, MFM is one of the ways. In Figure 1.26, we can see the MFM measurement concept. Depending on the forces between the magnetization of the tip and magnetic materials, a phase difference is given and MFM shows this phase difference for every point in its scanning area.

There are many differences between magnetic bubbles and vortices, such as magnitude, dipole energies, and external magnetic field range. Apart from these differences when looking at the spin distribution in the magnetic material, it is shown that magnetic bubble is basically dividing the micromagnetic configuration deviating from the other plane into two regions. When the dominant wall between these regions is examined, it has a complex structure with Bloch type in the center plane and Neel type on the upper and lower surfaces. This can be seen in Figure 1.27. Magnetic bubbles are also characterized by skyrmion numbers (which is the topological index) like vortices, but they are different due to the fact that they take integer values. Skyrmion number for 2D space can be calculated from the equation 1.2.

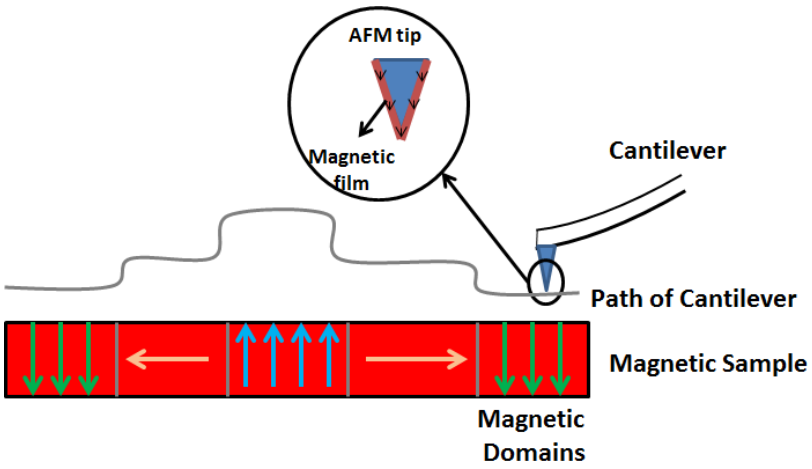


Figure 1.26. Illustration of MFM Measurement

$$n = \frac{1}{4\pi}\int \mathbf{M}\cdot\left(\frac{\partial \mathbf{M}}{\partial x}\times\frac{\partial \mathbf{M}}{\partial y}\right)dxdy \tag{1.2}$$

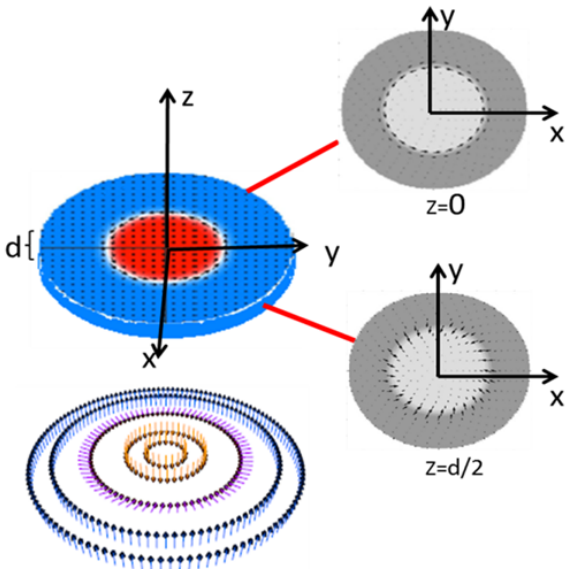


Figure 1.27. Illustration of magnetic configuration in a magnetic bubble [84, 85].

There is a debate about skyrmion and mangetic bubble. Actually, a magnetic bubble is a special type of skyrmion. The fundamental differences are the size of them

(bubble is bigger than skyrmion and its size is around several 100 nm)and skyrmion number (magnetic bubble takes few integer numbers). The biggest difference is the center of bubble, because in skyrmion the center is like a point but in bubble it is a wide region and this is the origin of the difference in the size of them. Therefore, in literature, while mentioning bubble, they are sometimes using skyrmion. There are two fundamental types of skyrmions known as Bloch type and Neel type skyrmion. They have different magnetic spin texture (due to domain wall spin texture) as can be seen in Figure 1.28. It is the same for magnetic bubble. In the Neel type magnetic bubble, the change in the local moment is Neel type domain structure but in the Bloch type magnetic bubble, domain wall type is Bloch type.

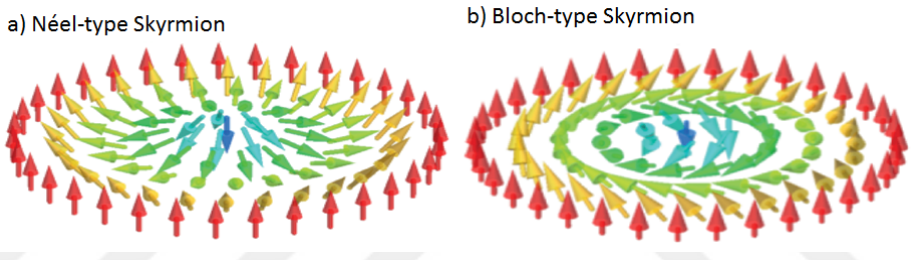


Figure 1.28. Magnetic texture of magnetic bubble [85].

In my study, I focus on the Bloch type magnetic bubble. As described before, magnetic bubbles are characterized by a topological constant called the skyrmion number. In Figure 1.29, four different magnetic texture are given with different skyrmion numbers [86].

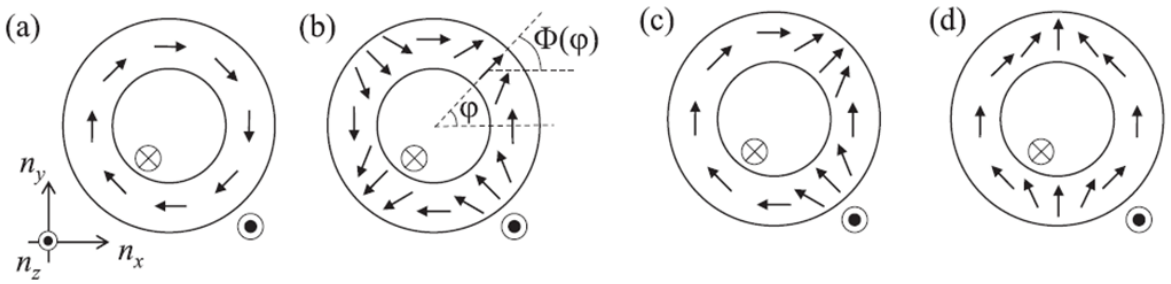


Figure 1.29. Skyrmion number and magnetic bubbles. a) skyrmion, N_{sk}=-1, b)antiskyrmion, N_{sk}=+1, c)and d) magnetic bubbles, N_{sk}=0.

There are also different types of magnetic bubbles depending on the direction of the magnetic moments [87]. Figure 1.30 shows three distinct types of magnetic bubbles and in Figure 1.29, c and d are Type II.

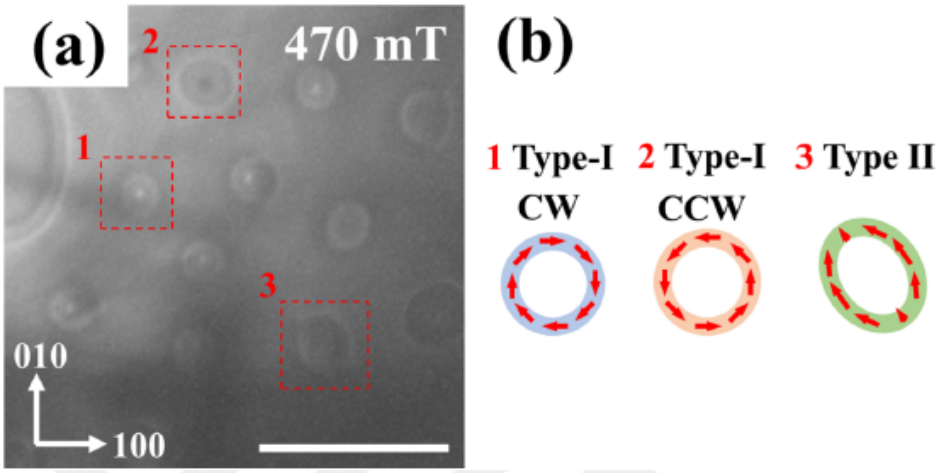


Figure 1.30. Lorentz TEM observations [87]

After the observation of magnetic bubbles, recently there have been many studies to obtain magnetic bubbles and to define physical parameters affecting them like the external magnetic field. The basic approach to obtain a magnetic bubble is fabricating PMA magnetic thin film and with applying external magnetic field, creation of magnetic bubbles [88,89]. Here, the anisotropic magnetic field H_k is also an important parameter affecting bubble nucleation. This can be seen in Figure 1.31 and also we can see the field dependence of the magnetic bubble nucleation.

In order to use magnetic bubbles for new technologies such as data storage or oscillator, the first thing to do is to create magnetic bubbles one by one and to be able to control them. Kirsten von Bergmann's study about *Magnetic bubbles with a twist* opened a new research subject [90], because if this can be dome, it means that magnetic bubble can be used in race track memory. In Figure 1.32 we can see this concept.

After this idea, Wanjun Jiang and his colleges(2016) came up with a new idea for bubble creation with blowing bubble. In Figure 1.33 we can see this concept. Following

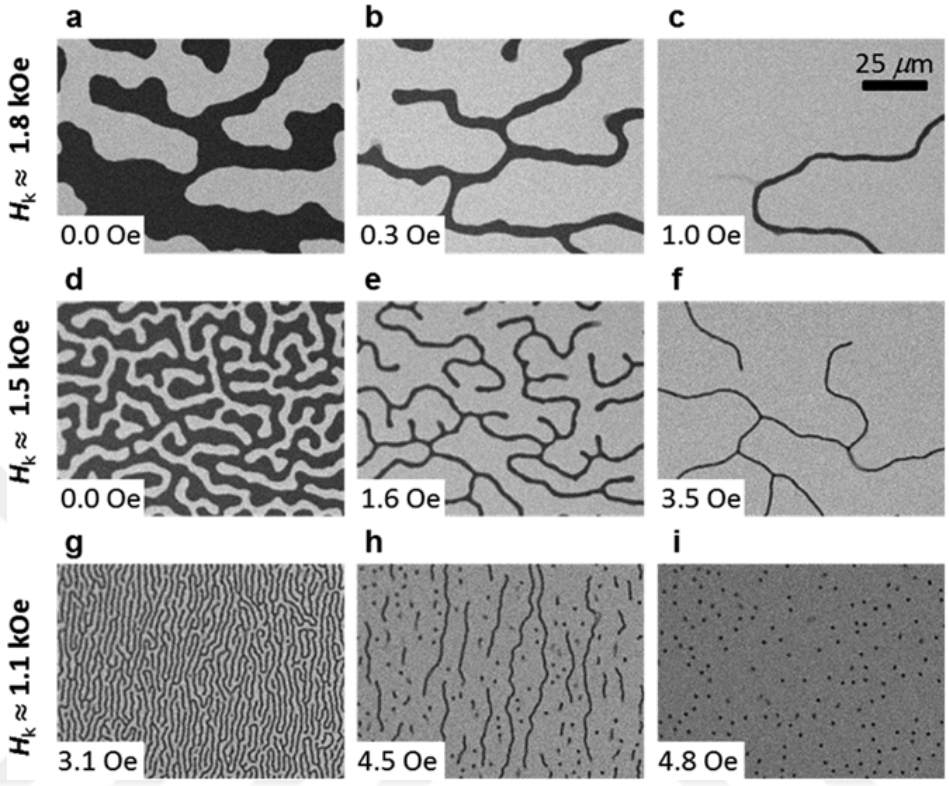


Figure 1.31. Evolution of magnetic domain patterns with perpendicular magnetic anisotropy [88].

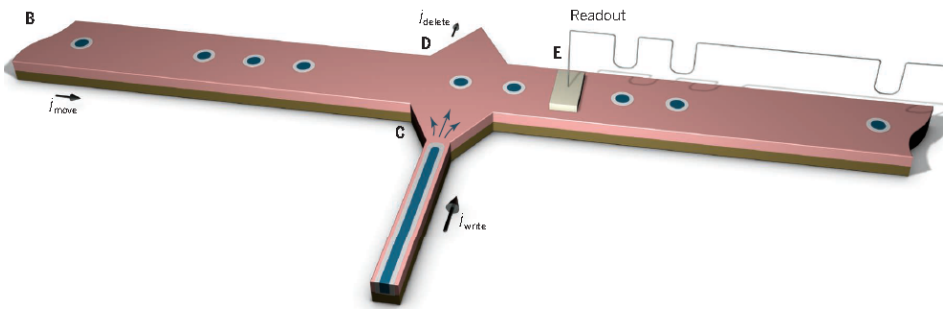


Figure 1.32. Skyrmions for future storage devices [90].

bubble blowing, they tried to move bubble with current pulse and also control its motion. From the displacement of bubble with current pulses (amplitude 0.5 MA/cm^2 and duration 10 μs), they measured in this study the average velocity of skyrmion as 1m/s.

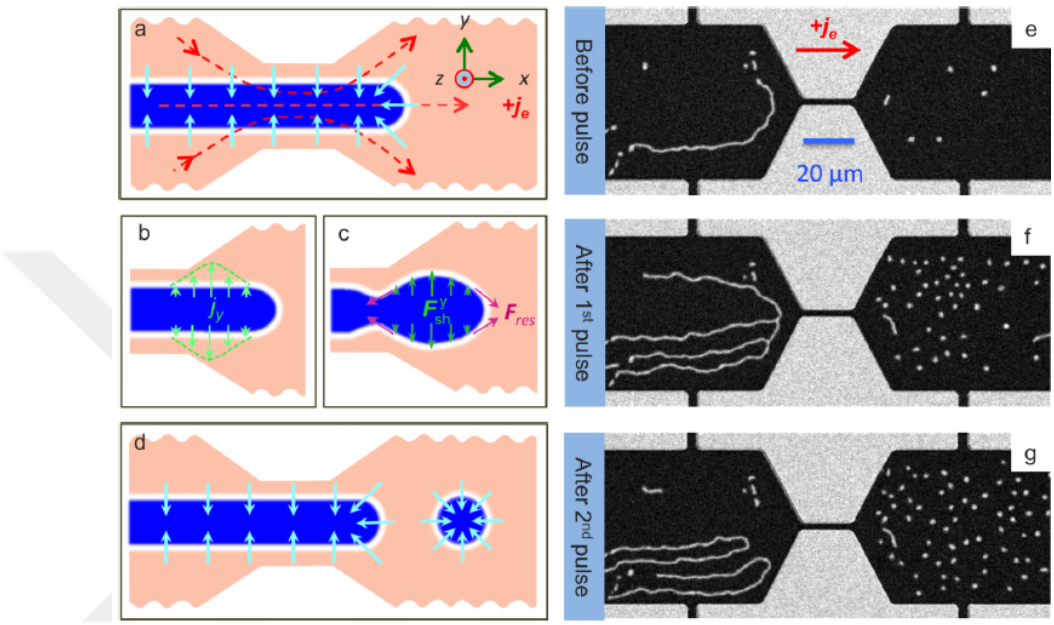


Figure 1.33. Schematics of magnetic skyrmion formation in constricted wires [91].

There have been many studies to understand the physics behind skyrmion motion by constructing simulation and theoretical calculations [92–95]. After controlling the skyrmion or bubble motion with current pulses, there is another study from Wanjun Jiang and his colleges(2016) aimed to observe skyrmion Hall effect. In Figure 1.34, for two different magnetized material, skyrmion motion under field (5 Oe) with current pulse is shown.

In addition to the study of magnetic bubbles in wires, there have been studies about magnetic bubbles in a disk or dot as well. One of them is T. Lui and his colleges' study. They tried to obtain stable single bubble in patterned dot arrays under in-plane magnetic field [97]. In this study, dependence of stable single bubble in the dot diameter, thickness and H_{max} AC in-plane magnetic field value were investigated. In Figure 1.35. we can see both experimental and simulation results.

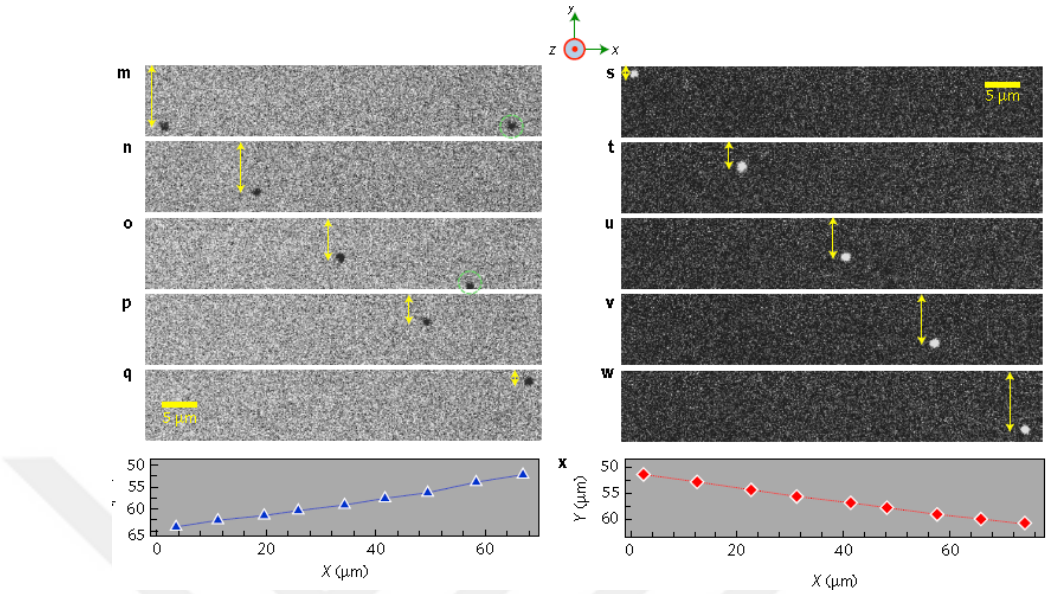


Figure 1.34. MOKE microscopy images of pulse current-driven skyrmion motion [96].

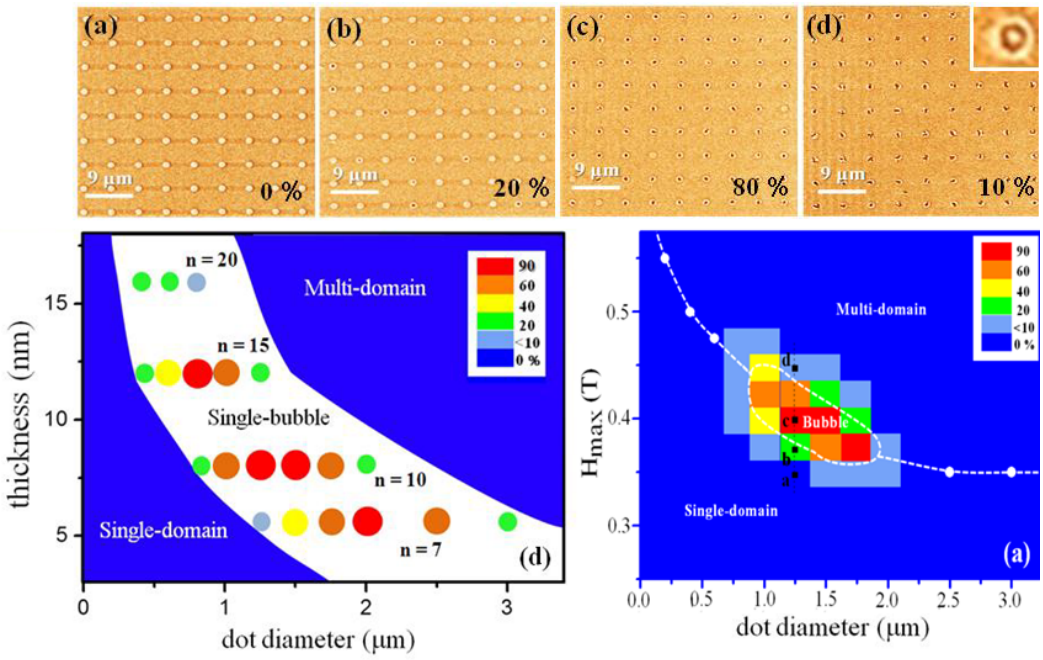


Figure 1.35. MFM images for 1.25 μm dot array and simulation results for thickness and H_{max} vs dot diameter [97].

Since the vortices are affected by the application of external magnetic fields, magnetic bubbles can make rotational motion under an external field and also magnetic bubbles can be converted into bubbles with different topological skyrmion numbers depending on the field size, as can be seen in Figure 1.36 [86, 98–102].

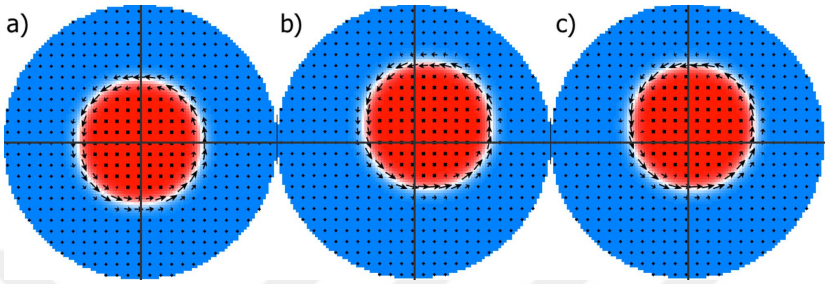


Figure 1.36. Snapshots from the simulation for a bubble with N=1 under external field gradient [99].

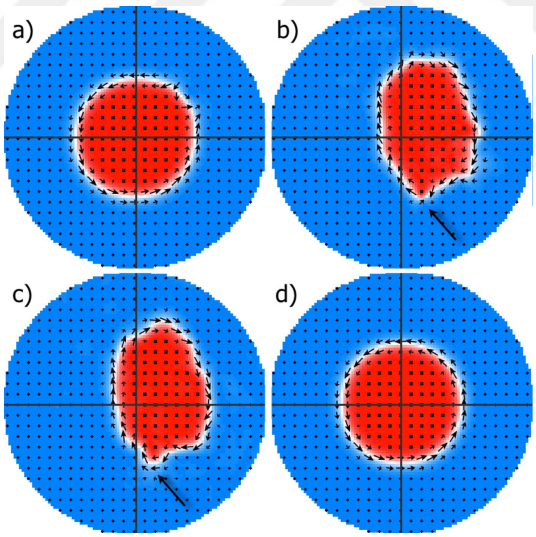


Figure 1.37. Snapshots from the simulation for a bubble with N=0 under external field gradient [99].

By applying a uniform magnetic field, the bubble diameter will periodically (with frequency about 1 GHz) enlarge and shrink through the motion of the domain wall. But as long as an external field gradient is concerned, since the domain wall motion will not be uniform in different directions, a shift from and toward the bubble center is expected when magnetic field is switched on and off, respectively. In Figure 1.37,

for N=0 type magnetic bubble, shrinking and moving from the center are clearly seen and then skyrmion number of the magnetic bubble changed from N=0 to N=1.

Beside the simulation and theoretical calculation, skyrmion motion under en external perpendicular magnetic field was experimentally observed [103, 104]. In Figure 1.38, this experiment's results are given. These images were taken by XMCD-PEEM system.

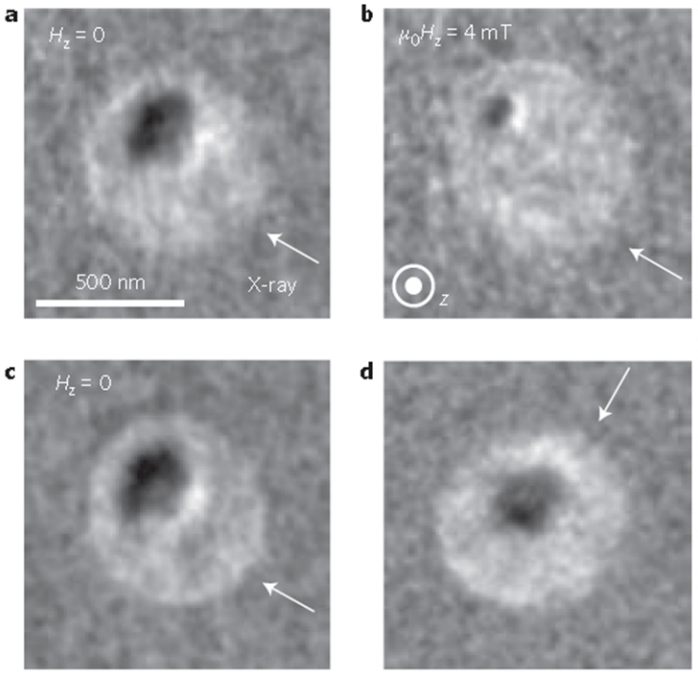


Figure 1.38. XMCD-PEEM image of the skyrmion during the application of an external magnetic field perpendicular to the film plane [103].

To use magnetic bubble in a spin-valve to fabricate spintronic oscillators based on the excitation of magnetic bubble, in literature there have been studies [105, 106]. G. Finocchio and his colleges (2013) made a research for this purpose by constructing a simulation [105]. In this study, schematic of the spin-valve point-contact geometry was given in Figure 1.39.

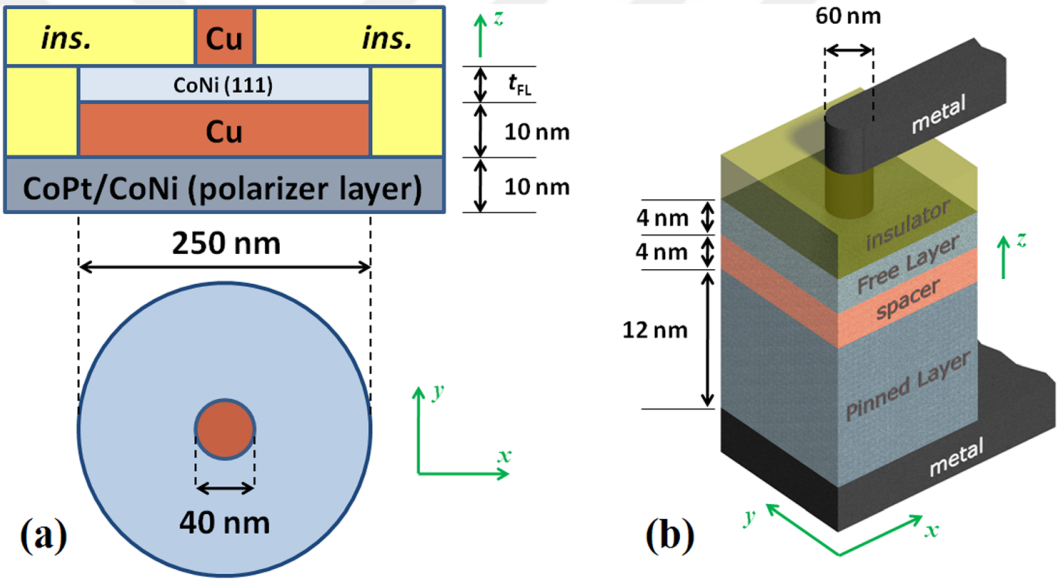


Figure 1.39. Schematic of the spin-valve point-contact geometry [105].

2. THREE DIMENSIONAL FINITE ELEMENT MODELING OF PCM

In this part, I introduce a 3D finite element model of the phase change memory (PCM)and discuss its implications for stable intermediate states.

2.1. Description of the Three-Dimensional Finite Element Modeling

For the three dimensional finite element modeling, I used COMSOL which is a finite element analysis solver and a Simulation software. COMSOL Multiphysics includes different kinds of physics such as Convection And Diffusion, Electromagnetic, Fluid Dynamics, Heat Transfer and Partial Differential Equations, and so on.

In this work, to understand the switching dynamics of the phase change memory devices during the phase transition, I constructed a three dimensional finite element model for the PCM cell with the dimensions given in modeling guide to simulate phase transition of a PCM cell having a single layer $Ge_2Sb_2Te_5$(GST) and used the electrical and thermal parameters of the phase change material (for GST). A PCM cell includes a phase change material layer, contact electrodes and also insulating layer. The three dimensional structure of the cell is given in Cartesian grids so as to address the complex geometry of the cell, clearly.

To visualize the complex nature of the switching dynamics in a PCM device, 3-D finite element simulations were handled by constructing separate submodels; an electrical model which involves a temperature and phase dependent electrical conductivity, a thermal model where joule heating caused by the electrical current serves as a heat source and involves temperature and phase dependent thermal conductivity as well as Seebeck coefficient for the GST material to account for thermoelectric effect, a phase change model that involves temperature dependent nucleation kinetics of crystallites. Coupling the submodel in the framework of the multiphysics approach allowed us to

accurately predict the percolation threshold for switching.

I define these submodels separately bearing in mind that the interaction between the submodels is taken into consideration during the execution of the simulation.

2.1.1. Electrical Model

For the electrical part, I implement a model to explain the electrical characteristics of the cell by solving the Laplace equation. In the electrical submodel Laplace equation, $\nabla.[\sigma \nabla F] = 0$ where σ is the electrical conductivity of the material, is solved iteratively (with 1ns time steps) for each mesh element in conjunction with the thermal submodel to obtain the spatial electrical potential distribution F(x,y,z) in the PCM device.

If the electrical conductivity is not a function of the electric field then Laplace equation can be applied easily. Because; above the threshold voltage, the electrical conductivity does not show any field dependence and it is only a function of temperature. Therefore, while working with high enough voltage values, the electric field dependence of conductivity can be neglected.

I sandwich the phase change material between two metal electrodes, which necessitates that I define the boundary conditions on the contact areas between materials. The boundaries of top and bottom surfaces of the metal electrodes and all external surfaces are chosen as the Dirichlet boundary condition and for interface surfaces, I consider Neumann boundary condition.

Dirichlet and Neumann boundary conditions are defined as;

$$y'' + y = 0$$

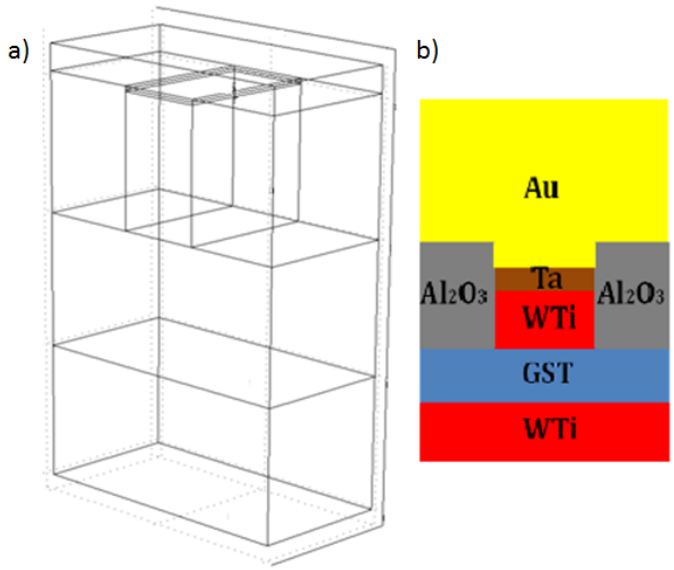


Figure 2.1. Three-dimensional structure of PCM in the simulation is drawn in the figure a and figure b shows the material types in the PCM device used in the simulation.

for a given boundary (from one side a , from other side b]; in the Dirichlet boundary condition, the solutions are,

$$y(a) = \alpha, \quad y(b) = \beta, \quad \alpha = \beta$$

in Neumann boundary condition, the solutions are,

$$y'(a) = \alpha, \quad y'(b) = \beta, \quad \alpha = \beta$$

where α and β are given numbers.

Electrical conductivity of metals change with temperature and the relation between conductivity and temperature is given by equation 2.1:

$$\sigma = \frac{1}{\rho_0(1 + \alpha(T - T_0))} \tag{2.1}$$

Where ρ_0 is resistivity at reference temperature T_0, α is temperature coefficient of material and T is current temperature.

A phase change material has amorphous and crystalline phases with different atomic structures, so that they have different physical properties such as electrical conductivity, resistivity and so on. Thus in this electrical model I have to account for the difference between the values of electrical conductivities for each different phase state. The transition between these two phases is prompted by changing the temperature. For the electrical model the electrical parameters for all materials are given in Table 2.1. below.

Table 2.1. The resistivity and temperature coefficient used values in the simulation

	Resistivity at T_0 [Ω.m]	**Temperature coefficient [1/K]**
GST_{Amorph}	1/3 [107]	-3.4×10^{-4}
GST_{Crys}	3.6×10^{-4} [107]	-3.4×10^{-4}
WTi	60.5×10^{-9}	86×10^{-6}
Al_2O_3	1×10^{15}	9.1×10^{-8}
Au	22.14×10^{-9}	1.36×10^{-6}
Ta	131×10^{-9}	6.5×10^{-6}

2.1.2. Thermal Model

I solve the heat conduction equation so as to determine the heat distribution inside the PCM device after an applied current induces a local heating in this device. The heat equation is solved iteratively in each mesh element to obtain the spatial distribution of temperature T(x,y,z) at each time step:

$$C\frac{\partial T}{\partial t} - \nabla - (\kappa \nabla T) = Q + Q_{th} \tag{2.2}$$

where C is the heat capacity, κ is the thermal conductivity. Q is the heat generated within the domain and $Q_{th} = T \times J \times \nabla S$ accounts for the contribution of thermoelectric effect to heating where S is the temperature dependent Seebeck coefficient and $\nabla S = \frac{dS}{dT}\nabla T$..

In the thermal model, I have to consider not only the temperature dependent thermal conductivity of each phase, but also the electrical contribution to thermal conductivity. Hence, I add Wiedemann-Franz equation to define corrected thermal conductivity of PCM completely. Wiedeman –Franz connects the electrical and thermal conductivity with the equation 2.3;

$$K = L.T.\sigma_e + K_{ph} \tag{2.3}$$

where L is Lorenz number, σ_e is electrical conductivity and K_{ph} is the phonon contribution to thermal conductivity which is temperature independent. K_{ph} values for amorphous and crystalline states are 0.3 [W/mK] and 0.7 [W/mK] [107], respectively .

Table 2.2. The thermal conductivity, density and heat capacity values used in the simulation

	Thermal Conductivity [**W/K.m**]	**Density** [**kg/m^3**]	**Heat Capacity** [**J/kg.K**]
GST_{Amorph}	0.3 [108]	6200 [109]	1.3×10^6 [109]
GST_{Crys}	0.7 [108]	6200 [109]	1.3×10^6 [109]
WTi	0.742	1×10^4	132
Al_2O_3	40	3.95×10^3	1880
Au	318	19.9×10^3	128
Ta	57.5	16.69×10^3	190

2.1.3. Phase Change and Percolation Model

In electrical and thermal model, I study the electrical and thermal characteristics of the device and as the last step, I add a phase change model to connect two metastable states so as to complete the electrical switching of the phase change device.

The phase change model is used to describe how the atoms in phase change material in the amorphous state are forming small crystalline nuclei and start to construct and grow a more arranged phase due to the temperature increase for each mesh element or vice versa. The crystalline nuclei can form at this point where the temperature has maximum value according to the applied voltage pulse. In Sun K. and *et.al* [109] simulation for three-dimensional phase random access memory, the phase transition is reported to start at the interface where the current is most efficiently confined because this is also the first point where the temperature will be high enough for the phase transition.

First, the nucleation starts in bulk material and then the growth rate needs to be calculated. Calculating the probability of nucleation is a first step and in second step, I

will study the temperature dependence of growth rate for this crystalline nucleus [110]. I will define a steady state but temperature dependent nucleation rate and describe the growth velocity of crystalline phase due to the classical nucleation theory.

The probability rate for the crystallization process depends on the nucleation rate, I_n , and growth velocity of the nuclei, V_g, equation 2.4:

$$\frac{dP}{dt} = I_n(T)\frac{1-P}{N} + V_g(T)\frac{1-P}{a_0} \tag{2.4}$$

where P is the probability of crystallization at a certain time, N the number of molecules per unit volume and a_0 is the atomic jump distance [108]. The temperature dependent nucleation can be defined by the following equation 2.5 [108]:

$$I_n(T) = \alpha_1\, N\, exp\Big(-\frac{E_{a1}}{k_B T}\Big) X exp\Big(-\frac{\Delta G^*}{k_B T}\Big) \tag{2.5}$$

where α_1 is a frequency factor, k_B the Boltzmann constant, and E_{a1} the activation energy for nucleation. The ΔG^* is the energy barrier to form a nucleus of critical size. Growth velocity is also temperature dependent and is expressed with equation 2.6 [108]

$$V_g(T) = \alpha_2\, d\, exp\Big(-\frac{E_{a2}}{k_B T}\Big) X \Big[1 - exp\Big(-\frac{\Delta G_v}{k_B T}\Big)\Big] \tag{2.6}$$

where α_2 is a frequency factor, d is the inter-atomic distance, E_{a2} the activation energy for the nuclei growth and ΔG_v is the Gibbs free energy, $\Delta G_v = \Delta H_v(1 - T/T_m)$

in which ΔH_v is latent heat. Simulation results will present how the crystallization in a bulk phase change material starts from a crystalline nucleus formation with the growth of its radius in time and finally a complete phase transition in this bulk according to the temperature distribution.

During phase transition; electrical, optical and thermal properties of the material change in a certain way that is known as percolation effect [111]. This effect leads to a nonlinear dependence of the experimental observable like the optical reflectivity and the electrical resistivity as a function of the crystallization degree, i.e., the volume fraction of crystallized material. I will apply the effective medium approximation that is presented by Bruggeman [112, 113] which describe how to calculate the electrical conductivity, thermal conductivity and the dielectric function for various shapes of composite materials as a function of the dopant and the host material properties.

Bruggeman effective medium approximation (EMA) is easily applicable. The electrical conductivity and thermal conductivity should be estimated for the full structure. For instance, the electrical conductivity of the active region is approximately given by the equation 2.7 [114]:

$$\sigma(f, \sigma_a, \sigma_c) = 0.25\Big((2\sigma_p - \sigma\prime_p) + \Big[(2\sigma_p - \sigma\prime_p)^2 + (8\sigma_a\sigma_c)\Big]^{1/2}\Big) \tag{2.7}$$

with $\sigma_p = (1-f)\sigma_a + f\sigma_c$ and $\sigma\prime_p = (1-f)\sigma_c + f\sigma_a$, where σ_a and σ_c are the electrical conductivities of amorphous and crystalline phases respectively. f is the crystallization fraction which is defined as the ratio of the volume occupied by the crystal phase to the total volume of the mesh element and is calculated for each mesh. This procedure is analogous for the thermal conductivity of the mixed phase.

The simulations provide a complete picture of the thermal profile, crystallization fraction inside the volume of the GST as well as the device resistance during and/or

after an applied pulse. The results are then compared with experimental findings, which in turn lead to optimization of some of the simulation parameters to better fit the experimental data such as nucleation and growth rates, which have to be adjusted differently for the two top contact geometry devices. The effect of nucleation and growth rate on the programming conditions is discussed in the experimental results section in detail.

2.2. Simulation Results

I apply a square step potential which has amplitudes ranging from 0.9 V to 1.5 V and pulse duration changes from 10 ns to 350 ns with 2 and 42 ns trailing edge (trailing edge is defined to be the time it takes for the voltage to drop from 90 % to 10 % of its amplitude). In the simulation, the potential is applied from the top electrode and the bottom electrode is chosen as ground. In Figure 2.2, at the beginning and end of the pulse, there is 0.05 DC voltage V to perform read operation. This allows me to measure the current and calculate the resistance of the device.

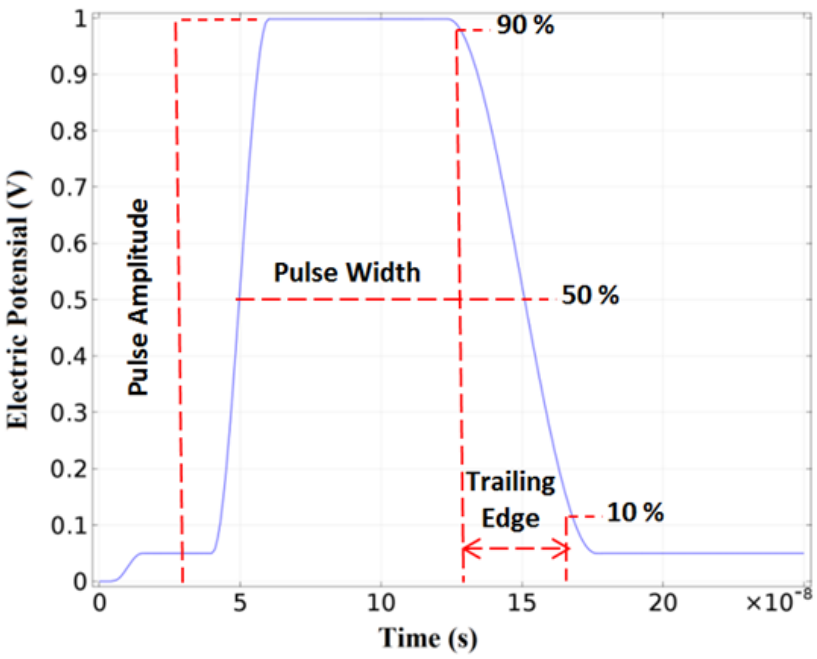


Figure 2.2. Applied Potential in the simulation for 1 V with 100 ns pulse width and 42 ns trailing edge.

Trailing edge and operation time are important factors for the simulation because I need to give enough time to the material to heat and cool down and so the operation time in my simulation is changed from 100 ns to 450 ns so as to observe the whole heating and cooling process. However for the above applied potential it is chosen as 100 ns with 42 ns trailing edge. Figure 2.3 shows the potential distributon for 1V, 100 ns with 42 ns trailing edge applied potential in the phase change memory cell.

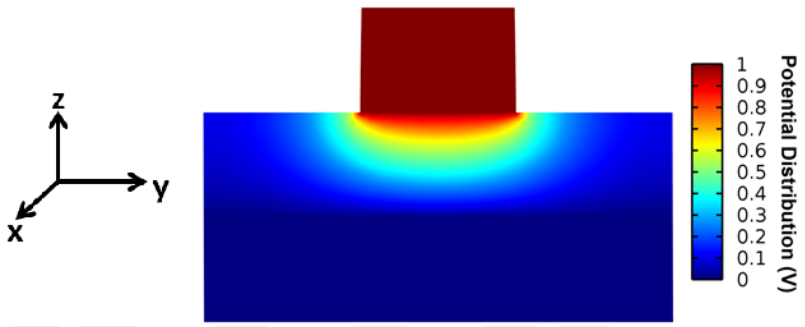


Figure 2.3. Potential Distribution in device during reset process at t = 100 ns for 1 V applied potential with 100 ns pulse width and 42 ns trailing edge.

When I apply a step potential between the two electrodes, a current passes through the whole device. I take into account the current change in z-direction because z direction is chosen as the symmetry axis of the device. The current change in time inside the cell is given in Figure 2.4.

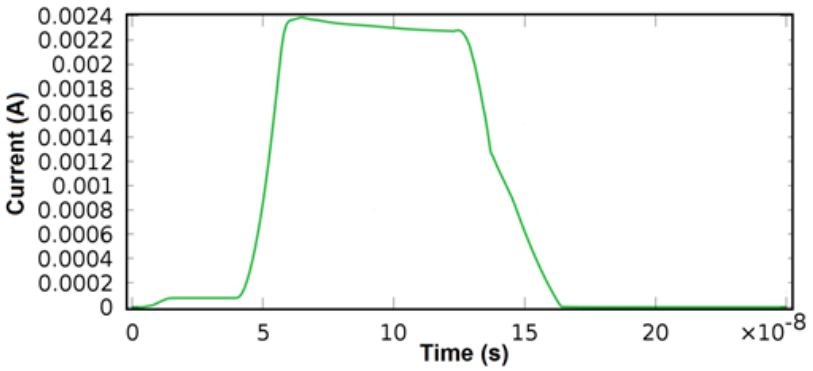


Figure 2.4. Current versus time graph at z = 75 nm for 1 V applied potential with 100 ns pulse width and 42 ns trailing edge.

As it can be seen from Figure 2.5, at the beginning of the pulse there is a current passing through the device because the initial condition is chosen as crystalline phase. At the point that the voltage pulse starts to decrease, also the current decays sharply following the trailing edge. During reset process, the material under goes a phase transition and therefore the current is very small because of the amorphization at the active region. When this current value is compared to literature it is confirmed that it is acceptable when the device dimensions are considered [108]. When we look at the current distribution inside the PCM cell, because of the shape of the top contact, namely sharp corners, current accumulates around the sharp corners as can be seen in Figure 2.5.

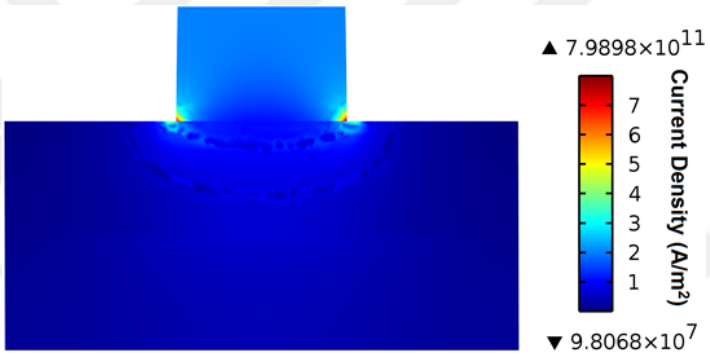


Figure 2.5. Current distribution through the PCM device at t =100 ns for 1 V applied potential with 100 ns pulse width and 42 ns trailing edge.

When the distribution of current density in z-direction is studied, according to the material properties in the structure, current density is obtained as in Figure 2.7.

The voltage pulse is applied from the top electrode so the current distribution shows a maximum point in top electrode (TE) and it decreases along z-direction until it reaches the bottom electrode. After the GST top electrode interface the current density decreases sharply inside the GST bulk because of the high electrical resistivity of GST.

The reason for the increase in current density in WTi top electrode is having a relatively small interface area of the electrodes. At the top layer, the current density will

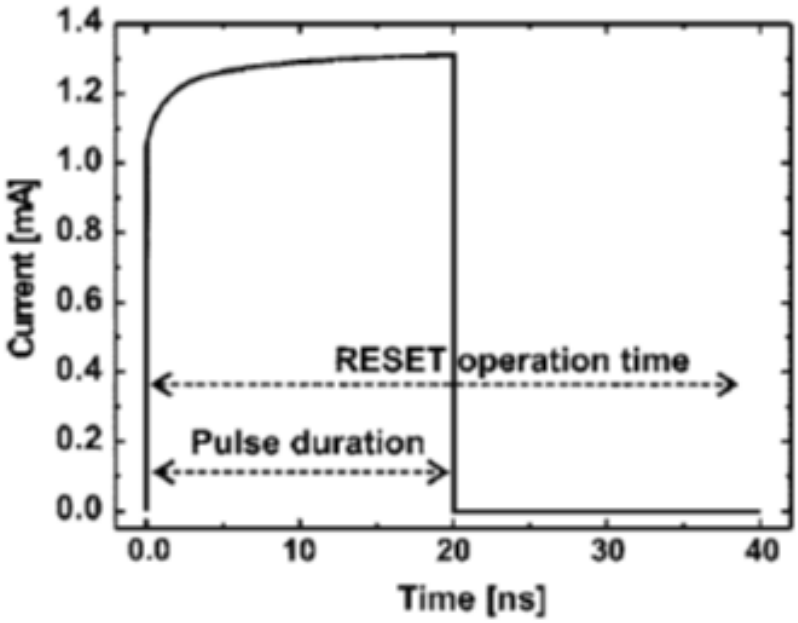


Figure 2.6. Current – time graph [108]

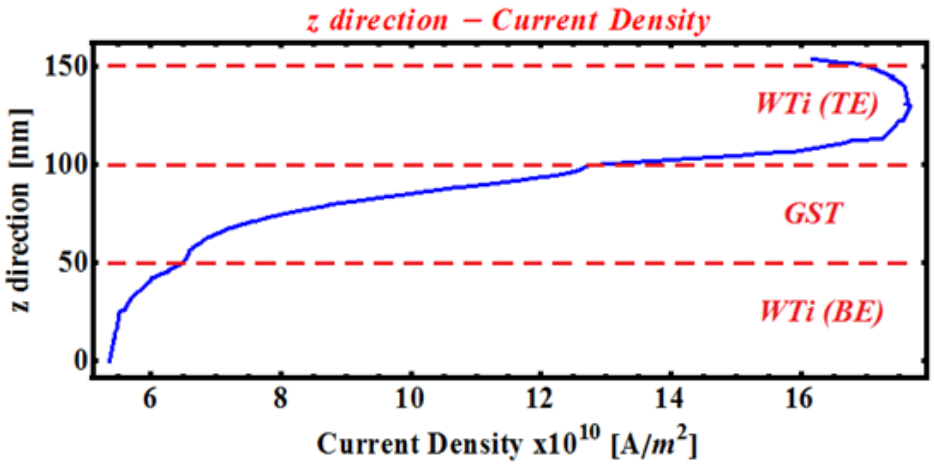


Figure 2.7. Current Density in the PCM cell for 1 V applied potential with 100 ns pulse width and 42 ns trailing edge.

increase while flowing through from Au layer to WTi top electrode because the surface area of the electrode decreases. The current density will decrease while passing from the top electrode (TE) to the GST bulk because of the high resistivity of GST material. In addition the dimensions of the bulk GST are bigger than the top electrode [108].

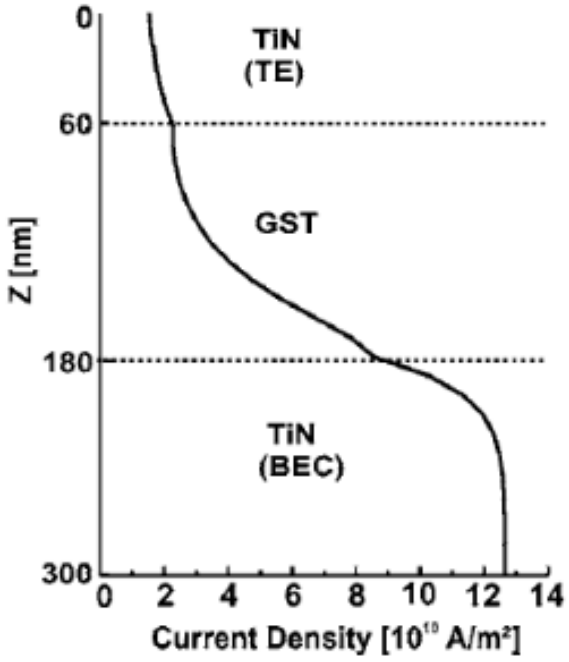


Figure 2.8. Current Density in the PCM cell [108].

The current density distribution in z-direction taken from the literature ([108]) is shown in Figure 2.8. Considering different device dimensions and structure our current density distribution in z-direction is consistent with the literature results.

When the step potential pulse is applied, a current will pass through the whole device and this current leads to local heating. For all different materials the temperature gradient will be different because of their different electrical and thermal conductivities. In the cell, Al_2O_3 is taken as insulator layer because of its high resistivity and low thermal conductivity. The current cannot pass through these insulator layers, therefore all current has to pass through the WTi electrodes and GST. The maximum temperature gradient is observed in GST bulk because of the electrical resistivity of GST.

As it is well known, all parts of GST bulk do not heat homogeneously, the maximum temperature point will be close to the top electrode in GST bulk because the current density is much higher at a point closer to the top electrode than the bottom electrode.

The temperature change for two different points in GST bulk during 280 ns operation time is given in Figure 2.9. In this graph the temperature change for two specific points; P1 and P2, whose positions are 75 nm and 60 nm from the top surface of the device, are given for 0.85 V operation voltage. The temperature increasing at these points have apparently similar characteristics to the applied potential change in time because of the strong dependence of the current flowing through device to the applied potential.

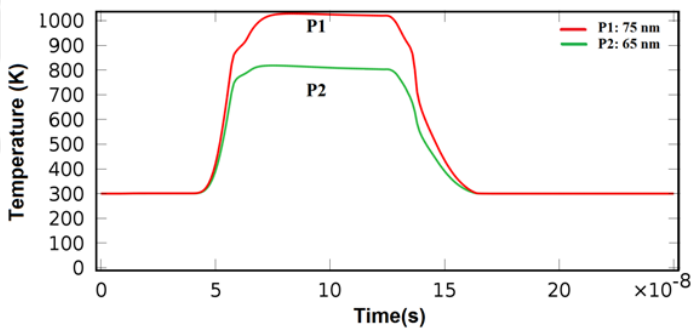


Figure 2.9. Temperature versus time of two different points in GST bulk for 1 V applied potential with 100 ns pulse width and 42 ns trailing edge.

These two points are also marked in Figure 2.10 which shows the temperature distribution inside the device for an operation time which is long enough for cooling down. Hence the scale on the right side scale of picture shows only a small temperature increase for bulk material after the cooling process. In addition it is understandable that the maximum temperature point is very close to the middle of the GST because of the high density of the current flowing through the GST.

Also temperature distribution in the device with respect to the z-direction is given in Figure 2.11. As it is indicated before, the maximum temperature point is near

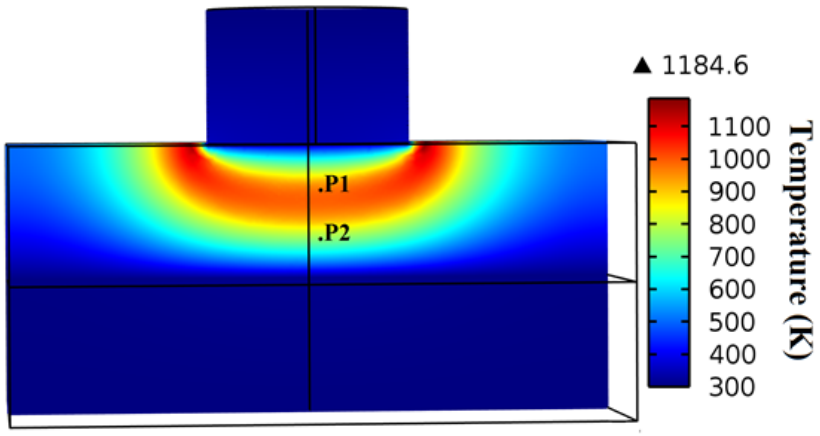


Figure 2.10. The temperature distribution in PCM device for 1 V applied potential with 100 ns pulse width and 42 ns trailing edge.

the middle of GST. Tungsten titanium WTi layer is on the top of the device and this material has a very good electrical conductivity, therefore in this layer current does not cause very much heating as it can be seen in Figure 2.10.

The top and bottom WTi electrodes have the same thicknesses in z-direction however their interface areas with GST are different. In addition their temperature distributions in z- direction reflect the differences in their current density values. Thus the slopes of the temperature distribution inside these electrodes are different.

Now we look at the temperature distributions inside the two different top contact shape PCM device. First of all, when we take a look at the 75 nm circular top contact PCM cell, temperature distributes uniformly inside the GST with 1 V applied potential with 100 ns pulse width and 42 ns trailing edge. As you can be seen in Figure 2.11 the maximum temperature 1029.7 K and the temperature distribution is uniform because of isotropic heating originating from the top contact shape.

However when I look at the square top contact shape PCM cell, it is a little different than the circular ones. Because of the top contact shape, there are some points near the corners of top contact which show current crowding effects. These

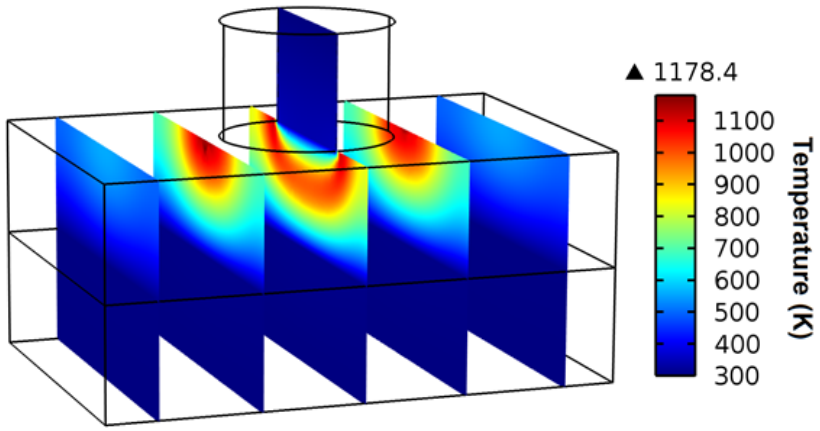


Figure 2.11. Temperature distribution inside the circular top contact PCM cell for 1 V applied potential with 100 ns pulse width and 42 ns trailing edge.

areas cause heterogeneous temperature distribution inside the PCM cell and therefore there are some hot spots. These hot spots are clearly visible in Figure 2.12. Here our top contact size is 90 nm and the applied potential is 1 V with 100 ns pulse width and 42 ns trailing edge.

It appears that although we applied the same potential, the circular contact has higher temperature than the square contact because the area of the top contacts are different and this affects the current density and the material temperature.

Here in Figure 2.14 It is clear how the temperature changes inside the PCM cell through the z-direction. However I took only t = 175 ns to see maximum temperature. When I compare my simulation results for the temperature distribution in z-direction with [44], it is clear that the temperature distribution has a maximum value in the GST bulk, although the slight difference for temperature value in top and bottom electrodes depends on the chosen electrode material and device structure.

Figure 2.15 summarizes clearly the temperature differences between square and circular top contact devices. Since most of the simulation parameters are temperature dependent, the temperature profile plays an important role in determining the phase change kinetics and the final phase of the material. The three dimensional temperature

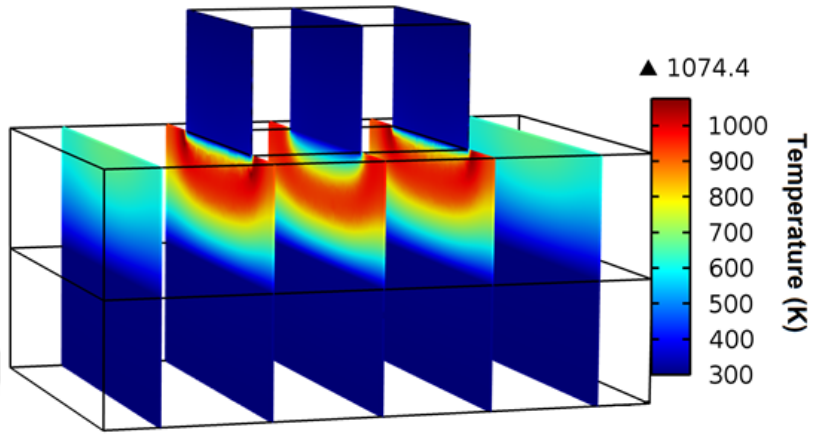


Figure 2.12. Temperature distribution inside the square top contact PCM cell for 1 V applied potential with 100 ns pulse width and 42 ns trailing edge.

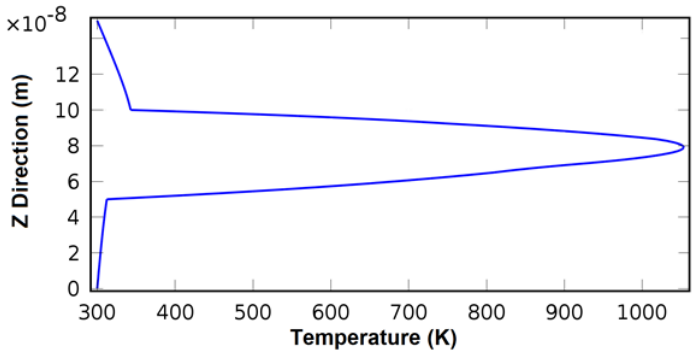


Figure 2.13. Temperature distribution in z-direction for 1 V applied potential with 100 ns pulse width and 42 ns trailing edge.

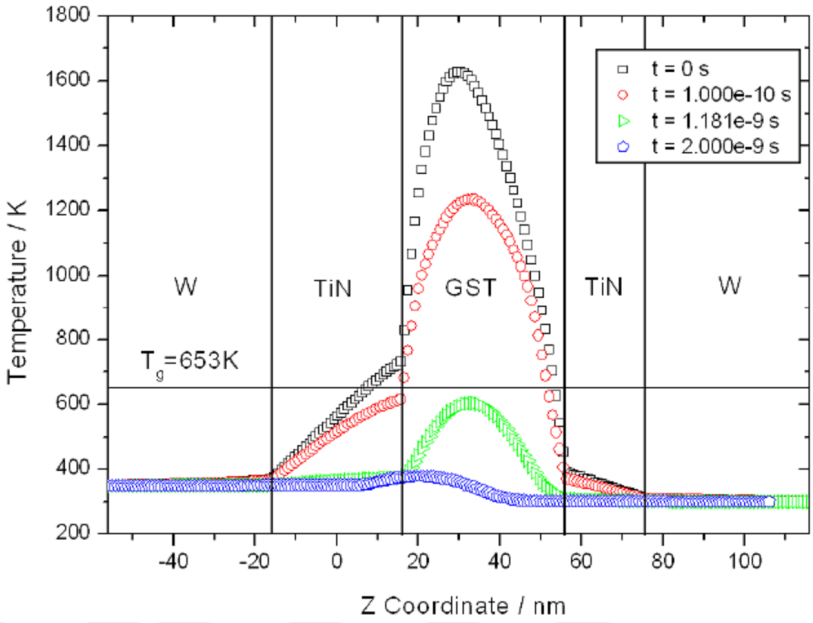


Figure 2.14. Temperature distribution in z-direction [109].

distribution inside the phase change layer is simulated during a voltage pulse of 1 V pulse amplitude with 100 ns width and 42 ns trailing edge. Figure 2.15 compares simulation results for two different geometry top-contact devices: a 75 nm diameter circular top-contact PCM cell (Figure 2.15 a-c) and a 90 nm square top contact (Figure 2.15 d-f) PCM cell.

Heating inside the device is illustrated by a color map of local temperature shown in horizontal (figures a-b and d-e) and vertical (figures c and f) slices of the device. The temperature is elevated in a dome-shaped region inside the GST layer, called the active region which is where the phase transition happens. Even though the highest temperatures achieved are around 1192 K for both devices, the temperature distributions are completely different. For the circular top contact PCM device the temperature is the highest at the periphery of the top contact with a homogeneous distribution, whereas for the square top contact PCM cell, the highest temperatures are only observed near the sharp corners of the top contact.

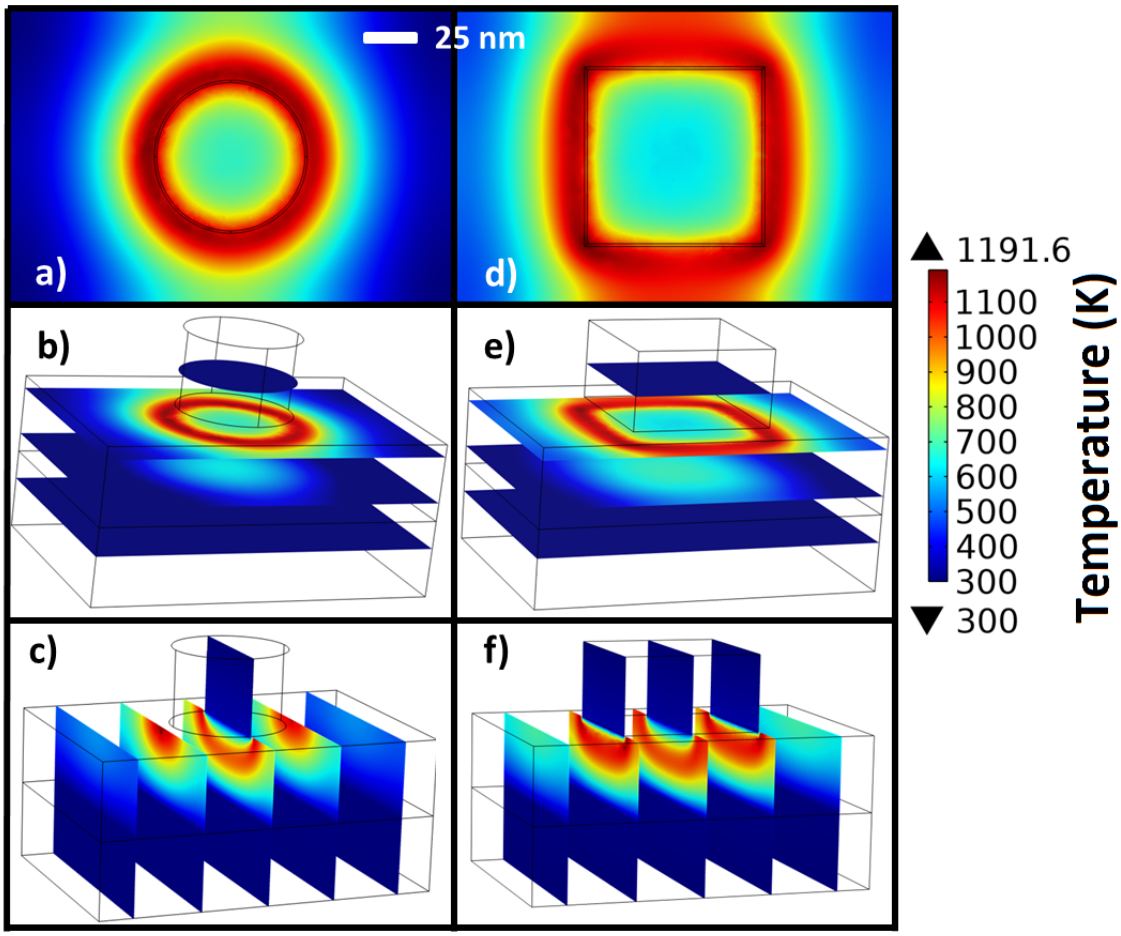


Figure 2.15. A three dimensional illustration of temperature distribution is plotted for different vertical and horizontal slices for a-c: 75 nm circular top contact PCM device and d-f: 90 nm square top contact device. During a programming voltage pulse of 1V, with 100 ns width and 42 ns trailing edge. Figures a and d specifically show the horizontal slice 5 nm below the interface between the top contact and the GST layer.

It is clearly visible in Figure 2.15 that the temperature distribution inside the square top contact device is heterogeneous around the edges of the top contact as a result of current crowding at the corners. This is what makes the square shape top contact a unique configuration to allow a non-uniform phase transition inside the GST active region. Under the same programming voltage PCM cells with circular and square top contact geometries yield different temperature distributions as a result of differences in current distributions throughout the GST.

2.2.1. Electrical Conductivity and Resistivity Results

GST material exhibits two different phases which have different atomic structure. In crystalline phase the atoms are arranged periodically as rock-salt structure. Hence the electrical conductivity of crystalline phase shows quite high values. Electrical conductivity vs temperature is given in Figure 2.16 for 0.85 V applied potential in 280 ns pulse duration. The electrical conductivity at room temperature is 2770 [S/m] and is increasing with temperature.

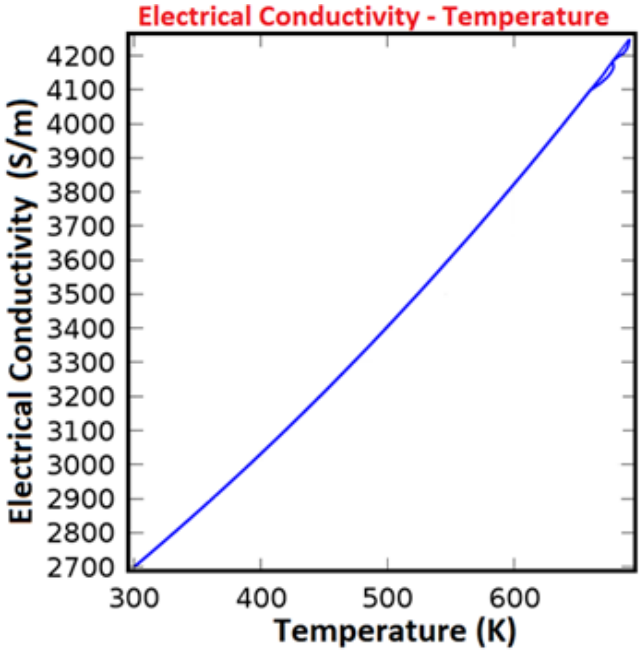


Figure 2.16. Electrical Conductivity versus temperature for Crystalline Phase 0.85 V applied potential with 100 ns pulse width and 42 ns trailing edge.

However, it is clear that the material temperature does not go a lot above the melting temperature (616 ^{0}C), therefore material does not undergo any phase transition. Thus after reaching the maximum temperature our material stays in the crystalline phase because applied potential is not high enough to heat our device above the melting point. Therefore, it can be seen from Figure 2.16 that even if after little change in the material structure, our material goes back to its initial phase, crystalline phase.

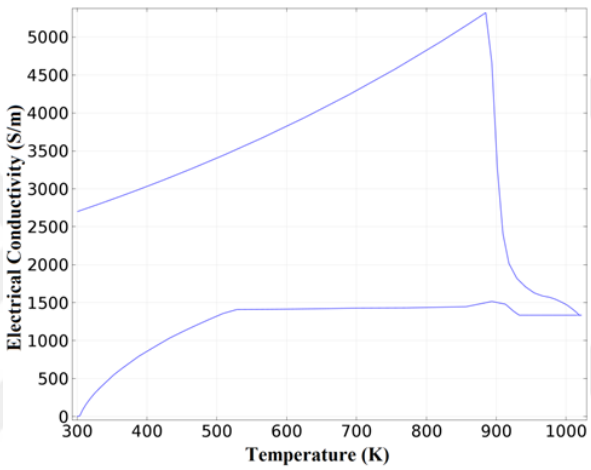


Figure 2.17. Electrical Conductivity versus temperature for Crystalline Phase 1 V applied potential with 100 ns pulse width and 42 ns trailing edge.

When I apply 1 V potential with 100 ns pulse width and 42 ns trailing edge to the device I obtain electrical conductivity versus temperature as seen in Figure 2.17. Electrical conductivity of the crystalline state vs temperature agrees with the literature [108]. When the temperature approaches the melting point electrical conductivity is affected and therefore, first its value decreases then after the phase transition it increases. Because, GST material can have enough time to recrystallize, so its value goes back to the value of the crystalline state.

For amorphous phase the electrical conductivity does not change with temperature so much because of the high resistivity of the amorphous phase, just a little increase. The high resistivity is due to disordered atomic arrangement. The initial value of the electrical conductivity for the amorphous state is 3 [S/m].

Because of being two different metastable states, resistivity of phase change material shows two different resistivity values, for crystalline and amorphous state resistivity are $3.6x10^{-4}$ $\Omega.m$ and 1/3 $\Omega.m$, respectively. Phase change material is a kind of semiconductor material which typically exhibits a decrease in resistivity as the temperature increase. Hence, in our simulation that the resistivity decrease of phase change material is observed as in Figure 2.18 for 1 V applied potential with 100 ns pulse width and 42 ns trailing edge.

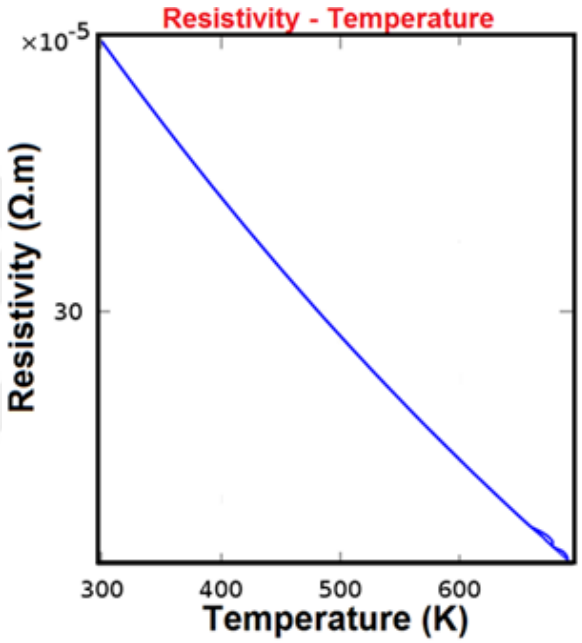


Figure 2.18. Resistivity versus temperature for Crystalline Phase 1 V applied potential with 100 ns pulse width and 42 ns trailing edge.

For the amorphous state, the resistivity also decreases with increasing temperature. Apparently the amorphous phase resistivity is much higher than the crystalline phase resistivity. The switching behavior of phase change material is observed after the nucleation process is included in the simulation, so that the phase transition is possible in the GST bulk. In phase change material the current does not pass through the device until the applied potential is above the threshold voltage. However, above this potential value the amorphous phase resistivity decreases allowing a current to pass through the device knowing as threshold switching.

However, adding the phase transition affects our result and as you can see from Figure 2.18, the temperature approaches the melting point, the resistivity is affected and therefore, first of all its value decreases very sharply then after phase transition this value is decreased very deeply. After phase transition our cell is in the amorphous phase anymore. Resistivity values of amorphous an crystalline state according to temperature are consistent with the literature values as is seen in below graph (Figure 2.19).

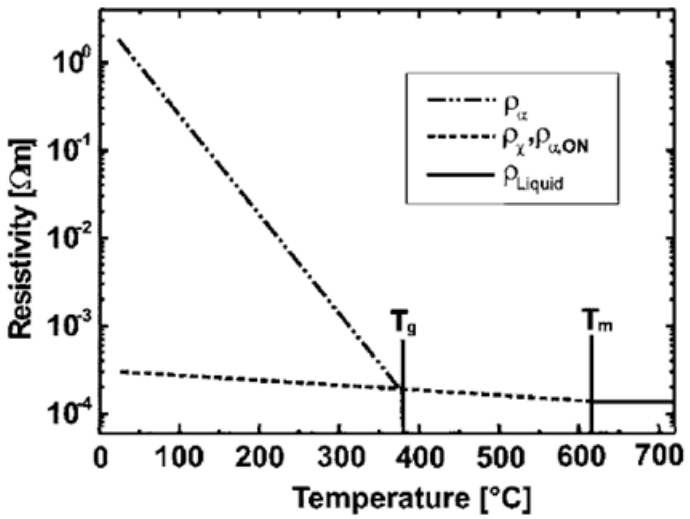


Figure 2.19. Resistivity versus temperature for Amorphous and Crystalline Phase REF 52.

2.2.2. Thermal Conductivity Results

Metastable states of the GST material exhibit not only two different electrical conductivity values but also two different thermal conductivity values. At room temperature the thermal conductivity value for he crystalline state is 0.7 [W/mK] and it increases with temperature as seen in Figure 2.20 for 1 V applied potential in 100 ns pulse duration with 42 ns trailing edge.

Initially my material is in the crystalline phase, the thermal conductivity of crystalline phase increases with temperature as expected from the formula (equation 2.3). At the melting temperature the thermal conductivity of crystalline phase should reach the value of the liquid phase. However, because of some uncertainties, thermal con-

ductivity decreases. After cutting the applied voltage, the material undergoes a phase transition to the amorphous phase.

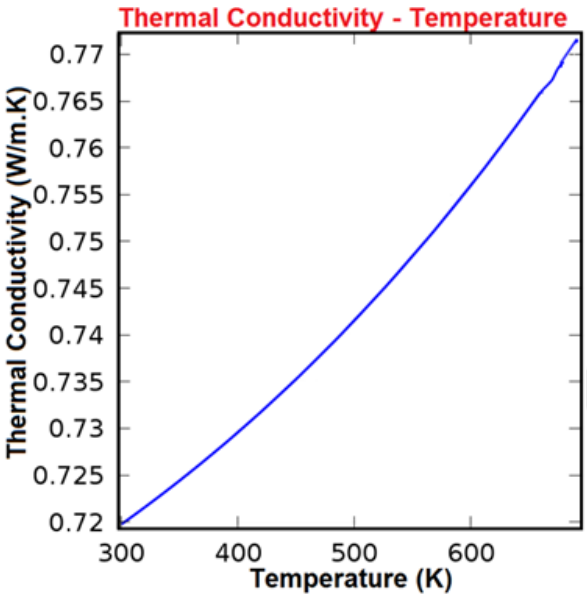


Figure 2.20. Thermal Conductivity versus temperature for Crystalline Phase for 1 V applied potential with 100 ns pulse width and 42 ns trailing edge [108].

The thermal conductivity of amorphous state at room temperature is 0.3 [W/m.K] and its increase with temperature is also given in Figure 2.20 for 1 V applied potential in 100 ns pulse duration with 42 ns trailing edge after adding phase transition. The thermal conductivity values of two metastable states vs temperature agrees with the literature [108]. Thermal conductivity value for crystalline phase is quite similar to the reference value; with the slight difference in liquid phase values because of some phase change and in the difference between crystalline and liquid phases.

The heat capacity is taken as a constant, $202 J/kg.K$, for both crystalline and amorphous phases for $T < 800$K. To account for the phase transition the latent heat is incorporated in the calculations as a smooth Gaussian near the melting point ($T_m = 892K$) as illustrated in Figure 2.22 [110, 116]. After adding heat capacity into the simulation, for a full switching operation, electrical and thermal conductivity for the horizontal slice 5 nm below the interface between the top contact and the GST layer

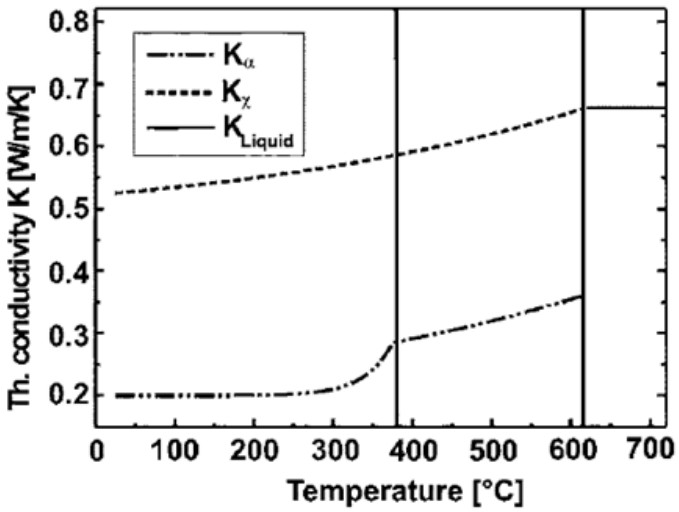


Figure 2.21. Thermal Conductivity versus temperature for Amorphous and Crystalline Phases [56].

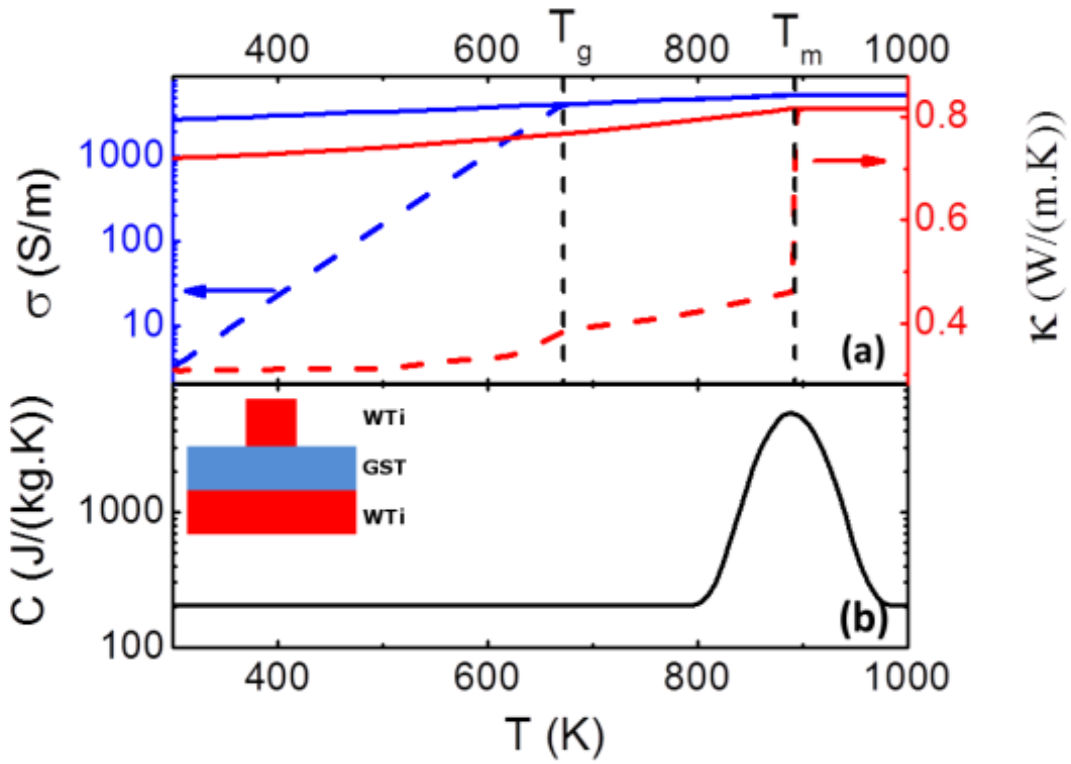


Figure 2.22. Results of Electrical Conductivity, Thermal Conductivity and Heat Capacity of the phase change material obtained from the simulation [115].

and heat capacity results are given in Figure 2.22. Beside the heat capacity of phase change material, we can see how the electrical conductivity and thermal conductivity change during phase switching in the simulation. Figure 2.22 shows that the results are consistent with literature results [56].

2.2.3. Phase Change Dynamics and Percolation Results

After completing the model, I managed to observe the phase transition from one state to the other. Initially our material is in the crystalline phase. For 1 V applied potential with 100 ns pulse width and 42 ns trailing edge the crystallization fraction, which is the parameter determining the crystalinity of the material, (which represents the crystallization ratio of the local area) at z = 80 nm, after reset process it can be seen in Figure 2.23.

As it can be seen from Figure 2.23, initially the crystallization fraction is 1 because the initial state of the material is crystalline phase. After reset operation the material undergoes a phase transition and it goes to the amorphous phase and in amorphous phase the crystallization fraction is 0. After a little re-crystallization, the crystallization fraction differs slightly increases during cool-down. It means that our material is predominantly in the amorphous phase.

When we consider the I-V characteristic of the PCM material, there are two different amorphous states as in Figure 1.10, amorphous off and amorphous on. If the current cannot pass through the device due to high resistance of the amorphous phase, this state is called as amorphous off. After a threshold voltage, the amorphous state starts to let a current flow inside the device and this amorphous state is known as amorphous on. After this, there is a current flow inside the device. However, this current flow cannot heat the material very much, but at some points, there occurs local crystallization. Following this, at a certain threshold value depending on the crystallization fraction inside the amorphous region, the current flow inside the material increases very sharply and the material undergoes a phase transition very fast due to increase in the temperature of the material. This threshold value of the crystallization fraction is

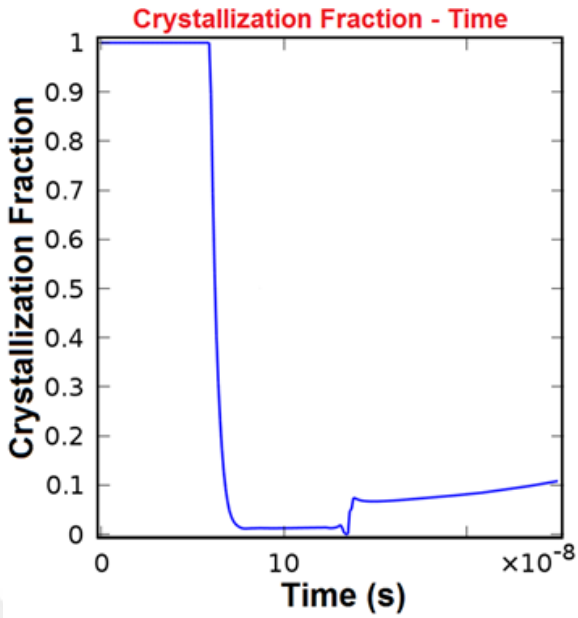


Figure 2.23. Crystallization fraction versus time for the GST material.

known as the percolation threshold, namely after this value there is a path inside the amorphous region where a current can pass from the top contact electrode to bottom contact electrode. Figure 2.24 shows both blocked situation (where percolation path does not occur because of low crystallization) and open situation (where percolation exists.

For the set operation, it is clearly observable that how the crystallization fraction of the active region changes during switching as can be seen in Figure 2.25. Here the active region is in amorphous phase, initially. Therefore, conductivity of the active region is the conductivity of amorphous phase. During the set operation, at the beginning there is negligible change of f due to low current. At a certain value, the active region's conductivity changes rapidly and goes to crystalline phase values because the active region undergoes a phase transition. This percolation threshold value is nearly 0.35. After this value, the crystallization rate increases and the active region switches to the crystalline phase very fast. The crystallization fraction is 1, it means the active region is crystalline. Figure 2.25 shows normalized electrical conductivity versus crystallization fraction during switching operation and the critical crystallization fraction

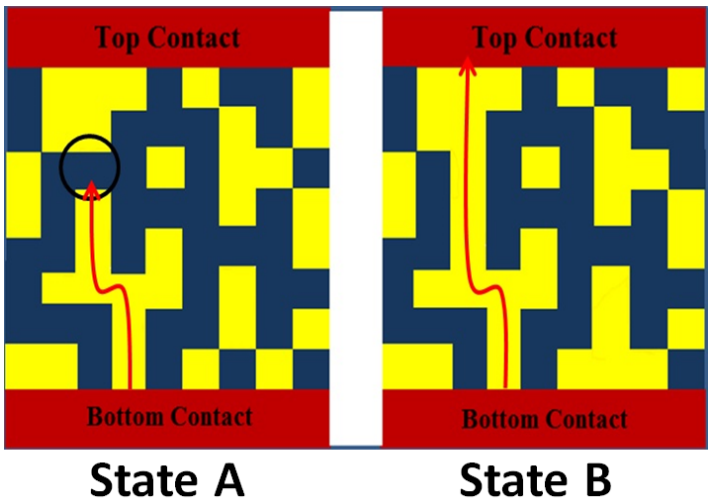


Figure 2.24. Percolation for blocked and open situation.

for percolation.

Now I focus on the phase transition for two different top contact shape PCM devices. The initial state of the material is the crystalline phase. After the reset operation for 75 nm circular top contact cell, the phase transition is shown in Figure 2.26. The crystallization fraction values 0 and 1 represent the amorphous and crystalline states, respectively. Because of uniform temperature distribution, phase distribution inside the cell is also uniform for 75 nm circular top contact PCM device.

For a 90 nm square top contact PCM cell, due to the heterogeneous temperature distribution inside the cell, the phase transition for the square top contact is also heterogeneous as can be seen easily from Figure 2.27.

Figure 2.28 summarizes the phase differences between square and circular top contact devices. The micro-structure inside the GST is simulated after the application of programming voltage pulses with various amplitudes to an all-crystalline state using a 100 ns width pulse with 42 ns trailing edge. Some of the simulation results are reported in Figure 2.28 for 75 nm circular top contact PCM device (Figure 2.28 a-c) and 90 nm square top contact device (Figure 2.28 d-f) to compare the effects of

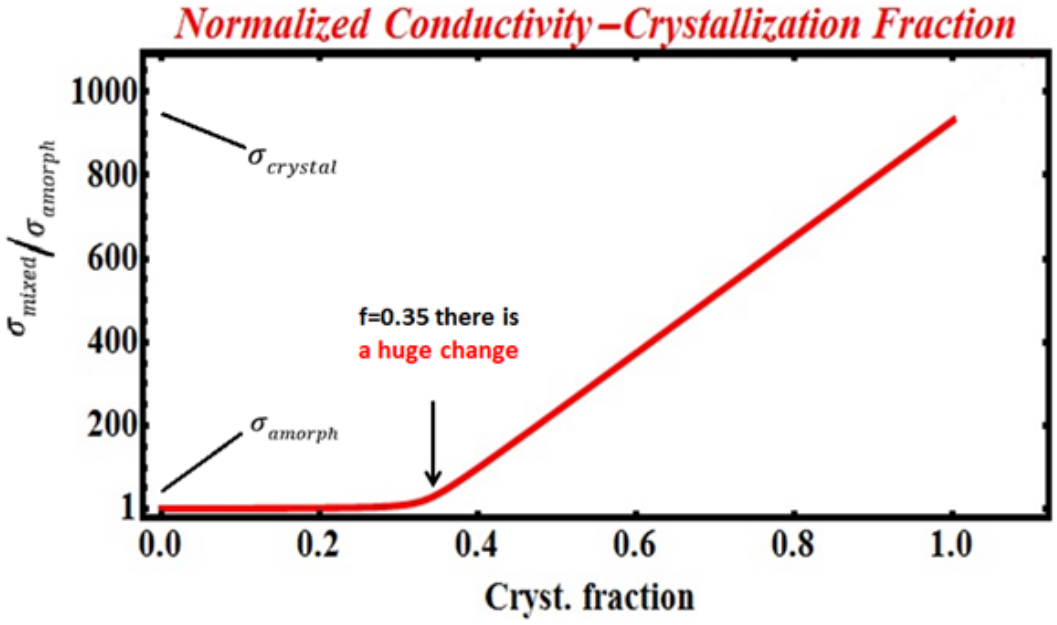


Figure 2.25. Normalized conductivity versus Crystallization fraction for 1 V applied potential with 100 ns pulse width and 42 ns trailing edge.

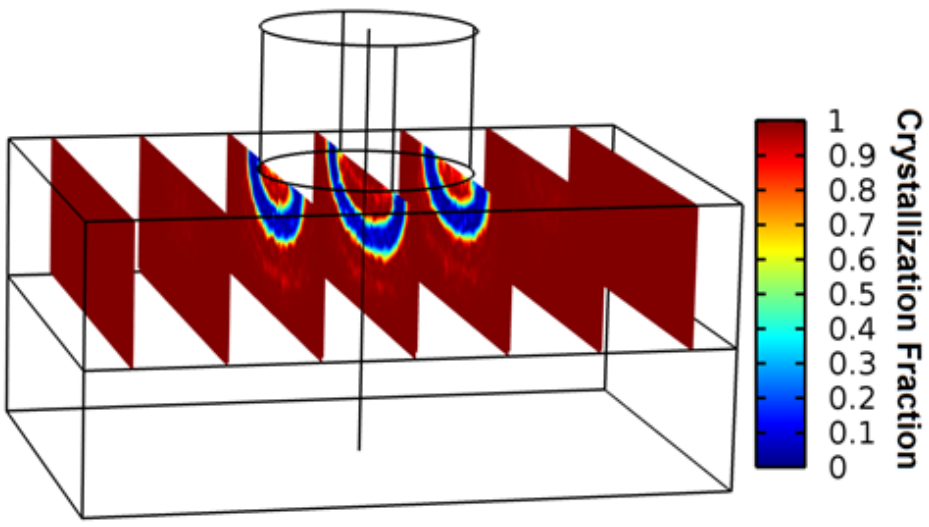


Figure 2.26. Crystallization fraction inside the circular top contact PCM cell after Reset operation for 1 V applied potential with 100 ns pulse width and 42 ns trailing edge.

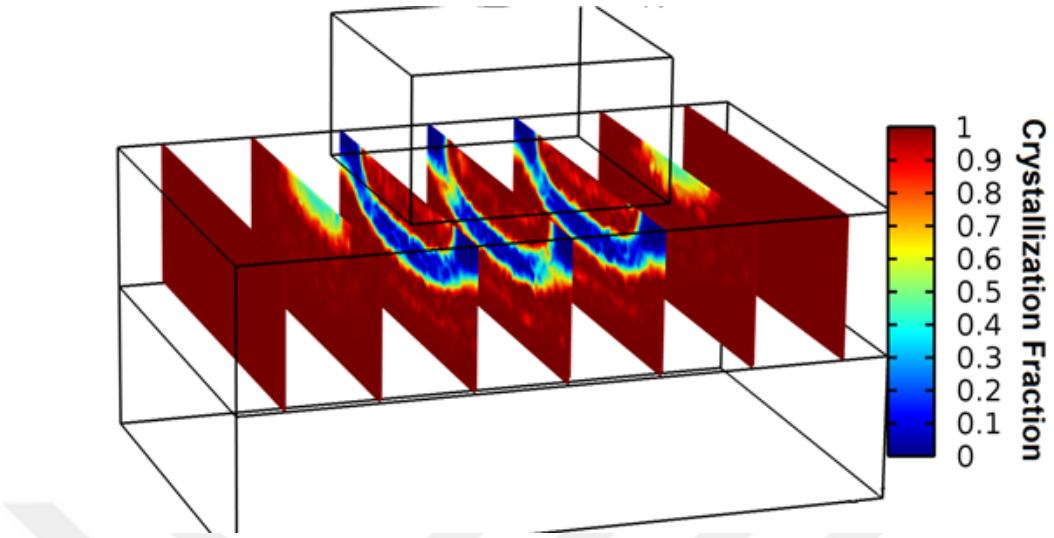


Figure 2.27. Crystallization fraction inside the square top contact PCM cell after Reset operation for 1 V applied potential with 100 ns pulse width and 42 ns trailing edge.

homogeneous and heterogeneous current distributions through the GST. The local crystallization fraction, f, is shown for the vertical cross section of the GST layer taken through the center of the device and for five vertical slices (Figure 2.28 c and f) to clarify the three dimensional phase distribution. Figure 2.28a demonstrates that the circular contact device is still in a crystalline, low resistance state (LRS) with a resistance of 1.7 kΩ after a 0.9 V pulse. A reset pulse of 1V is just enough for the device to switch to a high resistance state (HRS) of 167 kΩ, where the dome-shaped active region becomes amorphous (Figure 2.28b). This kind of a switching behavior with an amorphous dome-shaped region is common in PCM devices and has been confirmed with tunneling electron microscopy studies [108, 117–119]. Pulses below this reset voltage do not cause any drastic structural change in the circular device as seen in Figure 2.28a. For the PCM cell with the square top contact a reset state, i.e. an amorphous active region, with a resistance of 194 kΩ is achieved by a 1.3 V pulse applied to a set state with a resistance of 1.1 kΩ as seen in Figure 2.28d.

The interesting phenomenon seen in this device is that a pulse of 1 V, which is smaller than the reset pulse, induces a stable heterogeneous phase displaying different

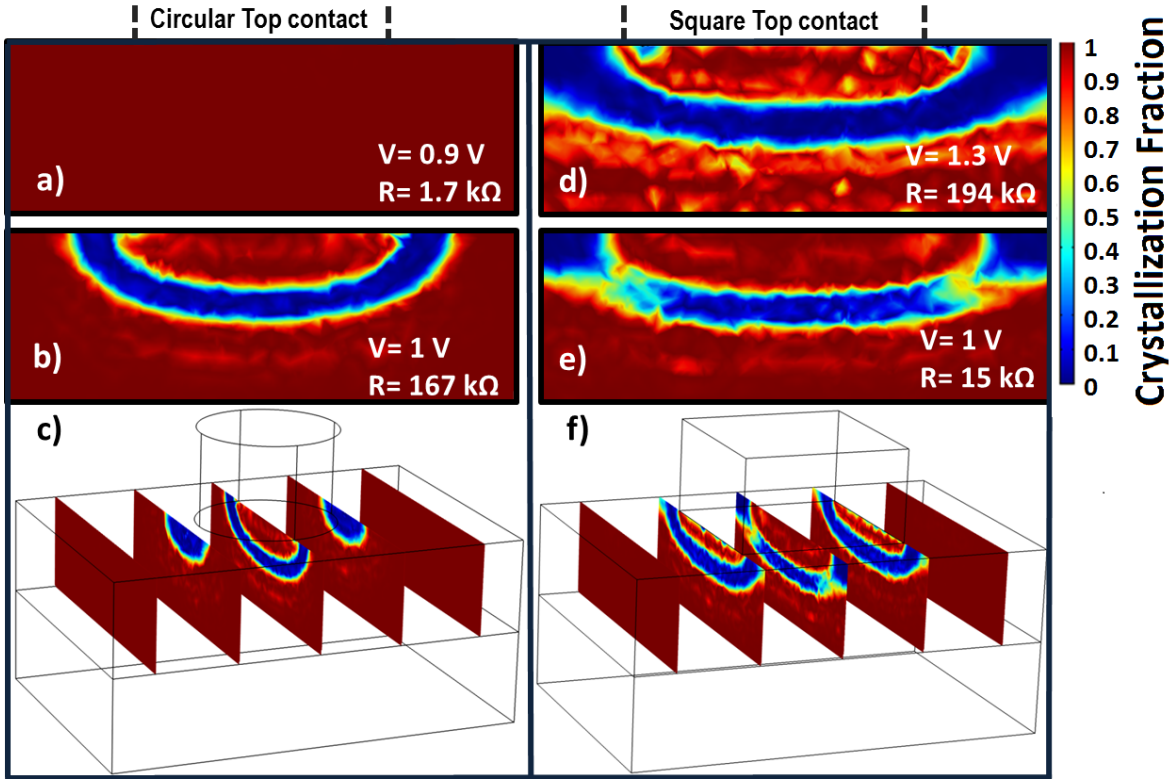


Figure 2.28. Crystallization fraction, f, inside the phase change layer is shown for circular (a-c) and square (d-f) top contact PCM cells after the application of a 100 ns reset pulse with a 42 ns trailing edge. The color scale corresponds to f = 1, red, for crystalline and f = 0, blue, for amorphous phases. The colors between the two represent regions with a mixture of crystalline and amorphous phases. A vertical cross-section of the device taken through the center is given for different pulse amplitudes resulting in different device resistances: a) 0.9 V, 1.7 kΩ; b) 1V, 167 kΩ; d) 1.3 V, 194 kΩ; e) 1 V, 15 kΩ (The figures represent a 150 nm width device and a set of dashed lines indicating the contact region are provided as guide to the eye). The three dimensional figures c and f correspond to the same pulse amplitudes as figures b and e, respectively.

regions with amorphous and crystalline phases co-existing as demonstrated by green to yellow color regions in Figure 2.28e-f. The resistance of the device in this state reads 15 kΩ which is an Intermediate Resistance State (IRS). The reason for such a mixed phase is the existence of hottest spots near the corners which facilitate a heterogeneous current distribution through the cell. For high programming pulses even though the temperature distribution inside the active region is in-homogeneous, the maximum temperature is well above the melting temperature and the rapid cooling after the pulse causes the active region to become amorphous. When the pulse amplitude is below the threshold for full amorphous phase (IRS programming range) the temperature is just above T_m and the hottest regions are subject to rapid cooling, hence the amorphous (blue) regions near the contact corners in Figure 2.28e, as well as the center of the active region which is subject to a thermal reservoir, hence the blue region around the center. The region between these two zones experiences a slower cooling process allowing some nuclei to form which leads to a mixed phase, the yellow-green colored areas in Figure 2.28e. We don't observe such a behavior in circular top contact devices since there aren't any non-uniformities in current and temperature distributions.

2.2.4. Nucleation and Growth Rate Results

Two important parameters affect the phase transition directly. These are nucleation rate (NR) and growth rate (GR). Initially, when I consider NR and GR values for the bulk GST, during the reset operation I could not get the amorphous phase due to high NR and GR because melted GST goes to crystalline phase in a very short time without staying in amorphous state. When I search for the reason behind this fast transition, I realized that I don't take into account the additional impurities inside the material. When I run my simulation for a smaller NR and GR ($5x10^4$ *and* $1.4x10^6$) ([115]) values I can observe the phase transition.

First, I look at the nucleation rate and its change with temperature and time. In Figure 2.29 shows the nucleation rate vs temperature. Nucleation starts after cooling and continues until below crystallization temperature because nucleation at the crystallization temperature is maximum. However crystallization occurs in reality at all

temperatures above room temperature.

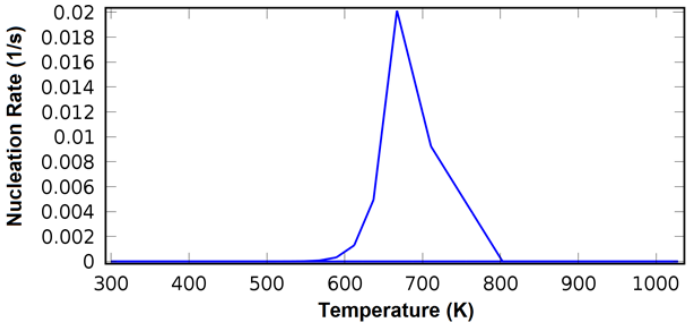


Figure 2.29. Nucleation rate versus temperature for the GST material for 1 V applied potential with 100 ns pulse width and 42 ns trailing edge.

Now I focus on how the nucleation rate changes with time because nucleation is important for crystallization. Nucleation rate is maximum at the crystallization temperature and during the reset operation at nearly $t = 150$ ns, the nucleation rate is maximum as can be seen in Figure 2.30.

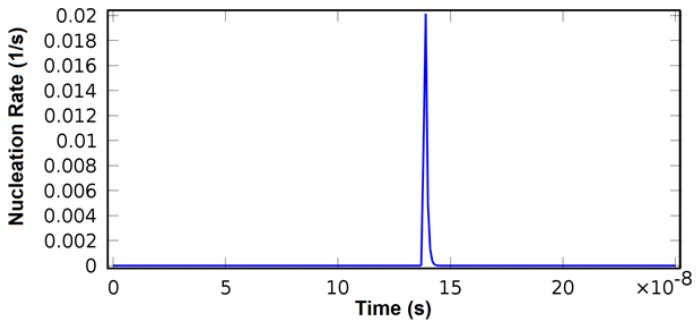


Figure 2.30. Nucleation rate versus time for the GST material for 1 V applied potential with 100 ns pulse width and 42 ns trailing edge.

The behavior is the same for the growth rate as in the nucleation rate, however the difference between nucleation and growth rate is that the growth rate is maximum after crystallization temperature because first nucleation is necessary to trigger growth. Therefore, the growth rate is maximum after nucleation rate and so it is valid for both temperature and time. Figure 2.31 and Figure 2.32 show how the growth rate changes with time and temperature.

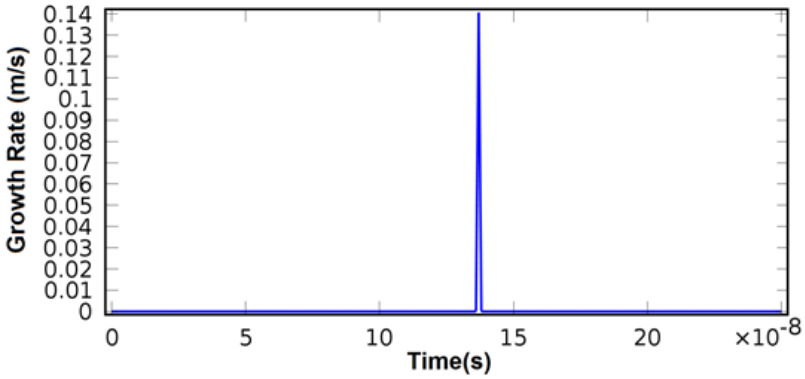


Figure 2.31. Growth rate versus time for the GST material for 1 V applied potential with 100 ns pulse width and 42 ns trailing edge.

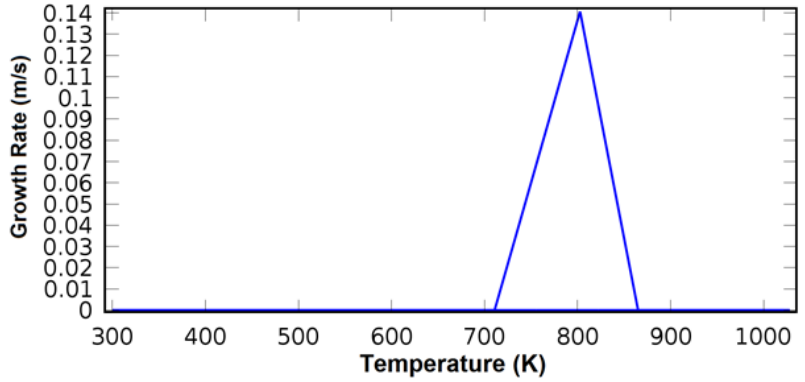


Figure 2.32. Growth rate versus temperature for the GST material for 1 V applied potential with 100 ns pulse width and 42 ns trailing edge.

After understanding the nucleation and growth rate, I apply different NR and GR for the device to see the effects in both square and circular top contact PCM device. In addition to different NR and GR values, I change the pulse width and pulse amplitude besides the trailing edge. From these simulations, I obtain the normalized resistance vs pulse width and amplitude. In Figure 2.33, the color scale represents normalized resistance of material.

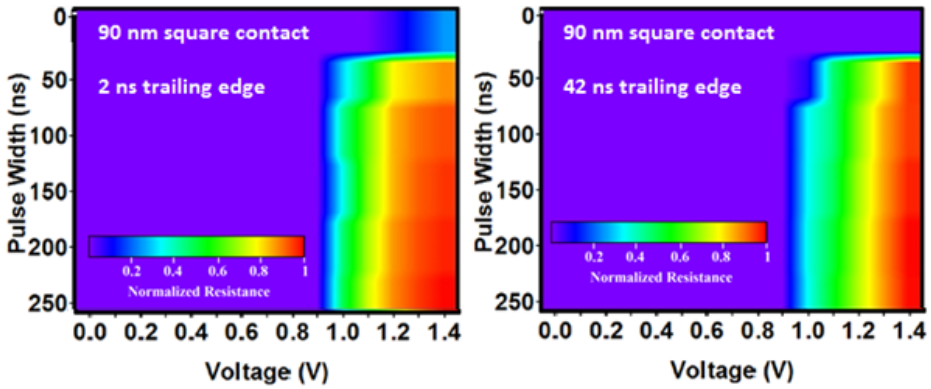


Figure 2.33. Pulse width and pulse amplitude corresponding to normalized resistance for 90 nm square top contact with 2 ns and 42 ns trailing edge.

As it can be seen from Figure 2.33, the width of the green band resistance decreases with increasing trailing edge and it is important to make the phase transition because if trailing edge is small, material cannot have enough time for re-crystallization after cutting the applied potential. Now we consider the effect of the NR and GR in phase change. Figure 2.34 shows how the NR and GR values are important to achieve phase transition. Figure 2.34 is for 90 nm square top contact shape and Figure 2.35 is for 75 nm circular top contact shape. It is the same for the circular contact shape as it is in square contact. High NR and GR values imply fast crystallization.

When I increase NR and GR values for 90 nm square contact with 2 ns trailing edge, depending on increasing NR and GR, our device undergoes phase transition very fast because the active region can turn on the crystalline phase in a very short time, therefore I want to show this reality with less trailing edge. If it happens even less time, in 42 ns trailing edge, I cannot make any phase transition from crystalline to

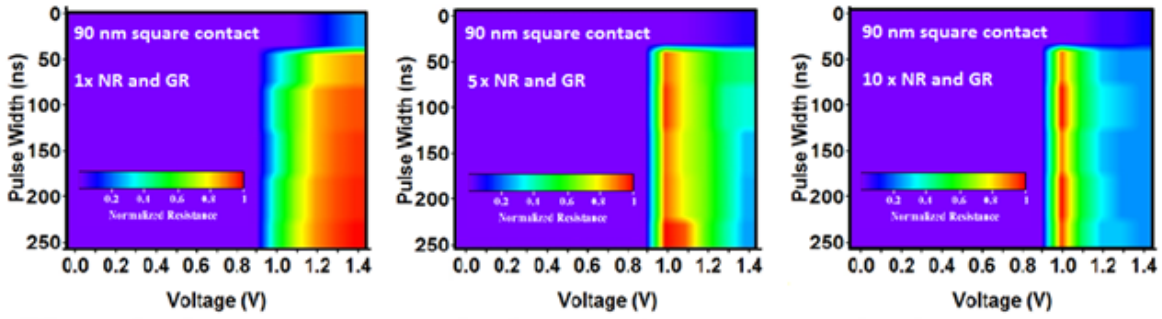


Figure 2.34. Pulse width and pulse amplitude corresponding to normalized resistance for 90 nm square top contact with 1, 5, 10 x NR and GR Values.

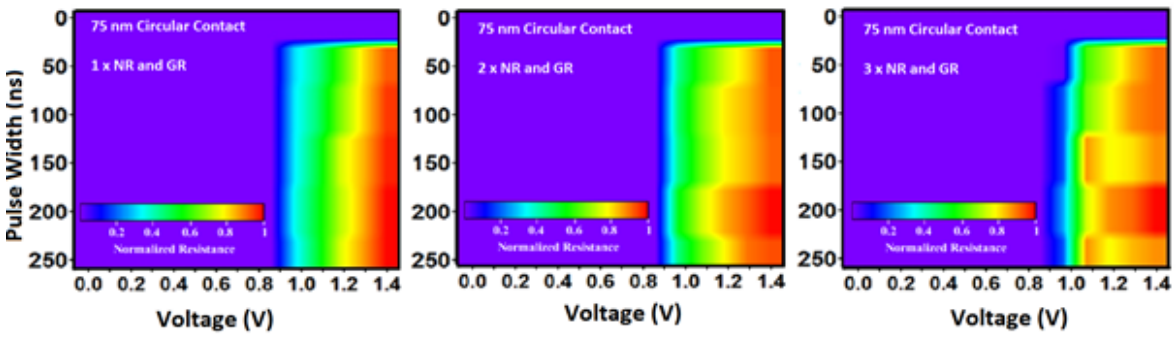


Figure 2.35. Pulse width and pulse amplitude corresponding to normalized resistance for 75 nm circular contact square top contact with 1, 2, 3 x NR and GR Values.

amorphous phase because melted PCM material goes very fast to the crystalline state. Therefore, it cannot be possible to make switching.

Now when I consider the NR and GR effect on the phase transition depending on top contact shape, I obtain the following results.

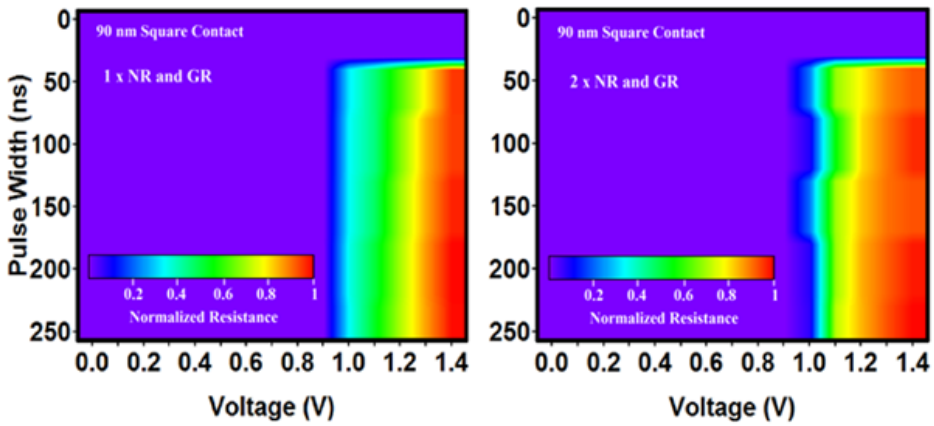


Figure 2.36. Pulse width and pulse amplitude corresponding to normalized resistance for 90 nm square top contact 42 ns trailing edge for two different NR and GR values.

As you can see from Figure 2.36, the width of the green band resistance decreases with increasing NR and GR. However, when I compare these results with experimental result, I find out that the square top contact cell with low NR and GR matches the experiment. However, the others does not match.

However when I take into account this fact for the circular top contact shape, I obtain Figure 2.37. Here, for the circular one, it is same again for the width of the band. However, in terms of comparing the experimental results, circular one differs from the square one because circular top contact cell with high NR and GR matched with the experimental result. When I focus on this situation, I realize that there are additional impurities and defects that cause a decrease in the NR and GR in the square top contact cell. The origin of these impurities is the device fabrication process because constructing sharp corners causes impurities during fabrication steps during ion milling. Therefore, there are additional impurities in the square top contact cell and because of them; NR and GR values of the square top contact cell are smaller than

that of the circular ones.

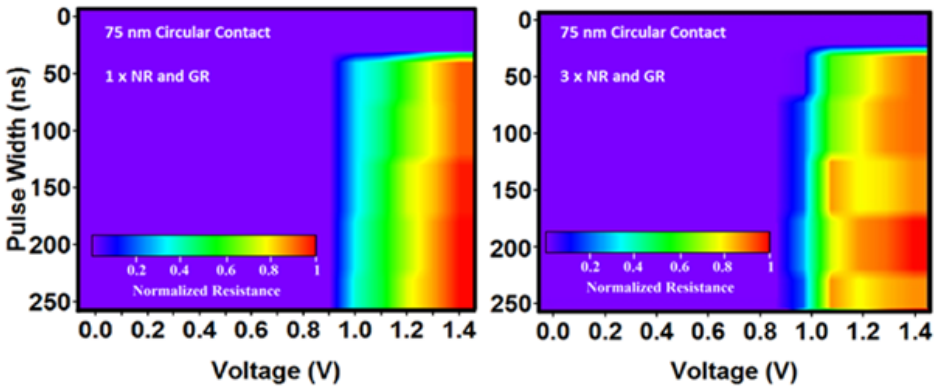


Figure 2.37. Pulse width and pulse amplitude corresponding to normalized resistance for 75 nm circular top contact with 42 ns trailing edge.

2.2.5. Intermediate Resistance State Results

After determining NR and GR values, I give different pulse widths and pulse amplitudes to obtain a resistance value between high and low values. I obtain the resistance of the material from the simulation and draw the normalized resistance graphs. First, I focus on the circular top contact cell results.

When I compare the simulation result with the experimental result, there is a little difference coming from initial assumption, not taking into account parameters (crystalline fraction, impurities electrical and thermal conductivities and so on). The important thing is that for square top contact cell, the simulation results give very consistent agreement with the experimental data.

In the experimental data, the light blue region represents intermediate resistance state corresponding to the intermediate logic state which originates from the top contact shape. From my observations, I obtain Figure 2.41. In this graph, it is clear to see that there is a light blue region as in the experimental data. Simulation data matches with the experimental data. Moreover, the width of this band can be controlled from the top contact shape of the cell. From the simulation, I can say that I could observe

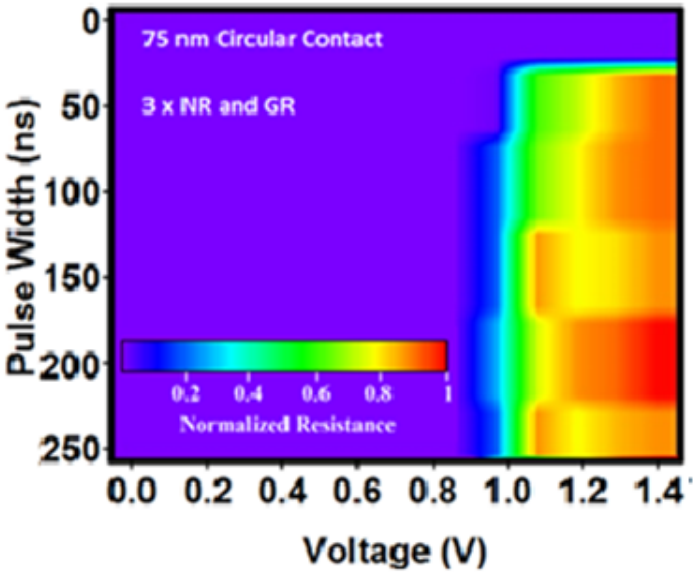


Figure 2.38. Normalized resistance vs pulse width & amplitude for 75 nm circular top contact with 42 ns trailing edge (simulation result).

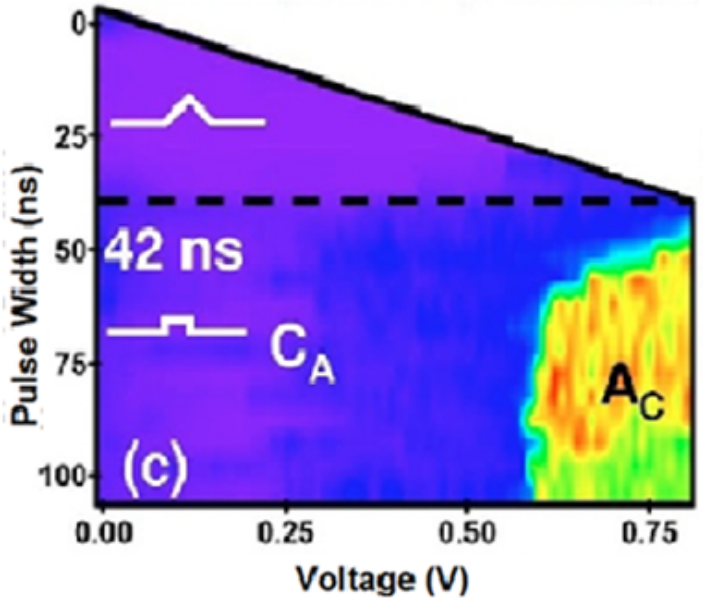


Figure 2.39. Normalized resistance vs pulse width & amplitude for 75 nm circular top contact with 42 ns trailing edge (experimental result).

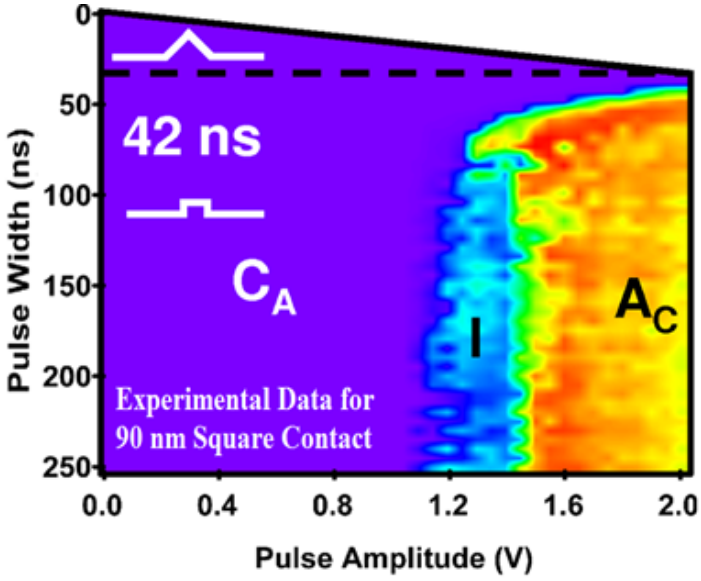


Figure 2.40. Normalized resistance vs pulse width & amplitude for 90 nm square top contact with 42 ns trailing edge (experimental result).

the intermediate logic state for 90 nm square top contact shape.

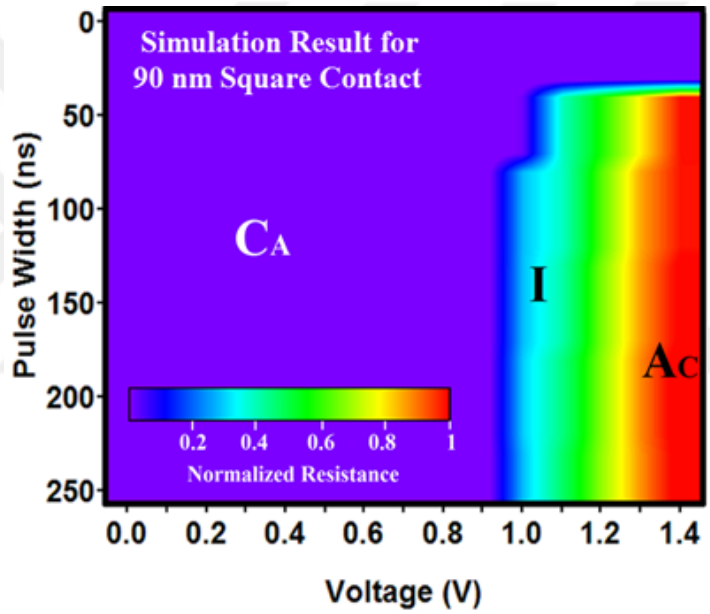


Figure 2.41. Normalized resistance vs pulse width & amplitude for 90 nm square top contact with 42 ns trailing edge (simulation result).

3. DRIFT OF RESISTANCE IN TIME

The schematic diagram of the standard test setup used for switching measurements in phase change memory devices is as shown in Figure 3.1. In this setup, a semiconductor parameter analyzer measures the electrical current dependence on the voltage while increasing the voltage at a rate as low as about 5 mV / sec to measure the current-voltage characteristics. Once the applied voltage reaches the maximum level, it is reduced to the same speed until it reaches the short circuit value again. The very low frequency triangular voltage signal obtained here is passed through an inductor of a filter called a bias tee and applied to a series connected load resistor and the tested phase change device circuit. In this experimental setup, the parameter analyzer plays two different roles. It is primarily responsible for the low reading signal required to measure the resistance of the device under test before and after switching. In addition, it measures the current-voltage characteristics to determine the threshold voltage after passing to amorphous phase. Apart from these, it acts as a kind of fuse protecting the tested phase change device (especially below 100 nm) from the current values that can be damaged by the device by controlling the maximum permissible current limit.

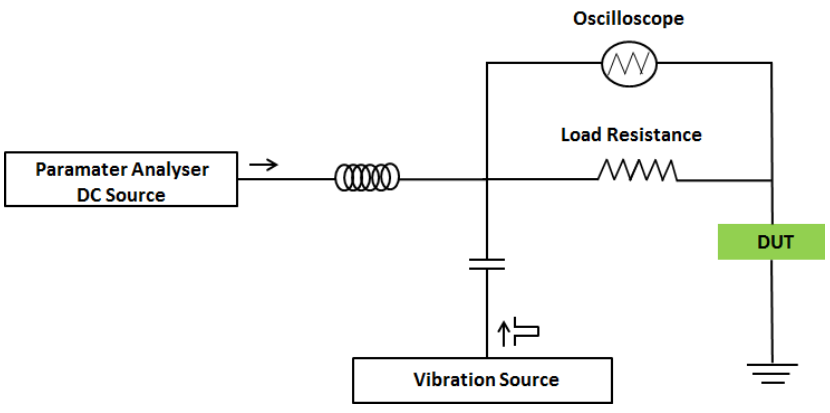


Figure 3.1. Phase change memory device measurement circuit diagram.

Pulse parameters must be adjustable, since the pulse width required for phase change device varies for each size, and even the pulse width and the width of the leading edge, may be different so that the switching can be done with electric pulses. Since the

signal obtained here typically has to be at around of 2-3 ns in the transition from the set (polycrystalline) state to the reset (amorphous) state, it is applied to the circuit by passing through a filter that passes high frequency signals, that is, through a capacitor. The capacitor also blocks low frequency signals from the parameter analyzer to protect the pulse source.

The tested phase change memory device has a protective characteristic by limiting the maximum value of the current allowed to flow through the device (usually around $1k\Omega$), and also because the resistance value does not change during the measurement, the voltage is measured from the voltage measured through an oscilloscope connected in parallel to itself allowing the current to be easily calculated with Ohm's law. One thing to note here is that the impedance of the device under test can never be matched (the output impedance of the circuit can never be fixed at 50 ohms) because the device under test changes from hundreds of ohms to mega ohms with resistive switching. Therefore, the reflection of a part of the sent electrical pulse is always inevitable. Hence, to avoid multiple reflections that may occur between the load resistor and the device being tested, as well as the use of SMA cables as short and high frequency compatible as possible, the load resistor should be at the practically possible nearest distance on the tested device. For this reason, the distance between two circuit elements can be reduced to 2-3 centimeters using very small surface mounting resistors. Thus, using the lumped circuit approximation, the conventional voltage sharing law between two series-connected resistors can be applied and the pulse signal loss caused by multiple reflections between the two resistors is avoided.

As can be seen in Figure 3.2, the most important part of this test setup is a probe station that allows electrical measurements of devices at the nanometer level. Phase change devices built on the silicon substrate placed on the platform of this station are located. Only the RF contact (gold probe) can be touched to the gold-plated contact areas to ensure that the contacts to these devices are compatible with the high frequencies. In order to see the contact, the contact area is enlarged by a camera system and reflected on a monitor so that the test operator can see it. The device is controlled by the computer and the data is automatically saved on the computer. This

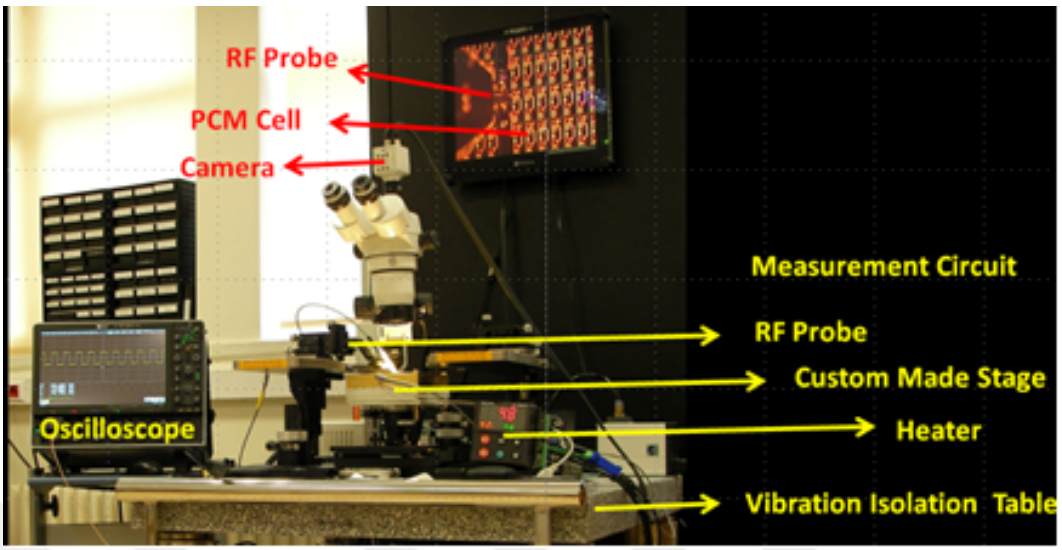


Figure 3.2. Experimental setup for measuring the switching characteristics of phase change memory devices.

is accomplished by the computer's parameter analyzer and remote source of the pulse source (or even the oscilloscope) via GPIB cabling and interfaces.

The samples to be measured here are structured by photo-lithography, electron beam lithography, ion etching and reactive plasma etching. GST thin film is prepared by RF magnetron sputtering method and other metallic layers by DC magnetron sputtering method. In this way, different sizes ($50nm - 1\mu m$) and contact geometry (square-circle) were obtained. The experimental characterization in this study will be carried out on these samples.

3.1. Experimental Results

Initially, the probe is connected to examine the initial condition of the PCM device, that is, the phase in which the reading process is being done., A voltage pulse that is too low for any phase change transition of the material or a low DC voltage may be used for reading. The resistance value is calculated by reading the current passing through the device by reading operation for a selected 130 nm square contact PCM device. Figure 3.3 is a graph of I-V and R-V for this device.

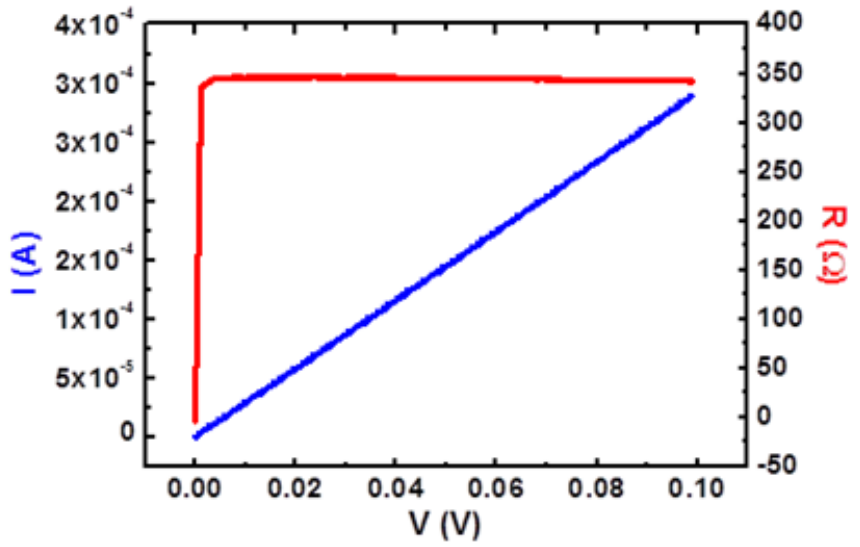


Figure 3.3. For a selected 130 nm square contact PCM device, I-V and R-V graphs after reading.

The reading voltage applied to determine the resistance value of the device increases up to 100 mV, and the resistance of the device is determined according to the current flowing through the device. The resistance of the device is approximately $\sim 350\Omega$. Based on this resistance value; we can say that the phase change material is in a crystalline phase. Because, in general the resistance of the device in the crystal phase is on the order of a few 100Ω. However, for large samples they may reach a few $k\Omega$ values.

If the device is not in the crystalline phase when we read the resistor, the 500 nm square contact PCM device has an initial value of 5.4 $k\Omega$ as in Figure 3.4. In order to bring device, which is not in a complete crystal phase, into the crystal phase, Set operation is performed and the voltage values to be applied for this operation are larger than the voltage values used for the reading operation. The following figure is an I-V and R-V graph for a PCM device initially having a resistance value of around 110 $k\Omega$ and shows the transition of the device into the crystal phase with a Set operation. The PCM device here is also a 130 nm square contact PCM device.

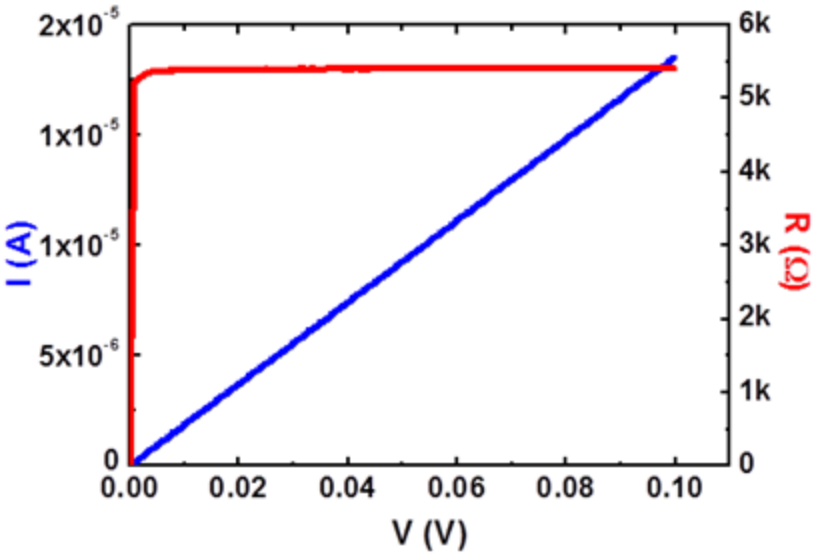


Figure 3.4. For a selected 500 nm square contact PCM device, I-V and R-V graphs after reading.

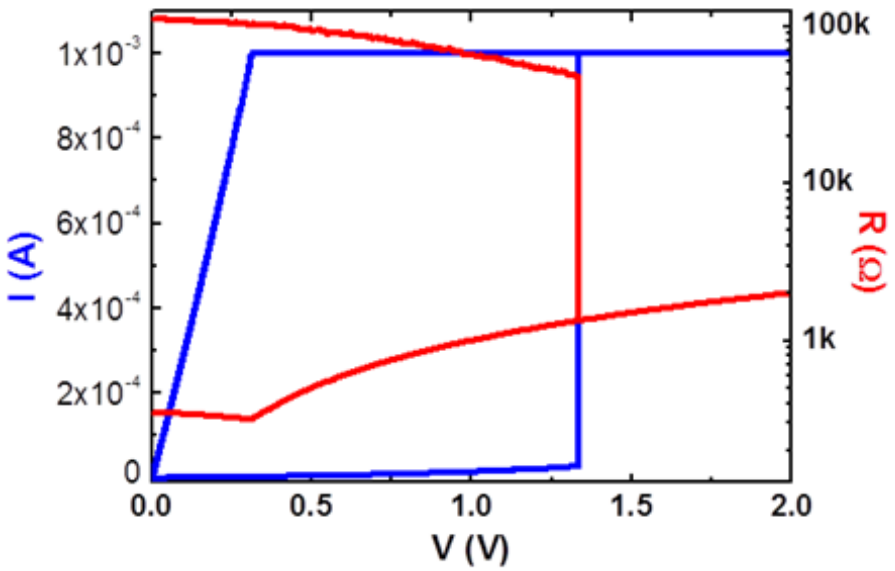


Figure 3.5. Set Operation for a selected 130 nm square contact PCM device.

Since the resistance value is initially high, the current through the device is too low to cause any heating on the device. Figure 3.5 shows the Set operation for 130 nm square contact PCM device. Depending on the applied voltage, the resistance of the device drops, but the resistance is still low enough for a current to pass. However, around 1.2 V, the resistance starts to decrease while the current begins to flow through it. Here we can clearly say that at this voltage, percolation has occurred on the device. Then, when the voltage begins to fall back from the maximum value, due to the Set operation, the phase change material transition into the crystal phase and since the phase change material is in the crystal phase, the resistance value is low. In the crystal phase, the resistance of the device is around $300 - 400\Omega$. Here, although the resistance value is greatly reduced, the current passing through the device does not exceed 1 mA. The reason behind this is that we limit the current with a 1mA to protect the system and the device.

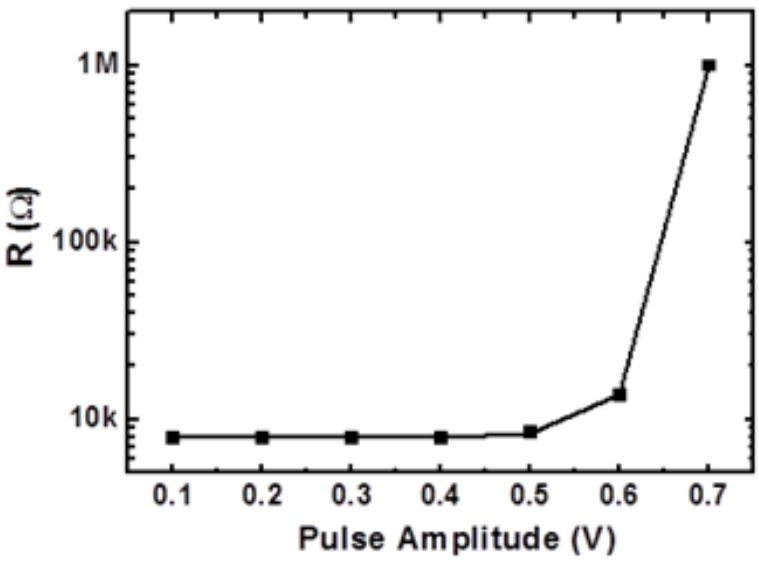


Figure 3.6. Reset Operation for a selected 75 nm circular contact PCM device.

When we want to switch from the crystalline phase to the amorphous phase through Reset operation, we see clearly the change of resistance with the voltage pulse that we need to apply on the device as in Figure 3.6. Initially, the device resistance is slightly increased since the resistance of the device is around $8 - 9\ k\Omega$, while the

resistance change during the Reset process does not change much at the beginning, but at around 0.6 V there is a significant change, because the material is in the amorphous phase. Because, the resistance value is changed from several $k\Omega$ to $M\Omega$. The properties of the voltage pulse applied here is a voltage pulse with a width of 25 ns and a 2 ns trailing edge.

Simulation results do not predict any intermediate resistance level for the circular contact, but as seen there in the experiment. We have seen that when we apply Reset operation to a square contact device, the intermediate resistance values of the material, as predicted by the the simulations, appear.

The applied voltage pulse is a voltage pulse with a width of 25 ns and a 2 ns trailing edge. As it can be seen in Figure 3.7, the material is still in the crystalline phase around 0.7 V while the resistance value is around 300Ω, but there is an intermediate region with a resistance value of around 10$k\Omega$ at 1 V. This region is the range of the values of the intermediate resistance that corresponds to the intermediate logic level.

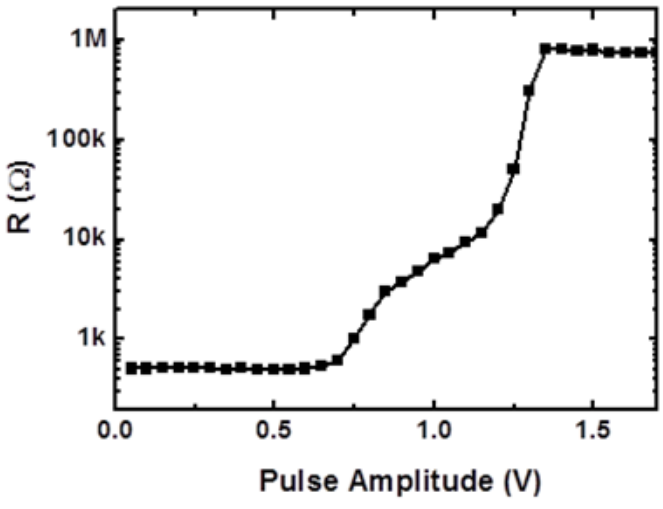


Figure 3.7. Reset Operation for a selected 130 nm square contact PCM device.

Figure 3.8 shows the Set process for the 130 nm square contact device in the amorphous phase. Since the resistance in the amorphous phase is very high, the current passing through the material is on the order of nA and this current cannot cause heating

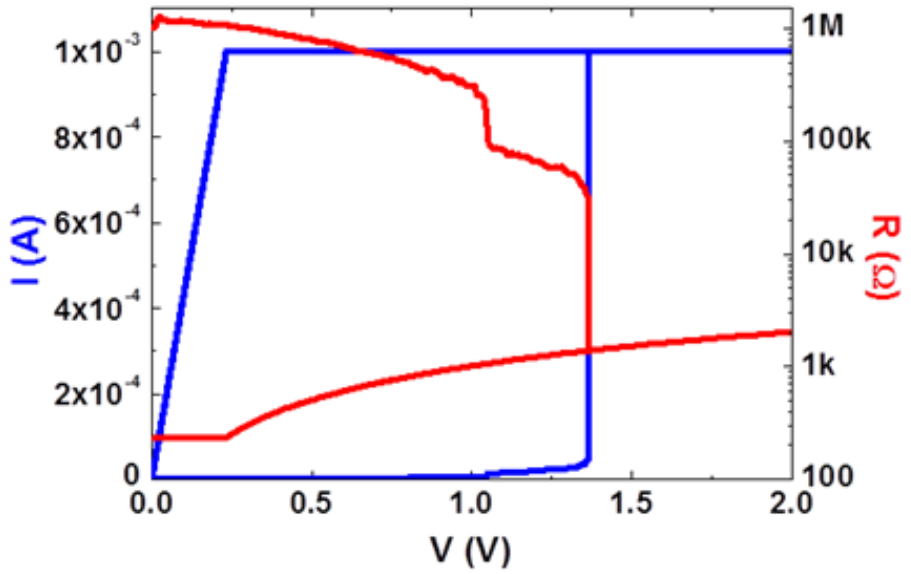


Figure 3.8. Set Operation for a selected 130 nm square contact PCM device.

on the material. The resistance value of the device is still high, although there is a slight decrease in the resistance value with increasing voltage. There is not much change in the resistance value of the material around 1 V and 1.4 V. The reason behind is that the amorphous material passes into the mixed phase state , namely intermediate resistance value. However, after the threshold voltage value of 1.4 V, the current starts to flow on the material and the resistance of the device is significantly reduced. As we mentioned earlier, when we limit the current value to 1mA in order to protect the device and the test elements, we cannot pass a current larger than this current value on the material. At the end of this Set operation, the final resistance of the device drops to $300 - 400\Omega$ and the device is in the crystalline phase.

Figure 3.9 shows how a 500 nm square contact PCM can be programmed to an intermediate resistance level. If the voltage applied to the device is kept around 2 V here, the material remains in this mixed phase and phase change material does not switch to the amorphous phase. In this case, an intermediate resistance level is reached for the square contact and it is more or less stable.

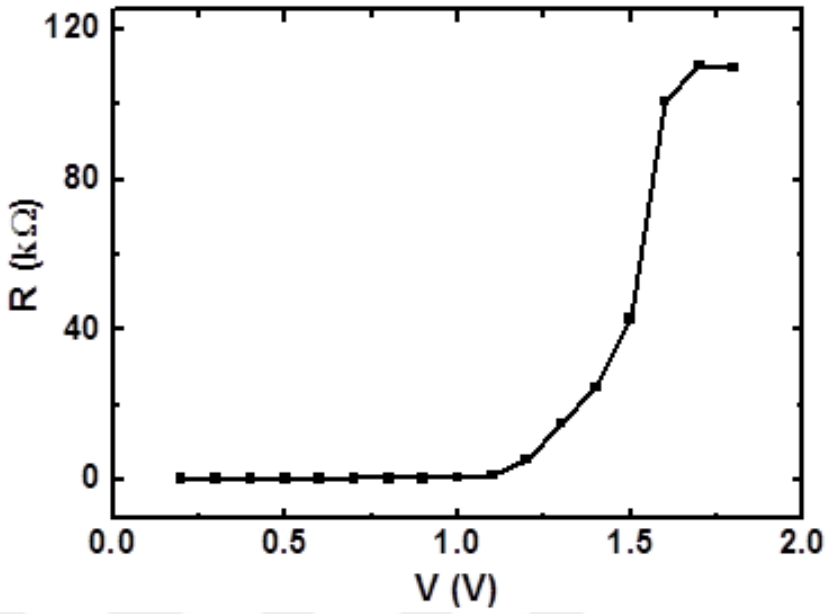


Figure 3.9. The voltage pulse applied to obtain intermediate resistance for a 500 nm contact PCM device and Resistance values.

Figure 3.10 is given to compare Reset operations (to manage switching from crystalline phase to amorphous phase) by showing experimental and simulation results for a selected 75 nm circular and a 90 nm square contact PCM device. Figure 3.10 a and Figure 3.10 c are for experimental results and Figure 3.10 b and Figure 3.10 d are the simulation results. When we take a look at the experimental and simulation results for a selected 75 nm circular contact PCM device, it is clear that in 75 nm circular contact does not give any intermediate resistance state (or mixed state).There is just an abrupt switching from crystalline to amorphous phase. Switching voltage and the amorphous resistance values are different due to having a simulation without impurities and other side effects coming from the material properties. However, for 90 nm square contact PCM device, it is clear that in both experimental and simulation results, there is an intermediate resistance state, which is stable, between crystalline and amorphous state. The different intermediate resistance state and voltage values are due to variations in material properties,defects introduced during fabrication and so on.

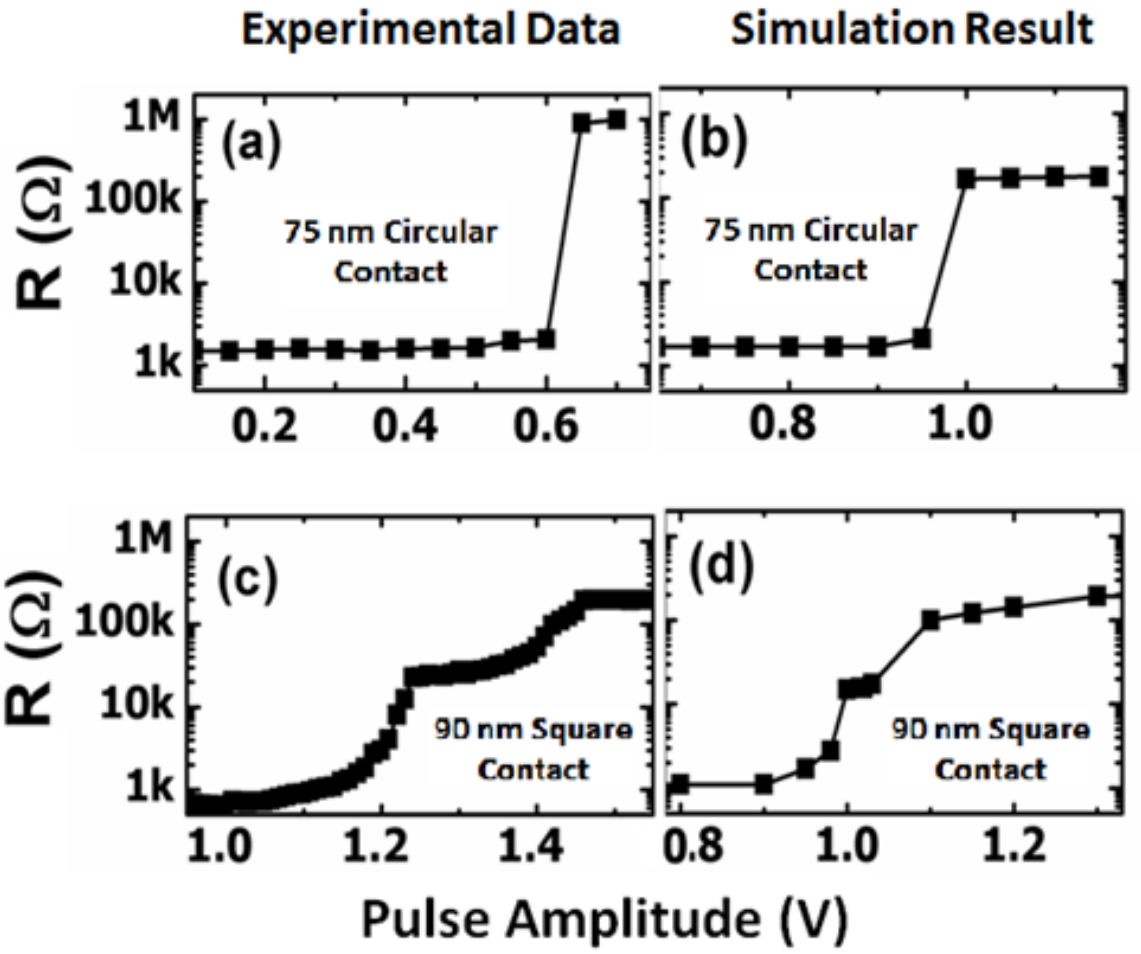


Figure 3.10. Reset Operations for a selected 75 nm circular and a 90 nm square contact PCM device. Experimental and Simulation results are given for comparison. a and c are the experimental results and b and d are the simulation results [115].

While describing the properties of the materials, it was mentioned that there was a gap of 25% in the material. These voids in the material and other external factors (such as ion bombardment) cause localized states in the material known as charge traps in the energy band gap. In describing the properties of amorphous materials, these charge traps are shown in the band diagram. In time, the number of these charge traps in the material will decrease, and it will be difficult for an electron in the valence band to pass through the charge trap to the conduction band. The decrease in the number of the electrons in the conduction band means that there is an increase in the resistance of the material. The theory explaining the importance of these charge traps in the forbidden energy band gap is called as structural relaxation and can explain the change in the resistance of the material. The next step is to show whether the device resistance values change in the Set, Reset and intermediate resistances drift in time. Let's first look at the resistance of a crystal in Set state over time.

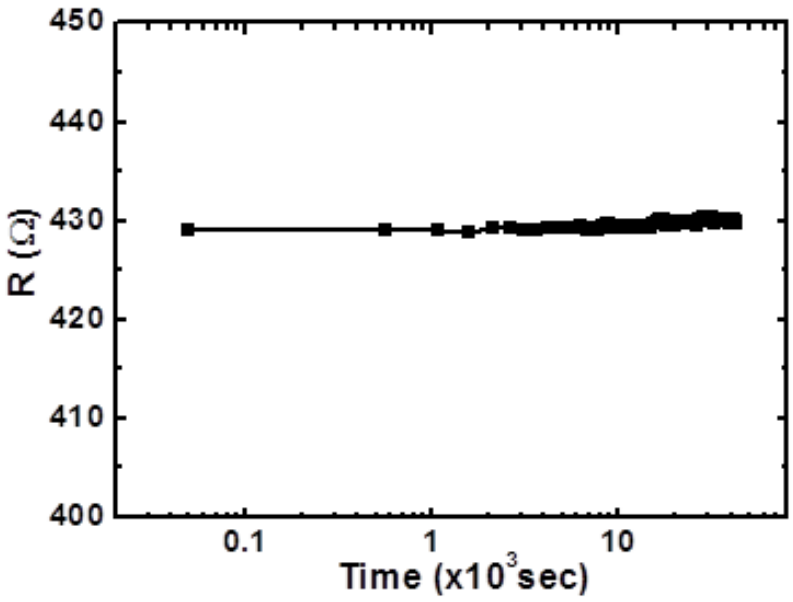


Figure 3.11. Resistance change of the crystalline phase (SET state) in time for a selected 130 nm square contact PCM device.

From Figure 3.11, the resistance of the material in the crystalline phase does not change over time. The ν parameter is an important parameter in the structural relaxation model for the behavior of a material in time. The following equation 3.1 is

used for this parameter.

$$R = R_0(\frac{t}{t_0})^{\nu} \tag{3.1}$$

The resistance of the device at the beginning of measurement is, R_0 and t_0 is the initial time. t shows the time passed and R shows the change in the resistance of the device in time. Figure 2.55 shows the change in $R/R_0 - t/t_0$, which is related to the structural relaxation of the material. Here, the slope of the fit obtained using the experimental results gives a structural relaxation parameter known as the ν parameter. From Figure 3.11 and using equation 3.1, we obtain Figure 3.12 and we found ν parameter as 0.0009 for a selected 130 nm square contact PCM device.

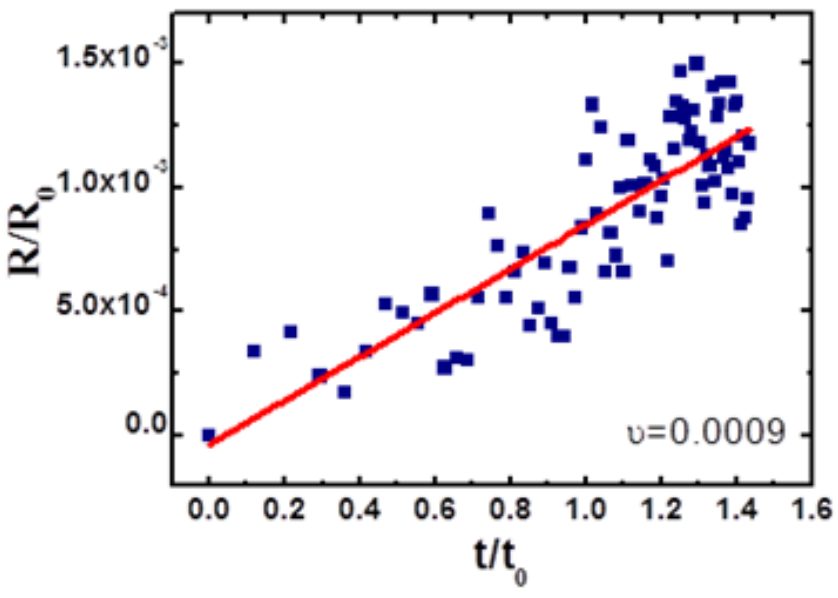


Figure 3.12. For a selected 130 nm square contact PCM device R/R_0–t/t_0. ν parameter is 0.0009.

We observed the resistance of the amorphous phase in the Reset state after observing that the crystal phase does not change with time in the Set state and it is given in Figure 3.13. The resistance of device is increasing with time and just in $40x10^3$s it reaches twice the resistance value after Reset operation.

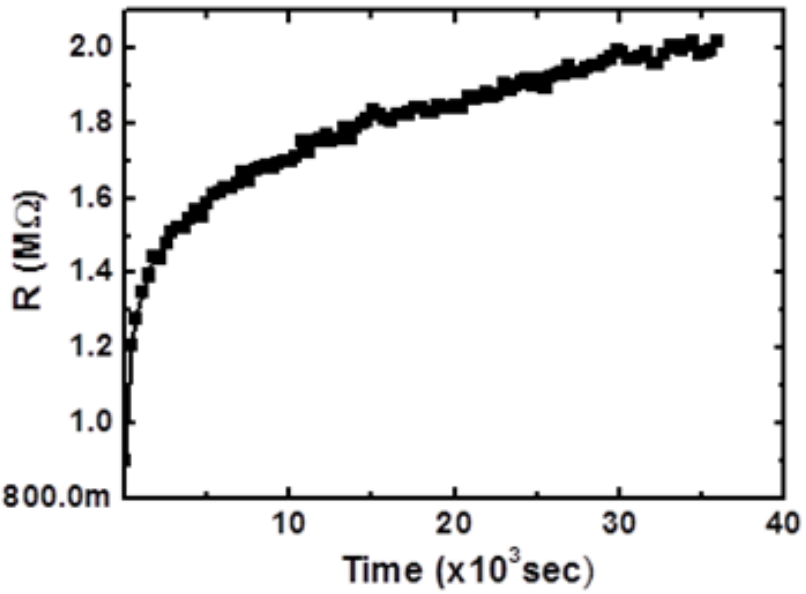


Figure 3.13. Resistance change of the amorphous phase (Reset state) in time for a selected 500 nm square contact PCM device.

From this increase, Figure 3.14 is plotted to find the ν parameter and it is found as 0.107. When we compare these experimental results with the literature, we can see that our results are consistent with the literature. In the literature, the ν parameter is less than 0.01 for Set state (LRS) and around 0.1 for Reset state (HRS) [59]. Figure 3.15 shows the ν parameters for the LRS and HRS from the literature.

Our goal in this project is to find the intermediate resistance values that correspond to the intermediate logic levels and determine the stability of these levels. Both the simulation and the experimental results above showed how the intermediate resistance levels are available in square contact PCM devices and how they can be obtained. Figure 3.16 shows how the intermediate resistance level changes in time for a 130 nm

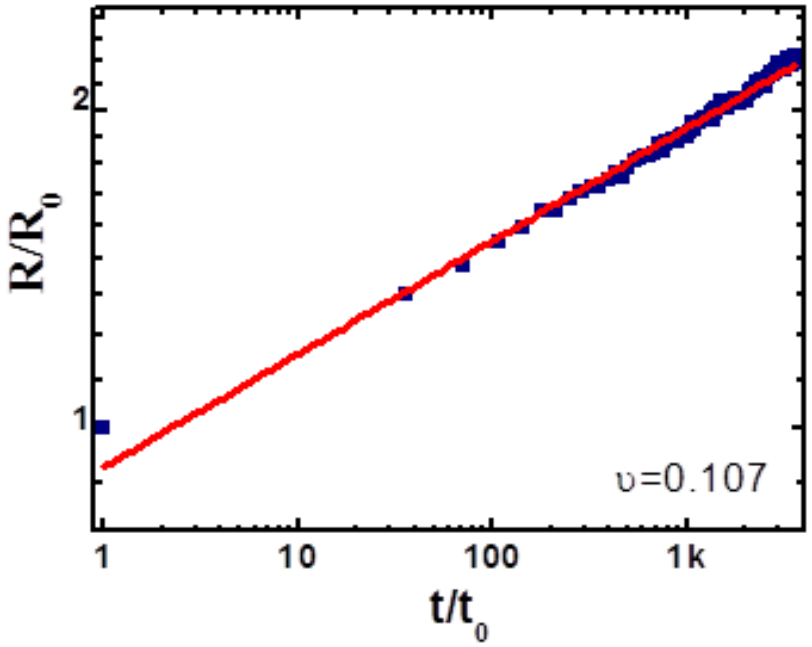


Figure 3.14. For a selected 500 nm square contact PCM device R/R_0–t/t_0. ν parameter is 0.107 and initial resistance value is 0.9 $M\Omega$.

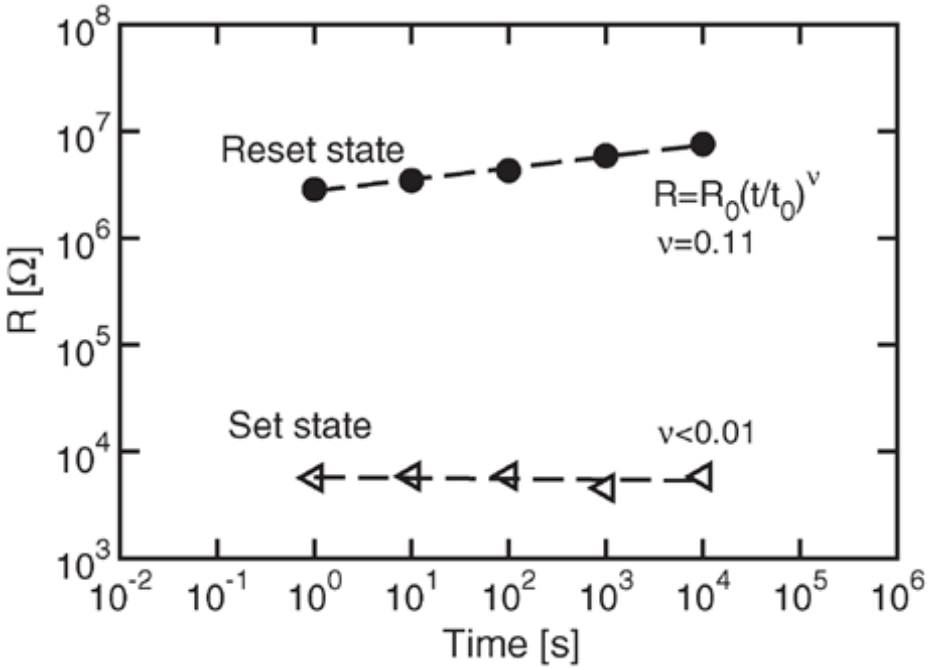


Figure 3.15. The resistance change of PCM device and the ν parameter is less than 0.01 for LRS and about 0.1 for HRS [59].

square contact PCM device. From Figure 3.16, the intermediate resistance level has a weak time dependence, and the ν parameter has a low value of 0.0102.

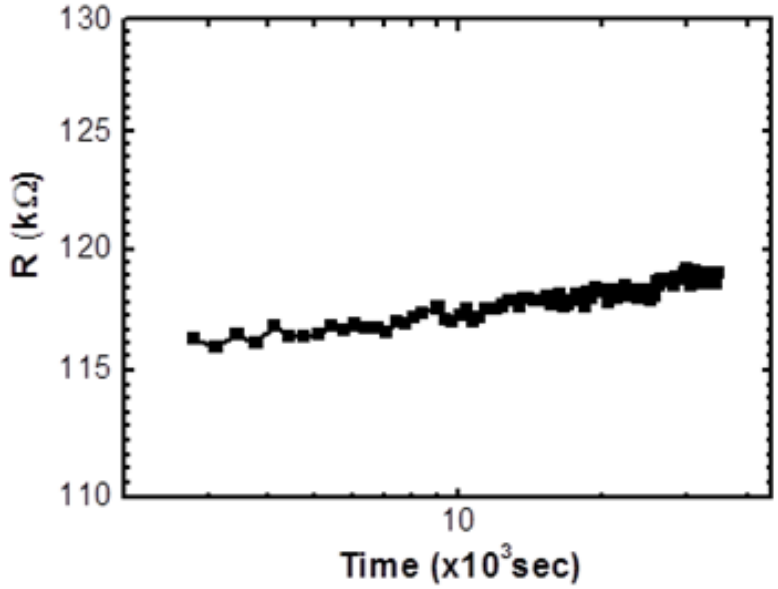


Figure 3.16. Resistance change for a selected 130 nm square contact PCM device and initial resistance value is 116 $k\Omega$.

Here the ν parameter proves that the intermediate resistance state (IRS) does not change much in time. This is because at the intermediate resistance level, the material is in the mixture of the crystal and amorphous phases. Besides, the charge traps in the crystal phase are scarce, and therefore, due to the less charge traps in this intermediate phase, the decrease in structural relaxation with the number of these charge traps in time has little effect on the resistance of the device. Thus, we can say that the intermediate logic level is stable and the intermediate logic level obtained using this intermediate resistance level is stable.

In Figure 3.18, we can see easily LRS, HRS and IRS simultaneously in one figure. to compare the stability of these states. After the observation of resistance drift, next thing to do is to understand the drift mechanism and to explain the physics behind it. In pursuit of this goal, I looked for the defect density, temperature and other physical parameters affecting the resistance drift of the device.

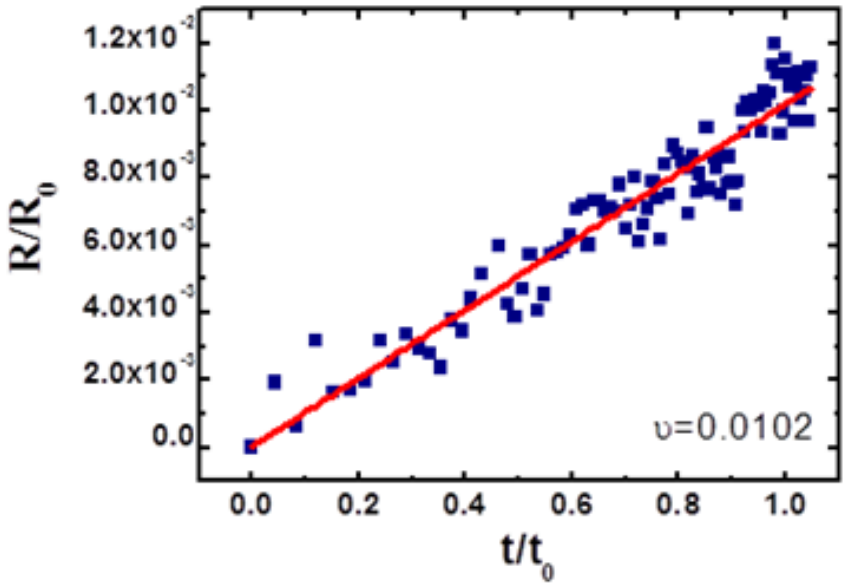


Figure 3.17. For a selected 130 nm square contact PCM device R/R_0–t/t_0. ν parameter is 0.0102.

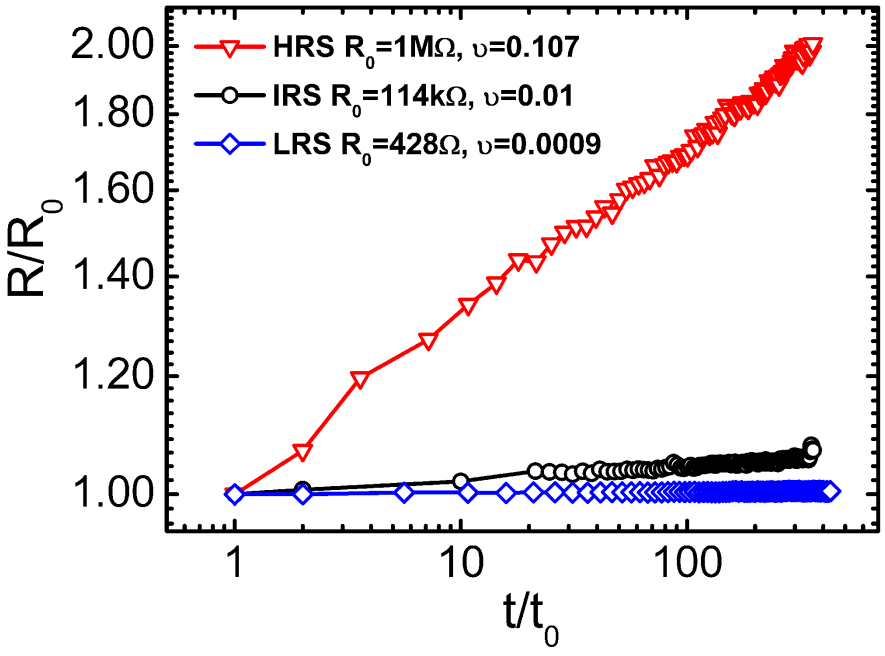


Figure 3.18. Resistance changes of LRS, HRS and IRS for a selected 130 nm square contact PCM device.

In Figure 3.19, the resistance versus temperature graph for LRS, HRS and IRS is given for 25^0C, 50^0C, 75^0C and 100^0C. In Figure 3.19, all three resistance levels are plotted against T for temperatures. The resistance of the device is decreasing with increase in the temperature. This is an expected result but the important result in this experiment is that the resistance of the intermediate state is changing less compared to HRS. For LRS, resistance change is very low.

The IRS displays an almost steady behavior with a low drift coefficient. $\nu = 0.0101 \pm 0.0003$ for this sample, an order of magnitude smaller than ν for HRS. While partial reset states display a variety of drift coefficient values depending on the exact resistance (smaller with decreasing resistance) in the range 0.02-0.09 [1, 121, 122], we have consistently observed much lower drift coefficients for the stable IRS (as low as 0.0016 as in the case of the sample in Figure 23.19). This indicates that IRS having a wider programming range is far more stable than a partial reset state, which is a mixed state including the amorphous and crystalline phases at the same time, but mostly in the amorphous phase.

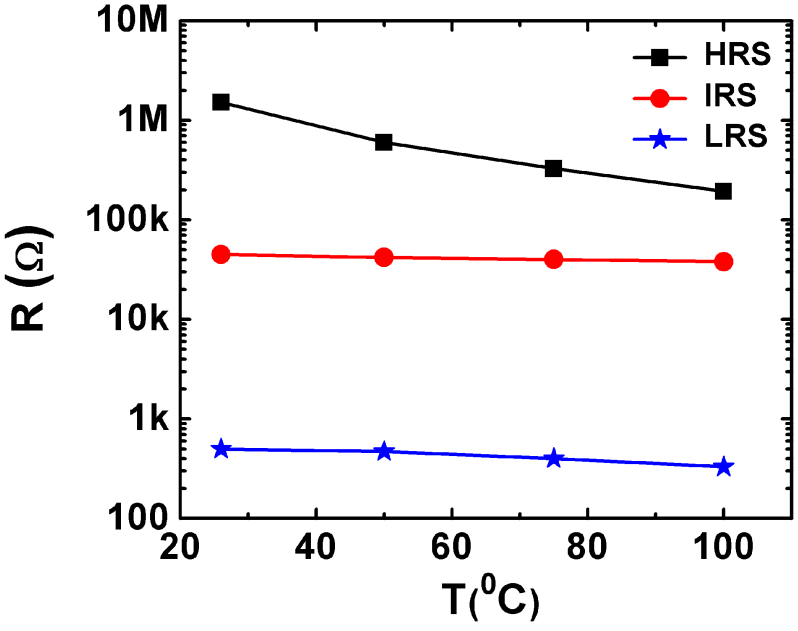


Figure 3.19. Temperature dependence of the initial resistance levels of HRS (squares), IRS (circles) and LRS (stars).

After the observation of change in the resistance with temperature increase, the next thing to do is to measure the resistance drift of the device for LRS, HRS and IRS at these given temperature values. From these results I obtained ν parameters for Reset and Intermediate states. In Figure 3.20, we can see the ν parameters depending on the temperature change. Beside these results, ν parameter for HRS increases until 75^0C then it starts to decrease. However, for IRS, ν parameter is increasing with temperature but, even so, the ν parameter is still very small compared to Reset state's ν parameter.

Lower drift coefficients in the IRS level can be explained by an increased number of defect states reducing the overall activation energy for traps, E_A. An analysis of the temperature dependence of the device resistances can help evaluate, E_A. The data follows Arrhenius formalism, equation 3.2.

$$R = R_0 exp\Big(\frac{E_A}{k_B T}\Big) \tag{3.2}$$

A considerable amount of change with temperature is observed for HRS and fit to the above equation yields a barrier activation energy of 0.23 eV, consistent with literature [56, 123]. There is minimal change for LRS and IRS. The IRS reveals a very small activation energy of 0.02 eV. Studies that evaluate behavior of E_A with annealing conditions and amorphous layer thickness show that it is smaller in devices with higher number of closely packed defect states and with very thin amorphous layers [1, 13, 124].

Resistance drift is monitored for the same sample, at different temperatures as displayed in Figure 3.20. Due to accelerated annihilation of bulk defect states, the resistance drift in HRS appears to increase with temperature, from 0.07 at room temperature to 0.12 at 75 ^{0}C after which it begins to decrease due to spontaneous crystallization. The interesting behavior is that the drift coefficient of IRS plateaus at this temperature having increased from 0.0016 to 0.02.

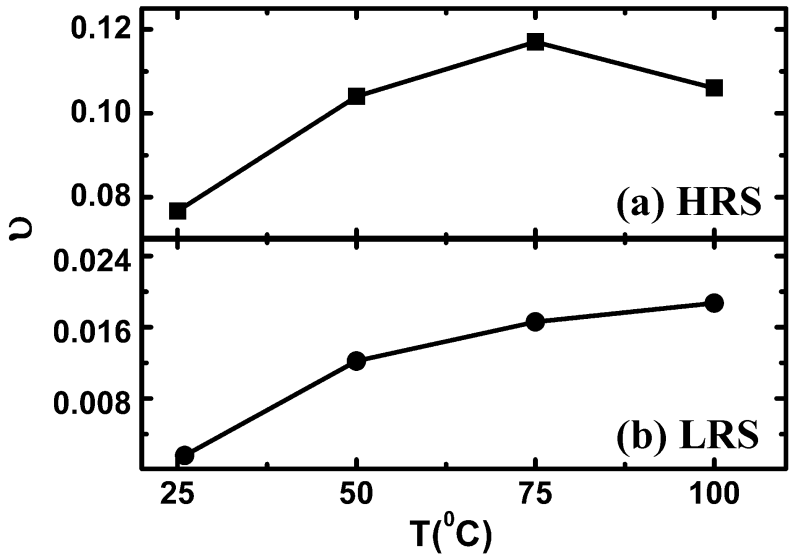


Figure 3.20. Variation of the drift coefficient with temperature for reset, (a), and intermediate, (b), states. Drift coefficients are extracted at each temperature from the resistance drift after programming.

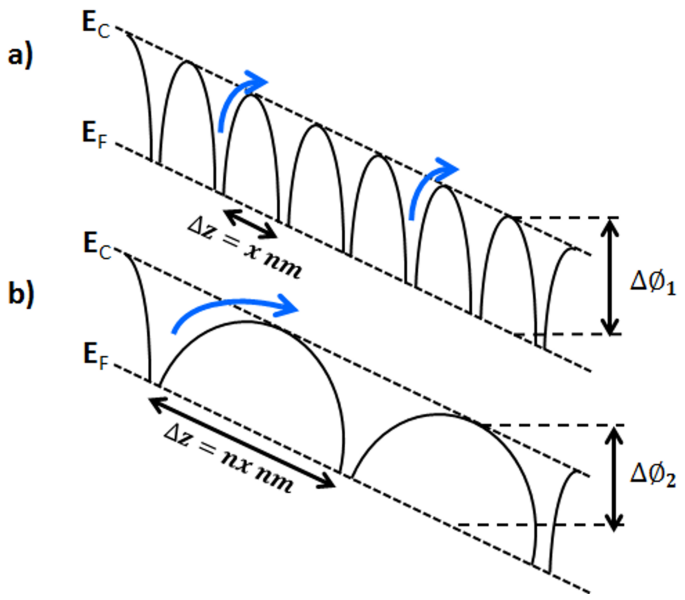


Figure 3.21. Schematic representation of the hopping conduction mechanism through traps in a PCM device.

In order to understand the conduction mechanism in the IRS, the data are compared with the existing models in the literature. Conduction through a PCM cell is dominated by thermally activated hopping of charge carriers across coulombic donor-like traps [59, 119]. The drift mechanism in the amorphous phase is explained by thermal annihilation of defects. Fig. 3.21 shows a schematic drawing of the energy profile for the amorphous phase. Defect energy levels are introduced between the Fermi level, E_F, and the conduction band, E_C. For relatively large number of defects, inter-trap distances are short and the barrier height depends linearly on the applied voltage bias, V, Poole voltage dependence is given [59].

$$\Delta\Phi_1 \approx E_C - E_F - \frac{qV\Delta z}{k_B T} \tag{3.3}$$

where q is the electron charge, current through the device and Δz is the distance between the traps.

As the trap concentration is reduced, the inter-trap distance gets bigger as illustrated in Fig. 3.21b, resulting in an increase of the device resistance. Poole-Frenkel model predicts that as the traps become independent, the energy barrier becomes [59].

$$\Delta\Phi_2 \approx E_C - E_F - q\sqrt{\frac{qV}{\pi\varepsilon u_a}} \tag{3.4}$$

where ε is the dielectric constant of the amorphous chalcogenide and u_a is the thickness of the amorphous region. In the hopping conduction mechanism the current through the device can be expressed as a function of the trap concentration in the gap above the Fermi level, $N_{T,tot}$;

$$I = 2qAN_{T,tot}\frac{\Delta z}{\tau_0}e^{-(E_C-E_F)/k_BT}\sinh\left(\frac{qV}{k_BT}\frac{\Delta z}{2u_a}\right) \tag{3.5}$$

where A is the area of the top contact and τ_0 is the characteristic attempt to escape time [123]. For large voltages, in the sub-threshold regime, $\Delta\phi$ and hence $ln(I(V))$ varies linearly with V. The slope of the $ln(I(V))$ curve, the so-called the Subthreshold Slope (STS), can be formulized.

$$STS = \frac{\partial ln(I)}{\partial V} = \frac{q}{k_BT}\frac{\Delta z}{2u_a} \tag{3.6}$$

The I-V characteristics are investigated in Figure 3.22. The inset shows the full switching dynamic starting from an HRS towards a crystalline state. The interesting behavior is that the device switches to the stable IRS before being set. In the sub-threshold voltage regime, $ln(I)$ is observed to scale linearly with V for both IRS and HRS, shown by dashed lines of Figure 3.22 indicating the existence of a high number of closely packed defect states. The amorphous thickness is estimated using the threshold voltage, V_{th}, and electric field F_{th}, $u_a = V_{th}/F_{th}$ [125]. This, together with the STS extracted from the fits to the I-V curve are utilized to calculate the inter-trap distance, Δz. Table 3.1 lists these parameters obtained from the I-V curves for the sample of Figure 3.22. and along with a different square contact sample.

At low voltages, electrons can hop between traps in forward and reverse directions reducing the current formula to a linear I-V regime [123].

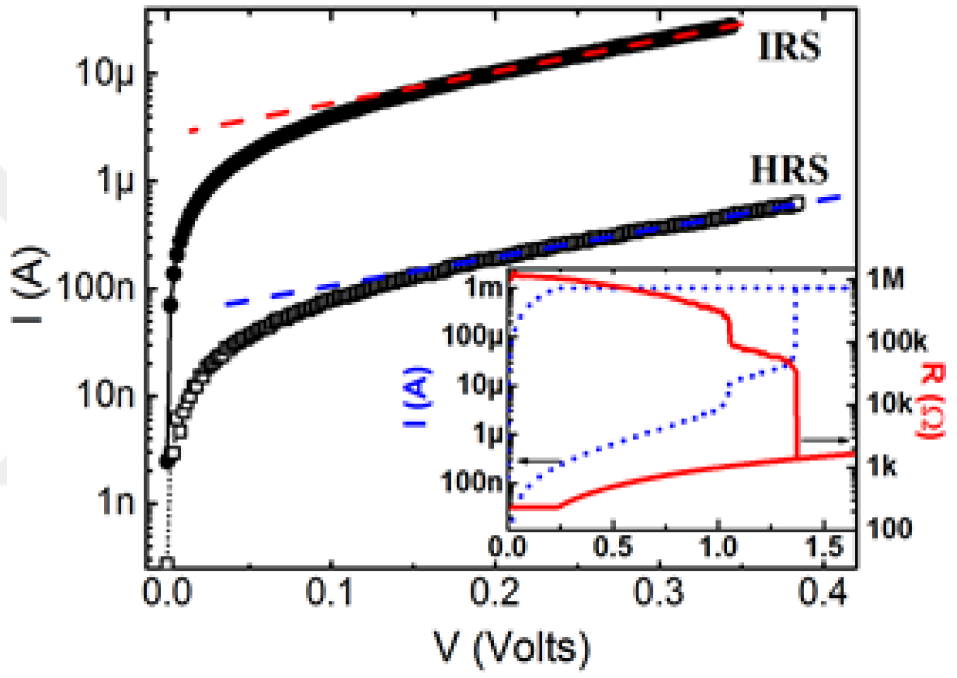


Figure 3.22. I-V characteristics in the subthreshold regime for reset (squares) and intermediate (circles) states of a 90 nm square contact PCM cell . The linear fits to lnI(V), indicated by dashed lines, reveal the STS. The inset shows the full switching dynamic, I on the left scale with a dotted line and R on the right scale with a solid line, starting from a HRS to an IRS then to LRS with a limit current of 1 mA.

$$I = \frac{q^2 A N_{T,tot} \Delta z^2}{k_B T \tau_0 u_a} e^{-(E_C - E_F)/k_B T} V \tag{3.7}$$

The slope of I(V), of Figure 3.22, in this regime yields the device resistance as 27 $k\Omega$ for IRS and 1.33 $M\Omega$ for HRS, also listed in Table 3.1. The total number of traps, $N_{T,tot}$, can be calculated using these resistance values in current equation 3.8.

$$N_{T,tot} \approx \frac{I}{V} \frac{k_B T \tau_0 u_a}{q^2 A \Delta z^2} e^{(E_C - E_F)/k_B T} \tag{3.8}$$

Table 3.1. Parameters Extracted From I-V Curves

Samples	State	STS	R ($k\Omega$)	u_a (nm)	Δz nm	ν	N ($\#/cm^3$)
A	IRS	5.29	22	13.2	3.5	0.002	2.9×10^{21}
A	HRS	4.67	3500	23.8	5.5	0.062	1.3×10^{19}
B	IRS	6.95	28	13	4.7	0.02	1.3×10^{21}
B	HRS	6.24	1330	20	6.8	0.11	2.1×10^{19}

An estimate for the energy difference between E_F and E_C can be acquired from temperature dependent measurements in the low bias regime. In [123] it is shown that at low bias E_A is independent of the voltage and $E_A = E_C - E_F - k_B T$. The activation energy estimated in II for HRS, 0.23 eV is used to calculate the energy difference as $E_C - E_F = 0.26\ eV$. Even though the activation energy term changes in time, this energy difference remains constant and is used to evaluate the time dependence of $N_{T,tot}$ for HRS and IRS.

It is evident from Table 3.1 that programming the device for an IRS induces a thinner amorphous layer. The inter-trap distance is smaller than that for the HRS indicating a larger number of defects, indeed two orders of magnitude difference is recorded for most samples. Figure 3.23 shows the variation of the number of defects as a function of wait time after programming which is acquired using the I-V data at each time using $E_A = E_C - E_F - k_B T$ T which is time independent. While HRS defect population decreases by a factor of 4, for a wait time of 100 minutes, the IRS defect population appears to be almost constant in time, suggesting a tiny decrease only in the second decimal digit.

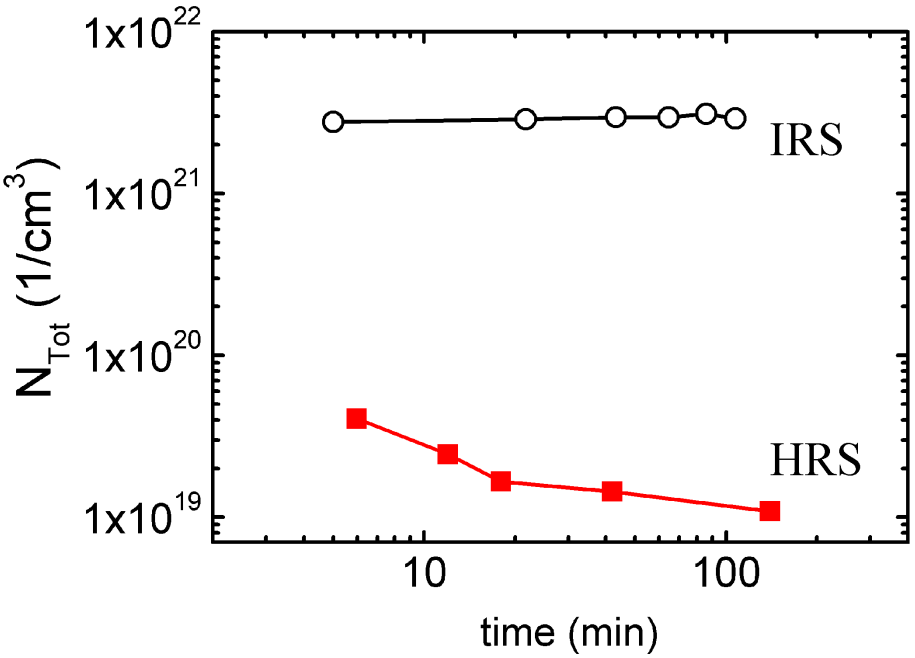


Figure 3.23. Effective number of defects is calculated for various wait times after programming in IRS and HRS.

For further clarification, we refer to a previous study of a comprehensive three dimensional finite-element model with adaptive meshing as discussed in detail in [123]. In summary, this model is a multi -physics approach that takes into account temperature and phase dependent electrical and thermal characteristics of the materials. In addition, homogeneous and heterogeneous nucleation and growth kinetics are considered to obtain a complete picture of the switching.

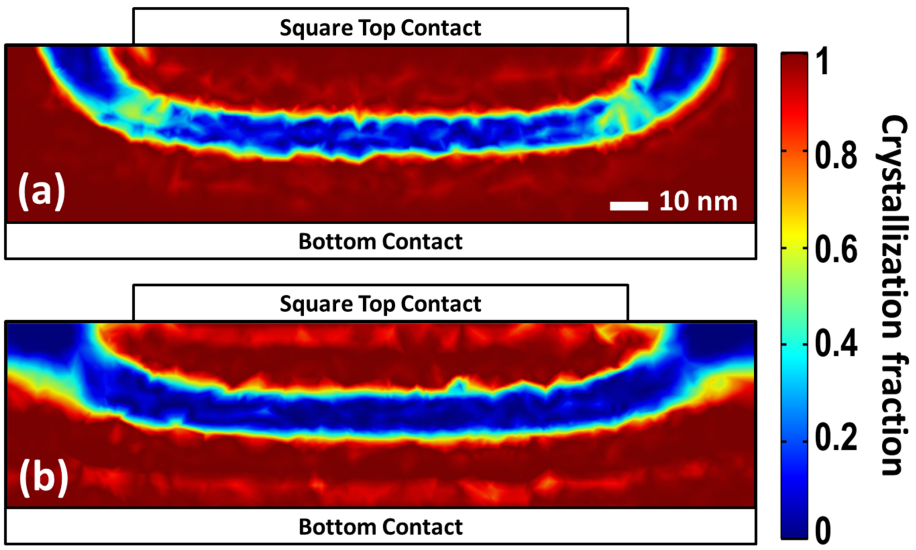


Figure 3.24. A simulation of the vertical cross-section of a 130 nm square top contact device taken through the center right after a programming pulse of 100 ns width and 42 ns trailing edge. Crystallization fraction, f, inside the phase change layer is shown in color code which corresponds to f = 1, red, for crystalline and f = 0, blue, for amorphous phases. The colors between the two represent regions with a mixture of crystalline and amorphous phases.

Figure 3.24 demonstrates the result of the simulation for a 130 nm square top contact PCM device, after a programming voltage pulse is applied to the set state. Phase transition occurs in a dome shape active region inside the GST layer [126, 127] which is fully amorphous for HRS of 178 $k\Omega$ achieved with a 1.1 V, 100ns pulse, Figure 3.24b. The IRS in Figure 2.67a is obtained by a 0.95V pulse and the corresponding resistance is 18.3 $k\Omega$. The amorphous region in the IRS is thinner and has areas with mixed phase indicated by yellow to green areas. These regions are a result of the current crowding effect which causes hot spots within the active region [115] and form current shunting paths. Therefore, IRS has lower resistance and much lower E_A. Increased number of defects in IRS is explained by the smaller amorphous thickness to amorphous-crystalline inter-facial area ratio. Therefore the conduction in IRS is dominated by interface states instead of bulk defects. This accounts for the surprisingly low drift coefficients for IRS. While annihilation of bulk defects cause a drastic resistance increase in HRS, they impose only a small change in IRS.

4. MAGNETIC BUBBLE STABILIZATION AND DYNAMICS

4.1. Deposition of Perpendicular Magnetic Anisotropy (PMA) Thin Film

Initially, I worked on producing magnetic thin films with perpendicular magnetic anisotropy (PMA), which is to be used in spin-valves and nano-micro dots and wires. The AJA magnetron sputtering system shown in Figure 4.1.a is used for the fabrication of the thin films. In addition, for magnetic characterization, Physical Properties Measurement System (PPMS) Vibrating Sample Magnetometer (VSM) in Figure 4.1b is used. With the consultations made, thin films with perpendicular magnetic anisotropy (PMA) were produced by obtaining repeatedly growing Co and Ni thin films on Ta/Pt sublayers. These films are also known as high spin polarized materials with high anisotropy and low damping in the literature.

The layers of the PMA material are shown in Figure 4.2. Here, 0.2 nm of Co material is grown on the 0.6 nm Ni layer by repeating these two layers 8, 10 and 15 (N = repeat numbers) times. The repeated structure was grown on Si substrates as follows,

Ta (5nm)/Pt(10nm)/$[$Co(0,2nm)/Ni(0.6nm)$]_N$/Co(0.2 nm)/Pt(5 nm)

The samples were fabricated on magnetron sputtering system starting at ultra-high vacuum conditions (around 2×10^{-8} Torr) and at a flow rate of 50 sccm of Ar at 3 mTorr pressure on Si substrate. At first, Co (0.2 nm) / Ni (0.6 nm) layers were grown by magnetron sputtering on Ti (5 nm) / Pt (10 nm) sublayers with 8, 10 and 15 repeats as shown in Figure 4.2 and then, these repeats end with Co (0.2 nm) for symmetry and finally coated with Pt (5 nm). Final Pt layer is used here to prevent the oxidation of the thin films.

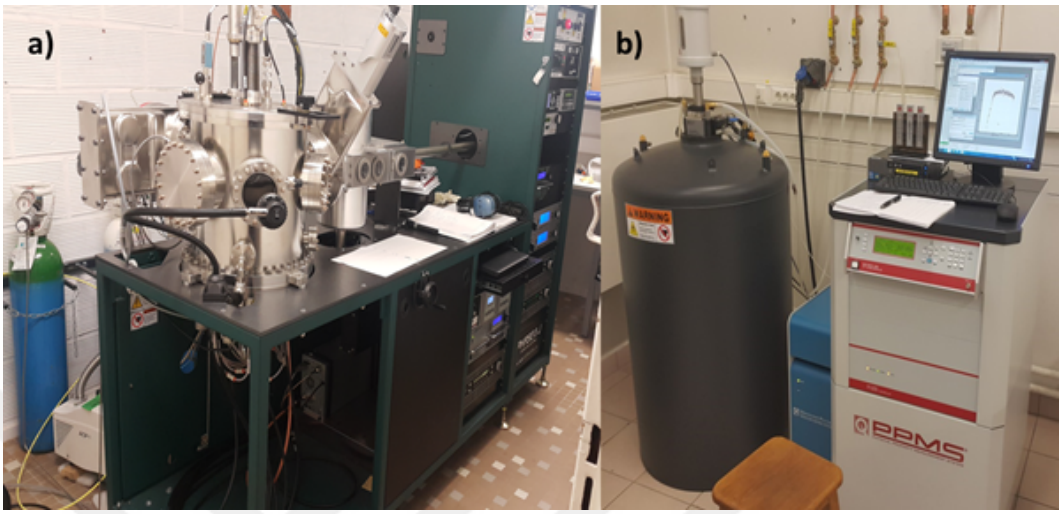


Figure 4.1. a) AJA magnetron sputtering system b) PPMS Vibrating Sample Magnetometer (VSM).

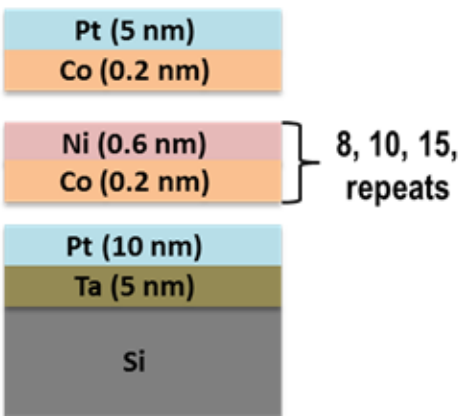


Figure 4.2. Magnetic thin film with perpendicular magnetic anisotropy (PMA) and the thickness of the layers and repeat numbers.

Table 4.1. Growing conditions and deposition rates of the materials in the PMA thin films

Materials	Ar Flow Rate (sccm)	Grown Pressure (mTorr)	DC Power (Watt)	Deposition Rate (Å/s)
Ta	50	3	50	0.3468
Pt	50	3	50	0.58293
Co	50	3	50	0.23245
Ni	50	3	50	0.2829
Cu	50	3	50	0.64375

Before, the deposition of the thin films, the first thing to do is to define the deposition rates of the materials that will be used for the future work. Then, the determination of the growth conditions of the layers has been started with Ta and Pt materials, which are first used as sublayers and capping layer. Table 4.1 gives the optimum growth conditions for these materials and the deposition rates in these conditions. Deposition rates of these materials at 50 sccm Ar flow rate, 3 mTorr pressure and 50W DC power are 0.3468 Å/s and 0.58293 Å/s for Ta and Pt, respectively; For Cu, it is 0.64375 Å/s for 50 W power. As the Cu material is used in the process of spin-valve fabrication, the deposition rate was already determined for this material. While the deposition rate of Co is 0.23245 Å/s at 50 sccm Ar flow rate, 3 mTorr pressure and 50W DC power, the deposition rate of Ni is 0.2839 Å/s at 50 sccm Ar flow rate, 3 mTorr pressure and 50W DC power. To determine the growth rates of materials, the thickness measurements of the grown materials were made by using X-ray powder diffraction (XRD) and the deposition rates of the materials were determined with high accuracy.

XRD measurements are based on the general Bragg diffraction to obtain a diffraction pattern for the substrate and grown materials placed in the system. For this given pattern, the materials and densities to use in the analysis step are added to the analysis

process. In addition, providing a general thickness range for the material ensures that the analysis process is completed in a shorter time. In the analysis step, the actual thickness value is obtained by overlapping of the patterns obtained from XRD and the given parameters.

Figure 4.3 shows the XRD measurement results for Pt and Co. The diffraction pattern obtained from XRD is blue and the red line is the obtained pattern in the direction of the given parameters. These two patterns are overlapped by changing the material parameters to obtain actual material thicknesses. The materials, densities and thickness of the materials are given in the above of the following figures.

Deposition rate is obtained by dividing the thicknesses by the deposition time. This process has been repeated many times for all materials. Determination of the deposition rates at each opening of the system is important to have high precision thicknesses.

The magnetic properties of the thin films were determined by a Vibrating Sample Magnetometer (VSM) integrated in the Physical Properties Measurement System (PPMS) in Figure 4.4.

4.1.1. Magnetic and Surface Characterization of the Thin Films

Plastic pipes were used for the magnetic characterization of the materials in the VSM. Depending on the type of measurements to be performed (perpendicular or in plane according to the material), the samples mounted in the pipe are placed into the VSM system. However, since the contribution from the empty pipe and silicon substrate needs to be subtracted from the received data by using VSM, only the background is measured and subtracted from the VSM data to obtain the actual data of the existing magnetic material.

Ta(5)/Pt(10)/$[Co(0,2)/Ni(0,6)]_N$/Co(0.2nm)/Pt(5nm) the multilayer structure was grown on Si substrate. The materials and the names are given below.

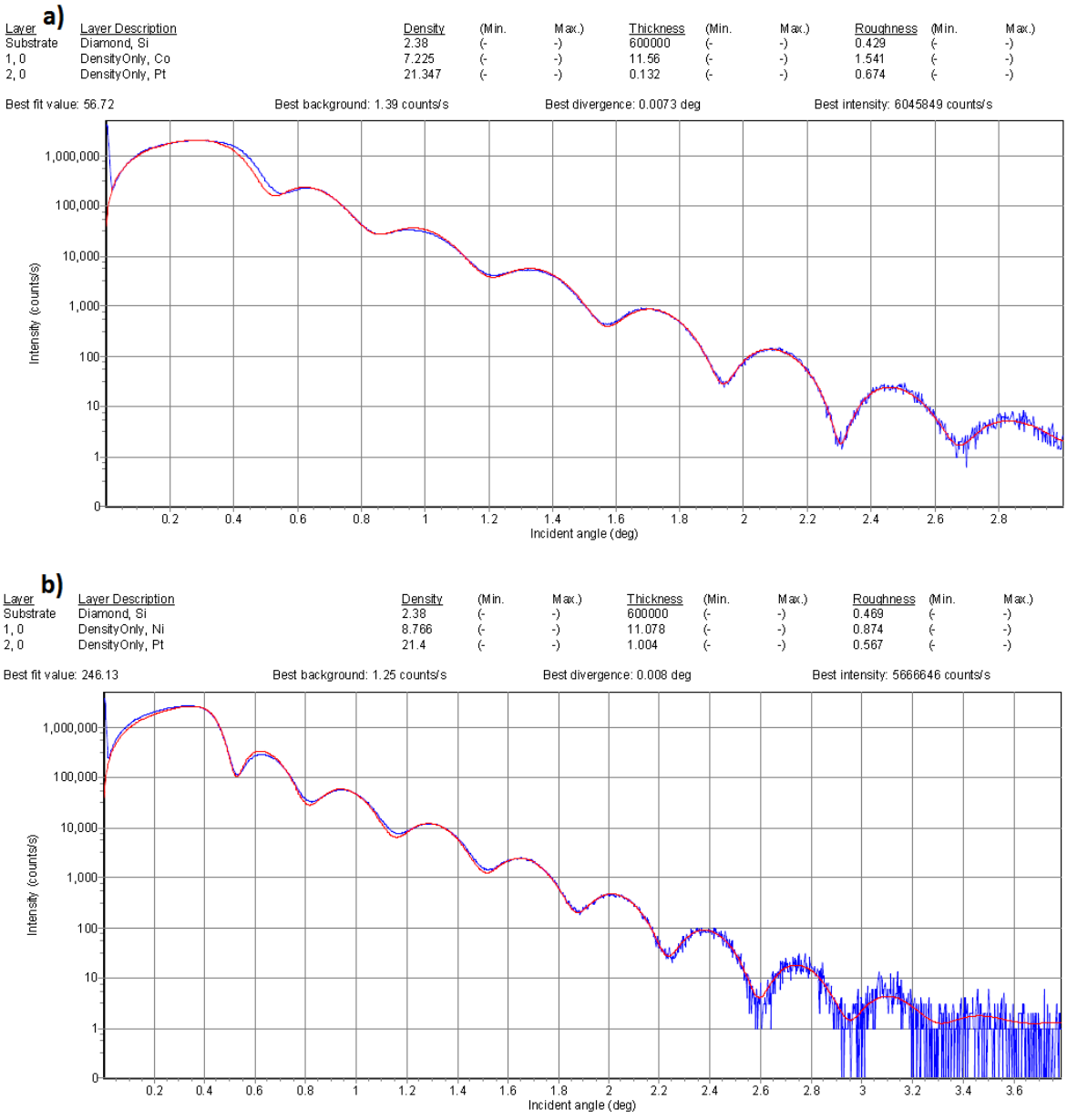


Figure 4.3. X-ray diffraction (XRD) measurements for grown C0 (a) and Pt (b) to obtain deposition rate.

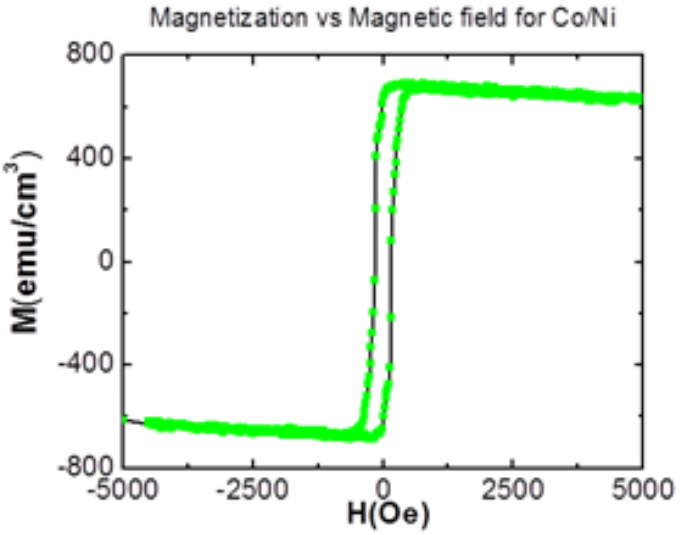


Figure 4.4. VSM results of the thin film with perpendicular magnetic anisotropy (PMA)under out of plane external magnetic field.

B1 Ta(5)/Pt(10)/$[Co(0,2)/Ni(0,6)]_{10}$/Pt(5nm)

B2 Ta(5)/Pt(10)/$[Co(0,2)/Ni(0,6)]_{8}$/Co(0.2nm)/Pt(5nm)

B3 Ta(5)/Pt(10)/$[Co(0,2)/Ni(0,6)]_{15}$/Co(0.2nm)/Pt(5nm)

B4 Ta(5)/Pt(10)/$[Co(0,2)/Ni(0,6)]_{10}$/Co(0.2nm)/Pt(5nm)

In Figure 4.5, the hysteresis measurements for different thin films under perpendicular magnetic field in VSM is given. As it can be seen from the graphs, the chosen materials show high magnetization properties. Figure 4.6 also shows the in-plane magnetic field magnetization curves of the same materials. From these results, it can be seen that the chosen materials in the project have a perpendicular magnetic anisotropy PMA.

In addition, using the magnetization hysteresis graphs at room temperature of the materials, the fundamental magnetic properties of the materials were obtained.

They are known as saturation magnetization M_s, the coercive field H_c, the anisotropic magnetic field H_k and the anisotropy coefficient K for all materials in Table 4.2.

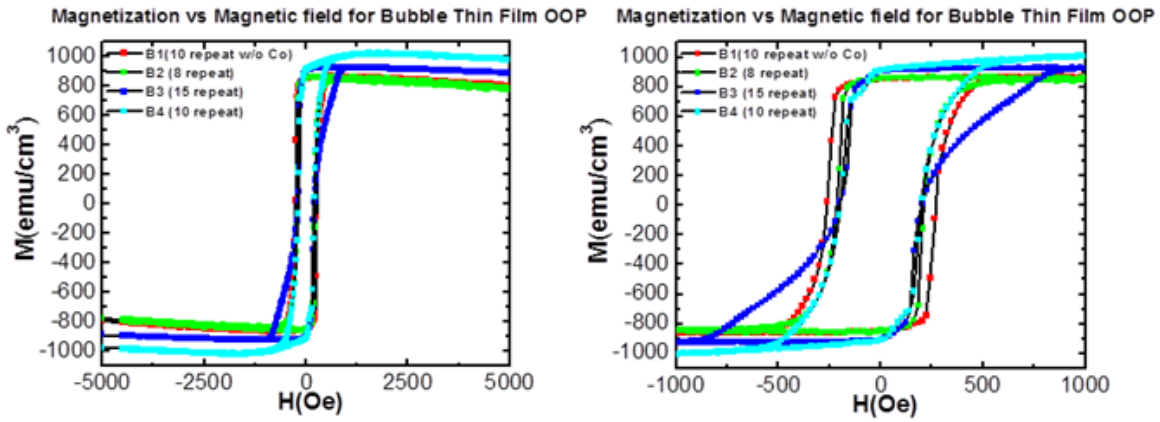


Figure 4.5. (Ta(5)/Pt(10)/$[Co(0,2)/Ni(0,6)]_N$/Pt(5nm)) PMA thin films out of plane VSM results at room temperature.

When the values given in Table 4.2 are taken into account, the saturation magnetization values for M_s are given both from the hysteresis measurement performed under the perpendicular magnetic field and from the hysteresis measurement obtained under the in-plane magnetic field. As you can see, there is a difference between these two values. For this reason, the M_s values obtained in the hysteresis measurement made under the in-plane magnetic field give a more accurate result when we consider the anisotropic effects. We also observed a high saturation magnetization value for each of these materials between 710(emu/cm^3) and 1015(emu/cm^3).

For the coercive field H_c values, it changes between 150 Oe and 250 Oe. This indicates the required magnetic field to change the magnetic orientation of the material. We also obtained the anisotropy field H_k values, which is an important magnetic property for the magnetic materials, from hysteresis measurements under in-plane magnetic field. These values are close to each other and vary between 6400 Oe and 6800 Oe. Finally, the K values, which are anisotropy energy densities of the materials, are obtained from the obtained M_s and H_k values. In the K calculations, the M_s values obtained from the in-plane magnetic field measurements are used.

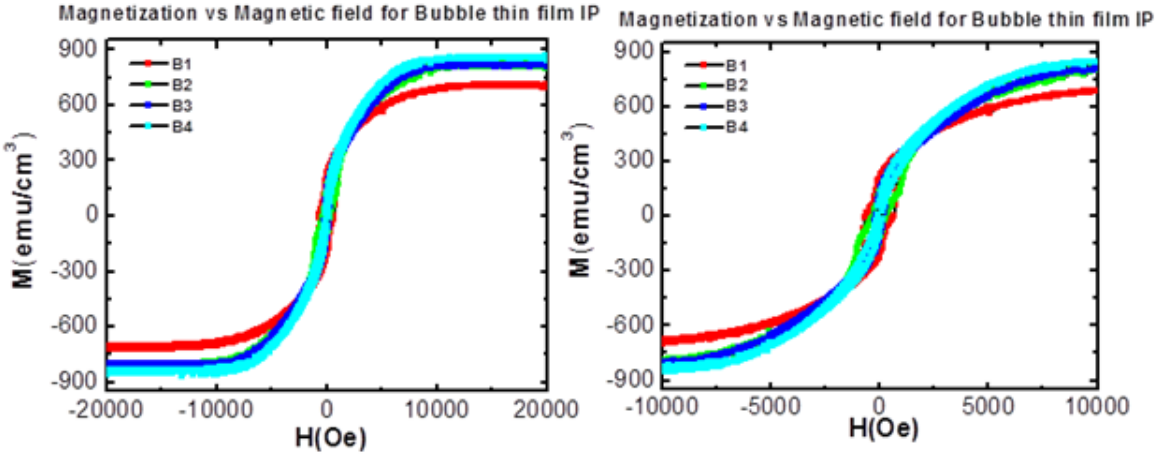


Figure 4.6. (Ta(5)/Pt(10)/[Co(0,2)/Ni(0,6)]$_N$/Pt(5nm)) PMA thin films in-plane VSM results at room temperature.

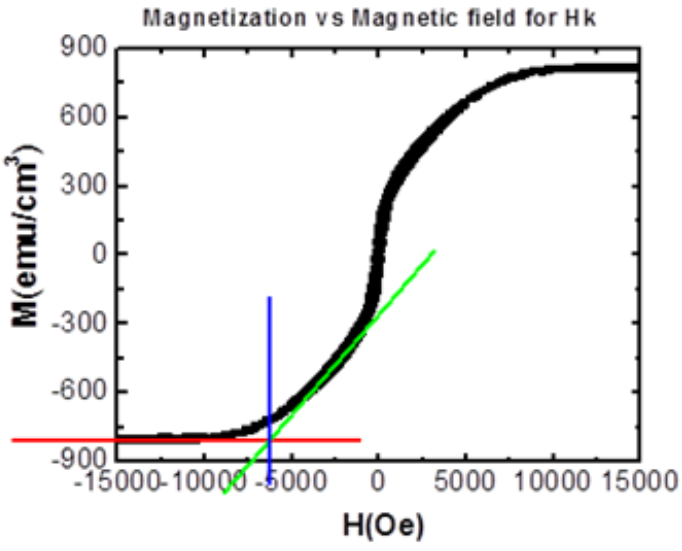


Figure 4.7. Line fit to find H_k value for (Ta(5)/Pt(10)/[Co(0,2)/Ni(0,6)]$_8$/Pt(5)) PMA thin film B2 from the in-plane VSM result at room temperature.

To obtain the H_k value, we need two line fits in the in-plane VSM result. One of them is added to the curve where the saturation magnetization is going to saturated condition, and the other is at place where the saturation magnetization is saturated. The cut-off point of these two linear-fit lines shows us where the value of H_k is. Figure 4.7 shows the process to find the H_k value for the material B2. H_k value was obtained as 6600 Oe. The anisotropic coefficient K is obtained from the equation 5.1.

$$K = \frac{H_k.M_s}{2} + 2\Pi.M_s^2 \tag{4.1}$$

From these results, we determined the material composition by looking at the high saturation magnetization, the anisotropy field values and the anisotropy energy density values and which one has sharp hysteresis with PMA. Therefore, the B2 material is selected for the next steps.

Table 4.2. Ms, Hc, Hk ve K values of the thin films

Samples	Ms (emu/cm^3)	H_c (Oe)	H_k (Oe)	K (erg/cm^3)
B1	850 (OOP) 710 (IP)	250	6800	5581353 (IP) $5.6 \times 10^5 J/m^3$
B2	840 (OOP) 820 (IP)	200	6600	6930813 (IP) $6.9 \times 10^5 J/m^3$
B3	920 (OOP) 815 (IP)	150	6400	6781448 (IP) $6.8 \times 10^5 J/m^3$
B4	1015 (OOP) 855 (IIP)	175	6800	7500165 (IP) $7.5 \times 10^5 J/m^3$

Surface topography of the Ta(5)/Pt(10)/$[Co(0,2)/Ni(0,6)]_8$/Co(0.2nm)/Pt(5nm) thin film is obtained by AFM and Figure 5.8 shows the AFM image of the thin film. In the surface analysis, the general structure is not too rough, but has a maximum height

of 1-3 nm. Grains are obviously observed in the smallest scale AFM image.

In Figure 4.8, I have given AFM and MFM images examined with a magnetic tip with low moment. The magnetic image for observation of magnetic bubble in dots or wires is taken after demagnetization under an AC in-plane applied magnetic field (Figure 4.9) that is a decreasing sine wave with 4-minute period and lasts 120 minutes from max 650 mT (6500 Oe) to zero fields. However, at first in order to saturate the material, a perpendicular magnetic field 7700 Oe is applied to material before the demagnetization process.

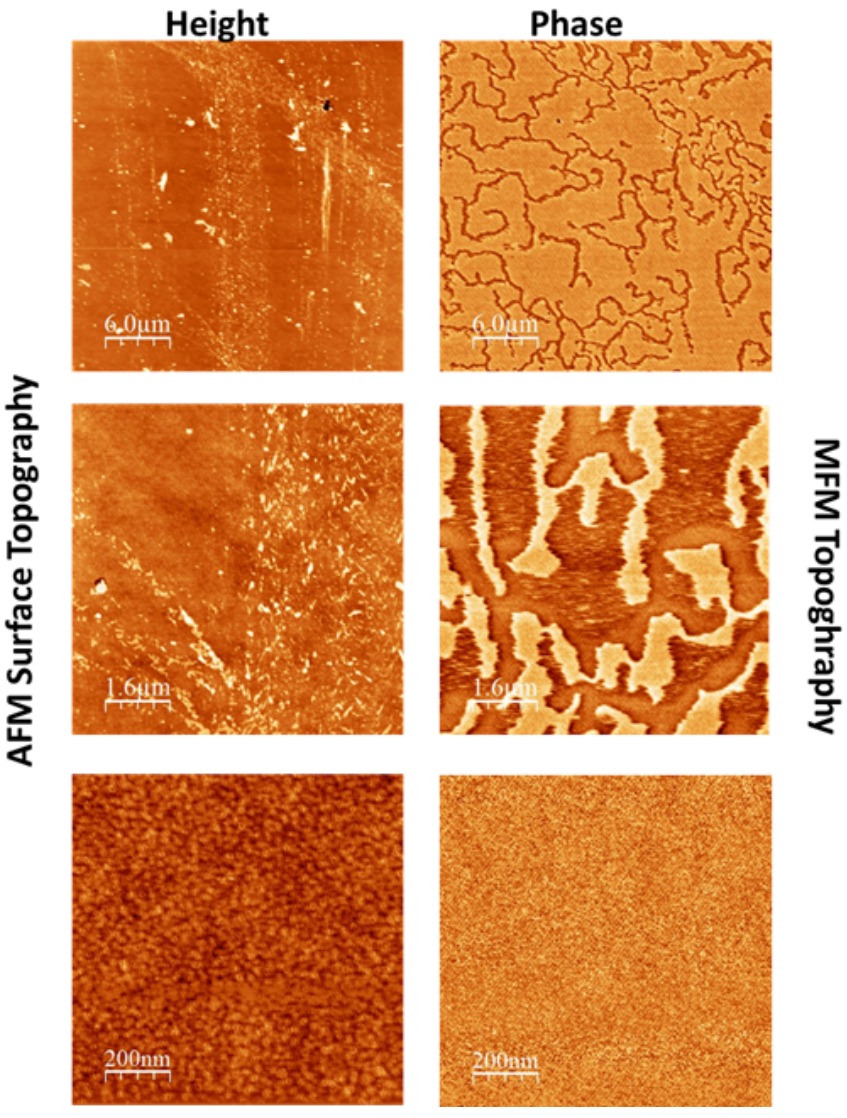


Figure 4.8. AFM surface topography and MFM image of the thin film.

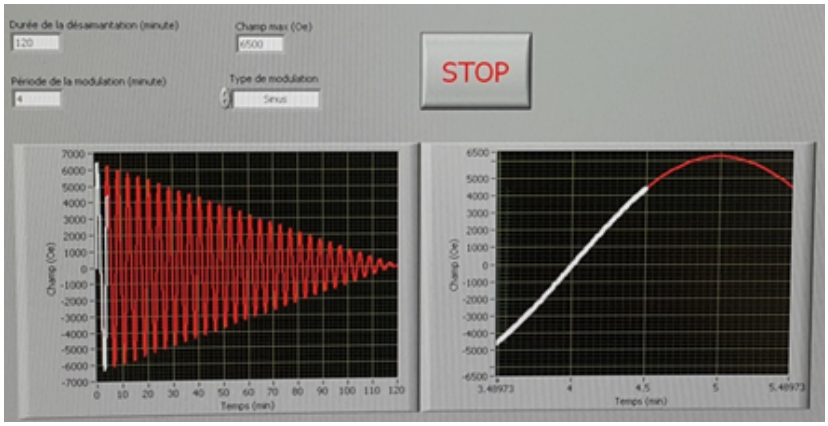


Figure 4.9. AC demagnetization field with 4-minute period and 120 minutes from max 650 mT (6500 Oe) to 0 fields.

In the MFM images in Figure 4.8, in three different scales, labyrinth domains (in the first two images) are seen in PMA materials. In the third smallest-scale images, the scan area is very small, so that there is no change in only one domain structure.

4.1.2. Fabrication of Nano-Micro Dot Arrays and Wires

By using thin films Ta(5)/Pt(10)/$[Co(0,2)/Ni(0,6)]_8$/Co(0.2nm)/Pt(5nm), nano-micro dot arrays with different dot diameters, changing from 100 nm to 3 μm to investigate bubble formation and it's diameter dependence, are fabricated. The electron-beam lithography system available in the clean room of the University of Lorraine was used for the patterning process.

Figure 4.10a shows the disk arrays' design and dose tests. Each set has 15×15 arrays and the dots are arranged with a distance of $3\times$ dot size between each other. First, a thin film Ta(5)/Pt(10)/$[Co(0,2)/Ni(0,6)]_8$/Co(0.2nm)/Pt(5nm) is deposited onto a full 2×2 inch Si substrate with magnetron sputtering method. After this process, the electron-beam lithography was used for the patterning step. At the same time, a 3×3 array was formed on the same structure and different electron beam doses for each region were applied for dose test. Figure 4.11 shows an optical microscope image of the dot arrays on the Si substrate after a patterning operation.

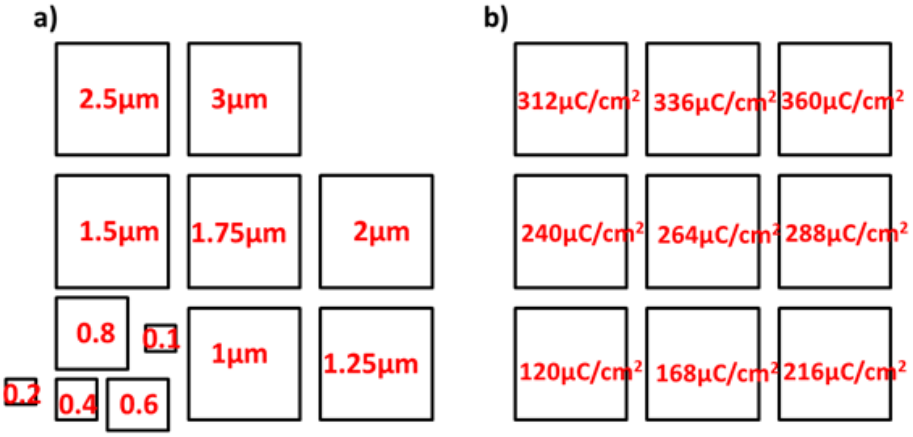


Figure 4.10. a) Nano-micro dot arrays pattern b) applied dose values.

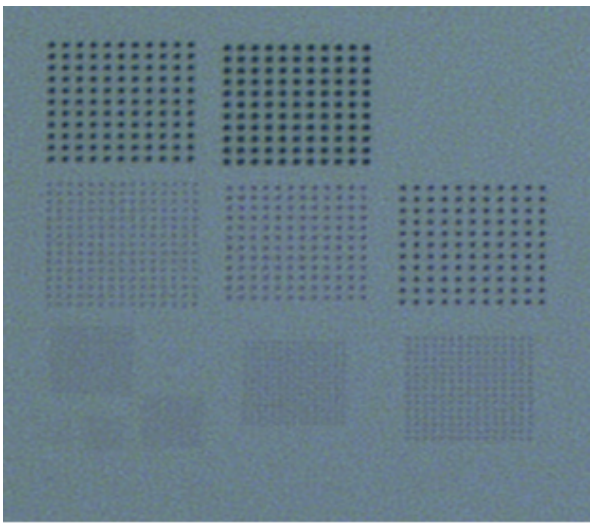


Figure 4.11. Optic microscope image of dot arrays after patterning process.

The used method for nano-micro dot arrays and wires for B2 is ion milling process. In this method, the thin film was first deposited on the Si substrate. Then it was coated with 280 nm PMMA by spin coating and heated to 180°C. Then, the electron beam lithography is used for the defined patterns to write with electron beams in specific doses. For the developing step, MIBK solution is used to remove exposed regions. Then, the sample is placed into the evaporator system for coating 40 nm Al on top of the sample by using electron beam evaporation. This process was followed by lift-off (NMP solvent, 60^0C) to remove PMMA resist from the surface sample (not exposed regions). The next step is ion milling to pattern. Finally, the patterning process is completed after chemical etching with the TMAH solution to remove the remaining Al layer.

Along with the dot array fabrication, micro-wires are also produced. Figure 4.12 shows a general pattern of the micro-wires that are produced and the dose test planned to be applied for the micro-wires. There are 10 wires designed for each different width from $0.2\mu m$ to $3\mu m$, except $4\mu m$, because for this one, there are 6 wires designed.

The width of micro-wires varies from $0.2\mu m$ to $4\mu m$. The dose to be applied varies from $282\mu C/cm^2$ from $120\mu C/cm^2$. This is different for only $4\mu m$ and the dose varies from $240\mu C/cm^2$ to $120\mu C/cm^2$. It is clearly visible in the following way. The length of the wires are $60\mu m$.

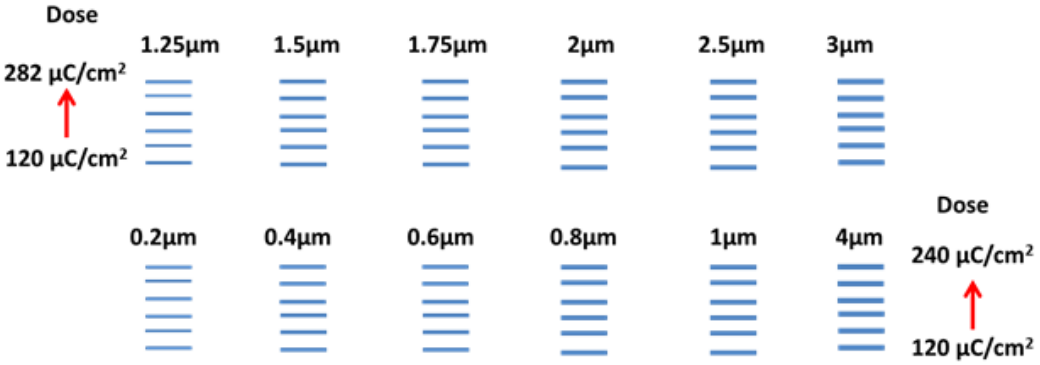


Figure 4.12. Nano-micro wires pattern and applied dose values.

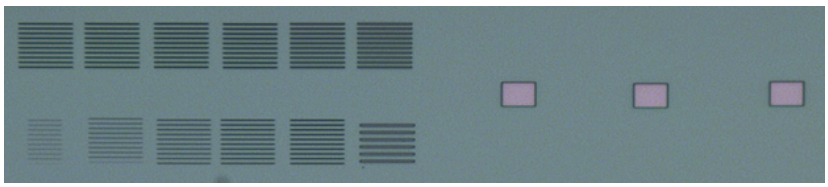


Figure 4.13. Optic microscope image of wires after patterning process.

Figure 4.13 shows optical microscope image of wires after patterning process The three square structures on the right side are markers placed to find the location of the wires. Figure 4.14 shows a complete view of all the structures after patterning process. There was not much variation in the results of the dose studies.

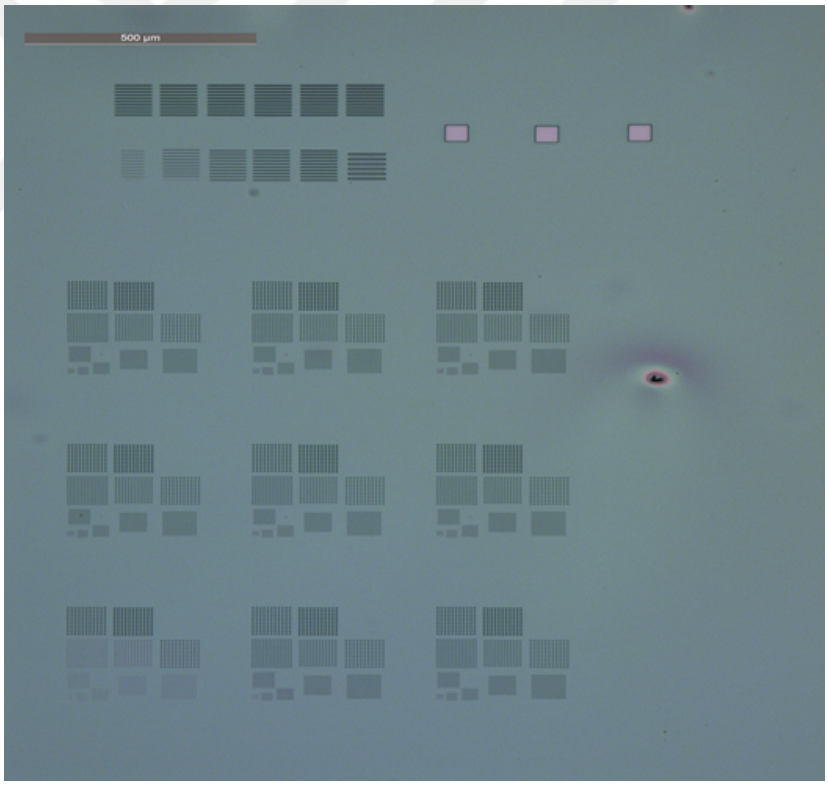


Figure 4.14. Optic microscope image of dot arrays and wires after patterning process.

Figure 4.15 is a schematic representation of the steps of the patterning process, ion-milling process for fabrication. As a result of the final stage of TMAH chemical etching, the structure in Figure 4.14 is obtained.

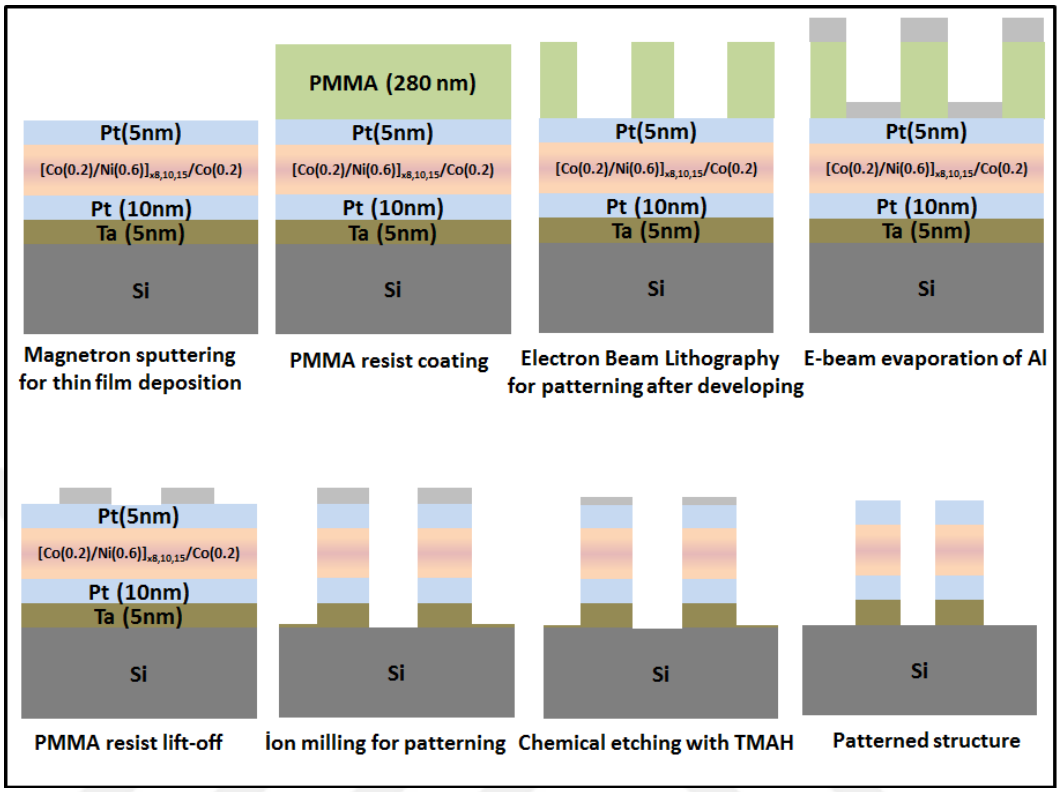


Figure 4.15. Ion milling process steps for patterning of nano-micro disk arrays and wires.

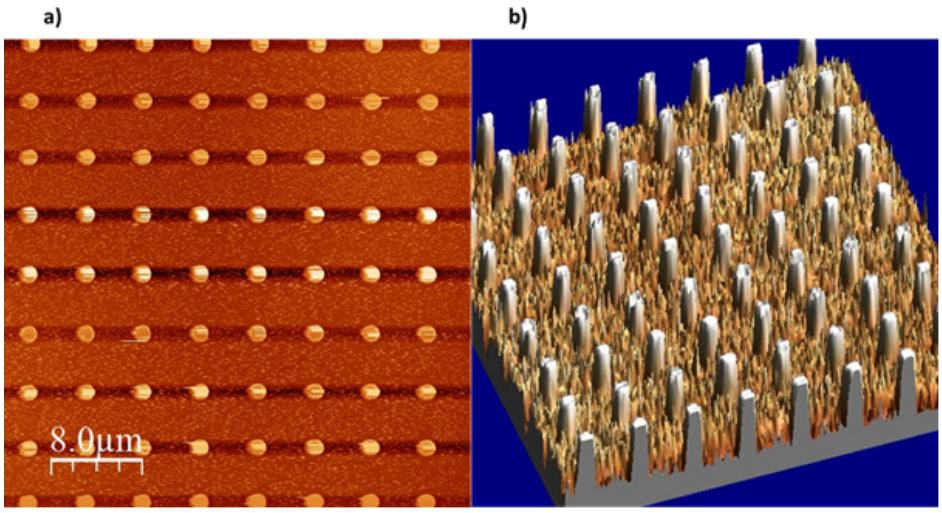


Figure 4.16. $3\mu m$ dot arrays AFM surface topography a) 2 D b) 3 D images.

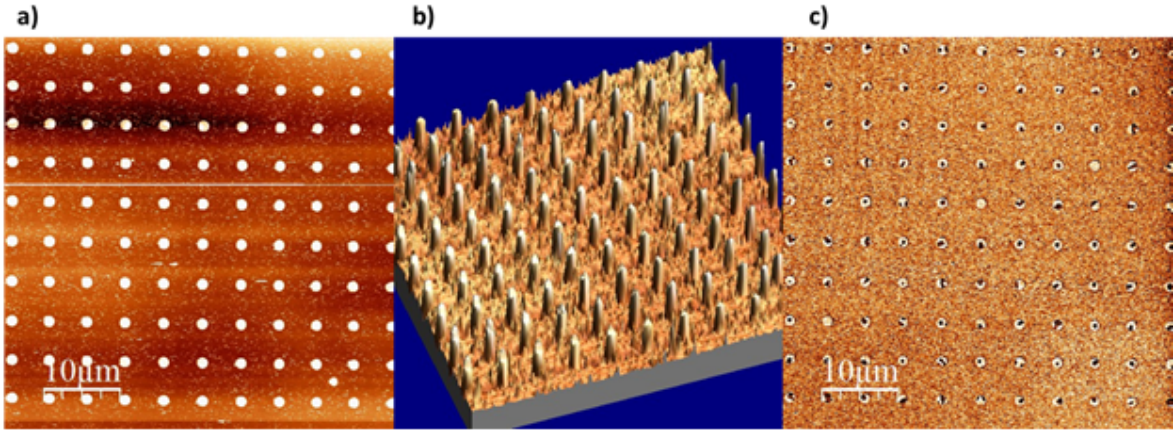


Figure 4.17. After 6500 Oe in-plane AC demagnetization 1.25μm dot arrays AFM and MFM images. a) 2D AFM b) 3 D AFM images c) MFM images.

4.1.3. Stabilization of Bubbles in Dot Arrays and Wires

The conditions of bubble formation in nano-micro dot arrays were first stated with AC demagnetization of the sample. MFM images were taken after different AC demagnetizations and bubble formation was investigated in different dot sizes. The magnetic configuration that we call bubble; it is a magnetic configuration that is inverse with the magnetic configuration of the remaining of dot, generally circular in shape, with no connection to the edge of a dot. Therefore, if the magnetic illustration of the dot is light, the bubble is dark; if the disc is dark, the bubble is light. This structure seems like having a ring shape in the dot. Figure 4.18 also shows examples for single-domain structures with yellow markers, bubble structures with red markers, and multi-domains structures with blue markers.

The dots that reached the saturation under perpendicular magnetic field 7700 Oe were demagnetized under the in-plane AC magnetic field, and for the dots with different diameters, we tried to obtain the AC demagnetization value, which gives the highest number of bubble formation because of MFM measurements. This will guide us in the future about whether bubble will exist after spin-valve fabrication, and which demagnetization values and dot sizes should give us the bubble structure.

The clear description of the AC demagnetization process is shown in Figure 5.19. However, before each AC demagnetization process, a magnetic field 7700 Oe is applied perpendicular to the sample to saturate the material. Initially, when starting with low demagnetization, there is only single domain on small and medium dot arrays and multi-domains in large radius dot arrays. Figure 4.18 shows MFM images for dot arrays with different diameters. Smaller diameter dot arrays have a single domain like the $1.0\mu m$ dot arrays.

Figure 4.19 shows the MFM images after different AC demagnetization for the $1.5\mu m$ diameter dot arrays. H_{max} values for AC demagnetization are shown on each image.

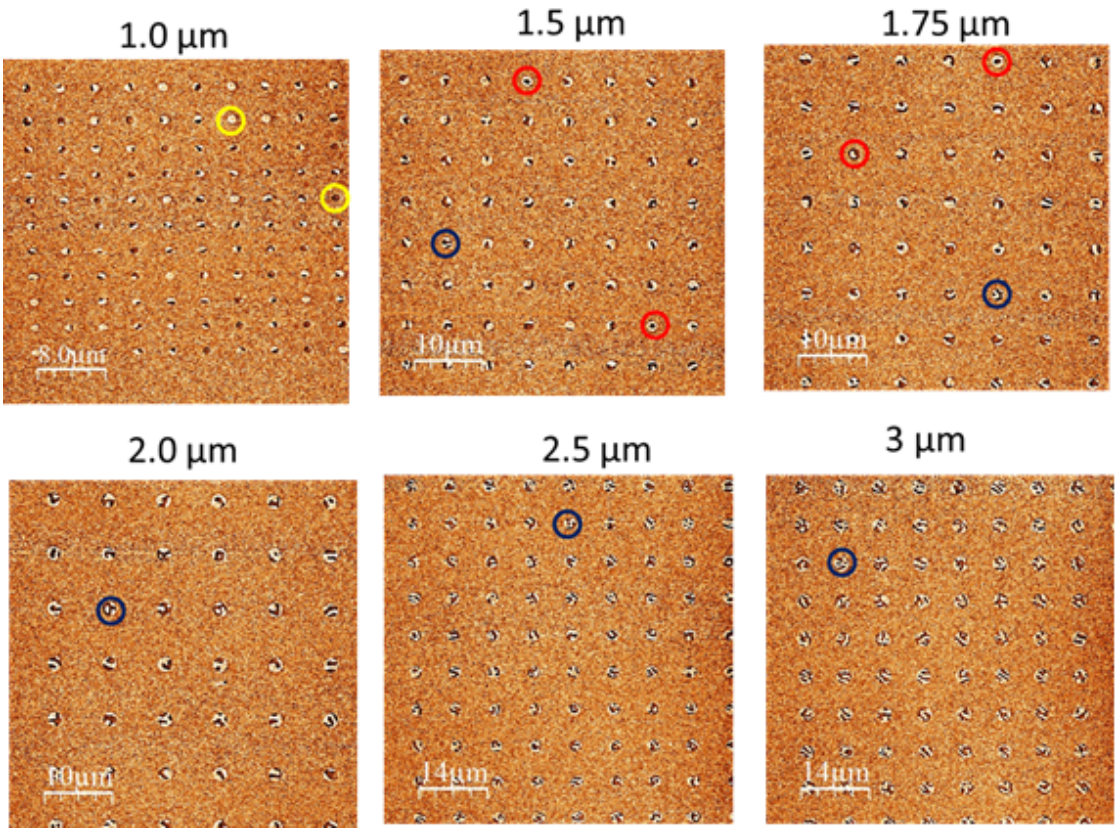


Figure 4.18. After 5000 Oe in-plane AC demagnetization, MFM images for different diameter dot arrays (yellow circles single domain structures, red ones bubbles and blue ones multi-domains, as examples of the magnetic structures).

Our goal is to obtain a suitable AC demagnetization value to form bubble in the dot arrays depending on the diameters. The best AC demagnetization value obtained as a result of MFM measurements was found to be the maximum value of 6500 Oe. This is the AC demagnetization value for which higher numbers of the bubble structure is obtained. Figure 4.20 shows the MFM images after 6500 Oe AC demagnetization for the dot arrays with diameter $1.0\mu m$, $1.25\mu m$ and $1.5\mu m$. It also shows numbers of the bubbles for each one, namely percentages.

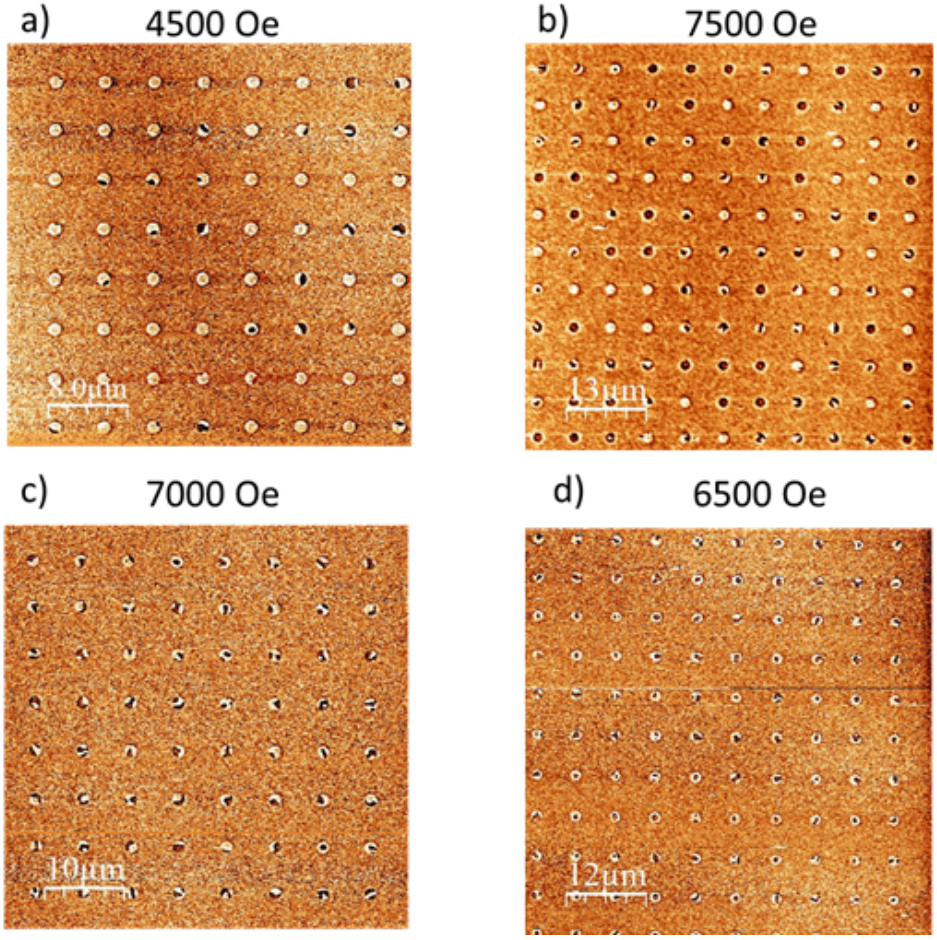


Figure 4.19. MFM images for $1.5\mu m$ dot arrays with different AC demagnetization treatments.

Here, 47% percentage for $1.5\mu m$ dot arrays is obtained, but this is a good start for spin-valve fabrication. After that, 6250 Oe AC in-plane demagnetization field, I observed 70% bubble formation in $1.5\mu m$ dot array and this is the highest rate of

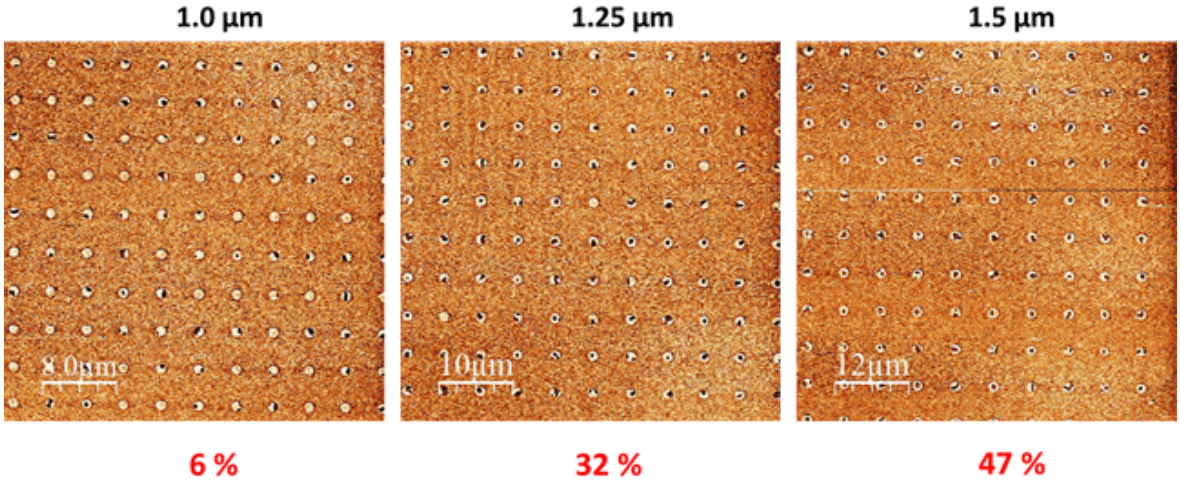


Figure 4.20. After 6500 Oe in-plane AC demagnetization, MFM images for different diameter dot arrays $1.0\mu m$, $1.25\mu m$ and $1.5\mu m$.

bubble formation. Figure 4.21 shows the magnetic bubble formation for $1.5\mu m$ at 6250 Oe AC in-plane demagnetization field.

In addition to bubble formation in the dot arrays, I have been also investigating the bubble formation condition for nano-micro wires through MFM images. First, it was investigated how AC demagnetization values affect the magnetic structure in the nano-micro wires. Figure 4.22 shows MFM images for $0.8\mu m$, $1.0\mu m$ and $1.2\mu m$ wires. H_{max} values for MFM measurements are given on the right side of each image. At low AC demagnetization values, the magnetic configurations in the wires are single domains, stripes, whereas stripes or multi-domains are observed at high AC demagnetization values. After this observation, for the best AC in-plane demagnetization field value, after the observation of bubble formation in dot arrays for given AC in-plane demagnetization field, I took MFM images to observe the magnetic configuration in wires. This gave me good magnetic bubble formation in wires. In Figure 4.23 shows this results for $0.8\mu m$, $1.0\mu m$ and $1.2\mu m$ wires.

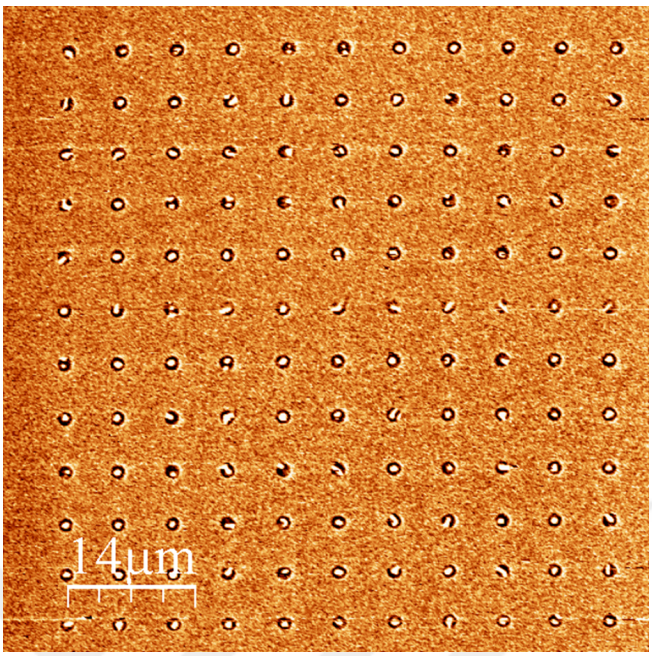


Figure 4.21. After 6250 Oe in-plane AC demagnetization, MFM image for 1.5μm dot array.

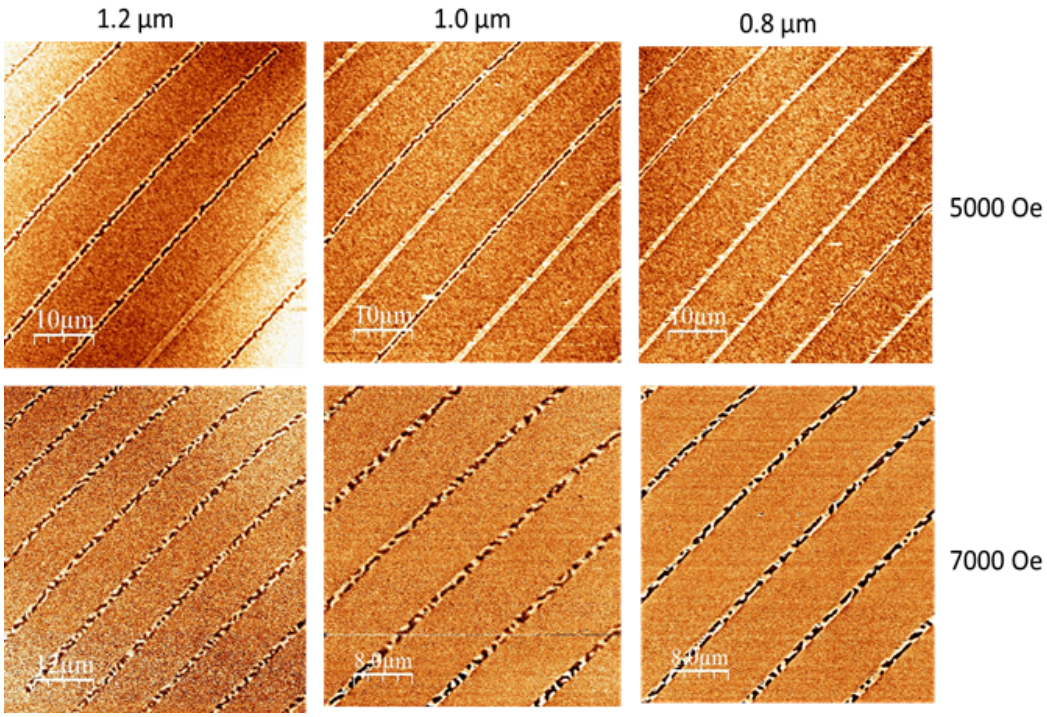


Figure 4.22. After 6500 Oe in-plane AC demagnetization, MFM images for different wire thicknesses 0.8μm, 1.0μm and 1.2μm.

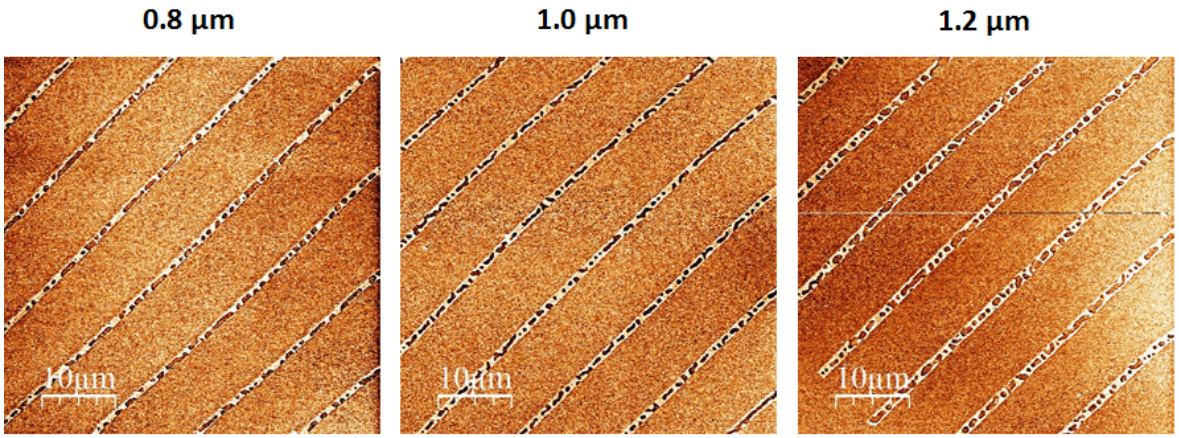


Figure 4.23. After 6250 Oe in-plane AC demagnetization, MFM images for different wire thicknesses $0.8\mu m$, $1.0\mu m$ and $1.2\mu m$.

4.1.4. Spin-Valve Thin Film Deposition and VSM Measurements

Another step of this study is to fabricate the spin-valve structure and to study the behaviors of the spin-valves having bubble under a current and/or magnetic field. For this purpose, first, spin-valve thin film preparation was studied. Figure 4.24 shows the schematic of the overall spin-valve structure.

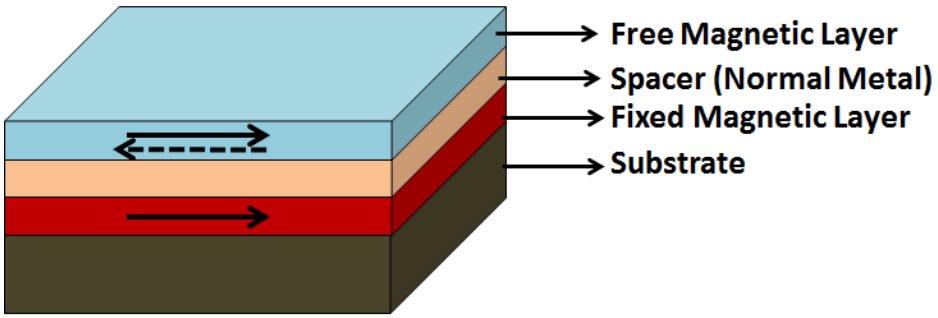


Figure 4.24. Schematic drawing of a Spin-valve structure.

At first, we need to decide the fixed magnetic layer structure in the spin valve and worked on it. For this purpose, to determine which Co thickness is deposited into the structure, while depositing the thin film for the spin valve, we kept the Pt thickness constant as 0.8 nm in the repeated layer and changed the thickness of Co in

the repeated layer as 0.2 nm, 0.3 nm, 0.4 nm, 0.5 nm and 0.6 nm.

Then, the same process is applied to determine which Pt thickness is suitable. Co thickness is kept constant as 0.2 nm, 0.3 nm, 0.4 nm, 0.5 nm and 0.6 nm and for each of them Pt thickness is changed as 0.4nm, 0.6nm, 0.8nm and 1nm. After that, from the VSM measurements we first decided the Pt and Co thickness as 0.6 nm and 0.3 nm respectively. For the Co layer thicknesses of 0.2 nm, 0.3 nm and 0.6 nm are listed below and two different structures are combined to investigate how they can exhibit a magnetic property.

A5 Ta(5)/Pt(20)/$[Co(0,3)/Pt(0,6)]_5$/Pt(5nm)

A6 Ta(5)/Pt(20)/$[Co(0,2)/Pt(0,6)]_5$/Pt(5nm)

A7 Ta(5)/Pt(20)/$[Co(0,6)/Pt(0,6)]_5$/Pt(5nm)

A8 Ta(5)/Pt(20) /[Co(0,6)/Pt(0,6)]/[Co(0,3)/Pt(0,6)]x5/Pt(5nm)

A9 Ta(5)/Pt(20) /$[Co(0,6)/Pt(0,6)]_2$/[Co(0,3)/Pt(0,6)]x5/Pt(5nm)

In addition, VSM measurements were made for different spin-valve thin films and the magnetic properties of the thin films were investigated by using PPMS-VSM. Figure 4.25 shows the VSM results for the materials listed above. It is clearly seen that these materials demonstrate PMA properties and we will use 0.3 nm and 0.6 nm for Co and Pt layer thickness, respectively.

After deciding the thicknesses of Co and Pt multi-layers, I deposited the hard layer of the spin-valve. In Figure 4.26, PPMS-VSM measurements for out of plane and in-plane are given and it is clearly seen that hard layer has PMA property with H_c around 1000 Oe. After that, to find H_k value for hard layer to compare with the free layer (having bubble), I analyzed the VSM data and Figure 4.27 shows that the H_k is around 10750 Oe.

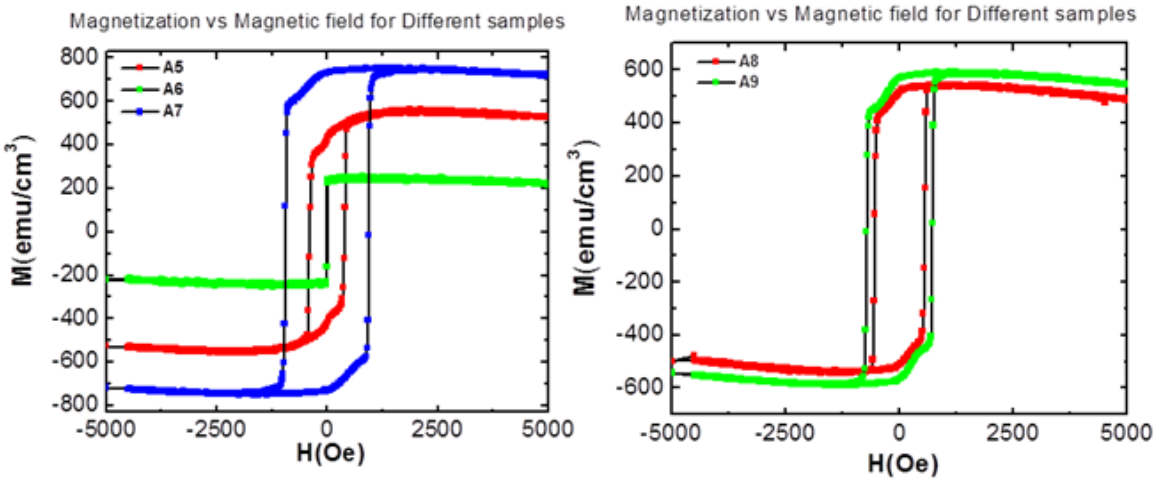


Figure 4.25. VSM data for as grown Co/Pt with PMA.

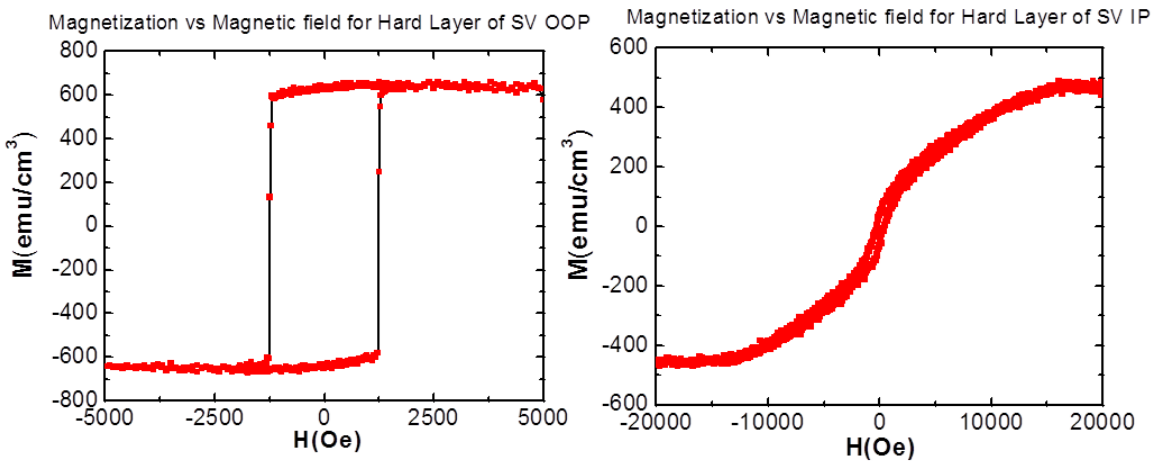


Figure 4.26. VSM measurements for out of plane and in plane of Hard (or Fixed) layer.

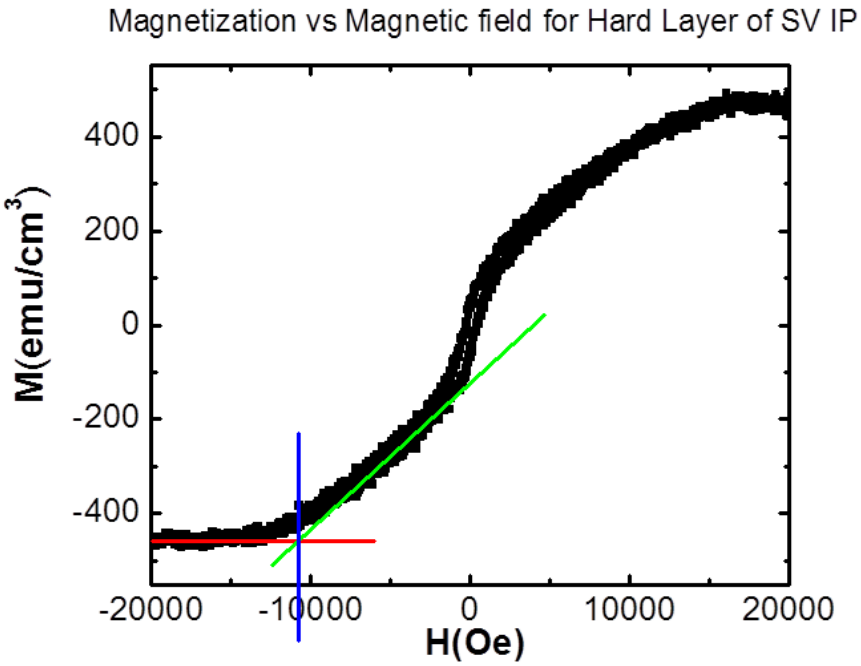


Figure 4.27. VSM measurement data analysis to find Hk for Hard (or Fixed) layer.

Appropriate combinations have been tried up to now to decide hard layer and free layers. The two different spin-valve structures and their VSM measurements are given in Figure 4.28 and Figure 4.29. The difference of these two structure is just change in the places of hard and free layers. However, as it can be understood from VSM measurements, it is not a suitable spin-valve.

Because of the different properties of different repetitive magnetic layers in the structure, it is expected to have a step in the hysteresis of the structure. For this reason, different combinations and different pressure conditions are examined. For this purpose, the magnetic properties of the spin-valve structure are investigated by changing the ambient pressure applied in the magnetron sputtering system. The ambient pressure was set as 3 mTorr, 4 mTorr, and 5 mTorr during thin film deposition. These different pressures are applied only for the magnetic layers and repetitive layers. Figure 4.30 shows the spin-valve structures and Figure 4.31 shows the VSM measurements for these spin-valve structures. We achieved a proper spin-valve structure from these results.

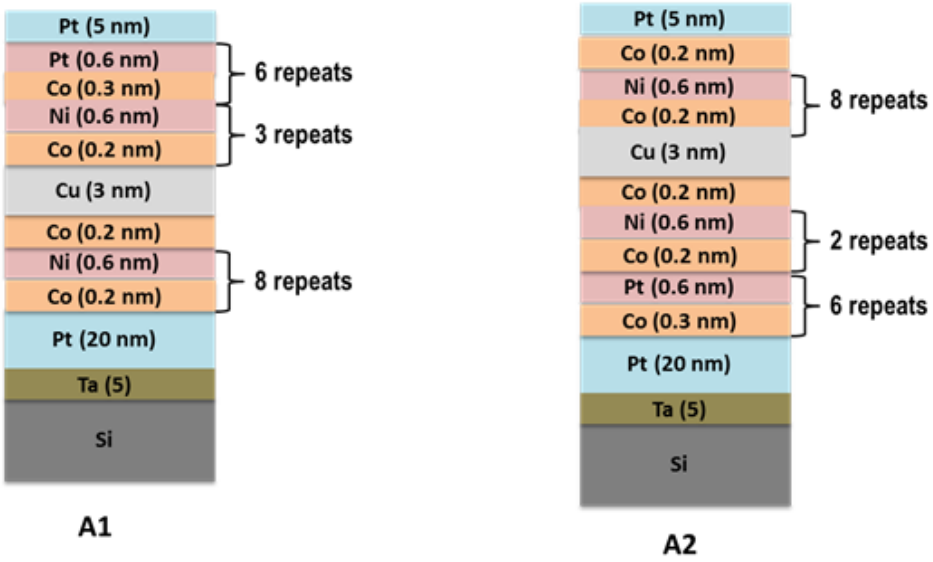


Figure 4.28. Spin-valve structures with layers and thicknesses.

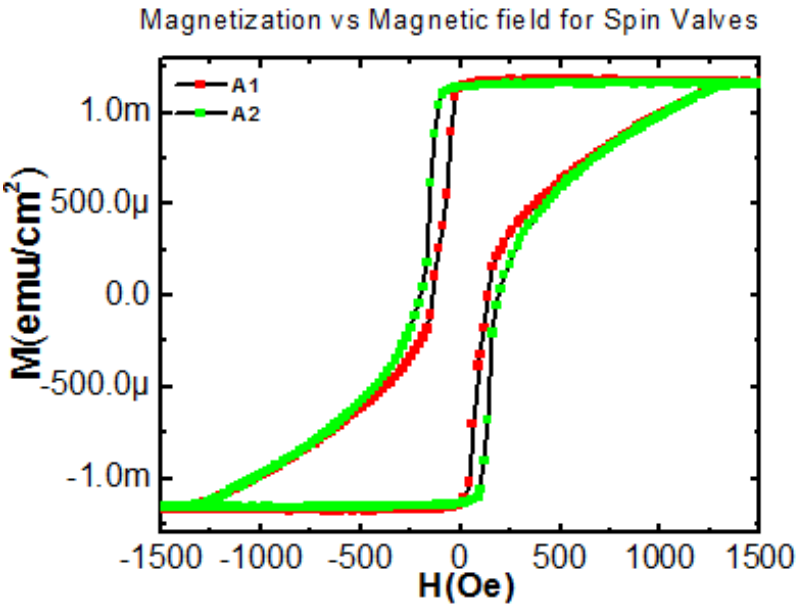


Figure 4.29. Spin-valve structure VSM results.

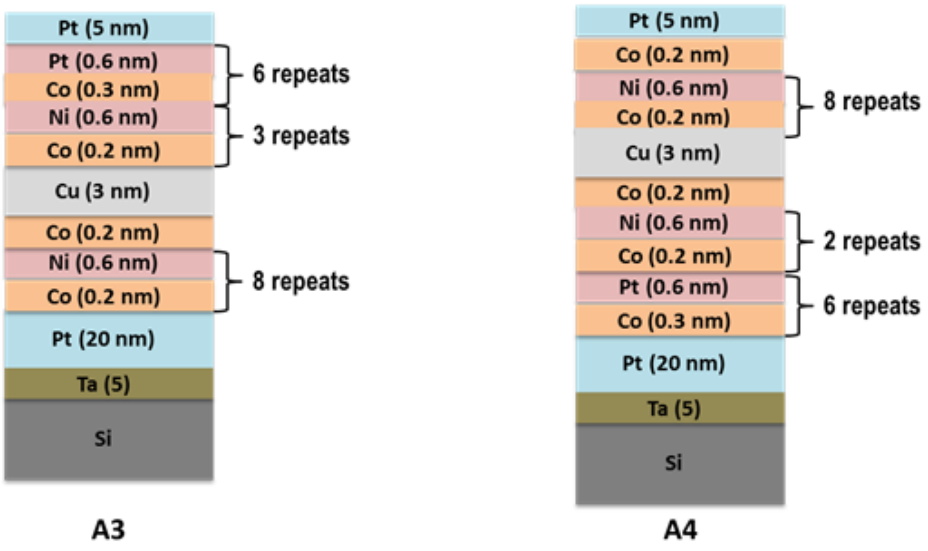


Figure 4.30. Spin-valve structures with layers and thicknesses.

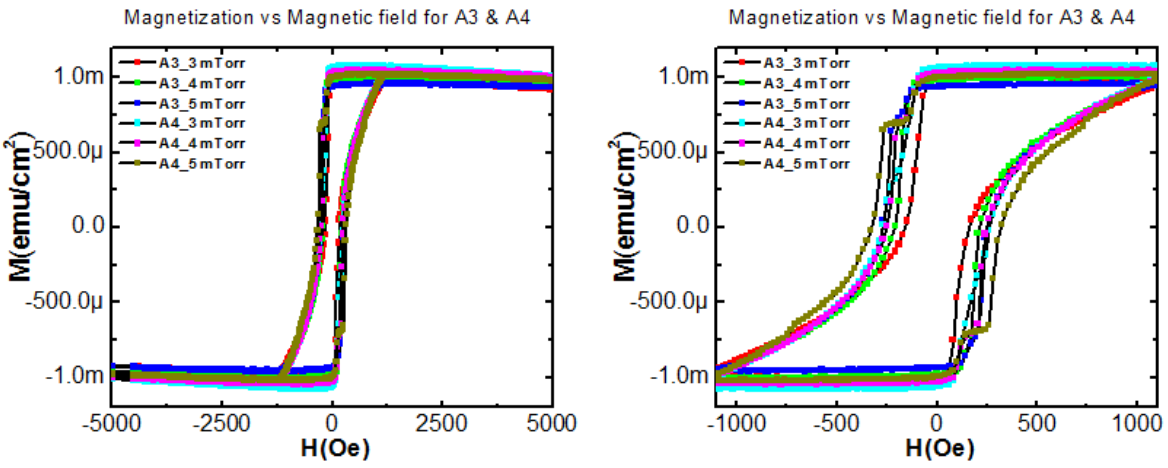


Figure 4.31. Spin-valve structure VSM results.

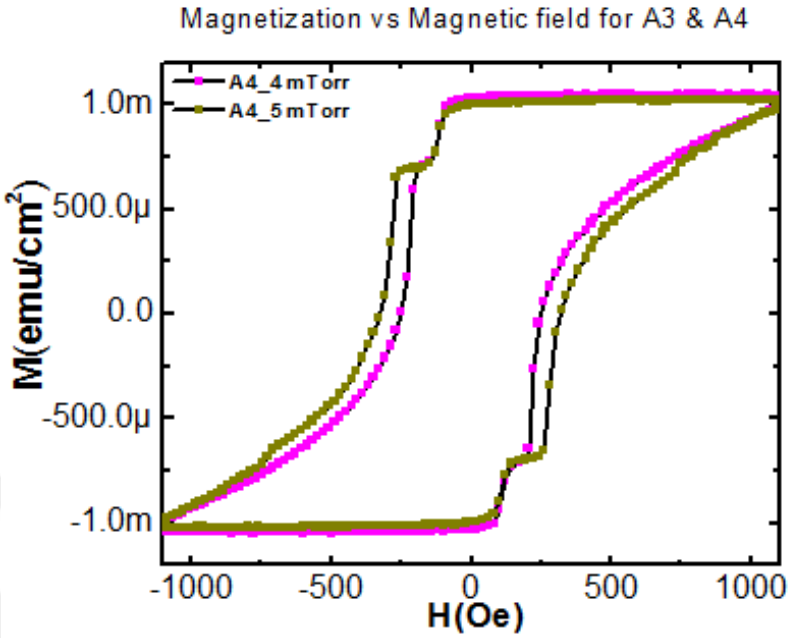


Figure 4.32. Spin-valve structure VSM results.

In Figure 4.32, steps are obtained in the hysteresis graphs for A4-4m Torr and A4-5m Torr materials as it can be seen from the VSM results. Especially, for A4-5m Torr material, the step is clearly visible. However, it is located at a different place than expected position in the hysteresis and size and shape is different. Because, while deposition of the thin film, we decided the numbers of repeat to have very close Ms values for hard and fee layers and for this reason, the expected step is close to the middle of the hysteresis. From these results, I assumed that there is a side affect coming from the other factors like wafer type. For this reason, I deposited again same thin films on different wafers like Si and Si+SiO_2(100 nm).

In Figure 4.33, we can see the VSM results for different wafer types at different deposition pressures. For Si wafer, we have narrow window comparing with Si+SiO_2 nm. From these VSM results, it is clear that Si+SiO_2(100 nm) has better results at different pressures, however, for our purpose, Si+SiO_2(100 nm)at 5 mTorr is suitable wafer type for the spin-valve deposition and device fabrication.

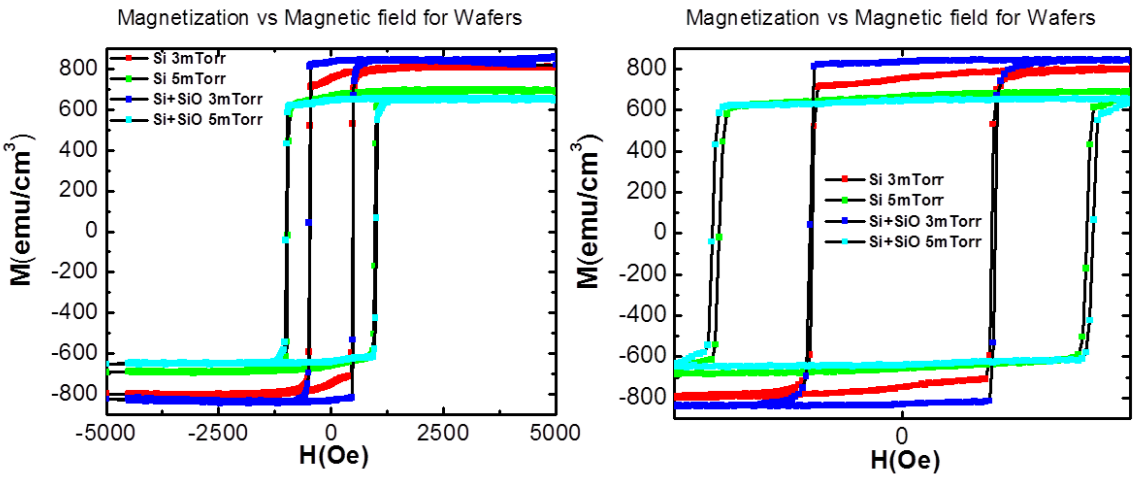


Figure 4.33. VSM results for different type of wafers.

In the point of view of previous information, I deposited above spin-valve structure on the the Si+SiO_2(100 nm) at 5 mTorr for magnetic layers and 3 mTorr for the other layers. After that, I conducted VSM experiment to obtain hysteresis graph, as can be seen in Figure 4.32. The desired step hysteresis shape was obtained in the VSM measurements. It can be foreseeable that the step should be close to the center of the graph of the when the magnetization values of the free and hard layers are considered, and the hysteresis result supports this argument, because the magnetization values of the free and fixed layers are chosen to be close. After observation of suitable spin-valve hysteresis, the next step to do is to fabricate new spin-valve nano and micro dots by using this thin film to nucleate bubble on them.

4.2. Single Bubble Formation Conditions in Spin-Valve Device

The bubble formation conditions in nano-micro spin-valve discs were first tested by AC in-plane external field demagnetization. MFM images were taken after different demagnetization conditions and bubble formation was investigated in different dot sizes. First, the samples were conditioned under out of plane magnetic field with 7700 Oe to reach saturation of magnetization. Then for different AC in-plane external magnetic field demagnetizations, I tried to observe bubble formation in patterned spin-

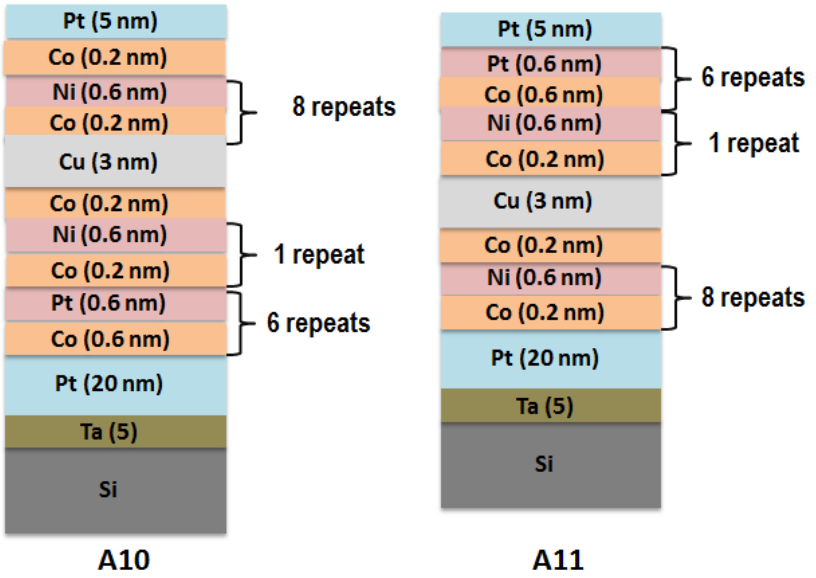


Figure 4.34. Spin-valve structures with layers and thicknesses.

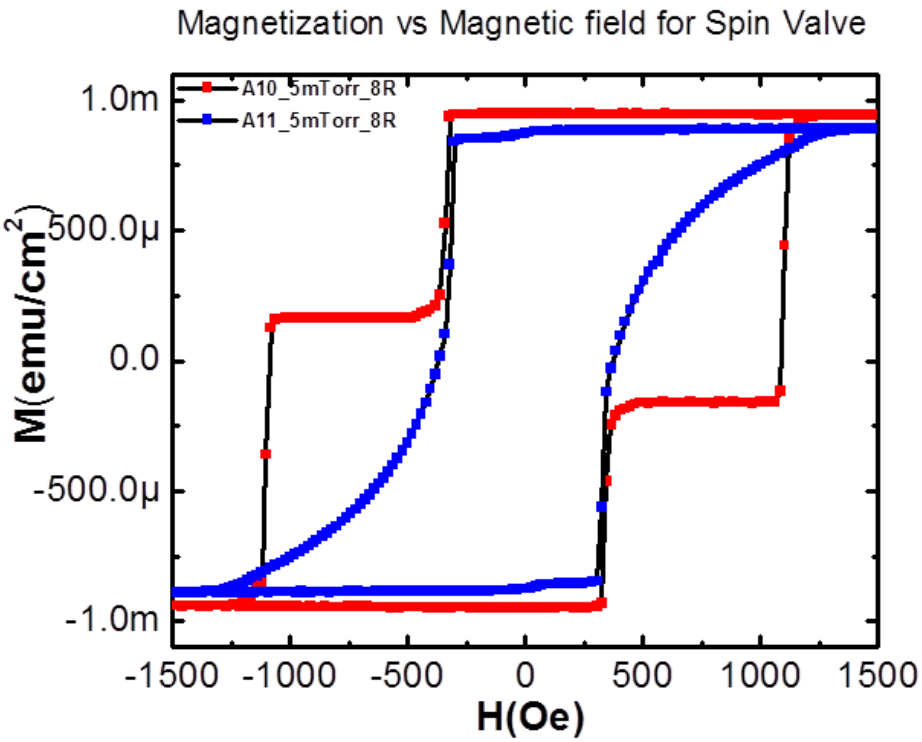


Figure 4.35. Spin-valve structure VSM results.

valve device depending on the size of the dots to determine the success rate of bubble nucleation. I used MFM to observe bubble formation in spin-valve device.

First, I applied 6450 Oe Hmax AC in-plane external field demagnetization after saturation field. Because in previous dot experiments, 6500 Oe gave higher success rate of bubble nucleation in 1.5μm dots. After demagnetization process, I took MFM images to observe bubble formation in patterned spin-valve device. Figure 4.35 shows MFM images for in 1.5μm dot array for different scanning rates. Here, it is clearly visible that there are many bubble in dots and beside this, in some dots there are some double bubbles or multi bubbles in dots. In addition to bubble formation, there are also labyrinth domains in dots. Our aim is to nucleate only one bubble in a dot to observe its behavior under AC external magnetic field in plane or out of plane or AC current with or without external field in plane or out of plane. From Figure 4.36, this bubble formation results is not suitable for future work then I looked at different dot size samples.

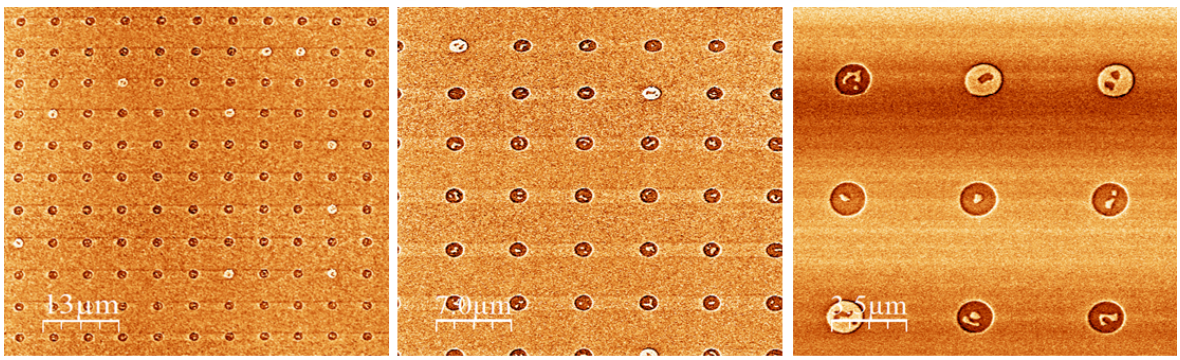


Figure 4.36. MFM images for 1.5μm dot size after 6450 Oe Hmax AC in-plane external magnetic field demagnetization.

For same demagnetization values, I took MFM images for 1.25μm dots and results are given in Figure 4.37. From Figure 4.37, in this sample there are many single bubbles, less double or multi bubbles, labyrinth domains and also single domains. The size of bubble is around 400 – 450 nm and this is smaller than the ones in the dot experiments (600 – 1000 nm). However, for the contacted spin-valve device, it is difficult to say that whether a dot has a single bubble after demagnetization process or not. Because

we need to know this for electrical experiments.

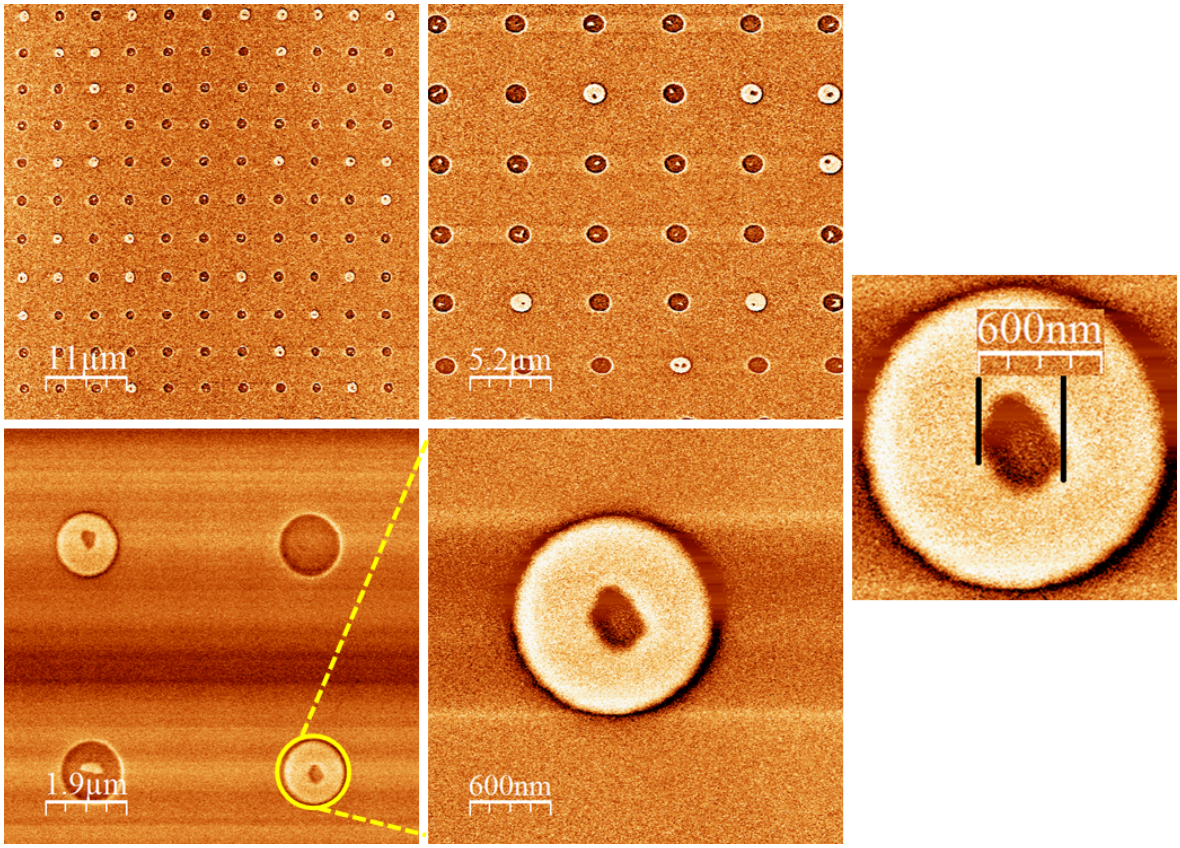


Figure 4.37. MFM images for 1.25μm dot size after 6450 Oe Hmax AC in-plane external magnetic field demagnetization.

After then, for same demagnetization values, I took MFM images for 1.0μm dots and results are given in Figure 4.38. From Figure 4.38, there are just many single bubbles and single domains. Even though we have just single bubble in dot, the problem is the number of bubbles because there are less number of dots having single bubble. There is also an interesting observation that for this dot size, we have just single domains and single bubble. That means that if we can increase the number of bubbles in array, then they will be only single bubbles.

For this purpose, during demagnetization process I increased H_{max} AC in-plane external field to 6950 Oe after 7700 Oe saturation field. In Figure 4.39, MFM images are given and it is clear that there are many single bubbles in 1.0μm dot array and

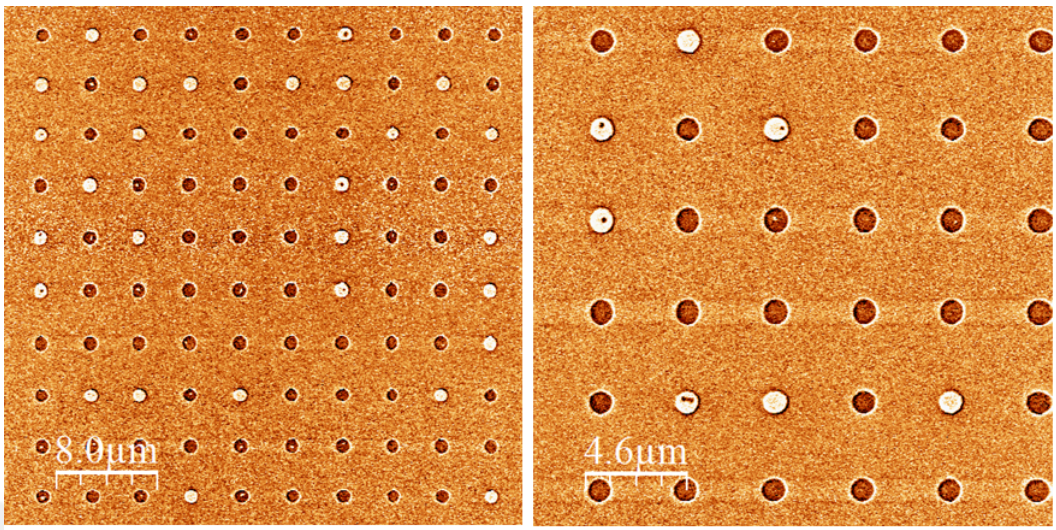


Figure 4.38. MFM images for 1.0μm dot size after 6450 Oe Hmax AC in-plane external magnetic field demagnetization.

less single domains. The size of bubble is around 400 – 450 nm and this is smaller than the ones in the dot experiments (600 – 1000 nm). However, this bubble size is very similar with previous 1.25μm dots spin-valve. Normally, even in previous dots experiment made to observe bubble formation, the size of bubbles are changing and even in same dot size. My assumption about the difference in bubble is coming from the effect of hard layer.

Beside dot array, I investigated bubble formation in wire for spin-valve thin films. For this observation, I took MFM images for different widths of wires to compare them and in Figure 4.40 we can see the MFM images for 0.2μm, 0.6μm and 1.0 μm. It can be seen from Figure 4.40 there are no magnetic configurations in the wires, other than single domains for different width of wires. These images were taken after H_{max} AC in-plane external field to 6450 Oe after 7700 Oe saturation field. The reason behind this may be due to strong hard layer.

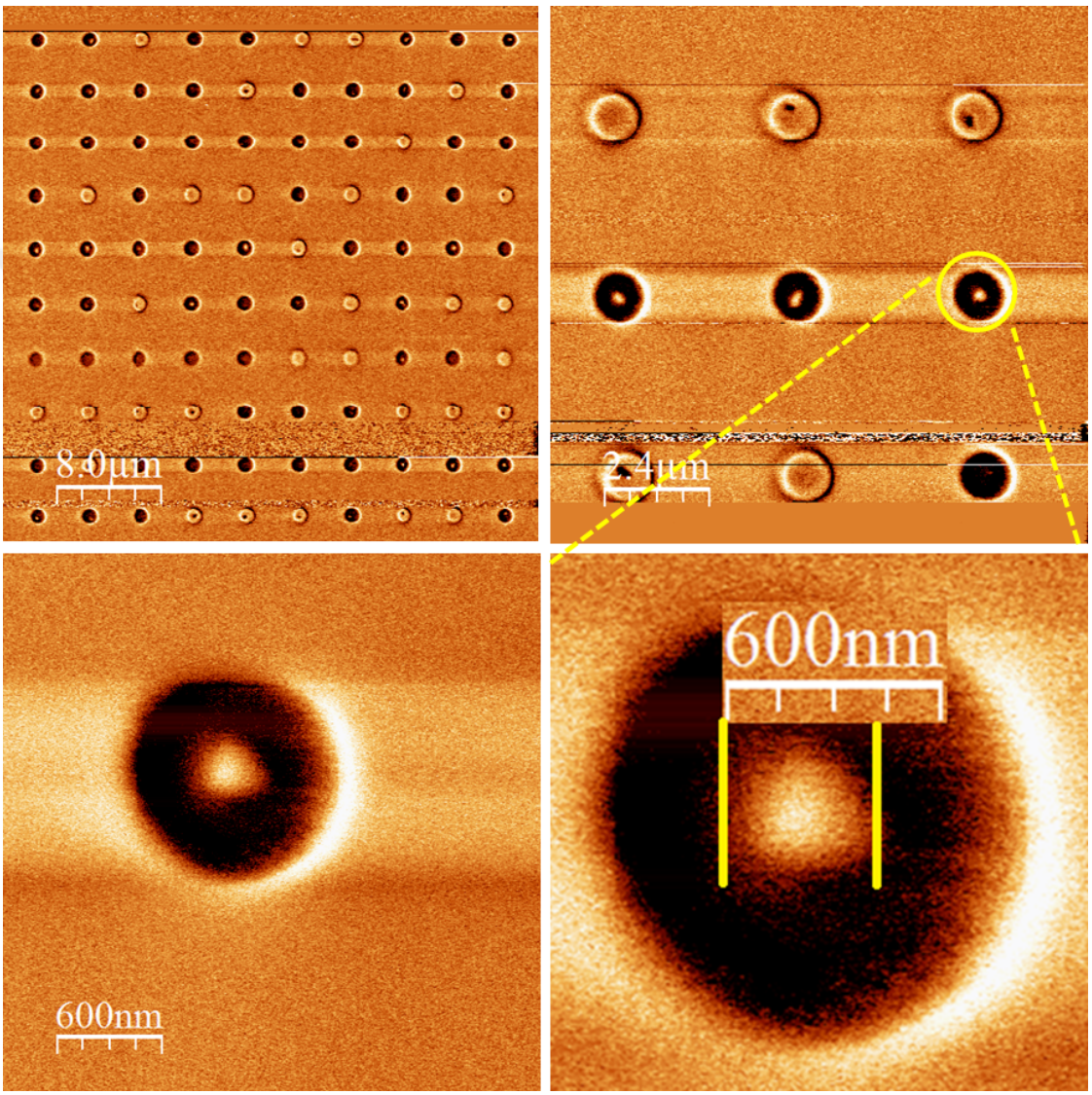


Figure 4.39. MFM images for 1.0μm dot size after 6950 Oe Hmax AC in-plane external magnetic field demagnetization.

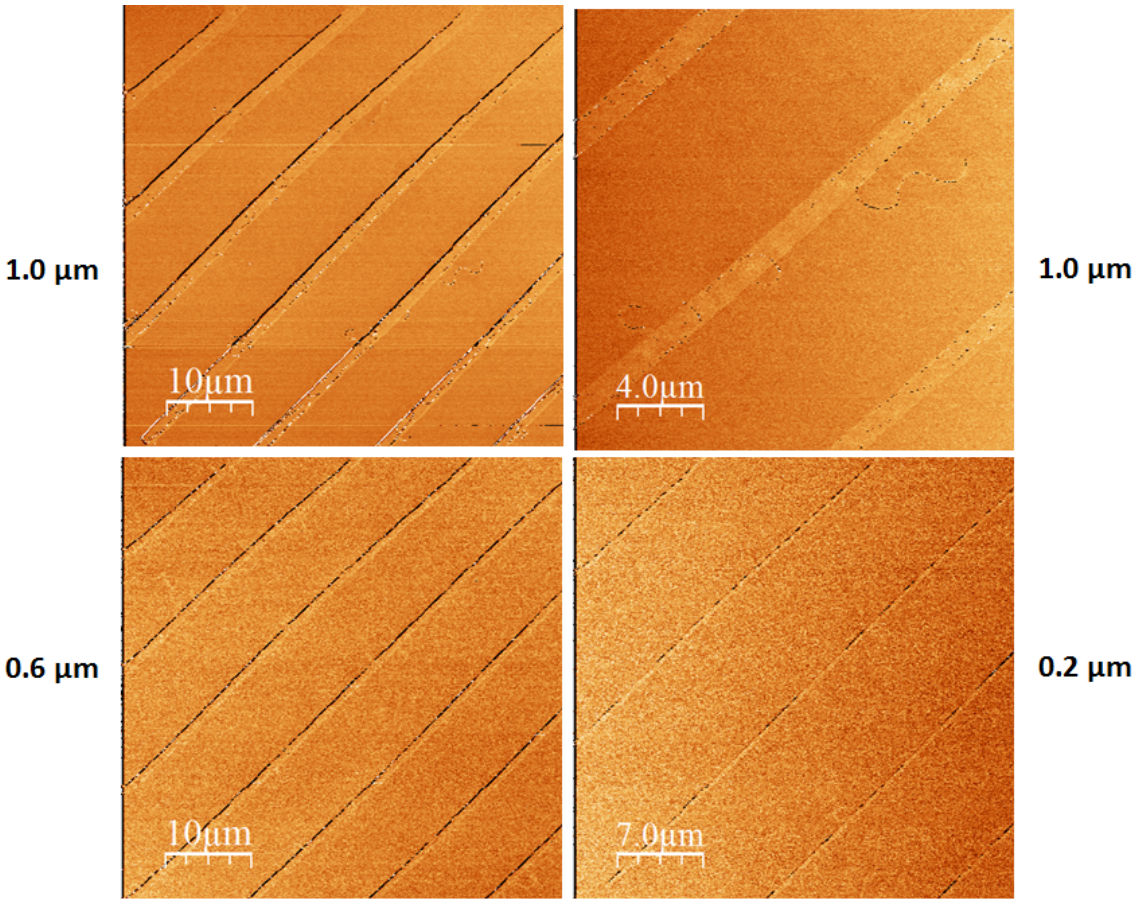


Figure 4.40. MFM images for different width wires after 6450 Oe Hmax AC in-plane external magnetic field demagnetization.

4.3. Fabrication of Nano-Micro Contacted Wires

By using thin films Ta(5)/Pt(10)/$[Co(0,2)/Ni(0,6)]_8$/Co(0.2nm)/Pt(5nm), nano-micro wires with different widths, changing from 800 nm nm to 1.2μm were fabricated to investigate bubble motion with induced current in the presence and absence of out of plane external magnetic field. The electron-beam lithography, evaporation, Ion mill etching systems available in the clean room of the University of Lorraine were used for the patterning process.

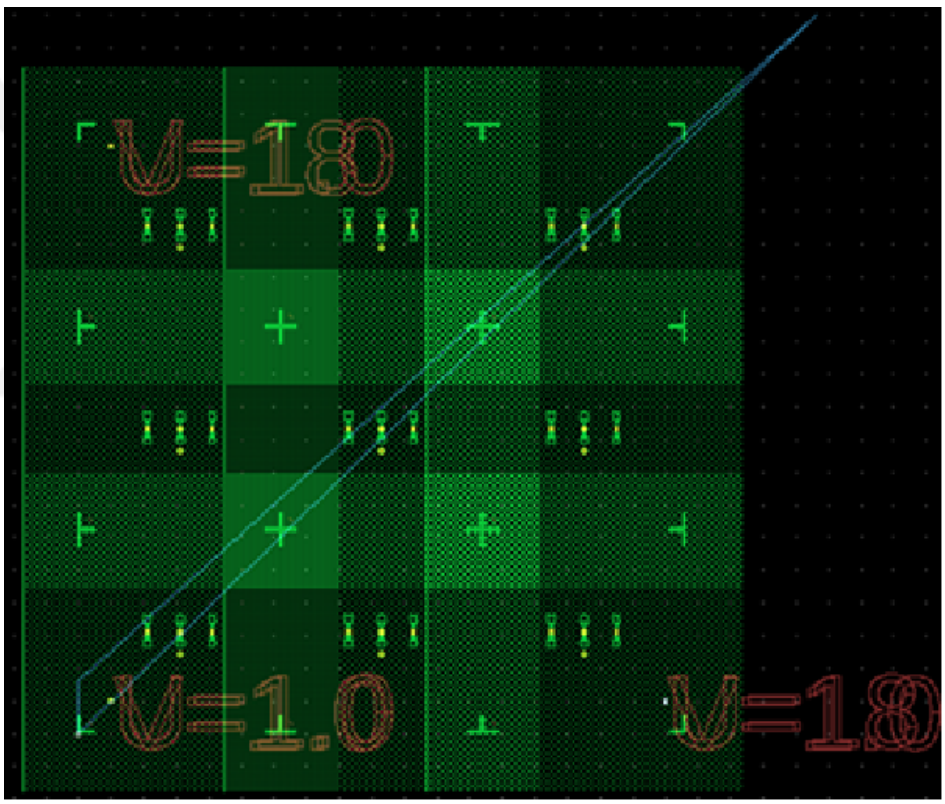


Figure 4.41. The contacted wires Layout editor design.

Figure 4.41 shows the contacted wires design from layout editor program. Each set has three contacted wires and the set is arranged with a same distance between each other. First, a thin film Ta(5)/Pt(10)/$[Co(0,2)/Ni(0,6)]_8$/Co(0.2nm)/Pt(5nm) is deposited onto a full 2x2 inch Si substrate with magnetron sputtering method and contacted wires were patterned quarter of deposited full 2x2 inch Si substrate. In every set, there are 800 nm, 1000 nm and 1200 nm-contacted wires. Totally, we have

26 contacted wires and the length of the wire is $20\mu m$. The most important issue in this patterning is aligned E-beam lithography. Because, there are wires and on top of them, gold (Au) contacts are deposited after aligned E-beam lithography.

The used method for Ta(5)/Pt(10)/$[Co(0,2)/Ni(0,6)]_8$/Co(0.2nm)/Pt(5nm) nano-micro contacted wires is ion milling process. The patterning procedures are listed as the following.

(i) The thin film was first deposited on the Si substrate. Then for contacted wires fabrication, quarter of deposited full wafer was used.

(ii) Then it was coated with totally 270 nm MMA/PMMA (bilayer resist) by spin quoting and heated to 180^0C.

(iii) Then, the electron beam lithography is used for the defined small markers around wires and global alignment markers.

(iv) For developing step, MIBK solution is used to remove exposed regions.

(v) Following E-beam lithography, the sample was placed into the evaporator system for Ti (10 nm) and Au (50 nm) evaporation. Ti is used as an adhesion layer and Au is for markers due to high contrast to see in aligned E-beam lithography.

(vi) This process was followed by lift-off (NMP solvent, 60^0C) to remove PMMA resist from the surface sample (not exposed regions).

(vii) For second procedure to pattern wires and markers, again it was coated with totally 270 nm MMA/PMMA (bilayer resist) by spin quoting and heated to 180^0C.

(viii) Then, aligned E-beam lithography was used for wires and other alignment markers.

(ix) For developing step, MIBK solution is used to remove exposed regions.

(x) Following aligned E-beam lithography, the sample was placed into the evaporator system for coating 40 nm Al on top of the sample by using electron beam evaporation.

(xi) This process was followed by lift-off (NMP Solvent, 60^0C to remove PMMA resist from the surface sample (not exposed regions).

(xii) The next step was ion milling to pattern. In this step, wires and second markers are patterned.

(xiii) The patterning process was completed after chemical etching with the TMAH solution to remove the remaining Al layer. Figure 4.42 shows the wire and markers around wire.

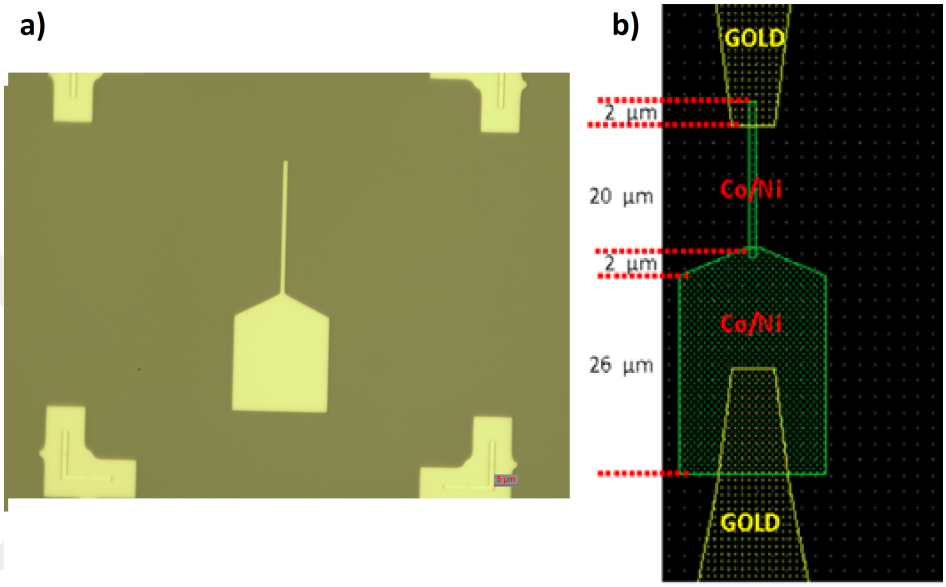


Figure 4.42. Optical microscope image of wire and markers after patterning process and dimension of wire.

(xiv) After patterning of wires, the next step was to place Au contacts on top of the wires. For this step, again, it was coated with totally 270 nm MMA/PMMA (bilayer resist) by spin quoting and heated to 180^0C.

(xv) Then, aligned electron beam lithography was used for contacts, sample numbers (this is for separation of samples after cutting the wafer) and big markers for cutting the wafer.

(xvi) Following E-beam lithography, the sample was placed into the evaporator system for Ti (10 nm) and Au (50 nm) evaporation. Ti is as an adhesion layer and Au is for markers due to high contrast.

(xvii) This process was followed by lift-off (NMP solvent 60^0C) to remove PMMA resist from the surface sample (not exposed regions). Figure 4.43 shows the contacts, wires and alignment markers.

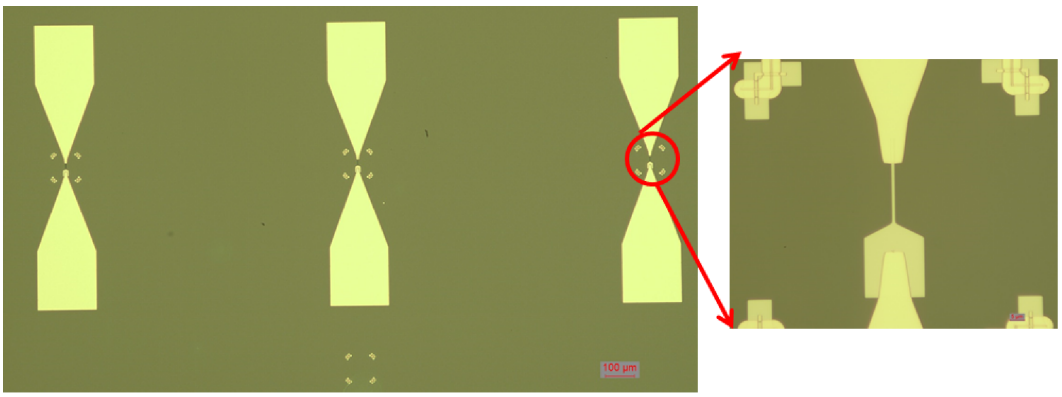


Figure 4.43. Optical microscope images of wires, contacts and markers after patterning process.

To see the whole pattern in E-beam lithography system, Figure 4.44 shows the all patterns (contacts, wires, global alignment markers, alignment markers, cutting markers, names of set of the samples).

4.4. Bubble Motion Induced By a Current Pulse Experiment Results

Before starting bubble motion with induced current pulse experiment, first I needed to nucleate bubble on the wire through AC in-plane external field demagnetization. For this purpose, I tried to find better demagnetization field value. I obtained good bubbles formation condition for this experiment in 5560 Oe H_{max} AC in-plane external field demagnetization. Because we do not want to have a lot of bubbles on the wire, we need just few bubbles to observe clearly any motion on them.

Before placing the sample into the MFM system, first sample, which has three wires, one set, was mounted on the sample holder then with Al wire, wire bonding on the contact of 0.8 μm wire because this wire has very good bubbles distribution on the wire as seen in Figure 4.45. To start experiment, we need to know whether the tip is good for this experiment or not. We used Asylum LM tip with frequency range 40 – 100 kHz and C (N/m) 0.5- 4.4. Even tips in the same box have different properties and we checked tip after mounting into the system to see whether the tip damages

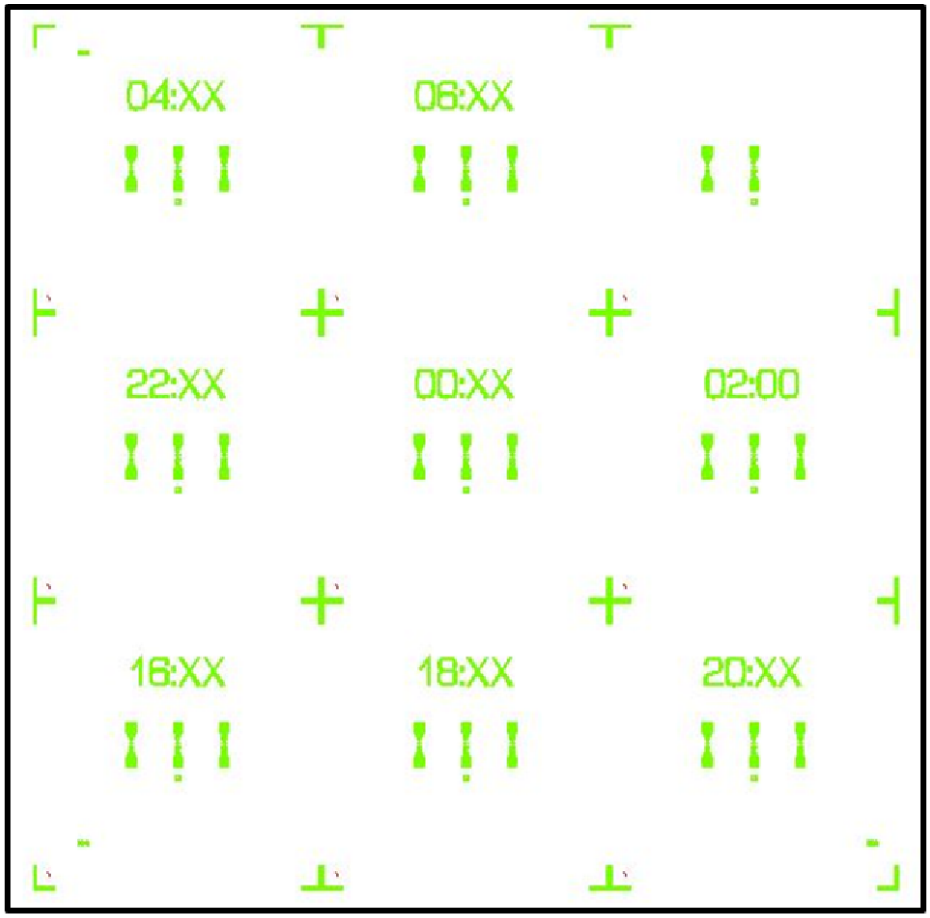


Figure 4.44. Image of wires, contacts and markers in the E-beam Lithography system.

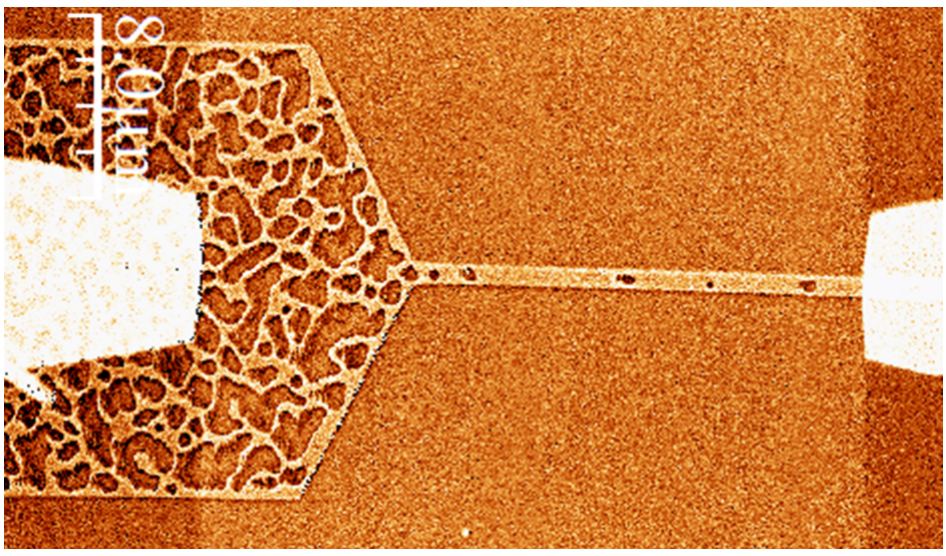


Figure 4.45. MFM Image of 0.8 μm wire. Bubbles are clear on the wire.

the bubbles or not, because the bubbles are very sensitive against any kind of external magnetic force. First, we checked this while scanning reservoir of the wire. In the first bubble motion with induced current pulse experiments were made under zero external magnetic field. In the second time, we applied out of plane external field, while sending current pulses (I will give detail with experiment results in the second part).

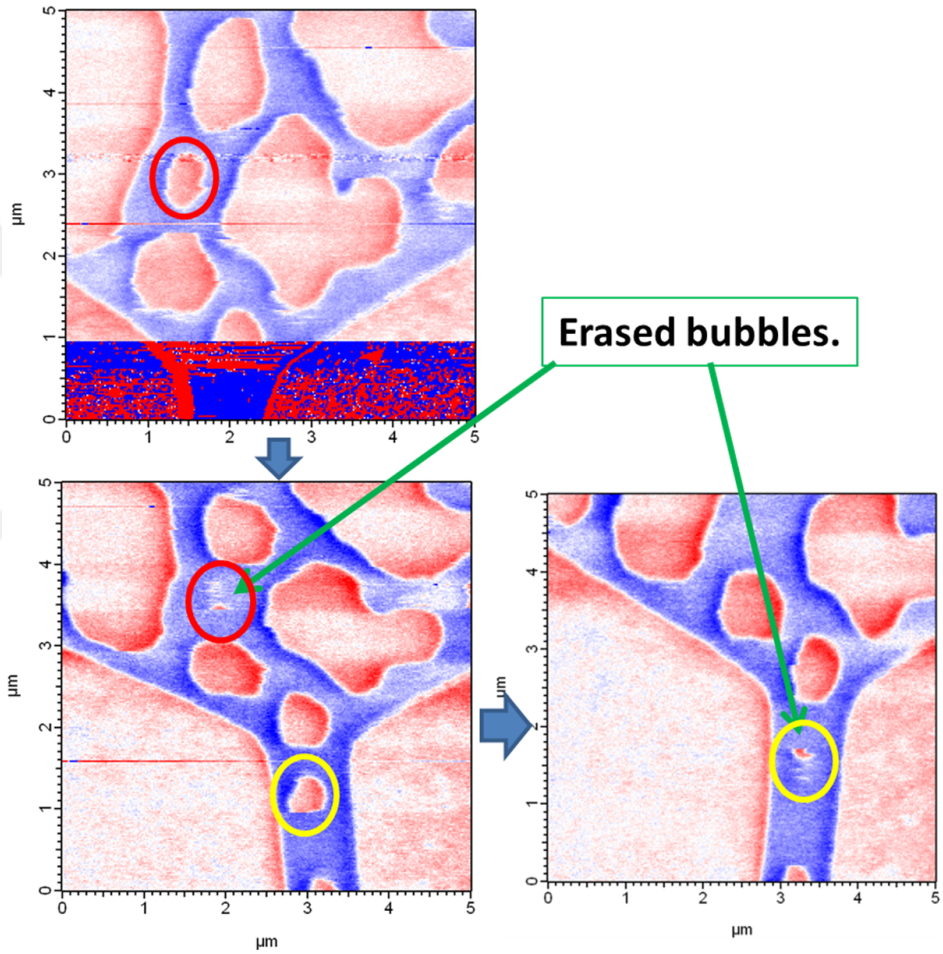


Figure 4.46. MFM Images of 0.8 μm wire. Bubbles are vanishing due to tip moment.

In Figure 4.46, we can see that a tip destroys bubbles and due to this, we changed tip and again we tested it in reservoir and when the tip did not change, we start to scan the wire to obtain initial case for comparison when there is a motion in bubbles positions.

4.4.1. First Experiment Results

Figure 4.47 is the initial MFM image and bubbles are clear. Here, red color and blue color correspond the magnetization directions into the surface and out of the surface, respectively.

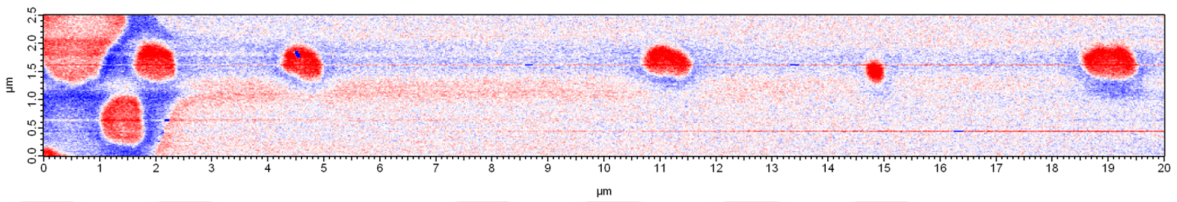


Figure 4.47. MFM Images of 0.8 μm wire. Bubbles are vanishing due to tip moment.

Before starting current pulse experiment, we applied 1 mA and -1 mA to find resistance of the wire and we calculate the resistance of wire as 270 Ω. We started with 1 V 200 ns pulse width, 1 pulse, current I = 3.7 mA and current density J = 1.75 10^{11} A/m^2 . After that, we increased the pulse amplitude, pulse width and numbers of pulses that we applied. For example, with 1000 pulse 3 V 1 μs pulse width, current I = 11.1 mA and current density J = 5.3 10^{11} A/m^2. There is no change in the bubble positions and shape. We can see in Figure 4.48.

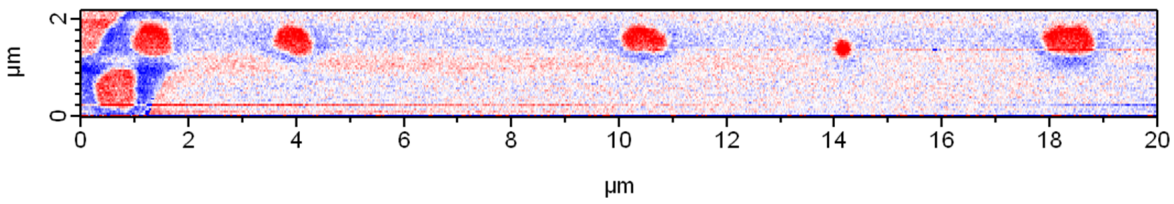


Figure 4.48. MFM Image of 0.8 μm wire after applying 1000 pulse 3 V 1 μs pulse width, current I = 11.1 mA and current density J = 5.3 10^{11} A/m^2.

We continued to increase the pulse amplitude and numbers of pulses and we observed annihilation of bubble after applying 1 pulse 4.4 V 1 μs pulse width, current I = 16.3 mA and current density J = 7.7 10^{11} A/m^2. In Figure 4.49 we can see the pulses and annihilation of bubble. During this experiment, we took MFM images after

applying current pulse(s) and we can see the current pulses and MFM after them in Figure 4.49.

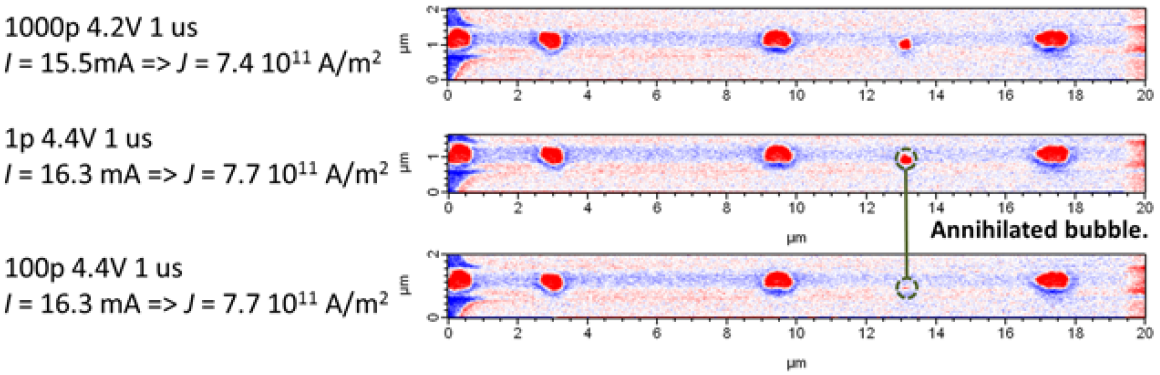


Figure 4.49. MFM Images of 0.8 μm wire after applying three different pulses and annihilation of bubble.

Beside annihilation of bubble, there is no change in the other bubbles and we could not observe any change in bubble position. Therefore, we continued to increase the pulse amplitude and we observed a small change in the size of the bubble in the middle of wire at 1 pulse 7 V 1 μs pulse width, current I = 25.9 mA and current density J = 12.3 10^{11} A/m^2. After this, when we applied same current pulse but 100 pulses, whole track turned into the two long stripes and we lost out bubbles. We can see this in Figure 4.50.

To continue the experiment, we need bubbles in the wire, therefore, without taking the sample out to put new sample, we tried to nucleate bubble with current pulse. For this process, first we used a magnet to magnetize the wire and we can see in the first of Figure 11. We took a MFM image after magnetization. Then, we applied 10000 pulse with 10 ms time difference between pulses 7 V 1 μs pulse width, current I = 25.9 mA and current density J = 12.3 10^{11} A/m^2. We used the same pulse, because this pulse made same change in the bubbles. After current pulse, when we took MFM image, we managed nucleation of bubble with current pulses. We can see clearly, in Figure 4.51. After nucleation bubble, we decreased the pulse width to 200 ns to avoid any destruction in the bubbles.

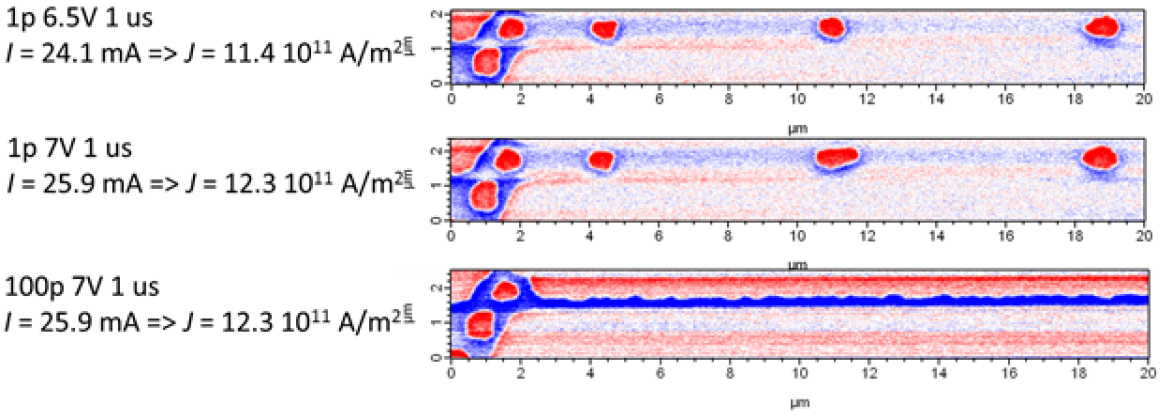


Figure 4.50. MFM Images of 0.8 μm wire after applying three different pulses, changing in the size of the middle bubble and later domains.

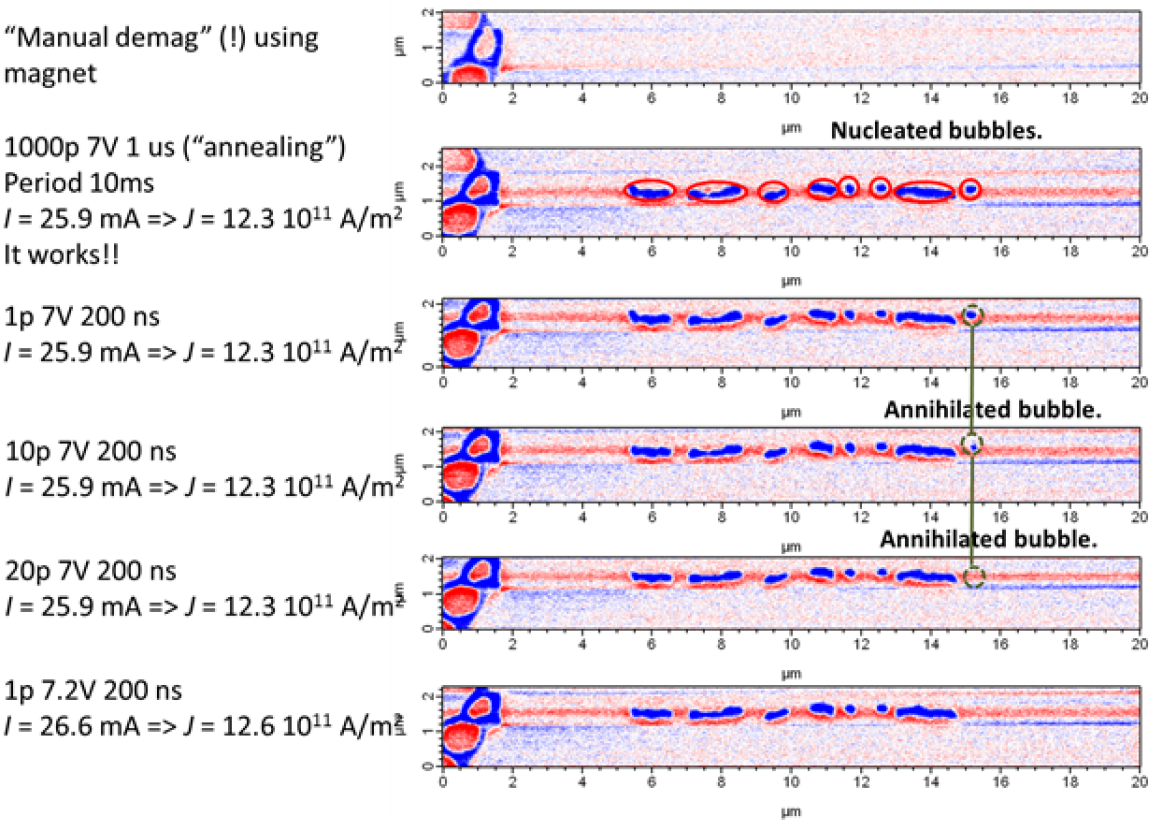


Figure 4.51. MFM Images of 0.8 μm wire after applying different pulses. Nucleation and annihilation of bubbles with current pulses are observed.

However, again with current pulse, we observed bubble annihilation, no bubble motion. Therefore, we increased the pulse amplitude and decreased the pulse width and we observed bubble nucleation with pulses. Figure 4.52 shows bubble formations and the interesting thing is that, some bubbles nucleated with current pulses are very small and their sizes around at most 100 nm, especially in the 1 pulse 8.2 V 100 ns pulse width, current I = 25.9 mA and current density J = 12.3 10^{11} A/m^2. After this, to see that, this process is reversible or not, we send negative current pulse, and we destroyed almost all bubbles and we obtained two long stripes and there are small bubbles in the red domain region.

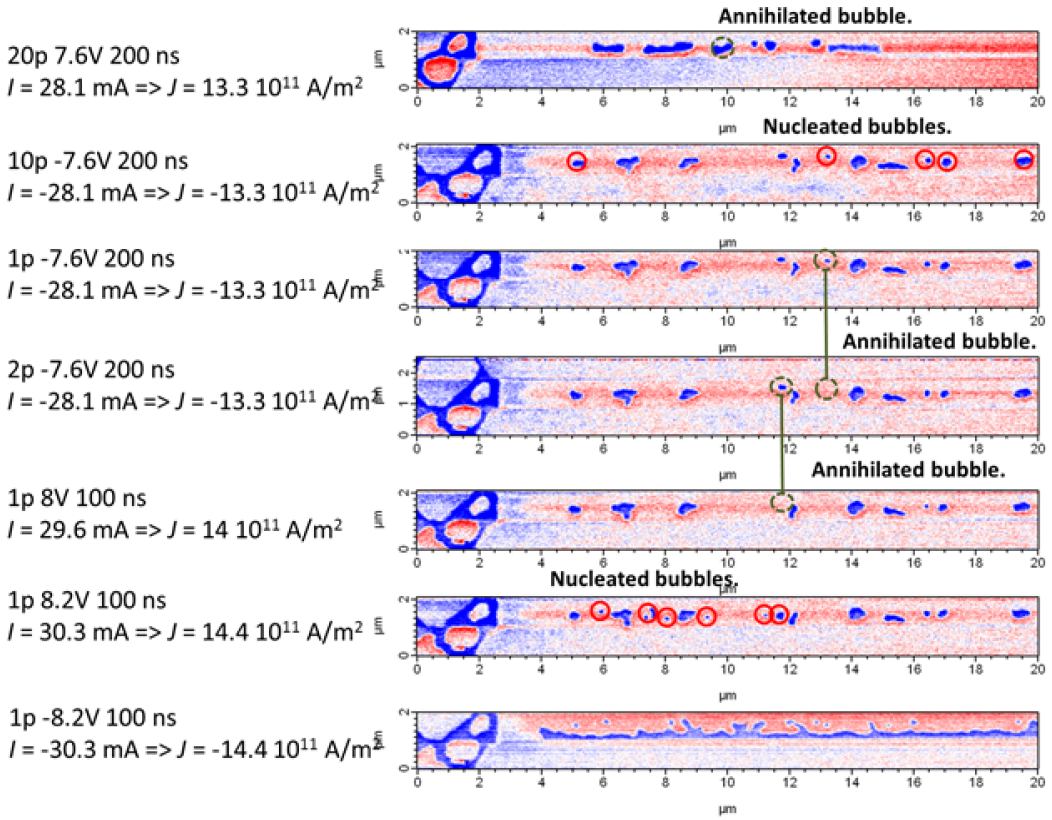


Figure 4.52. MFM Images of 0.8 μm wire after applying different pulses. Nucleation and annihilation of bubbles with current pulse are observed.

4.4.2. Second Experiment Results

From first experiment, I set the system according to first initial setup and measured resistance of wire as 265 Ω. However, when we started applying current pulses

and taking MFM after that, we observed that we are erasing the bubbles even at very low current amplitude. Figure 4.53 shows MFM images of initial state before sending current pulse and after one current pulse sending.

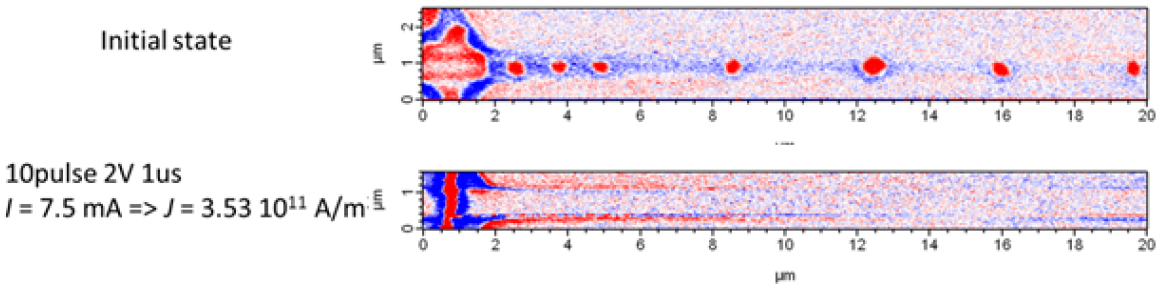


Figure 4.53. MFM Images of 0.8 μm wire after applying current pulse and annihilation of bubbles.

For this, we checked the tip whether the tip destroys or not the bubbles without any external magnetic field. In Figure 4.54, we can see tip destroyed the bubble in even reservoir of the wire.

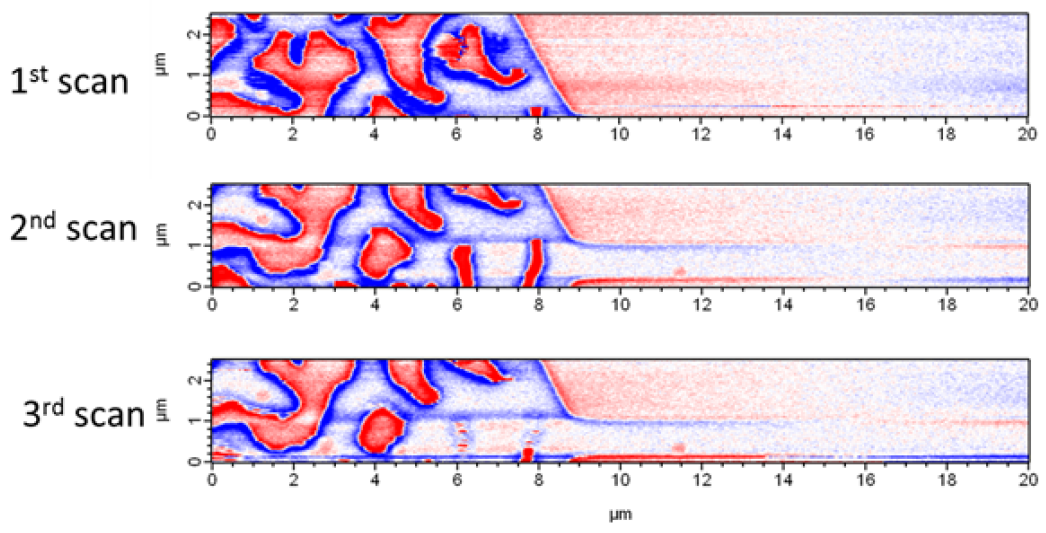


Figure 4.54. MFM Images of 0.8 μm wire to check tip, annihilation of bubble are observed in reservoir.

We observed erasing bubble with tip in many samples. While looking for the reason for this, we controlled the out of plane external magnetic field of the MFM

system. And field is the fundamental reason for this. Even if at very low magnetic field amplitude, bubbles are getting unstable and with magnetized tip and they are annihilated. Therefore, before mounting sample into the system, we checked the field value and first we scan wire without applying any current pulse to observe that tip does not erase the bubbles. We measured the resistance of wire as 227 Ω. In Figure 4.55, we can see MFM images to test tip and sample. In previous samples, we used 0.8 μm wires and then, for next experiment, we mounted of 1.0 μm wire. After future current experiments we used of 1.0 μm wire.

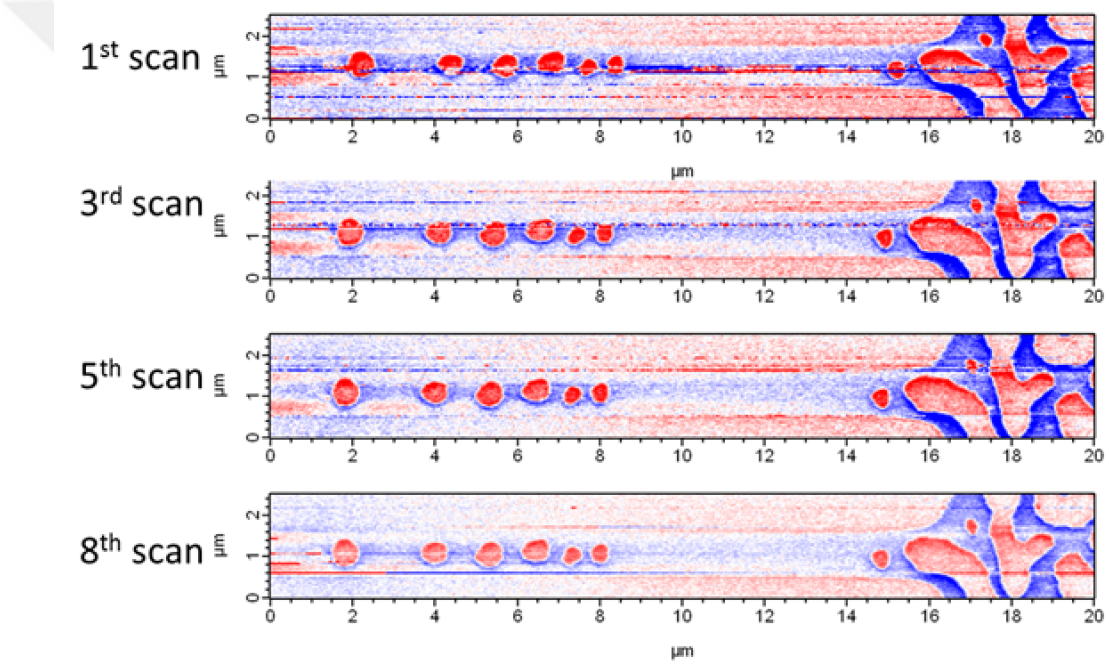


Figure 4.55. MFM Images of 1.0 μm wire to check tip.

After testing tip and sample, we started to apply current pulse for bubble motion on the wire. In Figure 4.56, we can see the applied current pulses and MFM images after current pulses. We observed enlargement of the bubbles on the wire and then destruction of the bubbles.

For the next experiment, we tried to nucleate bubble with current pulses. For this purpose, first I applied 292 Oe external magnetic field to saturate with current pulse. We can see this process in Figure 4.57. In first MFM image is saturation of

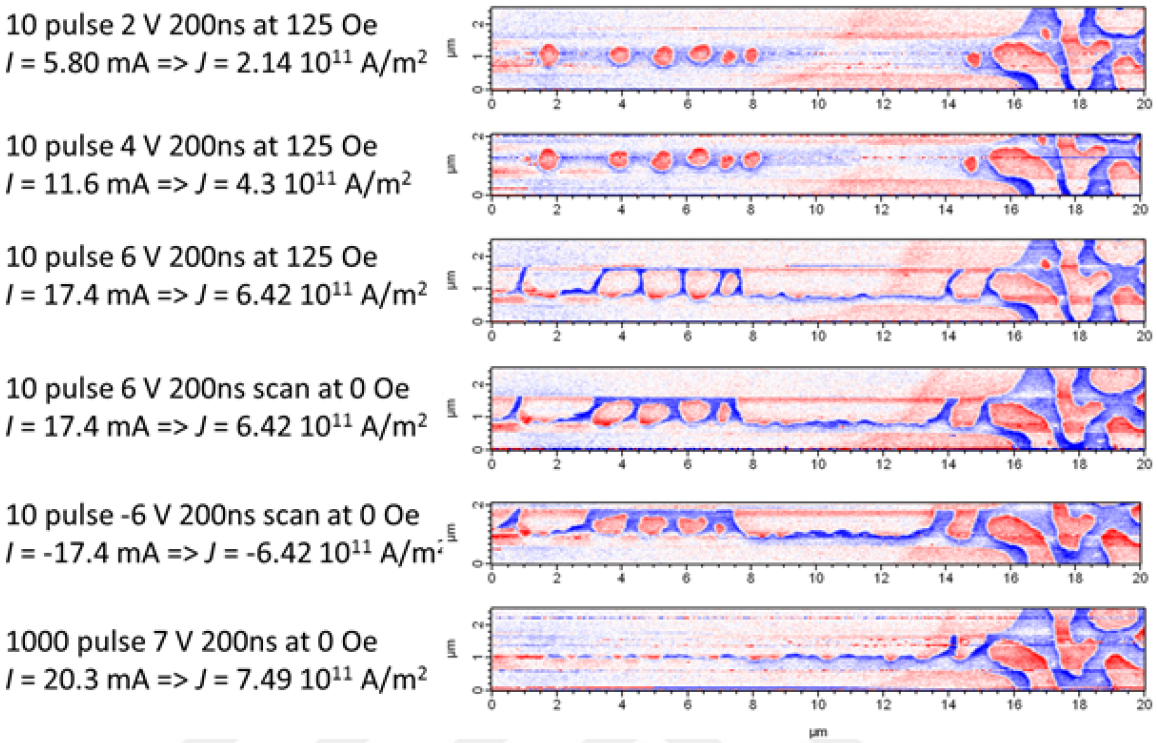


Figure 4.56. MFM Images of 1.0 μm wire after different current pulses.

wire. Then, I set the field -2 Oe for saturation the wire then I applied 10 pulse 7 V 1 μs pulse width, current I = 20.3 mA and current density J = 7.49 10^{11} A/m^2 for bubble formation. After this, I applied the same current at 5 Oe and, in MFM image, we can see the nucleated bubbles clearly in Figure 4.57. After bubble formation with current pulses, we continued the experiment.

To understand external magnetic field effect on the bubble motion with current pulse, I applied different current pulses under different external magnetic fields. We can see this in Figure 4.58, clearly. With increasing external magnetic field, we observed enlargement of bubble with the 10 pulses 6.5 V 500 ns pulse width, current I = 18.9 mA and current density J = 6.96 10^{11} A/m^2. After increasing the number of current pulses, we observed bubbles enlargement and combined of two magnetic structures (bubble and long magnetic configuration). After increasing external magnetic field value and current pulse amplitude, we observed enlargement of bubble and then, destruction of all bubbles. After then, we obtained big magnetic domains and we lost our bubbles. We

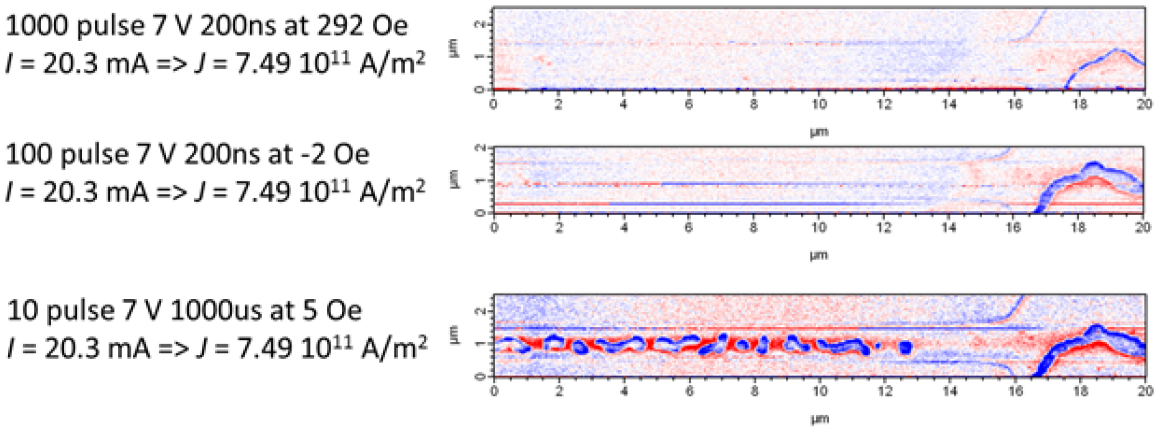


Figure 4.57. MFM Images of 1.0 μm wire to nucleate bubble with current pulse.

can see this in Figure 4.59. We cannot observe any bubble motion with current pulse under absence of and presence of external magnetic field. We applied very low field value because the bubbles are very sensitive against field and we took into consideration of the magnetization direction of bubbles and fields.

4.5. Bubble Motion Under In-plane External Magnetic Field in a Dot

To understand bubble motion under in-plane external magnetic field in a dot, we conducted an experiment to investigate. First, we had to find a very clean dot to prevent any contribution or side effect coming from defects or particles on the dot for magnetic configuration. We mounted the sample into the MFM system in which we can apply in plane or out of plane external magnetic field. We repeated the experiment again after first experiment results, because we wanted to observe that the results can be reproducible or not for different dots.

4.5.1. First Experiment results

After mounting the sample in to the MFM system, we took MFM first at zero in-plane external magnetic field to compare the MFM results with initial case. In Figure 4.60, we can see initial bubble in dot.

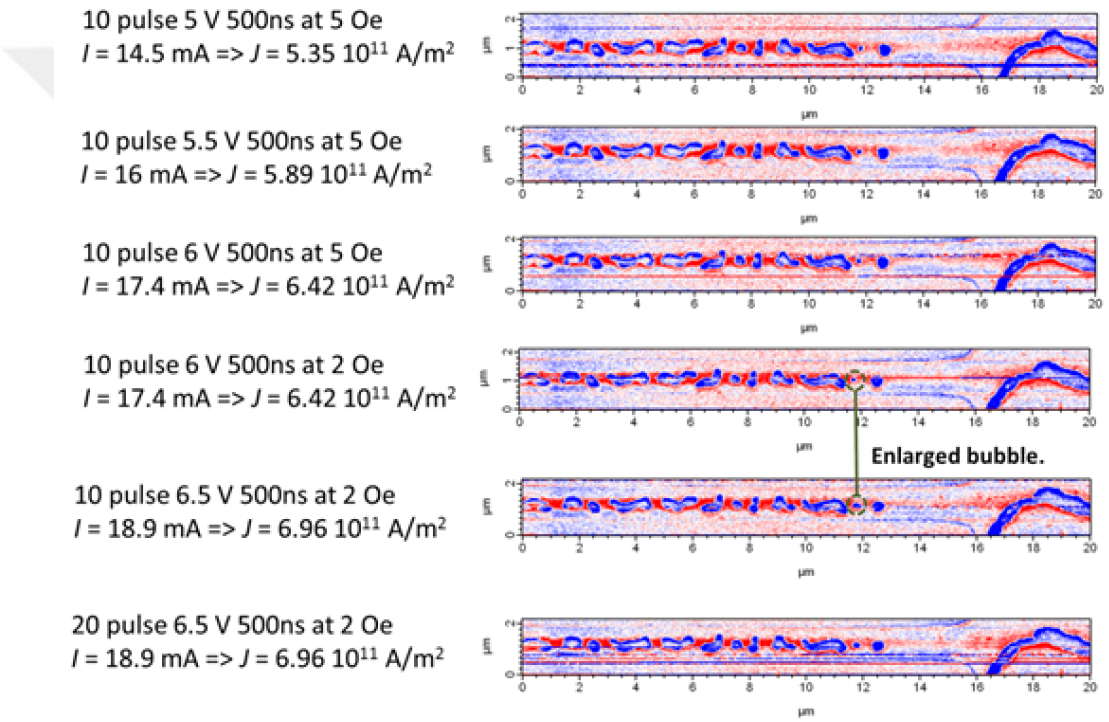


Figure 4.58. MFM Images of 1.0 μm wire after different pulses, and enlargement of bubbles.

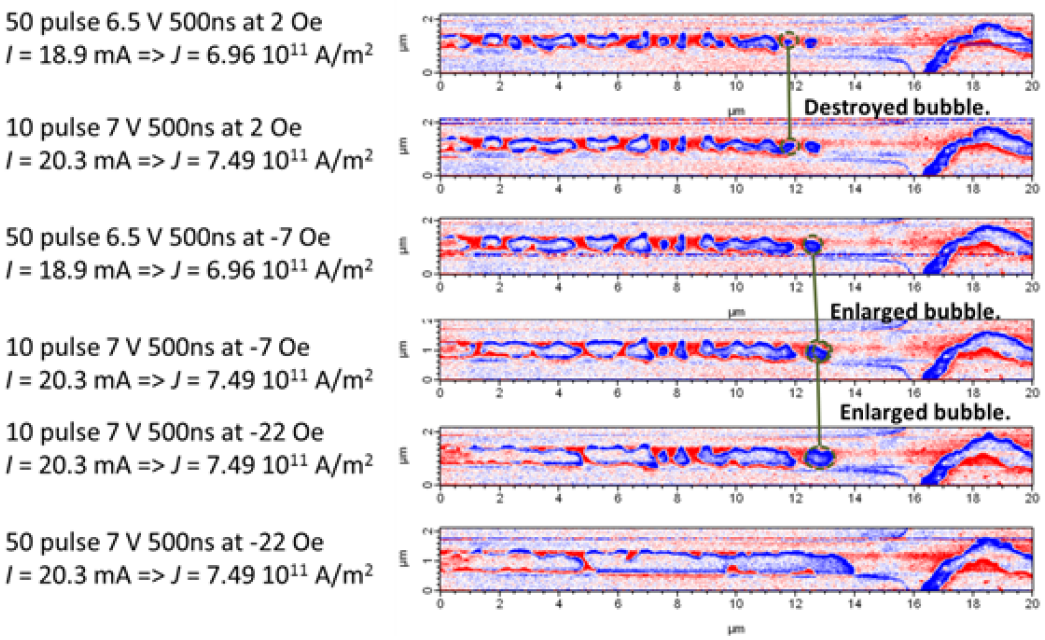


Figure 4.59. MFM Images of 1.0 μm wire after applying different pulses and, enlargement and destruction of bubbles.

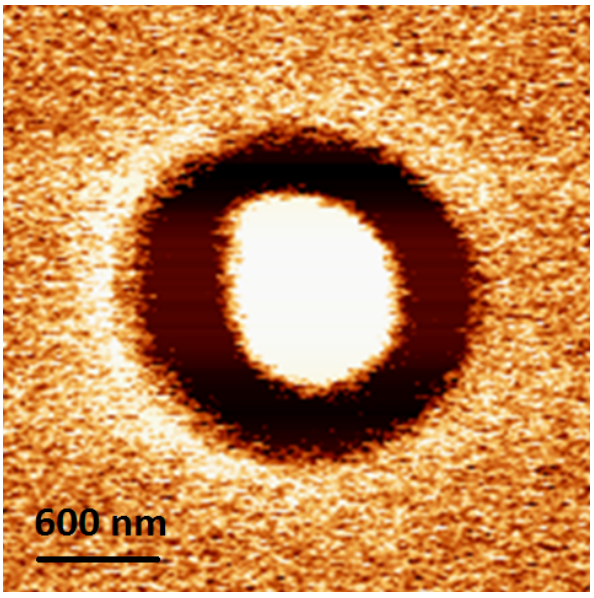


Figure 4.60. MFM image of 1.5 μm bubble in dot for initial case.

From zero field value, we started to increase the in-plane external magnetic field with 5 Oe step and at every increment of field value, we took MFM images to observe the bubble motion in dot with field. However, before increasing the field a lot, first we tried to apply the field from zero to 100 Oe then decreased to –100 Oe to observe whether there is a change with field value for initial case. Figure 4.61 shows the MFM images of dot at zero field value. Figure 4.61a is initial MFM image of dot at zero field and Figure 4.61b is MFM image of dot while passing from the zero field again. As you can see from Figure 4.61, even at zero fields, bubble shapes are different. The difference may come from the pinned points around bubble domain wall.

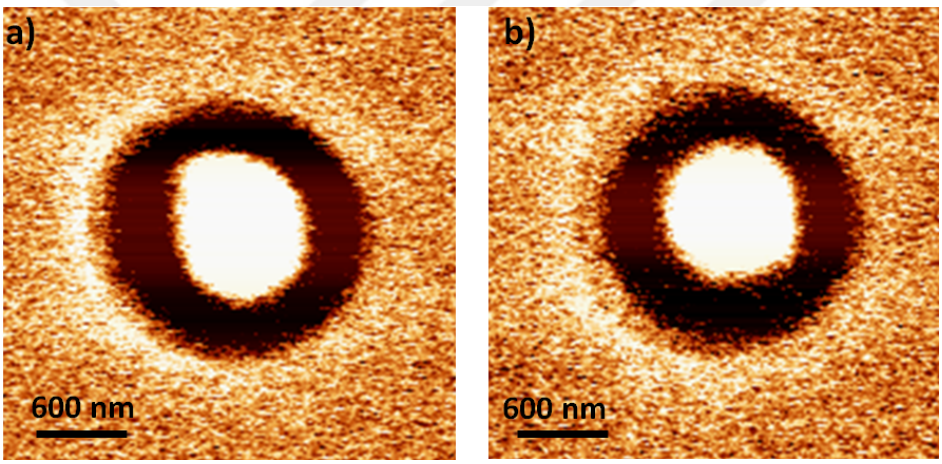


Figure 4.61. MFM images of 1.5 μm dot at zero fields.

It is clear to see the changes in the bubble shapes with field values, as can be seen in Figure 4.62. We observed very small changes in the bubble shapes. In some field values, just 5 Oe change is enough to cause change in the bubble shapes, in some values big field difference is necessary to see the change. In Figure 4.62, we can see this clearly. There are some disappearing deep and peak regions on the bubble shapes.

After that, we increased the magnitude of the in-plane external magnetic field up to -1600 Oe to see change in the bubble shape. In Figure 4.63, we can see the magnetic field value that MFM image started to change with increasing field. Figure 4.63a is the starting point for this, after this value MFM images changed a lot and after -300 Oe magnetic value, we observed starting ying yang like magnetic configuration in MFM

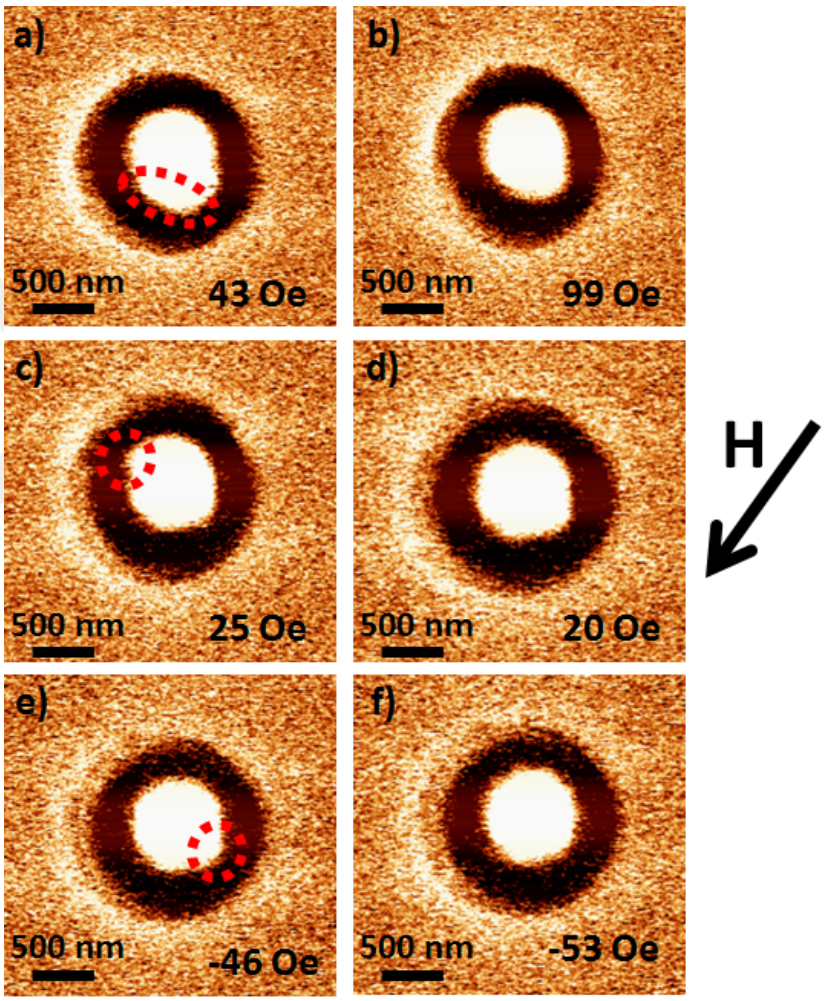


Figure 4.62. MFM images of 1.5 μm dot at different external magnetic field values.

images. In Figure 4.63 f, it can be seen this, clearly.

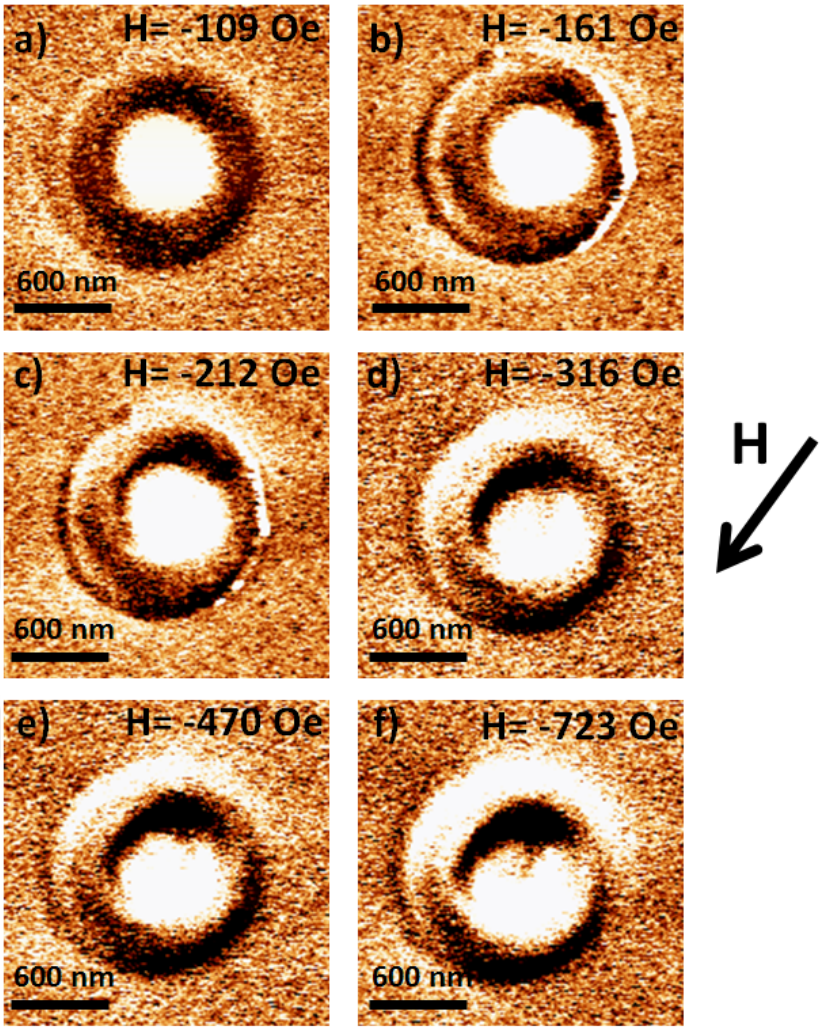


Figure 4.63. MFM images of 1.5 μm dot at different external magnetic field values.

Following observation this MFM images, we continued to increase the amplitude of the in-plane external magnetic field. In Figure 4.64, we can see all of the MFM images from the beginning of bubble shape to last bubble shape before saturation. After -1000 Oe, MFM images changed a lot and it turned to elliptic like shape.

4.5.2. Second experiment results

To understand the MFM images of the bubble in a dot under in-plane external magnetic field, we repeated the experiment to observe that this can be reproducible

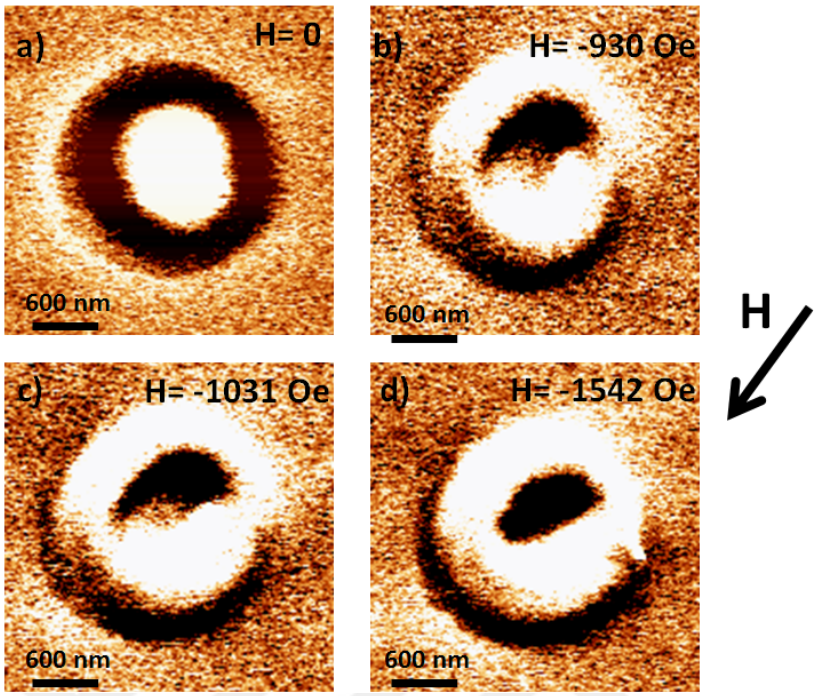


Figure 4.64. MFM images of 1.5 μm dot at different external magnetic field values.

or not. In second experiment, we used two dots instead of one dot to increase the possibility of having same results.

In Figure 4.65, we can see the results of second experiment. In the below one dot there is a small magnetic configuration on the upper side of the dot and it is not important for us, because we want to observe the behaviors of the bubbles in the middle of the dots. In the second experiment, we applied the in-plane field in the positive direction. Actually, for PMA magnetic material, there is not importance of the direction of the field, because field direction and magnetization are almost perpendicular to each other. With 450 Oe, we started to observe the same MFM image and with increasing field value, we obtained ying yang like MFM image around 600 Oe. After increasing the field, we managed to saturate the magnetization of the dots after 950 Oe. When we compared the results of first and second experiments, we can say that the magnetic field values to start observing ying yang like MFM image are different and we think that the initial magnetic structures are not same, also bubbles, and sample-to-sample variation may be another reason for this difference.

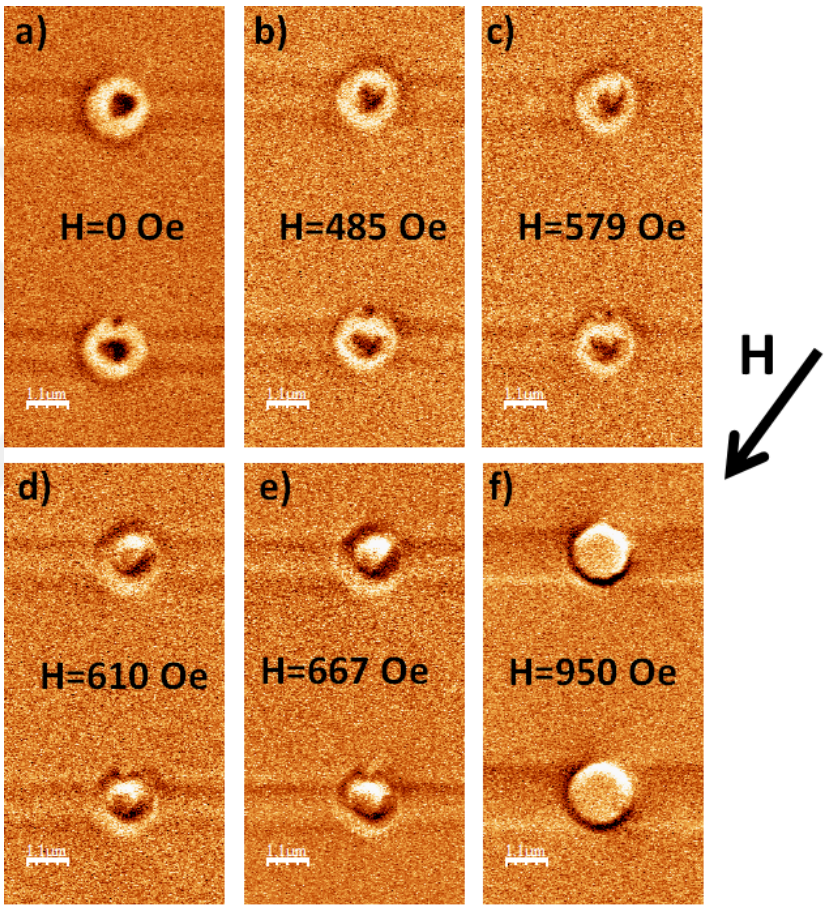


Figure 4.65. MFM images of 1.5 μm dot at different external magnetic field values in second experiment.

In Figure 4.66, we can see the simulation results for z component of the magnetization. From these results, it is difficult to explain the experiment results. Therefore, we conducted the experiment second times that whether first results are correct or not, but second experiment gave the same results as first one.

For a PMA magnetic material and bubble, which has been normally assumed not to have any in-plane component of the magnetization, being affecting with increase in the in-plane external magnetic field is not expected result. Therefore, after doing the same experiment again to other two dots and we observed the same type of behaviors. For this reason, to understand to MFM images and the physics behind the change in the shape of the bubble under field, we made a simulation and from the simulation, we tried to explain the physical mechanism for the MFM images.

To understand MFM images, We performed micromagnetic simulations to comprehend MFM images. Such a numerical study was performed by means of a state-of-the-art home-made solver, which integrates, with a finite difference approach, the Landau-Lifshitz-Gilbert equation:

$$\frac{d\mathbf{m}}{d\tau} = -\mathbf{m} \times \mathbf{h}_{eff} + \alpha_G \times \frac{d\mathbf{m}}{d\tau} \tag{4.2}$$

where $\mathbf{m}$ is the normalized magnetization of the ferromagnet and $\mathbf{h}_{\text{eff}}$ is the effective field, which includes the standard magnetic terms: exchange, demagnetizing, and out-of-plane uniaxial anisotropy. τ is the dimensionless time $\tau = \gamma_0 M_s t$, where γ_0 is the gyromagnetic ratio and M_s is the saturation magnetization of the ferromagnet, and α_G is the Gilbert damping. We simulated a disc of 1.5 μm of diameter, with a thickness of 6.4 nm (n=8 repeats), discretized with 300x300x1 cells of dimensions 5x5x6.4 nm^3. Other parameters were chosen as follows: exchange constant A=1.30x10^{-11} J/m, M_s=840x10^3 A/m, anisotropy constant K_U=6.90x10^5, α_G = 0.03. First, starting from a uniform out-of-plane configuration, we created a non-topological

bubble (skyrmion number zero) by means of a perpendicular-to-the-plane current, including a spin-transfer-torque term into the model. Then, with that bubble as starting point, we calculated the magnetic configuration with an increasing in-plane magnetic field (along y axis).

As the field increases, the bubble gets an enlarged shape along the direction of the field. A non-uniform multi-domain configuration is obtained for fields larger than 350mT, whereas, increasing further the field, the ferromagnet goes rapidly to the in-plane saturation.

In Figure 4.66, we can see the simulation results of z component of magnetization for different in-plane external magnetic field values. However, these results are not matched with the experimental results. At low field value, we have similar bubble shape but for high field values, the results are very different.

For this purpose, first we need to understand MFM images. Therefore first we learned MFM process and the physical mechanism behind MFM imaging. MFM feels the force between the tip and sample magnetization and the tip interacts with the magnetic field produced by the magnetic sample. The energy of this interaction can be defined by

$$E = -\iiint_{tip} \mathbf{H}(r)\mathbf{M}dV \tag{4.3}$$

where $\mathbf{M}$ is the tip magnetization and $\mathbf{H}$(r) is the magnetic field produced by the magnetic sample. The force coming from this interaction is $F = \nabla.E$. To find the force gradient, the equation is $F' = \nabla.F$ From this equation, the force gradient term is the second derivative of the energy originating from the interaction between the tip and material. Therefore, if there is a change in this force gradient, MFM image senses this change and according to change in the force gradient, MFM gives this in the phase

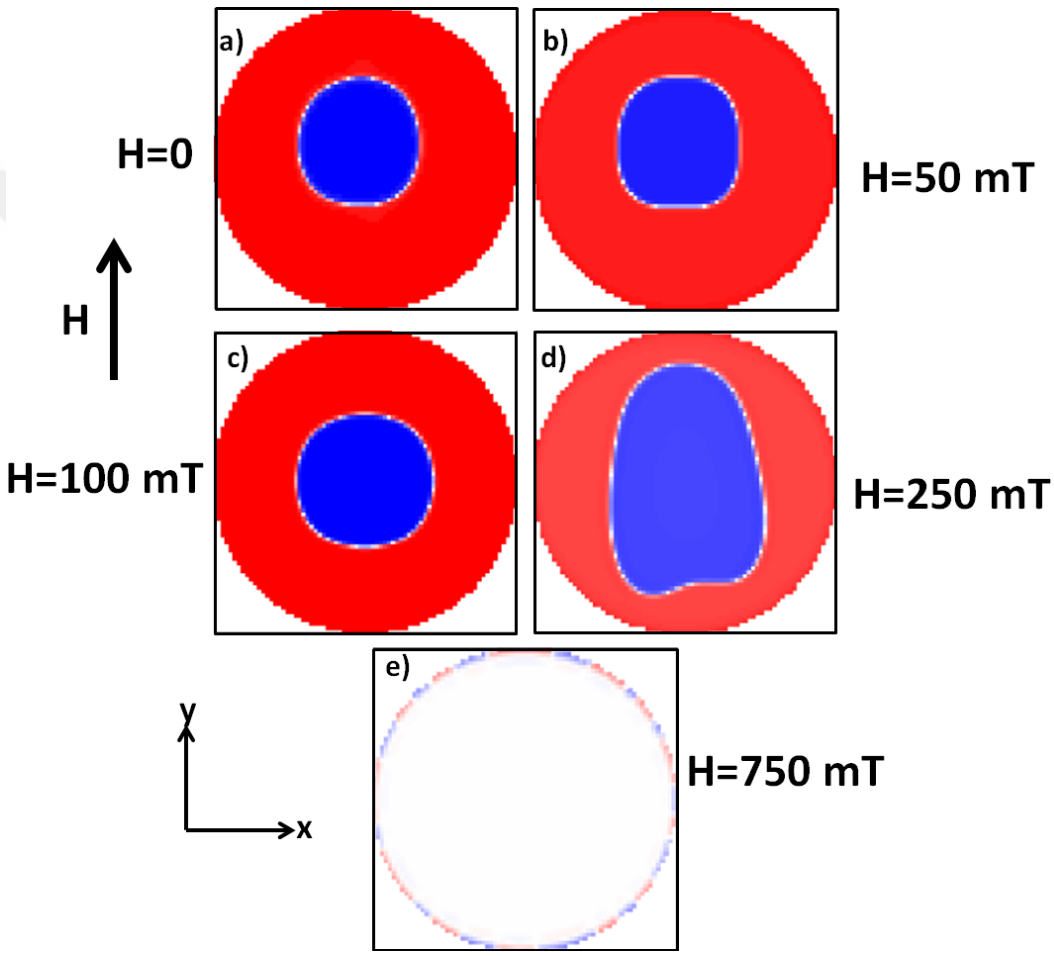


Figure 4.66. Simulation results of z component of magnetization for different in-plane external magnetic fields.

image.

In the simulation, a uniformly magnetized tip is assumed and for degree of the freedom, we define the axis of the tip as z-axis. Therefore, for the force and force gradient, we considered the z-axis. Then, for simulation, we take into account just,

$$F_z' = m_z \frac{\partial^2 H_z}{\partial z^2} \tag{4.4}$$

where m_z is the z component of the tip magnetization and H_z is the magnetic field in z direction originating from the magnetic sample. The reason behind considering just the z-axis is that for a PMA material, the magnetization of the material is almost perpendicular to sample surface and for the tip magnetization after magnetized the direction of the tip magnetization can be taken in z-axis.

In Figure 4.66, we can see the simulation results for the z component of the magnetization and tip magnetization. It is clear that for z component of the magnetization of a PMA material, the MFM images and simulation results are not matched each other for all different in-plane external magnetic field values.

From these simulation results, just taking z component of the force cannot explain the MFM images of the magnetic bubble under in-plane external magnetic field. Therefore, we have to consider the other components of the force between tip and sample. The force gradient can be defined as;

$$F_z' = m_x \frac{\partial^2 H_x}{\partial z^2} + m_y \frac{\partial^2 H_y}{\partial z^2} + m_z \frac{\partial^2 H_z}{\partial z^2} \tag{4.5}$$

where m_x ,m_y and m_z are the x, y and z components of the tip magnetization and H_x, H_y and H_z are the magnetic field components in the x, y and z directions originating from the magnetic sample. For the in-plane components of the magnetization, we took both x and y directions of magnetization but the external magnetic field is in the y direction in simulations and with increase in the external field values, the in-plane components of the magnetization tend to be aligned in the direction of the field. Therefore, the x component of the sample magnetization did not give a proper simulation results. However, for the y component of the sample magnetization we obtained very good simulation results corresponding with the MFM images.

Therefore, we took into account of all components of the magnetization, tilted tip and sample magnetization of the PMA sample. For this case, we made the simulation again and we obtained simulation results very similar to experimental results for different in-plane external magnetic field values. The magnetic field amplitude values do not overlap in the simulation and experiments. The reason behind this is impurities affecting the magnetization of the sample. At high external field, the dot went to saturation situation in both results.

We should not ignore a truth about magnetization of tip and sample that is not fully perpendicular to sample surface. There are tilted magnetizations for both of them, which cause force in the in-plane and with the external magnetic field; the force gradient originating from this force component is dominating the force gradient in the z direction. We can see this from Figure 4.66 and Figure 4.67. For low field values, we have magnetic bubble in MFM images as for z component of the simulation.

When we compare these results with experiment results, they overlap very well together and in Figure 4.68, we can see this clearly. However, in-plane external field values corresponding to images are different each other. For simulation, we observed the change in the image around 50 mT (500 Oe) but, in first and second experiments it is around 400 Oe. However, the image in Figure 5.68d is at 250 mT (2500 Oe) but in first experiment it is around 1500 Oe.

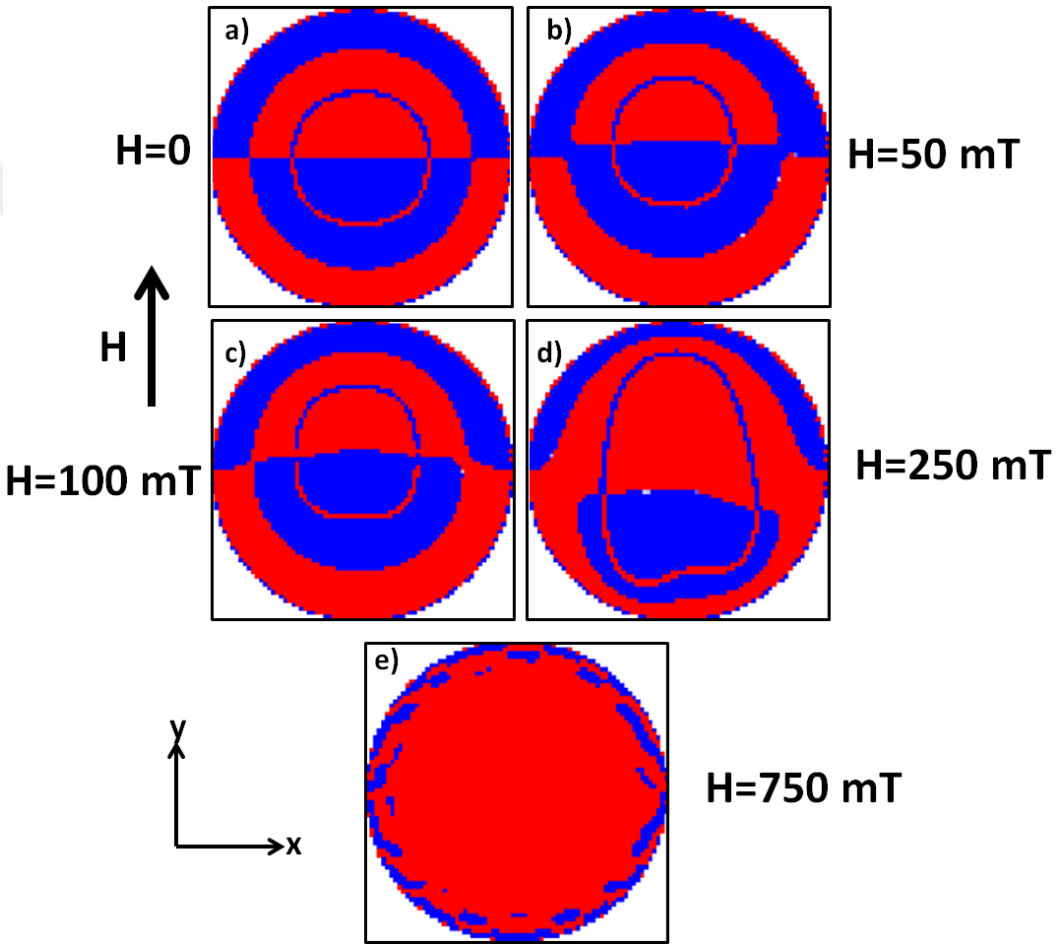


Figure 4.67. Simulation results of second derivative of y component of magnetization for different in-plane external magnetic fields.

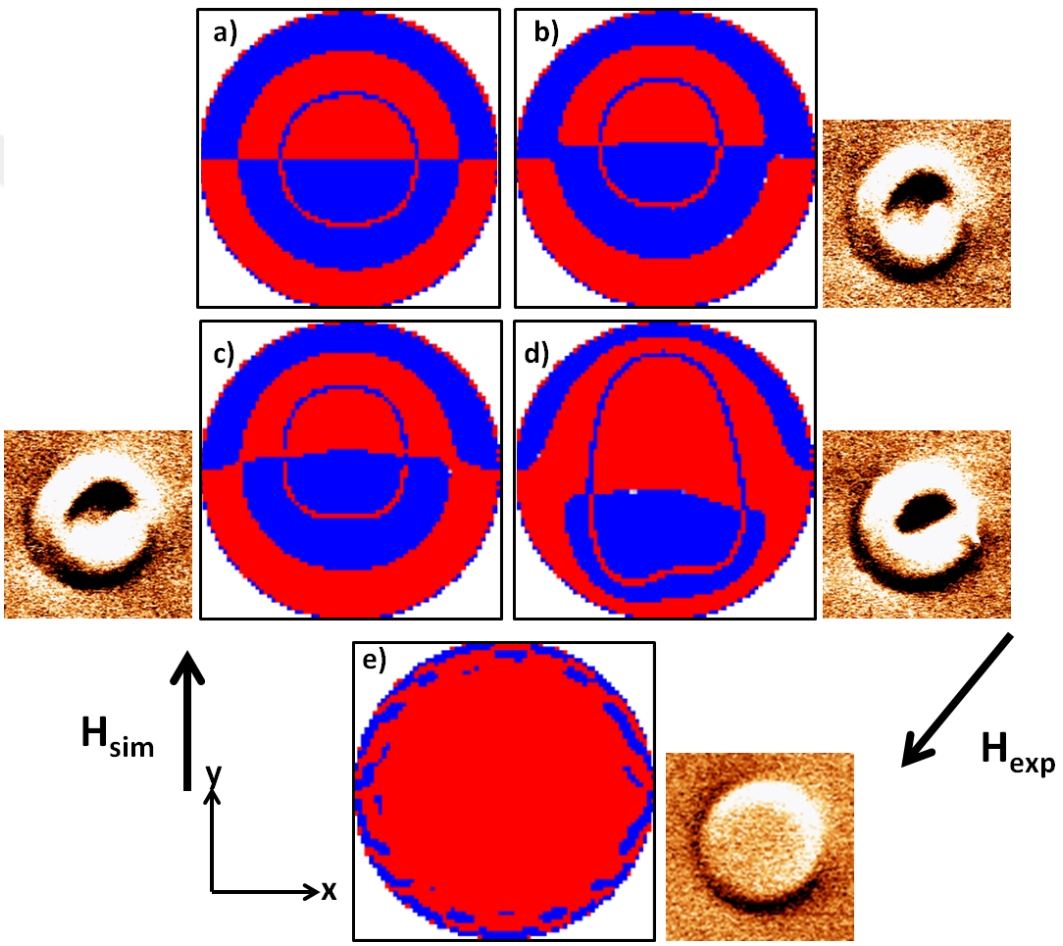


Figure 4.68. Comparisons of simulation and experimental results.

The physical explanation of these results is that both tip and sample magnetization are not fully in z direction and or in both, a little tilted in x or y direction or in both and with in-plane external magnetic field, these components are affected and aligned in the y direction which is the in-plane external field applied direction. Therefore, with external field these components are getting dominant and the force gradient originating from the interaction between these components are stronger with field and we observed this force gradient in MFM measurement. Therefore, we obtained these kinds of MFM images for bubble in a dot under in-plane external magnetic field.

5. CONCLUSION

5.1. Phase Change Memory Study Conclusions

This study aimed to investigate whether a PCM device using a single phase-change layer can have intermediate logic levels, and if there may be an intermediate logic level, determine the programming conditions and investigate the degree of stability of this level. For this purpose:

Three dimensional finite element model was constructed. In the simulations, research was conducted on which physical parameters are important for the square and circular contact PCM devices. For example, we observed that the nucleation rate and the growth rate are important physical parameters affecting the phase change. We have determined that these two parameters change depending on the contact shape. During the fabrication of a cornered contact geometry, the ion damage results in more defects in the square contact, leading to lower nucleation and growth rates.

The requirements for Set and Reset operation of the device were examined with simulations and the widths and amplitudes of the voltage pulses to be used were determined. For this purpose, the simulations showed how resistance values change in the square contact and circular contact depending on width and amplitude of the voltage with resistance maps. These programming conditions were used as starting point in experimental measurements. For example, for a PCM with a circular contact, a reset state was obtained with 1 V voltage amplitude with a 2 ns trailing edge and width of 50 ns. In the experimental measurements, the amorphous state at the $M\Omega$ resistance level was switched to crystalline using a 2 ns voltage-pulse with a 50 ns width with a 1V voltage amplitude.

We also determined how the percolation phenomenon occurs in the device and got a critical crystallization fraction of 35% for the percolation in the device.

Intermediate resistance levels (around $20k\Omega$, $50k\Omega$ and $120k\Omega$) were obtained between the amorphous and crystalline phase resistance values (several hundred Ω for crystal and $M\Omega$ for amorphous), which is a mixture of the amorphous and crystalline phases in the resulting PCM material. This was clearly demonstrated in simulations where the reason for the intermediate resistance levels was heterogeneous phase transitions in the device. We observed both in the simulations and the experiments that the intermediate resistance levels only occur in the square contact PCM device.

When we compared the experimental results with the simulation results, the intermediate resistance level was obtained at similar voltage pulses. (In the simulation, the intermediate resistance was obtained by a voltage pulse of 1 V amplitude with a width of 50 ns for the square contact, an intermediate resistance level of about $100k\Omega$ was obtained with a voltage amplitude of 1.1 V amplitude with a width of 50 ns in the experiment)

When we looked at the stability of the intermediate resistance values in time, we observed that these levels did not change with time. Because, when we looked at the resistance changes of the device in Set and Reset states, there was not much resistance change in the Set state and the Set state was stable but in the case of the Reset resistance values increase with time and it is seen that they are not very stable states. We analyzed this result in the framework of the structural relaxation model. It has been shown from the literature that the ν parameter for the Set state is < 0.01, for the Reset state the value ν parameter is about ~ 0.11 (REFFF). We found that for the Set state ν parameter was 0.0009 and that for the Reset it was 0.107. These results are consistent with the results in the literature. In addition, when we looked at the ν parameter for the intermediate resistance level, we have observed a value of 0.0102, which indicated that the intermediate resistance level was stable.

The resistance drift behavior observed in the reset state of all samples was found to be consistent with the conventional structural relaxation mechanism. The conduction characteristics obtained from sub-threshold I-V measurements reveal thermally assisted hopping of carriers through defect states introduced in the band gap of the

amorphous GST with an initial activation energy of 0.23 eV. The inter-trap distance was estimated to be 5.5-7 nm with an effective trap concentration on the order of 10^{19} $1/cm^3$. The drift coefficients of HRS (0.07-0.1) were strongly temperature dependent due to accelerated annihilation of bulk defects.

We compared the HRS with a stable intermediate state, IRS, with a wide range of programming amplitudes in samples with square contact geometry. Simulations showed that IRS had regions of mixed phase inside the active region of the GST. This region was thought to provide a large inter-facial area between the amorphous and crystalline regions and therefore a smaller amorphous thickness to amorphous-crystalline inter-facial area ratio. Our data suggested that the conduction was through defect states just like the HRS but with a smaller inter-trap distance and a much larger effective defect density, 10^{21} $1/cm^3$. This could be explained by considering the significant contribution of inter-facial defects to the total defect density in the case of a thin mixed phase active layer in IRS.

Furthermore, unlike the bulk defects that annihilate in time increasing the inter-trap distance, the inter-facial defects were found to be stable, yielding at least an order of magnitude decrease in the drift coefficient of the IRS. The residual low drift could still be attributed to the bulk structural relaxation mechanism, which explains the small increase of the drift coefficient with temperature.

We concluded that an intermediate, mixed phase state with a large programming window that was induced in a non-uniform current injection device displays much superior long-term stability compared to the fully amorphous reset state. Current in IRS was dominated by the conduction of carriers through inter-facial defect states which do not anneal away in time. Such a stable set of IRS levels can potentially be utilized in future multiple-bit-per-cell memory technologies that meet the long-term reliability and data stability requirements.

The results of this project were presented in many oral presentations and one poster presentation in four international conferences.

Patent applications have been made following the design of the optimum phase change memory device: (Phase Change Memory for Multiple Data Storage in a Single Cell - Turkish Patent Institute, Application No: 2014/06990)

We published two papers from this study. 1. "Three Dimensional Finite Element Modeling and Characterization of Intermediate States in Single Active Layer Phase Change Memory Devices" (the Journal of Applied Physics 2015) 2."Toward Multiple-Bit-Per-Cell Memory Operation With Stable Resistance Levels in Phase Change Nanodevices" (IEEE Transactions on Electron Devices 63(8):1-6 · January 2016)

5.2. Magnetic Bubble Study Conclusions

In the study, magnetic bubble formation was investigated in nano and micro disks produced from PMA materials. Suitable disk sizes and AC in-plane magnetic field for demagnetization conditions for bubble formation were determined. The results of the bubble formation of the study are as follows:

First, to determine the suitable layer thicknesses for Pt, Co and Ni to obtain PMA thin film, many thin film deposition were done and by measuring their magnetic proprieties through out PPMS-VSM system, we decided the thickness of Pt, Co and Ni in multilayers thin film. Then, thin films with PMA were deposited to observe bubble nucleation: Ta(5)/Pt(10)$[Co(0.2)/Ni(0.6)]_{x8,10,15}$/Pt(5) multi-layer thin films.

After dot arrays and wire patterning for 8 and 10 repeats thin films, we tried to determine proper in-plane AC external magnetic field for demagnetization. We used MFM system to observe magnetic configuration of dot arrays and wires. We applied H_{max} in-plane AC external magnetic field for demagnetization from 3500 Oe to 7000 Oe. But for 6500 Oe H_{max} value, we observed stable single magnetic bubble in dot arrays, especially between 1000 nm and 1500 diameters dot arrays. For other H_{max} values and other dot diameters, most of time, we observed single or multi domains magnetic configurations. From this results, it is clear that there is a diameter dependence for bubble formation in a dot.

For 6500 Oe H_{max} of in-plane AC external magnetic field for demagnetization , we observed as 6%, 31%, and 47% percentage bubble formation in dot arrays with diameters of 1000 nm, 1250 nm and 1500 nm, respectively. Following this results, 6250 Oe H_{max} of in-plane AC external magnetic field for demagnetization, we succeed 70% bubble formation on 1500 nm dot array.

Beside the dot arrays, we also investigated bubble formation in wires. While taking MFM for dot arrays, we took MFM for wires to observe magnetic configuration. For wires, it was same as dot arrays. We observed bubble formation wires 6500 Oe in-plane AC magnetic field for demagnetization condition and also wire thickness dependence. Because, we managed to form bubble in 800 nm, 1000 nm and 1200 nm thickness wires, but other wire (mostly single for thin wires, multi or stripes for thick wires). Especially, for 5560 Oe H_{max} value, we obtained suitable single bubble for bubble motion induced current pulse with or without external field in 800 nm wire.

Compared with the literature, the bubbles written in this way may carry the characteristic of being a magnetic soliton (skyrmion) in the form of domesticated wall structure. These bubbles, which can be moved by magnetic fields or current pulses on the wire without being affected by surface defects, are suitable candidates for magnetic logic circuits and three-dimensional magnetic memory units. Due to their skyrmion they have the potential to move at high speeds with low currents. However, from the wire experiments, we could not manage to move bubbles with current pulses for 800 nm and 1000 nm wires, even under out of plane external field.

Beside these results, we successfully nucleated bubbles with current pulses absence of the external field and presence of the external field. From these results, this is also important out put from this study.

Another part of this study is spin-valve production. In this context, the spin valve structure has been successfully fabricated. After fabrication of spin-valve, the next step was stable single bubble nucleation on the spin-valve. Therefore, we investigated suitable H_{max} in-plane AC external magnetic field for demagnetization. Beside H_{max}

dependence of bubble formation, we searched also diameter dependence.

We observed bubble formation in 1500 nm spin-valve arrays, but with stable single bubble, we obtained two and three bubbles in a spin-valve, also multi domains. However, in dot array experiment to form bubble, we observed the highest nucleation rate of bubble in 1500 nm dot. In addition to that, we obtained single bubble with different H_{max} than dot array experiment. On the contrary of 1500 nm spin-valve array, we observed stable single bubble formation in 1000 nm spin-valve array. Even 1250 nm spin-valve array has more single bubbles than 1500 spin-valve array.

Beside stable single bubbles in spin-valves, we also observed unstable bubbles. when we scanned second times the same areas, we lost some small single magnetic bubble. The reason behind this may be due to hard layer. because there is an exchange interaction between hard layer and free layer (magnetic bubble is formed in this layer, Co/Ni multilayers). This exchange interaction may be the reason for observing stable single bubble in 1000 nm spin-valve instead of 1500 nm spin-valve. Because in dot array experiment to form bubble in to dot, we observed the highest bubble formation rate in 1500 nm dot array.

In this study, we also investigated bubble motion under in-plane external magnetic field. While increasing the in-plane external field with 5 Oe increment, we took MFM images and when we compared the results, we observed very different MFM images like ying yang shape. First, we thought there may be a problem then we conducted the experiment second time. we got the same results. Then we tried to explain these MFM images. For this purpose, we made some simulation to understand them. From the simulation, we obtained that from the second derivative of the in-plane component of the magnetization has an important role for the MFM images. Because with external field, this component strength is increasing and also magnetic MFM tip has a in-plane component of tip magnetization. Both these in-plane components cause ying yang like MFM images.

The results of this project were presented and or will be presented in oral presentations and poster presentations in international conferences. We have one paper in progress from this study. 1. "Magnetic bubble motion under in plane external magnetic field"(in progress)

REFERENCES

1. Burr, G. W., M. J. Breitwisch, M. Franceschini, D. Garetto, K. Gopalakrishnan, B. Jackson, B. Kurdi, C. Lam, L. A. Lastras, A. Padilla *et al.*, "Phase change memory technology", *Journal of Vacuum Science & Technology B, Nanotechnology and Microelectronics: Materials, Processing, Measurement, and Phenomena*, Vol. 28, No. 2, pp. 223–262, 2010.

2. Raoux, S., W. Wełnic and D. Ielmini, "Phase change materials and their application to nonvolatile memories", *Chemical reviews*, Vol. 110, No. 1, pp. 240–267, 2009.

3. Yamada, N., E. Ohno, N. Akahira, K. Nishiuchi, K. Nagata and M. Takao, "High speed overwritable phase change optical disk material", *Japanese Journal of Applied Physics*, Vol. 26, No. S4, p. 61, 1987.

4. Lee, B. C., E. Ipek, O. Mutlu and D. Burger, "Architecting phase change memory as a scalable dram alternative", *ACM SIGARCH Computer Architecture News*, Vol. 37, pp. 2–13, ACM, 2009.

5. Wong, H.-S. P., S. Raoux, S. Kim, J. Liang, J. P. Reifenberg, B. Rajendran, M. Asheghi and K. E. Goodson, "Phase change memory", *Proceedings of the IEEE*, Vol. 98, No. 12, pp. 2201–2227, 2010.

6. Wełnic, W. and M. Wuttig, "Reversible switching in phase-change materials", *Materials Today*, Vol. 11, No. 6, pp. 20–27, 2008.

7. Hwang, Y., J. Hong, S. Lee, S. Ahn, G. Jeong, G. Koh, J. Oh, H. Kim, W. Jeong, S. Lee *et al.*, "Full integration and reliability evaluation of phase-change RAM based on 0.24/spl mu/m-CMOS technologies", *VLSI Technology, 2003. Digest of Technical Papers. 2003 Symposium on*, pp. 173–174, IEEE, 2003.

8. Xu, C., B. Liu, Y.-F. Chen, S. Liang, Z.-T. Song, S.-L. Feng, X.-D. Wan, Z.-Y. Yang, J. Xie and B. Chen, "Condensed Matter: Electronic Structure, Electrical, Magnetic, And Optical Properties: Switching Characteristics of Phase Change Memory Cell Integrated with Metal-Oxide Semiconductor Field Effect Transistor", *Chinese Physics Letters*, Vol. 25, pp. 1848–1849, 2008.

9. Lai, S. and T. Lowrey, "OUM-A 180 nm nonvolatile memory cell element technology for stand alone and embedded applications", *Electron Devices Meeting, 2001. IEDM'01. Technical Digest. International*, pp. 36–5, IEEE, 2001.

10. Bedeschi, F., R. Bez, C. Boffino, E. Bonizzoni, E. C. Buda, G. Casagrande, L. Costa, M. Ferraro, R. Gastaldi, O. Khouri *et al.*, "4-Mb MOSFET-selected/spl mu/trench phase-change memory experimental chip", *IEEE journal of solid-state circuits*, Vol. 40, No. 7, pp. 1557–1565, 2005.

11. Wuttig, M. and C. Steimer, "Phase change materials: From material science to novel storage devices", *Applied Physics A: Materials Science & Processing*, Vol. 87, No. 3, pp. 411–417, 2007.

12. Chen, M., K. A. Rubin and R. Barton, "Compound materials for reversible, phase-change optical data storage", *Applied physics letters*, Vol. 49, No. 9, pp. 502–504, 1986.

13. Pirovano, A., A. L. Lacaita, F. Pellizzer, S. A. Kostylev, A. Benvenuti and R. Bez, "Low-field amorphous state resistance and threshold voltage drift in chalcogenide materials", *IEEE Transactions on Electron Devices*, Vol. 51, No. 5, pp. 714–719, 2004.

14. Raoux, S., G. W. Burr, M. J. Breitwisch, C. T. Rettner, Y.-C. Chen, R. M. Shelby, M. Salinga, D. Krebs, S.-H. Chen, H.-L. Lung *et al.*, "Phase-change random access memory: A scalable technology", *IBM Journal of Research and Development*, Vol. 52, No. 4.5, pp. 465–479, 2008.

15. Wuttig, M. and N. Yamada, "Phase-change materials for rewriteable data storage", *Nature materials*, Vol. 6, No. 11, p. 824, 2007.

16. Liu, B., T. Zhang, J. Xia, Z. Song, S. Feng and B. Chen, "Nitrogen-implanted Ge2Sb2Te5 film used as multilevel storage media for phase change random access memory", *Semiconductor science and technology*, Vol. 19, No. 6, p. L61, 2004.

17. Yamada, N., E. Ohno, K. Nishiuchi, N. Akahira and M. Takao, "Rapid-phase transitions of GeTe-Sb2Te3 pseudobinary amorphous thin films for an optical disk memory", *Journal of Applied Physics*, Vol. 69, No. 5, pp. 2849–2856, 1991.

18. Attenborough, K., M. Lankhorst, W. Ketelaars, R. Wolters, W. Baks, R. Delhougne, D. Gravesteijn, F. Jedema, J. van Hulle, D. T. Castro *et al.*, "An alternative concept for phase change random access memory", *E* PCOS05*, 2005.

19. Gu, Y., Z. Song, T. Zhang, B. Liu and S. Feng, "Novel phase-change material GeSbSe for application of three-level phase-change random access memory", *Solid-State Electronics*, Vol. 54, No. 4, pp. 443–446, 2010.

20. Kao, K.-F., C.-M. Lee, M.-J. Chen, M.-J. Tsai and T.-S. Chin, "Ga2Te3Sb5—A Candidate for Fast and Ultralong Retention Phase-Change Memory", *Advanced Materials*, Vol. 21, No. 17, pp. 1695–1699, 2009.

21. Rao, F., Z. Song, L. Wu, B. Liu, S. Feng and B. Chen, "Investigation on the stabilization of the median resistance state for phase change memory cell with doublelayer chalcogenide films", *Applied Physics Letters*, Vol. 91, No. 12, p. 123511, 2007.

22. Rao, F., Z. Song, M. Zhong, L. Wu, G. Feng, B. Liu, S. Feng and B. Chen, "Multilevel data storage characteristics of phase change memory cell with doublelayer chalcogenide films (Ge2Sb2Te5 and Sb2Te3)", *Japanese journal of applied physics*, Vol. 46, No. 1L, p. L25, 2007.

23. Hong, S.-H., H. Lee, K.-I. Kim, Y. Choi and Y.-K. Lee, "Fabrication of multilevel switching high density phase change data recording using stacked GeTe/GeSbTe structure", *Japanese Journal of Applied Physics*, Vol. 50, No. 8R, p. 081201, 2011.

24. Hong, S.-H., H. Lee, Y. Choi and Y.-K. Lee, "Fabrication of multi-level switching phase change nano-pillar device using InSe/GeSbTe stacked structure", *Current Applied Physics*, Vol. 11, No. 5, pp. S16–S20, 2011.

25. Ielmini, D., S. Lavizzari, D. Sharma and A. L. Lacaita, "Physical interpretation, modeling and impact on phase change memory (PCM) reliability of resistance drift due to chalcogenide structural relaxation", *Electron Devices Meeting, 2007. IEDM 2007. IEEE International*, pp. 939–942, IEEE, 2007.

26. Li, J., B. Luan and C. Lam, "Resistance drift in phase change memory", *Reliability Physics Symposium (IRPS), 2012 IEEE International*, pp. 6C–1, IEEE, 2012.

27. Ovshinsky, S. R., "Reversible electrical switching phenomena in disordered structures", *Physical Review Letters*, Vol. 21, No. 20, p. 1450, 1968.

28. Kim, Y.-T., K.-H. Lee, W.-Y. Chung, T.-K. Kim, Y.-K. Park and J.-T. Kong, "Study on cell characteristics of PRAM using the phase-change simulation", *Simulation of Semiconductor Processes and Devices, 2003. SISPAD 2003. International Conference on*, pp. 211–214, IEEE, 2003.

29. Sun, Z., J. Zhou and R. Ahuja, "Structure of phase change materials for data storage", *Physical review letters*, Vol. 96, No. 5, p. 055507, 2006.

30. Wuttig, M., D. Lüsebrink, D. Wamwangi, W. Welnic, M. Gilleßen and R. Dronskowski, "The role of vacancies and local distortions in the design of new phase-change materials", *Nature materials*, Vol. 6, No. 2, p. 122, 2007.

31. Dronskowski, R. and P. E. Bloechl, "Crystal orbital Hamilton populations (COHP): energy-resolved visualization of chemical bonding in solids based on

density-functional calculations", *The Journal of Physical Chemistry*, Vol. 97, No. 33, pp. 8617–8624, 1993.

32. Kooi, B., W. Groot and J. T. M. De Hosson, "In situ transmission electron microscopy study of the crystallization of Ge 2 Sb 2 Te 5", *Journal of Applied Physics*, Vol. 95, No. 3, pp. 924–932, 2004.

33. Agaev, K. and A. Talybov, "Electron diffraction analysis of structure of GeSb2Te4", *Soviet Physics Crystallography USSR*, Vol. 11, No. 3, p. 400, 1966.

34. Karpinsky, O., L. Shelimova, M. Kretova and J.-P. Fleurial, "An X-ray study of the mixed-layered compounds of (GeTe) n (Sb 2 Te 3) m homologous series", *Journal of alloys and compounds*, Vol. 268, No. 1, pp. 112–117, 1998.

35. Kresse, G. and J. Hafner, "Ab initio molecular-dynamics simulation of the liquid-metal–amorphous-semiconductor transition in germanium", *Physical Review B*, Vol. 49, No. 20, p. 14251, 1994.

36. Blaineau, S., P. Jund and D. A. Drabold, "Physical properties of a GeS 2 glass using approximate ab initio molecular dynamics", *Physical Review B*, Vol. 67, No. 9, p. 094204, 2003.

37. Drabold, D. *et al.*, "Models and modeling schemes for binary IV-VI glasses", *Physical Review B*, Vol. 71, No. 5, p. 054206, 2005.

38. Akola, J. and R. Jones, "Structural phase transitions on the nanoscale: The crucial pattern in the phase-change materials Ge 2 Sb 2 Te 5 and GeTe", *Physical Review B*, Vol. 76, No. 23, p. 235201, 2007.

39. Akola, J. and R. Jones, "Binary alloys of Ge and Te: order, voids, and the eutectic composition", *Physical review letters*, Vol. 100, No. 20, p. 205502, 2008.

40. Caravati, S., M. Bernasconi, T. Kuhne, M. Krack and M. Parrinello, "Coexistence

of tetrahedral-and octahedral-like sites in amorphous phase change materials", *Applied Physics Letters*, Vol. 91, No. 17, p. 171906, 2007.

41. Errington, J. R. and P. G. Debenedetti, "Relationship between structural order and the anomalies of liquid water", *Nature*, Vol. 409, No. 6818, p. 318, 2001.

42. Kolobov, A., P. Fons, J. Tominaga, A. Ankudinov, S. Yannopoulos and K. Andrikopoulos, "Crystallization-induced short-range order changes in amorphous GeTe", *Journal of Physics: Condensed Matter*, Vol. 16, No. 44, p. S5103, 2004.

43. Kolobov, A. V., P. Fons, A. I. Frenkel, A. L. Ankudinov, J. Tominaga and T. Uruga, "Understanding the phase-change mechanism of rewritable optical media", *Nature materials*, Vol. 3, No. 10, p. 703, 2004.

44. Mott, N. F. and E. A. Davis, *Electronic processes in non-crystalline materials*, OUP Oxford, 2012.

45. Ielmini, D., D. Sharma, S. Lavizzari and A. Lacaita, "Physical mechanism and temperature acceleration of relaxation effects in phase-change memory cells", *Reliability Physics Symposium, 2008. IRPS 2008. IEEE International*, pp. 597–603, IEEE, 2008.

46. Pirovano, A., A. L. Lacaita, A. Benvenuti, F. Pellizzer and R. Bez, "Electronic switching in phase-change memories", *IEEE Transactions on Electron Devices*, Vol. 51, No. 3, pp. 452–459, 2004.

47. Kato, T. and K. Tanaka, "Electronic properties of amorphous and crystalline Ge2Sb2Te5 films", *Japanese journal of applied physics*, Vol. 44, No. 10R, p. 7340, 2005.

48. Street, R. and N. Mott, "States in the gap in glassy semiconductors", *Physical Review Letters*, Vol. 35, No. 19, p. 1293, 1975.

49. Ielmini, D. and Y. Zhang, "Evidence for trap-limited transport in the subthreshold conduction regime of chalcogenide glasses", *Applied Physics Letters*, Vol. 90, No. 19, p. 192102, 2007.

50. Redaelli, A., D. Ielmini, U. Russo and A. Lacaita, "Modeling and simulation of conduction characteristics and programming operation in nanoscaled phase-change memory cells", *Journal of Computational and Theoretical Nanoscience*, Vol. 5, No. 6, pp. 1183–1191, 2008.

51. Russo, U., D. Ielmini, A. Redaelli and A. L. Lacaita, "Modeling of programming and read performance in phase-change memories—Part I: Cell optimization and scaling", *IEEE transactions on electron devices*, Vol. 55, No. 2, pp. 506–514, 2008.

52. Ielmini, D., A. L. Lacaita and D. Mantegazza, "Recovery and drift dynamics of resistance and threshold voltages in phase-change memories", *IEEE Transactions on Electron Devices*, Vol. 54, No. 2, pp. 308–315, 2007.

53. Ielmini, D., A. L. Lacaita, A. Pirovano, F. Pellizzer and R. Bez, "Analysis of phase distribution in phase-change nonvolatile memories", *IEEE Electron Device Letters*, Vol. 25, No. 7, pp. 507–509, 2004.

54. Redaelli, A., D. Ielmini, U. Russo and A. L. Lacaita, "Intrinsic data retention in nanoscaled phase-change memories—Part II: Statistical analysis and prediction of failure time", *IEEE Transactions on Electron Devices*, Vol. 53, No. 12, pp. 3040–3046, 2006.

55. Russo, U., D. Ielmini, A. Redaelli and A. L. Lacaita, "Intrinsic data retention in nanoscaled phase-change memories—Part I: Monte Carlo model for crystallization and percolation", *IEEE Transactions on Electron Devices*, Vol. 53, No. 12, pp. 3032–3039, 2006.

56. Ielmini, D. and Y. Zhang, "Analytical model for subthreshold conduction and threshold switching in chalcogenide-based memory devices", *Journal of Applied*

Physics, Vol. 102, No. 5, p. 054517, 2007.

57. Ielmini, D., "Threshold switching mechanism by high-field energy gain in the hopping transport of chalcogenide glasses", *Physical Review B*, Vol. 78, No. 3, p. 035308, 2008.

58. Hill, R. M., "The Poole-Frenkel constant", *Thin Solid Films*, Vol. 8, No. 3, pp. R21–R24, 1971.

59. Ielmini, D., D. Sharma, S. Lavizzari and A. L. Lacaita, "Reliability impact of chalcogenide-structure relaxation in phase-change memory (PCM) cells—Part I: Experimental study", *IEEE Transactions on Electron Devices*, Vol. 56, No. 5, pp. 1070–1077, 2009.

60. Jonscher, A. and R. Hill, "Electrical conduction in disordered nonmetallic films", *Physics of thin films*, Vol. 8, pp. 169–249, 1975.

61. Emin, D., C. Seager and R. K. Quinn, "Small-polaron hopping motion in some chalcogenide glasses", *Physical Review Letters*, Vol. 28, No. 13, p. 813, 1972.

62. Emin, D., "Current-driven threshold switching of a small polaron semiconductor to a metastable conductor", *Physical Review B*, Vol. 74, No. 3, p. 035206, 2006.

63. Buchanan, K. S., P. E. Roy, M. Grimsditch, F. Y. Fradin, K. Y. Guslienko, S. D. Bader and V. Novosad, "Soliton pair dynamics in patterned ferromagnetic ellipses", *arXiv preprint cond-mat/0602509*, 2006.

64. Guslienko, K. Y., "Magnetic vortex state stability, reversal and dynamics in restricted geometries", *Journal of nanoscience and nanotechnology*, Vol. 8, No. 6, pp. 2745–2760, 2008.

65. Chien, C., F. Q. Zhu and J.-G. Zhu, "Patterned nanomagnets", *Physics today*, Vol. 60, No. 6, p. 40, 2007.

66. Hehn, M., K. Ounadjela, J.-P. Bucher, F. Rousseaux, D. Decanini, B. Bartenlian and C. Chappert, "Nanoscale magnetic domains in mesoscopic magnets", *Science*, pp. 1782–1785, 1996.

67. Choe, S.-B., Y. Acremann, A. Scholl, A. Bauer, A. Doran, J. Stöhr and H. A. Padmore, "Vortex core-driven magnetization dynamics", *Science*, Vol. 304, No. 5669, pp. 420–422, 2004.

68. Guslienko, K. Y., X. Han, D. Keavney, R. Divan and S. Bader, "Magnetic vortex core dynamics in cylindrical ferromagnetic dots", *Physical review letters*, Vol. 96, No. 6, p. 067205, 2006.

69. Van Waeyenberge, B., A. Puzic, H. Stoll, K. Chou, T. Tyliszczak, R. Hertel, M. Fähnle, H. Brückl, K. Rott, G. Reiss *et al.*, "Magnetic vortex core reversal by excitation with short bursts of an alternating field", *Nature*, Vol. 444, No. 7118, p. 461, 2006.

70. Cheng, X. and D. Keavney, "Studies of nanomagnetism using synchrotron-based x-ray photoemission electron microscopy (X-PEEM)", *Reports on Progress in Physics*, Vol. 75, No. 2, p. 026501, 2012.

71. Kim, D.-H., E. A. Rozhkova, I. V. Ulasov, S. D. Bader, T. Rajh, M. S. Lesniak and V. Novosad, "Biofunctionalized magnetic-vortex microdiscs for targeted cancer-cell destruction", *Nature materials*, Vol. 9, No. 2, p. 165, 2010.

72. Pribiag, V., I. Krivorotov, G. Fuchs, P. Braganca, O. Ozatay, J. Sankey, D. Ralph and R. Buhrman, "Magnetic vortex oscillator driven by dc spin-polarized current", *arXiv preprint cond-mat/0702253*, 2007.

73. Dussaux, A., B. Georges, J. Grollier, V. Cros, A. Khvalkovskiy, A. Fukushima, M. Konoto, H. Kubota, K. Yakushiji, S. Yuasa *et al.*, "Large microwave generation from DC driven magnetic vortex oscillators in magnetic tunnel junctions", *arXiv preprint arXiv:1001.4933*, 2010.

74. Keavney, D., X. Cheng and K. Buchanan, "Polarity reversal of a magnetic vortex core by a unipolar, nonresonant in-plane pulsed magnetic field", *Applied Physics Letters*, Vol. 94, No. 17, p. 172506, 2009.

75. Houssameddine, D., U. Ebels, B. Delaët, B. Rodmacq, I. Firastrau, F. Ponthenier, M. Brunet, C. Thirion, J.-P. Michel, L. Prejbeanu-Buda *et al.*, "Spin-torque oscillator using a perpendicular polarizer and a planar free layer", *Nature materials*, Vol. 6, No. 6, p. 441, 2007.

76. Ozatay, O., P. Gowtham, K. Tan, J. Read, K. Mkhoyan, M. Thomas, G. Fuchs, P. Braganca, E. Ryan, K. Thadani *et al.*, "Sidewall oxide effects on spin-torque- and magnetic-field-induced reversal characteristics of thin-film nanomagnets", *Nature materials*, Vol. 7, No. 7, p. 567, 2008.

77. Kent, A. D., "Spintronics: A nanomagnet oscillator", *Nature materials*, Vol. 6, No. 6, pp. 399–400, 2007.

78. Mourachkine, A., O. Yazyev, C. Ducati and J.-P. Ansermet, "Template nanowires for spintronics applications: nanomagnet microwave resonators functioning in zero applied magnetic field", *Nano letters*, Vol. 8, No. 11, pp. 3683–3687, 2008.

79. Choi, J., J. Wu, C. Won, Y. Wu, A. Scholl, A. Doran, T. Owens and Z. Qiu, "Magnetic bubble domain phase at the spin reorientation transition of ultrathin Fe/Ni/Cu (001) film", *Physical review letters*, Vol. 98, No. 20, p. 207205, 2007.

80. Ivanov, B., V. Stephanovich and A. Zhmudskii, "Magnetic vortices and the microscopic analogs of magnetic bubbles", *Journal of Magnetism and Magnetic Materials*, Vol. 88, No. 1-2, pp. 116–120, 1990.

81. Fukumura, T., H. Sugawara, T. Hasegawa, K. Tanaka, H. Sakaki, T. Kimura and Y. Tokura, "Spontaneous bubble domain formation in a layered ferromagnetic crystal", *Science*, Vol. 284, No. 5422, pp. 1969–1971, 1999.

82. Thiele, A., "Steady-state motion of magnetic domains", *Physical Review Letters*, Vol. 30, No. 6, p. 230, 1973.

83. Komineas, S., C. Vaz, J. Bland and N. Papanicolaou, "Bubble domains in disc-shaped ferromagnetic particles", *Physical Review B*, Vol. 71, No. 6, p. 060405, 2005.

84. Moutafis, C., S. Komineas, C. Vaz, J. Bland, T. Shima, T. Seki and K. Takanashi, "Magnetic bubbles in FePt nanodots with perpendicular anisotropy", *Physical Review B*, Vol. 76, No. 10, p. 104426, 2007.

85. Fert, A., N. Reyren and V. Cros, "Magnetic skyrmions: advances in physics and potential applications", *Nature Reviews Materials*, Vol. 2, p. 17031, 2017.

86. Koshibae, W. and N. Nagaosa, "Berry curvature and dynamics of a magnetic bubble", *New Journal of Physics*, Vol. 18, No. 4, p. 045007, 2016.

87. Kotani, A., H. Nakajima, Y. Ishii, K. Harada and S. Mori, "Observation of spin textures in La1- x Sr x MnO3 (x= 0.175)", *AIP Advances*, Vol. 6, No. 5, p. 056403, 2016.

88. Yu, G., P. Upadhyaya, X. Li, W. Li, S. K. Kim, Y. Fan, K. L. Wong, Y. Tserkovnyak, P. K. Amiri and K. L. Wang, "Room-temperature creation and spin–orbit torque manipulation of skyrmions in thin films with engineered asymmetry", *Nano letters*, Vol. 16, No. 3, pp. 1981–1988, 2016.

89. Westover, A. S., K. Chesnel, K. Hatch, P. Salter and O. Hellwig, "Enhancement of magnetic domain topologies in Co/Pt thin films by fine tuning the magnetic field path throughout the hysteresis loop", *Journal of Magnetism and Magnetic Materials*, Vol. 399, pp. 164–169, 2016.

90. von Bergmann, K., "Magnetic bubbles with a twist", *Science*, Vol. 349, No. 6245, pp. 234–235, 2015.

91. Jiang, W., W. Zhang, G. Yu, M. B. Jungfleisch, P. Upadhyaya, H. Somaily, J. E. Pearson, Y. Tserkovnyak, K. L. Wang, O. Heinonen *et al.*, "Mobile Néel skyrmions at room temperature: status and future", *AIP Advances*, Vol. 6, No. 5, p. 055602, 2016.

92. Iwasaki, J., M. Mochizuki and N. Nagaosa, "Current-induced skyrmion dynamics in constricted geometries", *Nature nanotechnology*, Vol. 8, No. 10, pp. 742–747, 2013.

93. Liu, Y., H. Yan, M. Jia, H. Du and A. Du, "Topological analysis of spin-torque driven magnetic skyrmion formation", *Applied Physics Letters*, Vol. 109, No. 10, p. 102402, 2016.

94. Lin, S.-Z., "Edge instability in a chiral stripe domain under an electric current and skyrmion generation", *Physical Review B*, Vol. 94, No. 2, p. 020402, 2016.

95. Legrand, W., D. Maccariello, N. Reyren, K. Garcia, C. Moutafis, C. Moreau-Luchaire, S. Collin, K. Bouzehouane, V. Cros and A. Fert, "Room-temperature current-induced generation and motion of sub-100 nm skyrmions", *Nano Letters*, Vol. 17, No. 4, pp. 2703–2712, 2017.

96. Jiang, W., X. Zhang, G. Yu, W. Zhang, M. B. Jungfleisch, J. E. Pearson, O. Heinonen, K. L. Wang, Y. Zhou, A. Hoffmann *et al.*, "Direct observation of the skyrmion Hall effect", *arXiv preprint arXiv:1603.07393*, 2016.

97. Liu, T., V. Puliafito, F. Montaigne, S. Petit, C. Deranlot, S. Andrieu, O. Ozatay, G. Finocchio and T. Hauet, "Reproducible formation of single magnetic bubbles in an array of patterned dots", *Journal of Physics D: Applied Physics*, Vol. 49, No. 24, p. 245002, 2016.

98. Finocchio, G., F. Büttner, R. Tomasello, M. Carpentieri and M. Kläui, "Magnetic skyrmions: from fundamental to applications", *Journal of Physics D: Applied Physics*, Vol. 49, No. 42, p. 423001, 2016.

99. Moutafis, C., S. Komineas and J. Bland, "Dynamics and switching processes for magnetic bubbles in nanoelements", *Physical Review B*, Vol. 79, No. 22, p. 224429, 2009.

100. Makhfudz, I., B. Krüger and O. Tchernyshyov, "Inertia and chiral edge modes of a skyrmion magnetic bubble", *Physical review letters*, Vol. 109, No. 21, p. 217201, 2012.

101. Vukadinovic, N. and F. Boust, "Three-dimensional micromagnetic simulations of magnetic excitations in cylindrical nanodots with perpendicular anisotropy", *Physical Review B*, Vol. 75, No. 1, p. 014420, 2007.

102. Vukadinovic, N. and F. Boust, "Three-dimensional micromagnetic simulations of multidomain bubble-state excitation spectrum in ferromagnetic cylindrical nanodots", *Physical Review B*, Vol. 78, No. 18, p. 184411, 2008.

103. Boulle, O., J. Vogel, H. Yang, S. Pizzini, D. d. S. Chaves, A. Locatelli, T. O. M. A. Sala, L. D. Buda-Prejbeanu, O. Klein, M. Belmeguenai *et al.*, "Room temperature chiral magnetic skyrmion in ultrathin magnetic nanostructures", *arXiv preprint arXiv:1601.02278*, 2016.

104. Yu, X., Y. Tokunaga, Y. Taguchi and Y. Tokura, "Variation of Topology in Magnetic Bubbles in a Colossal Magnetoresistive Manganite", *Advanced Materials*, Vol. 29, No. 3, 2017.

105. Finocchio, G., V. Puliafito, S. Komineas, L. Torres, O. Ozatay, T. Hauet and B. Azzerboni, "Nanoscale spintronic oscillators based on the excitation of confined soliton modes", *Journal of Applied Physics*, Vol. 114, No. 16, p. 163908, 2013.

106. Chen, S., Q. Zhu, S. Zhang, C. Jin, C. Song, J. Wang and Q. Liu, "Dynamic response for Dzyaloshinskii–Moriya interaction on bubble-like magnetic solitons driven by spin-polarized current", *Journal of Physics D: Applied Physics*, Vol. 49, No. 19, p. 195004, 2016.

107. Won, Y., J. Lee, M. Asheghi, T. W. Kenny and K. E. Goodson, "Phase and thickness dependent modulus of Ge2Sb2Te5 films down to 25 nm thickness", *Applied Physics Letters*, Vol. 100, No. 16, p. 161905, 2012.

108. Kim, D.-H., F. Merget, M. Först and H. Kurz, "Three-dimensional simulation model of switching dynamics in phase change random access memory cells", *Journal of applied physics*, Vol. 101, No. 6, p. 064512, 2007.

109. Sun, K., W. Feng, J. Y. Lee, B. Li and Y.-H. Xie, "3-D Finite Element Simulation of a Phase-change Random Access Memory Cell with a Self-insulated Structure", *MRS Online Proceedings Library Archive*, Vol. 1108, 2008.

110. Reifenberg, J., E. Pop, A. Gibby, S. Wong and K. Goodson, "Multiphysics modeling and impact of thermal boundary resistance in phase change memory devices", *Thermal and Thermomechanical Phenomena in Electronics Systems, 2006. ITHERM'06. The Tenth Intersociety Conference on*, pp. 106–113, IEEE, 2006.

111. Kim, D.-H., F. Merget, M. Laurenzis, P. H. Bolivar and H. Kurz, "Electrical percolation characteristics of Ge 2 Sb 2 Te 5 and Sn doped Ge 2 Sb 2 Te 5 thin films during the amorphous to crystalline phase transition", *Journal of applied physics*, Vol. 97, No. 8, p. 083538, 2005.

112. Bruggeman, V. D., "Berechnung verschiedener physikalischer Konstanten von heterogenen Substanzen. I. Dielektrizitätskonstanten und Leitfähigkeiten der Mischkörper aus isotropen Substanzen", *Annalen der physik*, Vol. 416, No. 7, pp. 636–664, 1935.

113. Wiener, O., "Lamellare doppelbrechung", *Physikalische Zeitschrift*, Vol. 5, No. 12, pp. 332–338, 1904.

114. Tsafack, T., E. Piccinini, B.-S. Lee, E. Pop and M. Rudan, "Electronic, optical and thermal properties of the hexagonal and rocksalt-like Ge2Sb2Te5 chalcogenide from first-principle calculations", *Journal of Applied Physics*, Vol. 110, No. 6, p.

063716, 2011.

115. Cinar, I., O. Aslan, A. Gokce, O. Dincer, V. Karakas, B. Stipe, J. Katine, G. Aktas and O. Ozatay, "Three dimensional finite element modeling and characterization of intermediate states in single active layer phase change memory devices", *Journal of Applied Physics*, Vol. 117, No. 21, p. 214302, 2015.

116. Peng, C., L. Cheng and M. Mansuripur, "Experimental and theoretical investigations of laser-induced crystallization and amorphization in phase-change optical recording media", *Journal of Applied Physics*, Vol. 82, No. 9, pp. 4183–4191, 1997.

117. Simpson, R., P. Fons, A. Kolobov, T. Fukaya, M. Krbal, T. Yagi and J. Tominaga, "Interfacial phase-change memory", *Nature Nanotechnology*, Vol. 6, No. 8, pp. 501–505, 2011.

118. Ielmini, D. and A. L. Lacaita, "Phase change materials in non-volatile storage", *Materials Today*, Vol. 14, No. 12, pp. 600–607, 2011.

119. Jeyasingh, R. G., D. Kuzum and H.-S. P. Wong, "Investigation of trap spacing for the amorphous state of phase-change memory devices", *IEEE Transactions on Electron Devices*, Vol. 58, No. 12, pp. 4370–4376, 2011.

120. Ozatay, O., B. Stipe, J. Katine and B. Terris, "Electrical switching dynamics in circular and rectangular Ge 2 Sb 2 Te 5 nanopillar phase change memory devices", *Journal of Applied Physics*, Vol. 104, No. 8, p. 084507, 2008.

121. Kim, S., B. Lee, M. Asheghi, F. Hurkx, J. P. Reifenberg, K. E. Goodson and H.-S. P. Wong, "Resistance and threshold switching voltage drift behavior in phase-change memory and their temperature dependence at microsecond time scales studied using a micro-thermal stage", *IEEE Transactions on Electron Devices*, Vol. 58, No. 3, pp. 584–592, 2011.

122. Braga, S., A. Cabrini and G. Torelli, "Experimental analysis of partial-SET state stability in phase-change memories", *IEEE Transactions on Electron Devices*, Vol. 58, No. 2, pp. 517–522, 2011.

123. Papandreou, N., H. Pozidis, T. Mittelholzer, G. Close, M. Breitwisch, C. Lam and E. Eleftheriou, "Drift-tolerant multilevel phase-change memory", *Memory Workshop (IMW), 2011 3rd IEEE International*, pp. 1–4, IEEE, 2011.

124. Fugazza, D., D. Ielmini, S. Lavizzari and A. Lacaita, "Distributed-Poole-Frenkel modeling of anomalous resistance scaling and fluctuations in phase-change memory (PCM) devices", *Electron Devices Meeting (IEDM), 2009 IEEE International*, pp. 1–4, IEEE, 2009.

125. Papandreou, N., A. Pantazi, A. Sebastian, E. Eleftheriou, M. Breitwisch, C. Lam and H. Pozidis, "Estimation of amorphous fraction in multilevel phase-change memory cells", *Solid-State Electronics*, Vol. 54, No. 9, pp. 991–996, 2010.

126. Faraclas, A., G. Bakan, F. Dirisaglik, N. E. Williams, A. Gokirmak, H. Silva *et al.*, "Modeling of thermoelectric effects in phase change memory cells", *IEEE Transactions on Electron Devices*, Vol. 61, No. 2, pp. 372–378, 2014.

127. Jeong, C., D. Kang, D. Ha, Y. Song, J. Oh, J. Kong, J. Yoo, J. Park, K. Ryoo, D. Lim *et al.*, "Writing current reduction and total set resistance analysis in PRAM", *Solid-State Electronics*, Vol. 52, No. 4, pp. 591–595, 2008.

APPENDIX A: MODELING OF PCM IN COMSOL MULTIPHYSICS

A.1. Model Navigator

(i) Start Comsol 4.3a and go to Model Wizard.

(ii) Click the 3D button.

(iii) Click Next.

(iv) In the Add Physics tree, select Heat Transfer¿Electromagnetic Heating¿Joule Heating (jh)

(v) Click add and from the Add physics tree, select Mathematics¿PDE Interfaces¿ Coefficient Form PDE (c)

(vi) Click add button, then Click Next.

(vii) Find the Studies subsection. In the tree, select Present Studies¿Time Dependent.

(viii) Click Finish.

A.1.1. Geometry Modeling

(i) From the Model Builder tree, Right-click Geometry under the Model 1, select the Block.

(ii) In the Block window, enter the following values of the block. In the Size and Shape setting window;

Width: $225e-9$

Depth: $150e-9$

Height:$50e-9$

In the Position setting window;

x: 0

y: 0

z: 0

(iii) Click Build all.

(iv) Right-click Geometry, select the Block.

(v) In the Block window, enter the following values of the block. In the Size and Shape setting window;

Width: $225e-9$

Depth: $150e-9$

Height: $50e-9$

In the Position setting window;

x: 0

y: 0

z: $50e-9$

(vi) Click Build all.

(vii) Right-click Geometry, select the Block.

(viii) In the Block window, enter the following values of the block. In the Size and Shape setting window;

Width: $90e-9$

Depth: $90e-9$

Height: $50e-9$

In the Position setting window;

x: $67.5e-9$

y: $30e-9$

z: $100e-9$

(ix) Click Build all.

Note: While constructing spherical heating device, we have to use following values for the top contact a a heater instead of the square top contact heating.

(x) Right-click Geometry, select the Sphere.

11. In the Sphere window, enter the following values of the block. In the Radius section, enter $75e-9$. In the Position setting window;

x: $112.5e-9$

y: $75e-9$

z: $1300e-9$

(xi) Click Build Selected.

(xii) Select all structures from displays one by one then right-click on the Geometry and under Booleans and Partitions choose Union.

(xiii) Click the Zoom Extent button on the Graphics toolbar.

A.1.2. Global Definitions

A.1.2.1. Parameters.

(i) In the Model Builder window, right-click Global Definitions and choose Parameters.

(ii) In the Parameters setting windows, locate the Parameters sections and enter the following settings.

(iii) In the Model Builder window, right-click Global Definitions and choose Step under Functions.

(iv) Enter H into the Function name in the Settings window.

(v) Under Parameters Enter T_m into the Location in the Settings window and From and To part enter 0 and 1.

(vi) Under Smoothing settings, enter 5 and check the box.

(vii) In the Model Builder window, right-click Global Definitions and choose Analytic under Functions.

(viii) Enter D into the Function name in the Settings window.

(ix) Under Definitions Enter d(H(T),T) into the Expression in the Settings window and for Arguments values, enter T and select Automatic from the Derivatives settings.

(x) Under Units settings, enter K into the Arguments and 1/K into the Function settings.

(xi) Under Plot Parameters, set the Lower limit and Upper limit as 884 and 894.

(xii) In the Model Builder window, right-click Global Definitions and choose Step under Functions.

(xiii) Enter H1 into the Function name in the Settings window.

(xiv) Under Parameters Enter t1 into the Location in the Settings window and From and To part enter 0 and 1.

Table A.1. Parameters 1

Name	Expression	Description
T0	300 [K]	Initial temperature
T_m	616 [degC]	Melting Point for GST
K1	0.2 [W/(m.K)]	Thermal conductivity for amorphous phase
K2	0.5 [W/(m.K)]	Thermal conductivity for crystalline phase
T_g	400 [degC]	Glass transiton point of GST
kb	$1.380e-23$ [J/K]	Boltzmann Constant
Γ	0.1 [J/m^2]	Amorphous - Crystalline Interface Energy
L_{wf}	$2.44e-8$[W.ohm/ K^2]	Wiedemann - Franz Constant
Ea1	2.19 [eV]	Activation Energy for Nucleation
Ea2	2.23 [eV]	Activation Energy for Diffusion
H_{v1}	$418.9e6$[J/ m^3]	Latent heat of GST
H_{v2}	$218.5e6$[J/ m^3]	Latent heat of GST
N_{homo}	$4.63e27$[m^{-3}]	molecules $\#/V$ for homogeneous nucleation
N_{hete}	$2.78e18$[m^{-3}]	molecules $\#/V$ for heterogeneous nucleation
d	$2.991e-10$[m]	Interatomic distance
Alpha	$4e25$[1/s]	Temp. coefficient
α_c	$-1.16e-3$[1/K]	σ_c Temp. coefficient
α_a	-0.0195[1/K]	σ_a Temp. coefficient
ϵ_a	16	Permittivity for amorphous GST
ϵ_c	30	Permittivity for crystalline GST
Cp	202 [J/kg.K]	Heat Capacity of GST
ρ_{gst}	6200 kg/ m^3]	Density of GST
A	$7.5e-4$[J^3 m^{-6}]	Interfacial surface free energy
L_{mesh}	$15e-9$[m]	Mesh Length
V_{mesh}	$225e-27$[m^3]	Mesh Volume
z_{homo}	$45e-9$[m]	Distance

Table A.2. Parameters 2

Name	Expression	Description
t1	$20e-9$ [s]	Time constant 1
t2	$20e-9$ [s]	Time constant 2
π	3.14	Pi constant
E	$1.602e-19$ [C]	Electron charge
ht	$1.054571726e-34$ [J.s]	Energy constant
p1	$5e19$ [cm^{-3}]	Volume constant 1
p2	$1e20$ [cm^{-3}]	Volume constant 2
Ef	0.31[eV]	Fermi Energy
W	1	Seebeck parameters

(xv) Under Smoothing settings, enter $10e-9$ and check the box.

(xvi) In the Model Builder window, right-click Global Definitions and choose Step under Functions.

(xvii) Enter H2 into the Function name in the Settings window.

(xviii) Under Parameters Enter t2 into the Location in the Settings window and From and To part enter 0 and 1.

(xix) Under Smoothing settings, enter $10e-9$ and check the box.

(xx) In the Model Builder window, right-click Global Definitions and choose Analytic under Functions.

(xxi) Enter D2 into the Function name in the Settings window.

(xxii) Under Definitions Enter H1(t[1/s])-H2(t[1/s]) into the Expression in the Settings window and for Arguments values, enter t and select Automatic from the Derivatives settings.

(xxiii) Under Units settings, enter s into the Arguments and 1/s into the Function settings.

(xxiv) Under Plot Parameters, set the Lower limit and Upper limit as 0 and $200e+-9$ (time, it can be define according to simulation time range).

A.1.3. Model 1

A.1.3.1. Variables.

(i) In the Model Builder window, right-click Definitions under the Model 1 and choose Variables.
(ii) In the Variables setting windows, locate the Variables sections.
(iii) In the table, enter the following settings.

A.1.3.2. Pairs.

(i) In the Model Builder window, right-click Definitions under the Model 1 and choose Contact Pair under Pairs.
(ii) In the General setting windows, locate Pair type edit field and check Contact Pair.
(iii) In the Source Boundaries setting windows, select boundary 15 from the Graphics.
(iv) In the Source Boundaries setting windows, select boundary 15 from the Graphics.
(v) Right-click Definitions and choose Pairs¿Contact Pair.
(vi) In the General setting windows, locate Pair type edit field and check Contact Pair.
(vii) In the Source Boundaries setting windows, select boundary 6 from the Graphics.
(viii) In the Source Boundaries setting windows, select boundary 6 from the Graphics.
(ix) Right-click Definitions and choose Contact Pair under Pairs.
(x) In the General setting windows, locate Pair type edit field and check Contact Pair.
(xi) In the Source Boundaries setting windows, select boundary 10, 12, 18, 19 from the Graphics.
(xii) In the Source Boundaries setting windows, select boundary 10, 12, 18, 19 from the Graphics.

Table A.3. Variables 1

Name	Expression
V1	$\mathrm{RRsR}_{\mathrm{pulses}}$
T_{m2}	$T_m - 10[K]$
σ_c	$2700.\exp(-\alpha_c.(T - T0)) * (T < T_m)[S/m]$ $+2700.\exp(-\alpha_c.(T_m - T0)) * (T >= T_m)[S/m]$
σ_{a2}	1332[S/m]
σ_a	$3[S/m]+$ $1332[S/(m * V)] * ((V1 - Vth1)/0.45) * (V1 >= Vth1) * (V1 < Vth2)$ $+1332[S/m] * (V1 >= Vth2)$
σ_{mixed}	$\sigma_{mixed2} * (T < T_m) + \sigma_c * (T >= T_m).\sigma_{mixed2} * (T < T_m)+$ $\sigma_c * (T >= T_m)$
σ_{mixed2}	$0.25.(2.\sigma_a - 3.\sigma_a.f + 3.\sigma_c.f - \sigma_c$ $+\sqrt{8.\sigma_a.\sigma_c + (2.\sigma_a - 3.\sigma_a.f + 3.\sigma_c.f - \sigma_c)^2})$
L_{wf}	$2.44e^{-8}$[W.ohm/ K^2]
Vth1	0.20[V]
Vth2	0.65[V]
K_{mixed}	K1+(K2-K1).f
K_{gst2}	$L_{wf}.T.\sigma_{mixed} + K_{mixed}$
E_{gst}	$\epsilon_a.u + (1 - u).\epsilon_c$
Cp_t	$Cp.(1 - d(H(T[1/K]), T)) * (T < T_m)$ $+H(T[1/K]).d(H(T[1/K]), T)[1/K].H_v1/\rho_{gst} + 1.2.Cp * (T > T_m)$
L_{grid}	$L_{mesh}/5$
In	$(T < T_m) * \alpha.\exp(-(Ea1 + G_e)/(kb.T))$
G_e	$A * z_{homo}[1/m]/((G_v)^2)$
G_v	$H_{v1}.(1 - T/T_m) * (T > T_g)$ $+H_{v2}.(1 - T.(1 - H_{v1}.(1 - T_g/T_m)/H_{v2})/T_g) * (T <= T_g)$

Table A.4. Variables 2

Name	Expression
f	u
G_{v1}	$G_v.(G_v >= -0.8e^8[J/m^3]) + (-0.8e^8[J/m^3]) * (G_v < -0.8e^8[J/m^3])$
Vg	G1 + G2 + G3 + G4 + G5
G1	$0.05430[m/s].\exp((T - 763[K]).(763[K] - T)/1341.62[K^2])$
G2	$0.022[m/s].\exp((T - 720[K]).(720[K] - T)/2271.38[K^2])$
G3	$0.009[m/s].\exp((T - 760[K]).(760[K] - T)/531.38[K^2])$
G4	$0.00086[m/s].\exp((T - 685[K]).(865[K] - T)/288[K^2])$
G5	$0.00145[m/s].\exp((T - 823[K]).(823[K] - T)/273.78[K^2])$
Vreset	1[V]
Vset	0.7[V]
Vread	0.05[V]
t_{reset}	$123.75e^{-9}$[s]
τ	$3e^8$[1/s]
Cp_r	$Cp+$ $10000.\sin((\pi/100).(T - 840[K])) * (T >= 840[K] \&\& T <= 930[K])$
RReR	$0.05[V] * flc1hs(t[1/s] - 10e^{-9}, 5e^{-9})$ $+1[V] * (flc1hs(t[1/s] - 50e^{-9}, 10e^{-9}) -$ $1 * flc1hs(t[1/s] - 200e^{-9}, 26.25e^{-9}))$
RSR	$0.05[V] * flc1hs(t[1/s] - 10e^{-9}, 5e^{-9})$ $+0.6[V] * (flc1hs(t[1/s] - 50e^{-9}, 10e^{-9}) -$ $1 * flc1hs(t[1/s] - 200e^{-9}, 26.25e^{-9}))$
t_{init}	$40e^{-9}$ [s]
Qth	$-T.(mod1.jh.normJ).SS$
S	$(((\pi^2).(kb^2).T)/(3.E.Ef)).(1 + W)$
SS	$(((7.T[1/K] - 220)/40)[V/(m.K)].f+$ $(-0.424.T[1/K] + 527.2)[V/(m.K)].(1 - f)).(T < T_m)+$ $150[V/(m.K)].(T >= T_m)$

A.1.4. Joule Heating (jh)

Joule Heating Model 1:

(i) In the Model Builder window, select Joule Heating (jh) under the Model 1 and choose Joule Heating Model 1.

(ii) In the Joule Heating Model 1 setting windows, locate the Conduction Current section.

(iii) In the Electrical conductivity edit field, check Linearized resistivity.

(iv) In the Reference temperature edit field, check User Defined and type 300 into the opening window and select Isotropic.

(v) In the Resistivity temperature coefficient edit field, check User Defined and type 0.0042 into the opening window.

(vi) In the Reference resistivity edit field, check User Defined and type $250e-9$ into the opening window and select Isotropic.

(vii) In the Joule Heating Model 1 setting windows, locate the Electric Field section.

(viii) In the Constitutive relation edit field, check Relative permittivity.

(ix) In the Relative permittivity edit field, check User Defined and type 3000 into the opening window and select Isotropic.

(x) In the Joule Heating Model 1 setting windows, locate the Heat Conduction section.

(xi) In the Thermal conductivity edit field, check User Defined and type 300 into the opening window and select Isotropic.

(xii) In the Joule Heating Model 1 setting windows, locate the Thermodynamics section.

(xiii) In the Density edit field, check User Defined and type $12e3$ into the opening window.

(xiv) In the Heat capacity at constant pressure edit field, check User Defined and type 320 into the opening window.

NOTE:Joule Heating Model 1 is for the top and bottom contacts parameters.

Initial Values 1:

(i) In the Model Builder window, select Joule Heating (jh) under the Model 1 and choose Joule Heating Model 1 and click Initial values 1.
(ii) In the Initial values 1 setting windows, locate the Initial values section.
(iii) In the T0 edit field, type 300[K].
(iv) In the V edit field, type 0.

Joule Heating Model 2:

(i) In the Model Builder window, right-click Joule Heating (jh) and choose Joule Heating Model.
(ii) In the Joule Heating Model 2 setting windows, locate the Conduction Current section.
(iii) In the Electrical conductivity edit field, check Linearized resistivity.
(iv) In the Reference temperature edit field, check User Defined and type 300 into the opening window.
(v) In the Resistivity temperature coefficient edit field, check User Defined and type 0 into the opening window.
(vi) In the Reference resistivity edit field, check User Defined and type $1/\sigma_{mixed}$ into the opening window.
(vii) In the Joule Heating Model 2 setting windows, locate the Electric Field section.
(viii) In the Constitutive relation edit field, check Relative permittivity.
(ix) In the Relative permittivity edit field, check User Defined and type E_{gst} into the opening window.
(x) In the Joule Heating Model 2 setting windows, locate the Heat Conduction section.
(xi) In the Thermal conductivity edit field, check User Defined and type K_{gst2} into the opening window.
(xii) In the Joule Heating Model 2 setting windows, locate the Thermodynamics section.

(xiii) In the Density edit field, check User Defined and type 6200 into the opening window.

(xiv) In the Heat capacity at constant pressure edit field, check User Defined and type Cp_r into the opening window.

(xv) In the Model Builder window, right-click Joule Heating (jh) and choose Temperature under Heat Transfer.

(xvi) In the Temperature edit field, type 300[K].

(xvii) In the Temperature setting windows, select boundary 3 and 16 boundary from the Graphics.

(xviii) In the Model Builder window, right-click Joule Heating (jh) and choose Ground under Electric Currents.

(xix) In the Ground setting windows, select only boundary 3 from the Graphics.

(xx) In the Model Builder window, right-click Joule Heating (jh) and choose Electrical Potential under Electric Currents.

(xxi) In the Electrical Potential setting windows, select only boundary 16 from the Graphics.

(xxii) In the Electrical Potential edit field, type V1.

(xxiii) In the Model Builder window, right-click Joule Heating (jh) and choose Continuity under Pairs.

(xxiv) In the Continuity 1 setting windows, select Contact Pair 1 from the Pairs.

(xxv) In the Model Builder window, right-click Joule Heating (jh) and choose Continuity under Pairs.

(xxvi) In the Continuity 2 setting windows, select Contact Pair 2 from the Pairs.

(xxvii) In the Model Builder window, right-click Joule Heating (jh) and choose Continuity under Pairs.

(xxviii) In the Continuity 3 setting windows, select Contact Pair 3 from the Pairs.

(xxix) In the Model Builder window, right-click Joule Heating (jh) and choose Heat Source under Heat Transfer.

(xxx) In the Heat Source window, select the layer then locate Heat Source values and edit Qth.

Coefficient Form PDE (c):

(i) In the Model Builder window, select Coefficient Form PDE (c).

(ii) In the Coefficient Form PDE setting windows, locate the Domain Selection section.

(iii) In the Domain Selection setting window, select 2 and 3 geometry from the Graphics.

(iv) In the Model Builder window, select Coefficient Form PDE (c) and choose Coefficient Form PDE 1.

(v) In the Coefficient Form PDE setting windows, locate the Diffusion Coefficient section.

(vi) In the Diffusion Coefficient edit field, check Isotropic.

(vii) Locate c section and type 0.

(viii) Locate the Absorption Coefficient section.

(ix) Locate a section and type $(In-(1-u).6.V_g/L_{grid})*(T < T_{m2}\&\&u >= 0\&\&u <= 1)[s/m^2] + \tau[s/m^2] * (T >= T_{m2}||u > 1||u < 0)$.

(x) Locate the Source Term section.

(xi) Locate f section and type $In*(T < T_{m2}\&\&u >= 0\&\&u <= 1)[s/m^2]+0*(T >= T_{m2}||u < 0) + \tau[s/m^2] * (u > 1\&\&T < T_{m2})$.

(xii) Locate Mass Coefficient section.

(xiii) Locate ea section and type 0.

(xiv) Locate Damping or Mass Coefficient section.

(xv) Locate d_a section and type 1.

(xvi) In the Model Builder window, right-click Coefficient Form PDE (c) and choose Pairs¿Continuity.

(xvii) In the Continuity 1 setting windows, select Contact Pair 1 from the Pairs.

(xviii) In the Model Builder window, right-click Coefficient Form PDE (c) and choose Pairs¿Continuity.

(xix) In the Continuity 2 setting windows, select Contact Pair 2 from the Pairs.

(xx) In the Model Builder window, right-click Coefficient Form PDE (c) and choose Pairs¿Continuity.

(xxi) In the Continuity 3 setting windows, select Contact Pair 3 from the Pairs.

Initial Values 1:

(i) In the Model Builder window, select Coefficient Form PDE (c) under the Model 1 and choose Coefficient Form PDE 1 and click Initial values 1.
(ii) In the Initial values 1 setting windows, locate the Initial values section.
(iii) In the u edit field, type 1 (Here, we have to be careful because if our material initially is crystalline, this value is 1.

However if our material initially is amorphous, this value is 0).

A.1.5. Mesh 1

(i) In the Model Builder window, right-click Mesh 1 and choose Free Tetrahedral.
(ii) In the Free Tetrahedral setting windows, locate Domain Selection and choose 1 geometry from the Graphics.
(iii) In the Size setting windows under the Free Tetrahedral 1, locate Element Size and check Predefined box.
(iv) From the Predefined, choose Extra coarse.
(v) In the Model Builder window, right-click Mesh 1 and choose Free Tetrahedral.
(vi) In the Free Tetrahedral setting windows, locate Domain Selection and choose 4 geometry from the Graphics.
(vii) In the Size setting windows under the Free Tetrahedral 2, locate Element Size and check Custom box.
(viii) In the Element size Parameters setting windows, check the maximum element size and type $20e-9$ into the opening window.
(ix) In the Model Builder window, right-click Mesh 1 and choose Free Tetrahedral.
(x) In the Free Tetrahedral setting windows, locate Domain Selection and choose 3 geometry from the Graphics.
(xi) In the Size setting windows under the Free Tetrahedral 3, locate Element Size

and check Custom box.

(xii) In the Element size Parameters setting windows, check the maximum element size and type $10e-9$ into the opening window.

(xiii) In the Model Builder window, right-click Mesh 1 and choose Free Tetrahedral.

(xiv) In the Free Tetrahedral setting windows, locate Domain Selection and choose 2 geometry from the Graphics.

(xv) In the Size setting windows under the Free Tetrahedral 2, locate Element Size and check Custom box.

(xvi) In the Element size Parameters setting windows, check the maximum element size and type $20e-9$ into the opening window.

A.1.6. Study 1

(i) In the Model Builder window, select Study 1 under the Model 1.

(ii) From the Study 1, select Time Dependent.

(iii) In the Time Dependent setting window, locate the Study settings.

(iv) In the Studying edit field, type range(0,$1e-9$,$350e-9$)

NOTE: This time range can be changed according to the simulation time and pulse duration.

(v) In the Model Builder window, right-click Study 1 and choose Compute.

(vi) After finishing simulation, from the Results, select what you want.